Advancing Transgenic Neuromodulation Tools with Translational Positron Emission Tomography Applications

Matthew A. Boehm

B.S., University of St. Thomas, 2014

A dissertation submitted in partial fulfillment of the requirements
for the degree of Doctor of Philosophy in the Department of
Neuroscience at Brown University

Providence, Rhode Island
February 2023

This dissertation by Matthew A. Boehm is accepted in its present form by the
Department of Neuroscience as satisfying the dissertation requirement
for the degree of Doctor of Philosophy.

Date_______________ ______________________________________
Michael Michaelides, Ph.D., Advisor

Recommended to the Graduate Council

Date_______________ ______________________________________
Theresa Desrochers, Ph.D., Committee Chair

Date_______________ ______________________________________
Charles Bradberry, Ph.D., Reader (co-advisor)

Date_______________ ______________________________________
Elliot Stein, Ph.D., Reader (co-advisor)

Date_______________ ______________________________________
Peter Rapp, Ph.D., Reader (committee member)

Date_______________ ______________________________________
Omar Gharbawie, Ph.D., External Reader

Approved by the Graduate Council

Date_______________ ______________________________________
Thomas A. Lewis, Ph.D., Dean of the Graduate School

Matthew A. Boehm

Predoctoral IRTA Fellow
National Institute on Drug Abuse
251 Bayview Blvd, Rm: 05A505
Baltimore, MD 21224

Contact:
matthew.boehm@nih.gov
matthew_boehm@brown.edu
(763)-528-1273

EDUCATION

Graduate	**Ph.D. in Neuroscience** Brown-NIH Graduate Partnership Program Brown University, Providence RI NIDA-IRP, Baltimore, MD	*Feb 2023*
Undergraduate	**B.S. in Biology** Minors: Chemistry and Psychology *Suma cum laude* University of St. Thomas, St. Paul, MN	*May 2014*

RESEARCH EXPERIENCE

Predoctoral IRTA Fellow, National Institutes of Health *Oct 2017-present*
National Institute on Drug Abuse, Baltimore, MD

Research Advisors: Dr. Mike Michaelides, Dr. Charles Bradberry and Dr. Elliot Stein

- Developing and validating PET applications for imaging chemogenetic and optogenetic neuromodulation tools in rodents and NHPs.

NIH-GPP Research Rotation, National Institutes of Health *Aug-Sep 2017*
National Institute on Alcohol Abuse, Rockville, MD

Research Advisor: Dr. Andrew Holmes

- Investigated the role of serotonergic neurons (5-HT_2) projecting to the nucleus accumbens using optogenetics in a mouse behavioral model of risky decision-making.

NIH-GPP Research Rotation, National Institutes of Health *June-July 2017*
National Institute on Drug Abuse, Baltimore, MD

Research Advisor: Dr. Mike Michaelides

- Investigated the relationship between cocaine exposure and zinc metabolism in mice using a total reflection X-ray fluorescence spectrometer for trace element analysis.

Brown-GPP Research Rotation, Brown University, Providence, RI *Spring 2017*

Research Advisor: Dr. Stephanie Jones (Dept. of Neuroscience)

- Investigated the effects of transcranial alternating current stimulation with electroencephalography during a tactile stimulation task in human volunteers.

Brown-GPP Research Rotation, Brown University, Providence, RI *Fall 2016*

Research Advisor: Dr. Karla Kaun (Dept. of Neuroscience)

- Investigated the role of octopamine neurons in alcohol induced hyperlocomotion using a *Drosophila melanogaster* behavioral model in combination with optogenetics.

Student Research Assistant, University of St. Thomas, St. Paul, MN *2014-2015*

Research Advisor: Dr. J. Roxanne Prichard (Dept. of Psychology)

- Investigated the interactions of tobacco use, depression, and anxiety on sleep health in emerging adult populations.

Student Research Assistant, University of St. Thomas, St. Paul, MN *2013-2014*

Research Advisor: Dr. Leah M. Domine (Dept. of Biology)

- Developed and utilized a cost-efficient method for quantifying methane efflux emissions in prairie pothole wetlands.

PUBLICATIONS

Bonaventura J, **Boehm MA**, Jedema HP, Solís O, Pignatelli M, Song X, Richie CT, Zhang S, Gomez JL, Lam S, Morales M, Gharbawie OA, Pomper MG, Stein EA, Bradberry CW, Michaelides M. Noninvasive opsin localization predicts structural and functional brain connectivity. *Science Translational Medicine* (in revision).

Boehm MA, Bonaventura J, Gomez J, Solis O, Stein EA, Bradberry CW, and Michaelides M. (2021). Translational PET applications for brain circuit mapping with transgenic neuromodulation tools. *Pharmacology, Biochemistry and Behavior,* 204: 173147. https://doi.org/10.1016/j.pbb.2021.173147

Boehm, MA, Jedema, H, Bonaventura, J, Gharbawie, O, Gomez, J, Stein, EA, Bradberry, CW, and Michaelides, M. (2021). Validation of PET-compatible chemogenetic tools in squirrel monkeys. *Journal of Cerebral Blood Flow and Metabolism*, 41(1, suppl): p. 44. https://doi.org/10.1177/0271678X211061050

Hu F, Morris PJ, Bonaventura J, Fan H, Mathews WB, Holt DP, Lam S, **Boehm M**, Dannals RF, Pomper MG, Michaelides M, Horti AG. (2021). ^{18}F-labeled radiotracers for in vivo imaging of DREADD with positron emission tomography, *European Journal of Medicinal Chemistry* 113047, ISSN 0223-5234. https://doi.org/10.1016/j.ejmech.2020.113047

Bonaventura J, Lam S, Carlton M, **Boehm MA**, Gomez JL, Solís O, Sánchez-Soto M, Morris PJ, Fredriksson I, Thomas CJ, Sibley DR, Shaham Y, Zarate CA & Michaelides M. (2022). Reply to “Distinct functions of S-ketamine and R-ketamine in mediating biobehavioral processes of drug dependency: comments on Bonaventura et al” by Insop Shim. *Mol Psychiatry* (2022). https://doi.org/10.1038/s41380-022-01666-9

Bonaventura J, Lam S, Carlton M, **Boehm MA**, Gomez JL, Solís O, Sánchez-Soto M, Morris PJ, Fredriksson I, Thomas CJ, Sibley DR, Shaham Y, Zarate CA & Michaelides M. (2022). Reply to “Comments to pharmacological and behavioral divergence of ketamine enantiomers by Jordi Bonaventura et al.” by Chen et al.. *Mol Psychiatry* 27, 1863–1865 (2022). https://doi.org/10.1038/s41380-022-01480-3

Bonaventura J, Lam S, Carlton M, **Boehm MA**, Gomez JL, Solís O, Sánchez-Soto M, Morris PJ, Fredriksson I, Thomas CJ, Sibley DR, Shaham Y, Zarate CA & Michaelides M. (2021). Pharmacological and behavioral divergence of ketamine enantiomers: implications for abuse liability. *Molecular Psychiatry,* https://doi.org/10.1038/s41380-021-01093-2

Roseboom PH, Mueller SAL, Oler JA, Fox AS, Riedel MK, Elam VR, Olsen ME, Gomez JL, **Boehm MA,** DiFilippo AH, Christian BT, Michaelides M, Kalin NH. (2021). Evidence in primates supporting the use of chemogenetics for the treatment of human refractory neuropsychiatric disorders. *Molecular Therapy*, 29(8): https://doi.org/10.1016/j.ymthe.2021.04.021

Bonaventura J, Eldridge M, Hu F, Gomez J, Sanchez-Soto M, Abramyan A, Lam S, **Boehm MA**, Ruiz C, Farrell M, Moreno A, Faress IM, Andersen N, Lin J, Moaddel R, Morris P, Shi L, Sibley DR, Mahler S, Nabavi S, Pomper M, Bonci A, Horti A, Richmond B, Michaelides, M. (2019). High-potency ligands for DREADD imaging and activation in rodents and monkeys. *Nature Communications,* 10: 4627. https://doi.org/10.1038/s41467-019-12236-z

Boehm MA, Lei QM, Lloyd RM, Prichard JR. (2016). Depression, anxiety and tobacco use: overlapping impediments to sleep in a national sample of college students. *Journal of American College Health* 64(7): 565-574 https://doi.org/10.1080/07448481.2016.1205073

PRESENTATIONS

Conference Presentations:

Boehm M, Levinstein M, Stein EA, and Michaelides M. A dual chemogenetic strategy for cell-type specific bidirectional neuromodulation. Accepted for poster presentation at: *Society for Neuroscience Annual Meeting*, San Diego, CA, Nov 16, 2022

Boehm MA, Jedema H, Bonaventura J, Gharbawie O, Gomez J, Stein EA, Bradberry CW, Mike Michaelides. Validation of PET-compatible chemogenetic tools in squirrel monkeys. Oral presentation, *International Symposium of Functional Neuroreceptor Mapping (NRM)* virtual meeting, Dec 14, 2021

Boehm MA, Bonaventura J, Gomez J, Jedema H, Solís O, Stein EA, Bradberry CW, Michaelides M. PET compatible opsins for translational optogenetics*.* Poster presentation, *Society for Neuroscience Annual Meeting,* virtual, Nov 5, 2021

Boehm MA, Bonaventura J, Gomez J, Jedema H, Lu H, Stein EA, Bradberry CW, Michaelides M. Advancing translational chemogenetic tools using positron emission tomography*.* Poster presentation*, Society for Neuroscience Annual Meeting*, Chicago, IL, Oct 20, 2019

Boehm MA, Effinger D. History of psychedelics in neuroscience – from 19th century to modern medicine. Poster presentation, *Society for Neuroscience Annual Meeting*, Chicago, IL, Oct 19, 2019

Boehm MA, Justinova Z, Gomez J, Bonaventura J, Jedema H, Michaelides M, Bradberry CW, Stein EA. A closer look at transcranial magnetic stimulation through in vivo neuroimaging. Poster presentation, *Society for Neuroscience Annual Meeting*, San Diego, CA, Nov 5, 2018

Boehm MA, Novaczyk Z, Domine L, Cotner JB. Prairie pothole wetlands are important sources of methane to the atmosphere*.* Poster presentation, *Ecological Society of America Meeting*, Sacramento, CA, Aug 14, 2014

Prichard JR, **Boehm MA,** Lei QM. Depression, anxiety and tobacco use: overlapping impediments to sleep in a national sample of college students. Poster presentation, *Associated Professional Sleep Societies' Annual SLEEP Meeting*, Minneapolis, MN, June 2, 2014

Other Presentations:

"Translational PET applications for transgenic neuromodulation tools". Oral presentation, Brown-NIH Graduate Partnership Program Seminar, virtual, Feb 23, 2022

"Advancing optogenetic tools with PET compatible opsins". Poster presentation, NIH Graduate Research Symposium, virtual, Feb 18, 2022

"ChRERα – A novel PET compatible opsin for translational optogenetics". Poster presentation, NIDA-IRP Poster day, virtual, May 19, 2021

"A novel PET compatible opsin for translational optogenetics". Oral presentation, Brown-NIH Graduate Partnership Program Seminar, virtual, Jan 15, 2021

"Advancing novel neuromodulation tools using positron emission tomography". Oral presentation, Brown University In-House Seminar Series, Providence, RI, Jan 21, 2020

"Improving neuromodulation methods in nonhuman primates". Brown-NIH Graduate Partnership Program Seminar, Bethesda, MD, April 19, 2019

"A closer look at Transcranial Magnetic Stimulation through in vivo neuroimaging" Brown University In-House Seminar Series, Providence, RI, April 27, 2018

TEACHING EXPERIENCE

Sheridan Center for Teaching and Learning, Brown Univ, Providence, RI *Fall 2021*

Supervisor: Dr. Mary Wright

- Completed 9-week workshop on teaching at college/university level
- Topics covered: Bloom's taxonomy/learning objectives, creating an inclusive classroom, critical reflection on teaching outcomes, active learning strategies
- Activities: Designing lesson plans/syllabus in field of study (i.e., neuroscience), writing a teaching philosophy statement, practice teaching session

Teaching Assistant, Dept. of Biology, Univ. of St. Thomas, St. Paul, MN *2012-2013*

Supervisor: Anthony Lewno

- Assisted/graded undergraduates in laboratory activities for two biology courses
- *General Biology* (2 semesters)
- *Biological Communication & Energetics* (2 semesters)

STEM Learning Community Leader, Dept of Biology, Univ. of St. Thomas *2011-2013*

Supervisor: Dr. Dayius Turvold Celotta

- Led study groups for undergraduate students in two core biology courses
- *Genetics, Ecology & Evolution* (2 semesters)
- *Biological Communication & Energetics* (2 semesters)

INDUSTRY EXPERIENCE

Associate Laboratory Technician, WuXi AppTec, St. Paul, MN *2015-2016*

Supervisor: Joshua Kamrud

- Performed operations to maintain mammalian cell culture lines for in vitro testing
- Performed in vitro toxicology assays for testing medical devices/materials
- Experience with GLP and aseptic technique in BSL-2 lab

AWARDS AND DISTINCTIONS

Predoctoral Intramural Research Training Award National Institutes of Health, Bethesda, MD	*2016 - Present*
NIDA Outstanding Poster Award National Institute on Drug Abuse, Baltimore MD	2021
Summa cum laude, University of St. Thomas, St. Paul, MN	*2014*
Paul Germann Scholarship, Dept. of Biology, University of St. Thomas	2013
E.D.G.E. Award, Biology Department, University of St. Thomas	*2011*
Wallin Scholarship, Wallin Education Partners, Minneapolis, MN	*2010*

CONFERENCES ATTENDED

Society for Neuroscience Annual Meeting, San Diego, CA	*Nov, 2022*
International Symposium of Functional Neuroreceptor Mapping, Virtual	*Dec, 2021*
Society for Neuroscience Annual Meeting, Virtual	*Nov, 2021*
Society for Neuroscience Annual Meeting, Chicago, IL	*October, 2019*
Society for Neuroscience Annual Meeting, San Diego, CA	*November, 2018*
Society for Neuroscience Annual Meeting, Washington, D.C.	*November, 2017*
Society for Neuroscience Annual Meeting, San Diego, CA	*November, 2016*
Ecological Society of America Annual Meeting, Sacramento,	*August, 2014*
Associated Professional Sleep Societies SLEEP Meeting, MN	*May-June, 2014*

ACKOWLEDGEMENTS

Brown University Dept. of Neuroscience and the NIH Graduate Partnership Program

Mike Michaelides as primary advisor/mentor at NIDA-IRP

Charles Bradberry and Elliot Stein as co-advisors at NIDA-IRP

Theresa Desrochers as thesis committee chair at Brown University

Jordi Bonaventura (Univ of Barcelona) for invaluable training and research contributions

Hank Jedema (NIDA-IRP) for major contributions in squirrel monkey experiments

Current and former BIMN/Michaelides lab members (Juan Gomez, Oscar Solís, Marjorie Levinstein, Emilya Ventriglia, Reece Budinich, Fallon Curry, Meghan Carlson, Sherry Lam, Dondre Marble and Kelsey Wright).

NIDA-IRP Neuroimaging Research Branch

NIDA-IRP Genetic Engineering and Viral Vector Core (Chris Ritchie)

NIDA-IRP Confocal and Electron Microscopy Core (Shiliang Zhang, NIDA-IRP CEMC)

NIDA-IRP vet staff (Dr. Ira Baum, Dr. Jazmyne Taylor and Phil White)

OITE Staff (Sharon Milgram, Phil Wang, Phil Ryan, Laura Marler)

Support of friends and family, especially my partner Kathleen Huntzicker, parents Ellen and Don, sister Morgan and the Kastl family.

TABLE OF CONTENTS

Signature Page……………………………………………………………….…………………iii

Curriculum Vitae…………………………………………………….……..…………………iv

Acknowledgements…………………………………………….…………………..……x

Table of Contents…………………………………..…………………...………………xi

List of Tables and Figures…………..…………………………………………..………xv

Chapter 1: Introduction……………………………………………………………………1

1.1 Transgenic Neuromodulation Technologies……..……………………………………...2

1.1.1 Genetically engineered transgenes and viral vector targeting…...……..…..4

1.1.2 Chemogenetic neuromodulation tools…………..……………………..……7

1.1.3 Optogenetic neuromodulation tools……………..………………………...…9

1.1.4 Obstacles for translational and clinical applications………………………....10

1.2 PET Applications for Brain Imaging…………..…………………….……………..…..11

1.2.1 Overview of PET imaging in neuroscience and medicine……….........…...11

1.2.2 Measuring brain activity with FDG-PET………………………..………..…12

1.2.3 Combining FDG-PET with transgenic neuromodulation tools for metabolic mapping of brain circuits……………………………………………………......15

1.2.4 Localizing chemogenetic receptor expression with PET-reporters……..…17

1.2.5 Other PET-reporters for mapping transgene expression………..……..….21

1.3 Summary and Significance…………………..……………………………………....23

1.3.1 Improving the translational capacity of transgenic tools……….…………...23

1.3.2 Conclusions and future directions…………………..………………………24

1.4 Table and Figures for Chapter 1..…………………………………………………..….26

1.5 References……………………………………………………...…………….……..31

Chapter 2: Developing a Novel PET Compatible Opsin for Translational Optogenetics……………………………………………………………………41

2.1 Abstract……………………………………………………………………………42

2.2 Introduction………………………………………………………………………43

2.3 Results……………………………………………………………………………46

2.3.1 In vitro characterization of ChRERα binding and function……………46

2.3.2 ChRERα trafficking and subcellular localization in the rat brain…………47

2.3.3 ChRERα activation alters brain activity and behavior in rodents…………48

2.3.4 FES-PET localizes ChRERα in the brain of individual rats………………50

2.3.5 FES-PET localizes ChRERα in NHPs and predicts structural and functional brain connectivity……………………………………………52

2.4 Discussion…………………………………………………………………………55

2.5 Methods……………………………………………………………………………59

2.6 Figures for Chapter 2……………………………………………………………70

2.7 Acknowledgements………………………………………………………………81

2.8 References…………………………………………………………………………82

Chapter 3: Developing a Dual Chemogenetics Approach for Bidirectional Neuromodulation in Rodents and NHPs…………………………………………88

3.1 Abstract……………………………………………………………………………89

3.2 Introduction………………………………………………………………………90

3.3 Results……………………………………………………………………………95

3.3.1 AAV-mediated co-expression of hM3Dq and PSAM^4-GlyR in rat brain.....95

3.3.2 Measuring effects of hM3Dq and PSAM^4-GlyR agonism on brain activity with FDG-PET in rats………………………………………96

3.3.3 Chemogenetic induced locomotor effects in rats……………………….…...….97
3.3.4 Imaging hM3Dq with [^{18}F]J07 and PSAM^{4}-GlyR with [^{18}F]ASEM in rats….....98
3.3.5. Dual imaging of hM3Dq and PSAM^{4}-GlyR with [^{18}F]J07 and [^{18}F]ASEM in squirrel monkeys ……………………..…………………………..……99
3.3.6 Measuring effects of J60 and uPSEM^{817} on brain activity in squirrel monkeys with FDG-PET (pre- and post-AAVs)…..……………..………102
3.4 Discussion………………………………………………………..………..………103
3.5 Methods………………………………….……………….……….…………110
3.6 Figures for Chapter 3……………….…………….…………………..……113
3.7 Acknowledgements……………..………………………….….…………123
3.8 References……………………………………….……….…………….124

Chapter 4: Discussion and Future Directions

Chapter 4: Discussion and Future Directions…………………………………………128
4.1 Summary of Optogenetic Experiments…………………………..…………………129
4.1.1 ChRERα – the first PET-compatible opsin…………………………………129
4.1.2 Adapting ERαLBD/FES PET-reporter system to image other opsins……130
4.2 Summary of Chemogenetic Experiments………..…………………………………131
4.2.1 Developing a dual chemogenetics approach using DREADDs and PSAMs for bidirectional neuromodulation …………..………………………………131
4.3 Comparing [^{18}F]FES, [^{18}F]J07, and [^{18}F]ASEM for Imaging Transgenic Receptor/Opsin Expression……………………………….……………………134
4.4 Applications and Significance………………………………………………….…136
4.4.1 Characterizing structural/functional connectivity relationships………..…136
4.4.2 Advancing optogenetic/chemogenetic capabilities for NHP research…..137

4.4.3 Translational potential - imaging gene therapy technologies……………138

4.5 Limitations and Future Directions……………………………………………140

4.5.1 Refining transgene delivery systems……………………………………140

4.5.2 Strategies for improving sensitivity and specificity of imaging transgenes using PET-reporters………………………………………………………141

4.6 Conclusions…………………………………………………………………………142

4.7 References…………………………………………………………………………143

Appendix A: Supplementary Figures for Chapter 2……………………………146

Appendix B: Adapting the ERαLBD/FES PET-reporter system to other constructs……152

Appendix C: Supplementary Figures for Chapter 3……………………………..154

Appendix D: Supplementary Figures for Chapter 4……………………………..160

List of Tables and Figures

Chapter 1. Introduction

Table 1. *PET applications for brain imaging and example radiotracers*…………………...26

Figure 1*.* *Neuromodulation with chemogenetic and optogenetics tools*……………........27

Figure 2. *FDG-PET for measuring brain activity*…………………………………….......28

Figure 3. *PET-reporters for in vivo mapping of chemogenetic receptor expression*….29

Chapter 2: Developing PET-compatible Opsins for Translational Optogenetics

Figure 1. *Development and in vitro characterization of ChRERα binding and function*.....70

Figure 2. *ChRERα trafficking and subcellular localization in the rat brain*…………….71

Figure 3. *ChRERα activation alters brain activity and behavior in rodents*……………72

Figure 4. *Noninvasive localization of ChRERα in the brain of individual rats…………74*

Figure 5. *Localizing ChRERα in squirrel monkeys with [^{18}F]FES*…..…………………..76

Figure 6. *Subcellular ChRERα localization in left M1 and PPC in squirrel monkey*…..78

Figure 7. *[^{18}F]FES-PET and ChRERα predict functional brain connectivity in monkeys*…80

Chapter 3: Developing a Dual Chemogenetics Approach for Bidirectional Neuromodulation in Rodents and NHPs

Figure 1. *AAV-mediated co-expression of hM3Dq and PSAM^{4}-GlyR in left M1 of rat*…..113

Figure 2. *Measuring effects of hM3Dq and PSAM4-GlyR on brain activity with FDG-PET*……………………………………………………………………….114

Figure 3*.* *PSAM^{4}-GlyR and hM3Dq actuation produce distinct effects on locomotor behavior in rats*…………………………………………………………………116

Figure 4. *PET localization of hM3Dq and PSAM^{4}-GlyR in rat M1 with [^{18}F]J07 and [^{18}F]ASEM coincides with immunofluorescent labeling in post-mortem histology*…118

Figure 5. *Localizing hM3Dq and PSAM4-GlyR expression in squirrel monkeys with [^{18}F]J07 and [^{18}F]ASEM*…………………………………………………………..120

Figure 6. *Measuring effects of hM3Dq and PSAM4-GlyR on brain activity with FDG-PET in squirrel monkeys*…………………………………………………...121

Appendix A. Supplemental Figures for Chapter 2

Figure A1. *Anti-ChR2 IHC and immuno-EM confirm ChRERα expression in the right AAV site and downstream projection areas in rats, related to Ch2-Fig. 2*….146

Figure A2. *Effects of light stimulation on brain activity in ChRERα vs. Control Rats using FDG-PET, related to Ch2-Fig. 3*……………………………………..….147

Figure A3. *Visualizing ChRERα in rats with [18F]FES-PET (SUV and SUVR), related to Ch2-Fig.4*………………………………………………………..148

Figure A4. *Visualizing ChRERα in squirrel monkeys with [18F]FES-PET, related to Ch2-Fig. 5*…………………………………………………………...149

Figure A5. *Anti-ChR2 IHC and immuno-EM confirm ChRERα expression in contralateral M1 in squirrel monkey, related to Ch2-Fig. 6*…………………151

Appendix B. Adapting the ERαLBD/[^{18}F]FES PET-reporter system to image other transgenic constructs

Figure B1. *Attaching ERαLBD to image red-light sensitive opsins (i.e., ChRmine)*….152

Figure B2. *Imaging other transgenic constructs with ERαLBD and [18F]FES-PET (i.e., PSAM-ERα and JAWS-ERα)*……………………………………..153

Appendix C. Supplementary Figures for Chapter 3

Figure C1. *FDG-PET in hM3Dq/PSAM^{4}-GlyR rats following saline or 0.1mg/kg J60 or uPSEM^{817}*……………………………………………………….……..154

Figure C2. *Localizing hM3Dq and PSAM4-GlyR in rats with [^{18}F]J07 and [^{18}F]ASEM*….155

Figure C3. *Pre-AAV FDG-PET scans in squirrel monkeys*……………………………..157

Figure C4. *Pre-AAV [^{18}F]ASEM and [^{18}F]J07 PET scans in squirrel monkeys*……….159

Appendix D. Supplementary Figures for Chapter 4

Figure D1. *Endogenous binding comparison of [^{18}F]ASEM, [^{18}F]J07 and [^{18}F]FES in pre-AAV squirrel monkeys*…………………………………………………....160

Figure D2. *A comparison of [^{18}F]J07, [^{18}F]ASEM and [^{18}F]FES for localizing transgene expression in squirrel monkeys*……………………………………………….161

Figure D3. *Baseline image subtraction method with FES-PET improves S:N for cleaner ChRERa visualization in squirrel monkey*……………………………………163

Chapter 1: Introduction

This chapter was adapted from the following publication:

Matthew A. Boehm.[1,2], Jordi Bonaventura[1], Juan L. Gomez[1], Oscar Solís[1], Elliot A. Stein[1], Charles W. Bradberry[1], Michael Michaelides[1,3]. Translational PET applications for brain circuit mapping with transgenic neuromodulation tools. *Pharmacology Biochemistry & Behavior*. 204: 173147. (2021). https://doi.org/10.1016/j.pbb.2021.173147

[1] : National Institute on Drug Abuse Intramural Research Program, Neuroimaging Research Branch, 251 Bayview Blvd, Baltimore, MD 21224, USA
[2] : Department of Neuroscience, Brown University, Providence, RI 02906, USA
[3] : Department of Psychiatry & Behavioral Sciences, Johns Hopkins School of Medicine, Baltimore, MD, 21202, USA

1.1 Transgenic neuromodulation technologies

The ability to manipulate neuronal activity with precise spatial and temporal control is essential for interrogating the neurobiological mechanisms underlying behavior and nervous system processes. Modern developments in transgenic neuromodulation technologies (i.e., chemogenetics and optogenetics) have transformed neuroscience research by enabling the manipulation of neuronal populations and circuits with incredible specificity in awake behaving subjects. Innovative genetic targeting strategies (e.g., viral vector serotypes, cell-type specific promoter/enhancer sequences, recombinase inducible transcription systems) can be used to transduce specific cell populations with transgenes encoding proteins whose expression can alter neuronal activity with administration of a selective compound (i.e., chemogenetics) or controlled light stimulation (i.e., optogenetics). The ability to map highly specific neuroanatomical projections and manipulate neuronal activity in investigational settings has opened the door to explore novel clinical interventions (Assaf and Schiller, 2019; Curado et al., 2020; Iyer et al., 2016; Kätzel et al., 2014; Weir et al., 2017). However, safe and reliable strategies for delivering and monitoring transgenic tools are needed to enhance the translational potential of chemogenetic and optogenetic technologies.

Chemogenetic neuromodulation is based on the premise that a neuronal system can be manipulated by introduction and expression of an exogenous transgenic receptor that responds selectively to an otherwise inert agonist. Ideally, chemogenetic receptor constructs should lack constitutive activity and be unaffected by endogenous neurotransmitters. In conjunction, ideal chemogenetic agonists should be potent and selective for their respective chemogenetic receptors and lack affinity for endogenous receptors to avoid off-target effects. Although some instances of constitutive activity have been observed and complete binding specificity has not yet been achieved (MacLaren et al., 2016; Saloman et al., 2016), several systems have demonstrated sufficient selectivity to allow effective chemogenetic applications (Armbruster et al., 2007; Magnus et al., 2019; Marchant et al., 2016; Vardy et al., 2015). These systems are well suited for sustained neuromodulation in freely moving subjects with titratable effects that can last hours depending on the chemogenetic compound dosage, route of administration, chemical half-life and duration of exposure (Grund et al., 2019; Magnus et al., 2019; Stachniak et al., 2014). Although these tools are ideal for use in untethered animal behavioral experiments, chemogenetic technologies lack the temporal control required to interrogate temporally precise brain processes and behaviors.

In contrast, optogenetic neuromodulation systems can be used to manipulate neuronal activity with exceptional temporal precision. These tools rely on the transduction and expression of light sensitive transmembrane opsins that open or close ion channels in response to light stimulation (Boyden et al., 2005; Zhang et al., 2006, 2007). When expressed in neurons, these transgenic opsins can promote or inhibit cell firing of action potentials and can be utilized for spatiotemporally refined brain circuit manipulations. However, light delivery usually requires optical fiber implantation and tethering, which restricts the range of behavioral models that can be assessed during optogenetic manipulation of neuronal activity (Deisseroth, 2011; Tye and Deisseroth, 2012). In addition, overexpression of transgenic opsins can be damaging to cells and can affect endogenous receptors when light stimulation is administered at high intensities for long periods of time (Yizhar et al., 2011; Zimmermann et al., 2008). Moreover, the necessity of delivering light to target brain areas presents an obstacle for translational and clinical applications.

Despite their limitations, innovative applications of chemogenetic and optogenetic technologies have opened a new range of possibilities in preclinical research, and the potential for developing translational and clinical applications is becoming actualizable. For example, chemogenetic and optogenetic tools have been proposed as potential treatments for sleep apnea (Curado et al., 2020), pain (Iyer et al., 2016; Weir et al., 2017), epilepsy (Kätzel et al., 2014), vision restoration (Gaub et al., 2015) and neurodegenerative disorders (Assaf and Schiller, 2019). However, new strategies for implementing and monitoring transgenic tools are needed for safe and effective use in humans. One major challenge is the fundamental need to track the location and function of chemogenetic receptors and opsins noninvasively and longitudinally in vivo, and we propose translational molecular imaging with positron emission tomography (PET) can be leveraged to safely monitor such transgenic constructs for this purpose. Recent studies demonstrate the use of PET for characterizing the functional effects of chemogenetic and optogenetic stimulation on brain activity, while development of selective PET-reporter molecules enable innocuous visualization of chemogenetic receptor location and occupancy (Bonaventura et al., 2019; Magnus et al., 2019; Nagai et al., 2020). This introduction summarizes current research combining the use of transgenic tools with PET imaging for in vivo mapping and manipulation of brain circuits and outlines future directions for translational applications.

1.1.1 Genetically engineered transgenes and viral vector targeting

Recent advancements in gene editing technologies and delivery systems allow precise engineering of DNA constructs (i.e., transgenes) that can be packaged in recombinant viral vectors (i.e., capsids lacking viral DNA) for transduction into cells. Transgene expression can be directed to specific neuronal populations to enable targeted brain manipulations with chemogenetic and optogenetic tools (see Fig. 1A). Most preclinical studies utilize recombinant adeno-associated viruses (AAVs) for transgene delivery because these vectors are relatively versatile and safe to use, although methods with lentiviral vectors have also been effectively implemented (Frecha et al., 2008; Taymans et al., 2007). AAV serotypes with distinct transduction properties can be combined with various targeting strategies to direct transgene expression to specific cell populations based on anatomical projections, genetic identifiers, and/or inducible activation systems (Rothermel et al., 2013; Shevtosa et al., 2005; Tague et al., 2018). One commonly used approach is to employ distinct genetic promoter sequences as a practical and effective method for targeting specific cell types (Luo et al., 2008). Available promotor sequences include the human synapsin (hSyn) 1 promoter for pan-neuronal expression, CaMKII for targeting excitatory neurons, GAD67 and mDlx for GABAergic interneurons, and DRD1a for cells expressing dopamine D1 receptors (Dimidschstein et al., 2016; Durieux et al., 2011; Kügler et al., 2003; Watakabe et al., 2015).

Additional strategies for targeted transgene expression include the use of inducible transcription systems and recombinase dependent systems (e.g., Cre-loxP, Dre-rox, Flp-recombinase). These systems can be employed through the development of transgenic animal lines such as mouse strains engineered to express a recombinase in specific cells. For example, in transgenic D1-Cre recombinase mice, an AAV containing DNA strands with two loxP sites flanking a gene of interest (e.g., chemogenetic or optogenetic transgenes) can be injected into a target brain region, such that expression of the transgene will only occur in cells that also express Cre recombinase under control of the dopamine D1 receptor promoter (Saunders et al., 2012). However, this approach is largely restricted to rodents because of breeding logistics necessary for developing transgenic animal lines.

Alternatively, inducible transcription systems can be applied through dual injection strategies such as the use of Cre recombinase and loxP containing vectors in multiple brain sites to target the projection areas of specific cell populations. For example, Oguchi et al., 2015 demonstrated a double injection technique with two different AAVs to express a transgene in the prefrontal network of macaques in a projection-specific manner. A local vector incorporated the Cre-On double floxed sequence while a retrograde vector containing Cre recombinase was injected at downstream axon terminals, therefore only cell bodies with projections to areas with the second vector expressed the given transgene. This latter intersectional approach is more widely applicable than the use of transgenic animal lines for translational purposes because it can be more readily implemented in non-transgenic animals and NHPs (O'Shea et al., 2018).

Nonetheless, conventional use of AAV vectors in the brain require intracranial injections, which are invasive and substantially restrict practical applications in humans. The development of AAVs capable of delivering genes through systemic or intravenous administration may provide a solution to this translational obstacle by circumventing the need for intracranial injections. Efforts are underway to develop new AAV capsid variants such as AAV-PHP capsids that can be used for noninvasive targeted gene delivery throughout the peripheral and central nervous system (Bedbrook et al., 2018; Challis et al., 2019; Chan et al., 2017). Altogether, genetic engineering technologies provide a wide array of targeted transduction approaches to express transgenic constructs (i.e., chemogenetic receptors and opsins) in specific cell populations and circuits, and advancements in this field aim to bolster the translational potential of neuromodulation with these tools.

1.1.2 Chemogenetic neuromodulation tools

The term chemogenetics encompasses the process of genetically engineering macromolecules to selectively interact with and respond to specific chemical stimuli. Chemogenetic neuromodulation techniques have mainly been used for interrogating the role of neuronal activity in preclinical research and are especially useful in animal behavioral models (Burnett and Krashes, 2016; Smith et al., 2016; Sternson and Roth, 2014). The most widely used chemogenetic tools rely on the transduction and expression of exogenous transgenic receptors (e.g., modified G protein-coupled receptors (GPCRs) and ligand-gated ion channels (LGICs)) that can promote or inhibit neuronal activity upon administration of a highly potent and selective compound (Armbruster et al., 2007; Conklin et al., 2008; Wess et al., 2013). Although they lack the temporal control of other neuromodulation techniques such as optogenetics, these tools are well suited for sustained brain circuit modulations in freely behaving subjects (see Fig. 1B).

One of the primary types of chemogenetic systems used in neuroscience research are designer receptors exclusively activated by designer drugs (DREADDs). This technology utilizes mutant versions of specific GPCRs that are activated by selective chemogenetic actuator ligands instead of endogenous ligands (Pei et al., 2008). Some DREADD systems utilize mutated human muscarinic acetylcholine receptors (Armbruster et al., 2007), while others adapt GPCRs such as opioid or adrenergic receptors (Conklin et al., 2008; Vardy et al., 2015). These tools can be used to excite or inhibit neuronal activity depending on the type of receptor-coupling used. For instance, activation of the hM3Dq receptor initiates Gq protein signaling which promotes intracellular calcium release and consequently increases neuronal activity. In contrast, the hM4Di receptor can decrease neuronal activity through the activation of inhibitory Gi/o proteins (Lee et al., 2014). DREADDs were first shown to be activated by clozapine-N-oxide (CNO) (Armbruster et al., 2007) and later in vivo by clozapine (an FDA approved drug) converted from the administered CNO (Gomez et al., 2017). Although multiple effective DREADD actuators exist, some have been shown to produce off-target effects at doses relevant for activating DREADDs (MacLaren et al., 2016), and therefore efforts to improve the potency and selectivity of DREADD ligands has been a continued focus in the field. A series of compounds for DREADDs was developed through testing the structure-activity relationships of CNO analogs such as C21 (Chen et al., 2015; Thompson et al., 2018), and various others have been identified as potent DREADD agonists with relatively favorable selectivity including deschloroclozapine (DCZ), fluorinated clozapine analogs (i.e., JHU37160) and the FDA approved drug olanzapine (Bonaventura et al., 2019; Nagai et al., 2020; Weston et al., 2019). Nonetheless, dose ranges need to be carefully considered to minimize off-target effects of chemogenetic agonists (Upright and Baxter, 2020).

Aside from DREADDs, another form of chemogenetic system utilizes the ligand binding domain of the α7 nicotinic acetylcholine receptor (nAChR) coupled with the ion pore domains of other LGICs. These hybrid modular receptors are termed pharmacologically selective actuator modules (PSAMs), and they are activated through the binding of pharmacologically selective effector molecules (PSEMs) (Magnus et al., 2011). The latest generation of PSAMs (PSAM^4) were recently developed through screening various mutations in the α7 nAChR ligand binding domain in search of enhanced channel interaction with the smoking cessation drug varenicline (Magnus et al., 2019). By combining these modified binding domains with various ion pore domains, chimeric LGICs were created to modulate neuronal activity in response to varenicline at concentrations much lower than the dosage used in clinical treatments targeting endogenous nicotinic receptors (Kaur et al., 2009; Rollema et al., 2010). The two most well characterized of these PSAMs, PSAM^4-GlyR and PSAM4-5HT3, utilize the glycine receptor chloride channel (GlyR) and the serotonin cation channel (5-HT3R) and are intended to decrease or increase neuronal activity, respectively, although overall effects may vary if altering GABAergic inhibition (Magnus et al., 2019; Gantz et al., 2020). Like clozapine and olanzapine for DREADDs, the ability for selective activation of PSAMs using varenicline (an FDA approved drug) extends the translational potential of these chemogenetic tools for use in humans.

1.1.3 Optogenetic neuromodulation tools

In contrast to chemogenetic tools, optogenetic neuromodulation enables precise spatiotemporal manipulation of brain activity through the expression of transmembrane opsins with light sensitive ion channels that excite or inhibit neuronal cells in response to light (see Fig. 1C) (Boyden et al., 2005; Zhang et al., 2006, 2007). To date, a variety of opsins with unique characteristics have been developed to permit excitation or inhibition of neuronal activity (e.g., channelrhodopsins and halorhodopsins). These opsins can be engineered to be permeable to different ions, distinct in their kinetics and sensitive to light at specific wavelengths (see reviews Duebel et al., 2015; Lin, 2011). Optogenetics can be used to interrogate precise neuronal and circuit processes when applied to in vitro neuronal networks, in situ brain slices and in vivo experiments in anesthetized or awake behaving animals (Deisseroth, 2011; Mattis et al., 2012). Although optogenetic techniques allow excellent spatiotemporal control of neuronal manipulations, conventional light delivery usually necessitates hardware implantation and tethered animals. This restricts the range of applications that can be assessed during light-induced alterations in neuronal activity. In addition, the physical presence of implants or heat resulting from prolonged light stimulation can be damaging to cells (including those without opsins), and the need for targeted light delivery in brain tissue presents an obstacle for translational applications in larger subjects such as NHPs and in humans (Williams and Denison, 2013; Yizhar et al., 2011). Unsurprisingly, in vivo optogenetic technologies have predominately been developed in rodents thus far. Applications in NHPs have progressed more slowly due to a variety of practical obstacles (i.e., lack of techniques for verifying transduction efficacy and transgene expression in vivo), but a recently launched open resource platform may facilitate the ability of NHP researchers to compare and optimize methods (Bliss-Moreau et al., 2020; Tremblay et al., 2020). Despite the challenges, optogenetics has been effectively applied in numerous NHP neuroscience studies, and the clinical use of opsins is already being implemented for vision restoration in patients with retinitis pigmentosa (Busskamp et al., 2012; RetroSense Clinical trial #NCT02556736). Continuing efforts are underway to improve translational potential by fine-tuning viral vector efficacy, enhancing the sensitivity of opsins at longer wavelengths, and developing wireless or skull permeant light sources (Büning and Srivastava, 2019; Chen et al., 2020; Wang et al., 2020).

1.1.4 Obstacles for translational and clinical applications

The rapid expansion and ongoing refinement of chemogenetic and optogenetic technologies presents an opportunity to develop transgenic neuromodulation applications for human therapies. Pathologies such as epilepsy, chronic pain, and Parkinson’s disease, which currently have poor therapeutic prognoses, are ideal candidates for such approaches (Alcacer et al., 2017; Iyer et al., 2016; Walker and Kullman, 2020). However, a major obstacle for practical use in translational models (i.e., NHPs) and in humans is the need to monitor the location and function of chemogenetic receptors and opsins in vivo noninvasively and longitudinally. Conventional practices for confirming the expression of transgenic proteins in preclinical settings mainly rely on postmortem histology. When euthanasia is not desirable, such as in longitudinal experiments in NHPs, invasive in vivo techniques (e.g., calcium imaging, fiber photometry, implanted recording electrodes) can be used to indirectly assess transgene expression. However, aside from being intrusive, these indirect approaches are of low throughput and do not allow for assessing transgene expression directly, which is particularly important when studying novel transgenes or developing new vectors for transgene delivery. As such, the development of minimally invasive and longitudinal monitoring strategies is necessary to improve the translational potential and application of these tools in NHPs and humans. We suggest the versatile translational molecular imaging capabilities of positron emission tomography (PET) may offer solutions to these challenges. Recent developments in the field demonstrate how PET imaging techniques can be leveraged to monitor chemogenetic receptor expression and function as well as functional effects of optogenetic stimulation for translational brain circuit mapping and manipulation. The following sections describe various applications of PET imaging for in vivo mapping and manipulation of neuronal circuits with transgenic tools, highlighting recent advancements in the field that may facilitate chemogenetic and optogenetic applications in translational models and potentially human therapies.

1.2 PET applications for brain imaging

1.2.1 Overview of PET imaging in neuroscience and medicine

PET is a translational molecular imaging modality with a diverse range of applications in neuroscience and medicine (Zimmer and Luxen, 2012). PET imaging relies on the injection of biologically relevant radiolabeled compounds (radiotracers) that produce gamma ray photons upon radioactive decay. When positrons emitted by the radiotracer collide with electrons in annihilation events, pairs of 511 keV photons are released at ~180° angles and detected by an array of photodetectors surrounding the subject, and these events can be computed to reconstruct three-dimensional volumetric and dynamic parametric images (Saha, 2005). The translational and repeatable nature of PET along with the extensive variety of compounds amenable for radiolabeling makes it a uniquely versatile tool for imaging neurobiological functions in vivo. However, radioactive decay of PET radiotracers necessitates their production be near the location of use, and therefore applications are restricted to select facilities. Radionuclides are primarily generated in particle accelerators called cyclotrons, and PET radiotracers typically incorporate [^{15}O], [^{13}N], [^{11}C], or [^{18}F], which are radioisotopes with half-lives of ~2-min, 10-min, 20-min, and 110-min, respectively. To date, over 200 PET radiotracers have been described for various types of brain imaging, with radiolabeled compounds available for examining brain activity patterns, neurotransmitter systems, neuroinflammation and other biomarkers used to characterize brain function and disease (Zimmer and Luxen, 2012), (see Table 1). The extensive utility of PET brain imaging applications is made possible by the existence of radiotracers with diverse chemical structures and biological relevance. The most optimal radiotracers have good blood-brain barrier penetration and exhibit high affinity and selectivity for their neurobiological targets. In addition, there are a variety of experimental designs and analytic approaches to interpret PET data in biologically meaningful ways, such as radioligand displacement (which can be used as a measure of receptor occupancy or neurotransmitter release) and a variety of kinetic modeling techniques for quantitative and parametric assessments. Overall, the adaptability of PET applications offers a unique and powerful approach for translational molecular imaging in the brain.

1.2.2 Measuring brain activity with FDG-PET

Two general approaches have been developed to utilize PET for measuring brain activity. These approaches take advantage of the oxidative energy demands required by ion pumps to restore and maintain ion gradients following neuronal activation. One of these methods relies on infusion of [^{15}O]-labeled H2O to measure cerebral blood flow as a proxy for neuronal activity.

The rapid half-life (~2-min) of the radiotracer enables multiple acquisition periods during a scan session, but it also limits scanning duration and restricts use to facilities with direct cyclotron access. Although useful in certain scenarios, this method has largely been replaced by functional magnetic resonance imaging (fMRI), which typically utilizes changes in blood oxygenation level dependent (BOLD) signal to characterize brain activity with better spatial and temporal resolution. Aside from cerebral blood flow measures, brain activity can also be characterized using readout measures of glucose metabolism. The radiofluorinated glucose analog [^{18}F]2-fluoro-2-deoxy-D-glucose (FDG) is among the most widely used radiotracers in clinical PET imaging with multiple indications (e.g., monitoring cancer and neuroinflammation) (Galldiks et al., 2019), and it can also be leveraged as a proxy measure of brain activity. Seminal autoradiography studies with the analogous [^{14}C]-labeled and tritiated ([^{3}H]) 2- deoxy-D-glucose (2-DG) (Alexander et al., 1981; Sokoloff et al., 1977) paved the way for the development of FDG-PET brain imaging techniques. These studies established a close link between glucose metabolism and brain activity, as ion pumps depend on oxidative metabolism of glucose to restore and maintain ion gradients following neuronal activation. Just as in the original 2-DG method, FDG is transported into active cells via glucose transporters (GLUT) and is then used as a readout measure of glucose metabolism (Reivich et al., 1979). After undergoing initial phosphorylation by hexokinase II, the converted FDG-6-phosphate cannot move on through glycolysis and is temporarily trapped inside cells (see Fig. 2A). Importantly, this process of metabolic trapping allows brain activity to be imaged after it occurs as a cumulative average, which enables measuring whole-brain activity in awake and freely moving subjects. The FDG-6-phopshate undergoes radioactive decay and is eventually metabolized, allowing subjects to be imaged in a repeated and longitudinal manner. Standard uptake values (SUVs) normalizing for injected dose and body weight are often used to quantify FDG uptake, especially when serum concentration data are unavailable (Huang, 2000). In addition, PET based kinetic modeling of FDG uptake (e.g., arterial two-compartment or reference tissue modeling) enables quantitative characterizations of glucose transport and metabolism (Bentourkia and Zaidi, 2007).

The rate of FDG uptake into the brain is dependent on the route of radiotracer administration (i.e., intraperitoneal- i.p. or intravenous- i.v., bolus or continuous; see Fig. 2B-C). Bolus injection of FDG can provide a cumulative snapshot of brain activity corresponding to the rate of local radiotracer uptake, and it is suited for assessing brain activity during freely moving behavior because brain activity can be imaged after it occurs. Intraperitoneal administration will result in a longer uptake period (30-40 min) than an i.v. injection (5-10 min) (Aarons et al., 2012). Thus, the route of administration can be adapted to obtain the temporal resolution necessary to examine the effect of interest. Although bolus techniques have the advantage of being able to image brain activity after it has occurred, they can only provide a measure of the average brain activity level that occurred during the 5-40 min uptake period. Alternatively, a continuous infusion of FDG can be administered throughout the scanning period to enable dynamic scans which are reconstructed as a series of snapshots to improve temporal resolution (e. g., 5-min time bins vs. 20-min average) and to extend uptake periods (40+ min). This method of continuous infusion has been referred to as functional FDG-PET (fFDG-PET) and can be used to image changes in brain activity throughout the scanning session (Villien et al., 2014), (see model data in Fig. 2C.). However, even with continuous fFDG-PET the temporal resolution (minutes) is limited in comparison to other whole-brain imaging methods (seconds/milliseconds) (e.g., fMRI, MEG, EEG), but new and continuing developments in scanner technology have enabled simultaneous use of PET with other imaging modalities such as fMRI to improve the interpretability of brain activity measurements (Musafargani et al., 2018; Sander et al., 2020).

1.2.3 Combining FDG-PET with transgenic neuromodulation tools for metabolic mapping of brain circuits

FDG-PET can be applied as an effectively noninvasive approach for assessing the in vivo performance of chemogenetic and optogenetic constructs and their functional effects on brain activity patterns. The FDG radiotracer can be injected following the administration of a chemogenetic ligand or during light pulses in anesthetized or awake behaving animals to generate whole-brain metabolic maps of cell-specific functional circuits. One such strategy has been termed DREADD-assisted metabolic mapping (DREAMM) and can be used to derive functional brain maps induced by chemogenetic manipulation of distinct cell populations and circuits (Anderson et al., 2013; Klawonn et al., 2018; Mazzone et al., 2018; Michaelides et al., 2013; Michaelides and Hurd, 2015; Urban et al., 2015). For example, DREAMM has been applied to evaluate whole-brain effects of hM4Di activation in prodynorphin-expressing neurons in the rat periamygdaloid cortex and prodynorphin- and proenkephalin-expressing medium spiny neurons in the nucleus accumbens shell (Anderson et al., 2013; Michaelides et al., 2013). In one of these studies (Michaelides et al., 2013), it was shown that distinct brain networks were activated during conditions of awake vs. anesthetized chemogenetic activation. During anesthetized FDG uptake, chemogenetic activation led to changes in FDG accumulation in brain regions that were more proximally related to the anatomical circuits being manipulated, whereas during awake FDG uptake, chemogenetic activation led to changes in FDG accumulation in brain regions that extended beyond the anatomical circuit manipulated and were recruited as a function of the chemogenetic induced behavioral effects. These observations emphasize both the utility of this functional imaging approach as well as the importance of considering such factors in experimental design and interpretation when using FDG-PET (Cho et al., 2020; Michaelides et al., 2013).

FDG-PET has also been used to assess the in vivo efficacy of newly developed DREADD ligands. For example, FDG-PET was performed following i.p. administration of the fluorinated clozapine analog JHU37160 (J60) in transgenic D1-Cre mice expressing DREADDs under the control of the dopamine D1 receptor promoter. These scans showed distinct brain activation profiles of hM4Di and hM3Dq in DREADD- expressing mice compared to wildtype mice at doses of 0.1 mg/kg (Bonaventura et al., 2019). In another recent study, systemic injection of the highly potent DREADD actuator DCZ in NHPs with unilateral expression of hM3Dq in the amygdala produced dose-dependent increases of FDG uptake in this brain region with effects observed at doses as low as 1 μg/kg (Nagai et al., 2020). Importantly, this effect was not observed in the contralateral amygdala or in animals lacking hM3Dq, demonstrating the selectivity of DCZ by inducing activation only in regions expressing DREADDs.

Aside from imaging brain responses to chemogenetic neuromodulation, FDG-PET can also be combined with optogenetic neuromodulation to interrogate functional activation patterns among specific brain regions. This has been demonstrated in characterizing responses to optogenetic stimulation of neurons in the nucleus accumbens (NAc) of awake rats (Thanos et al., 2013). Increases in FDG uptake indicated enhanced activity in the stimulated region as well as the ipsilateral striatum, somatosensory cortex, periaqueductal gray (PAG), and multiple contralateral sites which were consistent with areas showing increased c-Fos expression. Decreased uptake in the retrosplenial cortex, cingulate gyrus and secondary motor cortex was also observed. In another study, FDG-PET was used to evaluate neurofunctional changes before and after optogenetic stimulation of the dorsal PAG (dPAG), a region implicated in the generation of panic disorders (He et al., 2019). Optogenetic stimulation of excitatory neurons in the dPAG of rats resulted in post-stimulation increases of FDG uptake in the dPAG and downstream areas such as the cingulate cortex, cerebellar lobule, and the septohypothalamic nucleus. Decreases in FDG uptake were also observed in the basal ganglia, frontal cortex, primary somatosensory and motor cortex post-stimulation (He et al., 2019). Overall, these studies demonstrate the utility of FDG-PET for validating the function of transgenic neuromodulation tools and for whole-brain metabolic mapping of cell-type specific functional networks.

1.2.4 Localizing chemogenetic receptor expression with PET-reporters

Transgenic tools cannot be employed confidently without verifying their anatomical location and function. In most preclinical studies using chemogenetics or optogenetics, the location of transgene expression is verified through postmortem histology techniques and usually necessitates the inclusion of a gene for a reporter protein into the AAV-transgene construct (e.g., epitope tags or fluorescent proteins) which is transduced in addition to the transgenic receptor or opsin. Although usually not problematic, reporter proteins have the potential to compromise the function of the neuromodulatory protein and the viability of the cells that express it, underscoring the importance of functional validation and longitudinal monitoring (Galvan et al., 2019). In addition to genetic reporters for postmortem histology, in vivo functional measurements using technologies such as photometric biosensors, fiber photometry and electrophysiological recordings can be used for indirect monitoring of chemogenetic receptors and neuromodulatory opsins. However, these techniques are cumbersome and invasive, and they would not be widely adaptable for clinical applications. Additionally, they rely on expected functional effects and do not directly measure the presence of chemogenetic receptors or transgenic opsins.

A promising alternative strategy has emerged for direct and effectively noninvasive visualization of chemogenetic receptors. Since chemogenetic tools are based on receptor-binding ligands, using radiolabeled PET ligands that are selective and of high affinity for chemogenetic receptors can be suitable for in vivo mapping of chemogenetic receptor expression and the brain circuit(s) they occupy. One of the first demonstrations of this used [^{11}C]-radiolabeled clozapine-N-oxide (CNO) to localize DREADDs in mice expressing hM4Di (Ji et al., 2016), but low brain penetrance and affinity of CNO limits the sensitivity of this approach (Gomez et al., 2017; Raper et al., 2017). DREADDs have also been successfully visualized using [^{11}C]clozapine and [^{11}C]DCZ in rodents and NHPs (Gomez et al., 2017; Nagai et al., 2016; Nagai et al., 2020). While effective, these radiotracers have a relatively short half-life as they possess the ^{11}C radionuclide (~20-min), which makes their application impractical at institutions without direct cyclotron access for radionuclide production. Although most clinical PET centers have cyclotron access, DREADD radioligands with longer half-lives could enhance accessibility for preclinical research labs and improve the ease of use in clinical settings.

Therefore, to expand access to this approach, there is a push to develop selective fluorinated DREADD ligands that can be radiolabeled with 18F for a longer half-life (~110-min). For example, fluorinated compounds based on potent clozapine analogs (Chen et al., 2015) have recently been developed (Bonaventura et al., 2019; Hu et al., 2020), and of these compounds, the first high affinity and selective ^{18}F labeled DREADD ligand – [^{18}F]JHU37107 – was shown to successfully localize hM3Dq and hM4Di in rodents and NHPs (see Fig. 3A-E.). The use of [^{18}F]JHU37107 to detect DREADD expression was tested in rats with unilateral expression of hM3Dq or hM4Di in the right motor cortex. DREADD specific binding of [^{18}F]JHU37107 was observed both at the local AAV injection site and known anatomical projection sites including the contralateral motor cortex, striatum and motor thalamus (Fig. 3B-D.). This pattern was consistent with results from postmortem immunohistochemistry in brain slices (Fig. 3C-D.). In addition, a rhesus macaque expressing hM4Di in the right amygdala was imaged with [^{18}F]JHU37107, and specific labelling of hM4Di receptors was observed unilaterally in this region (Fig. 3E.). This body of work demonstrated the first ever detection of DREADDs using an ^{18}F labeled PET ligand in rodents and NHPs.

Aside from mapping the anatomical location of DREADD receptors, PET studies with radiotracers like [^{11}C]clozapine, [^{18}F]JHU37107 and [^{11}C]DCZ enable validation of the in vivo target engagement of selective ligands at DREADD receptors through competitive binding experiments. For instance, dose-dependent reductions in [^{11}C]clozapine occupancy of DREADDs were observed following pretreatment with various doses of CNO in NHPs expressing hM4Di in the rostromedial caudate (Nagai et al., 2016). This type of approach can facilitate the development of novel chemogenetic ligands by providing a metric for comparing the in vivo receptor occupancies of different actuator compounds. For example, [^{11}C]clozapine-PET was used to quantify DREADD occupancies of fluorinated clozapine analogs JHU37152 (J52) and JHU37160 (J60) in comparison with the DREADD agonist C21 in rodents and NHPs (Bonaventura et al., 2019). Treatment with J52 and J60 occupied DREADDs (decreased [^{11}C]clozapine binding) at doses 10-100 times lower than those required by C21 (i.e., 0.1 mg/kg vs. 1-10 mg/kg), which was consistent with the superior potencies of J52 and J60 for producing DREADD-specific behavioral effects. The potent receptor occupancy of J60 was also confirmed by blocking the binding of [^{18}F]JHU37107 with a 0.1 mg/kg dose of J60 in transgenic DREADD- expressing mice (Bonaventura et al., 2019; Hu et al., 2020).

In another recent study, a highly potent clozapine analog − DCZ − was shown to exhibit greater selectivity for DREADDs (lower affinity for endogenous receptors) compared to clozapine in vitro and was subsequently radiolabeled with [^{11}C] to systematically compare dose-dependent hM4Di receptor occupancies of CNO, C21 and DCZ using [^{11}C]DCZ-PET in NHPs (Nagai et al., 2020). The dose of DCZ required to reach 50% DREADD occupancy in vivo was ~20-fold lower than CNO and ~60-fold lower than C21. This was consistent with DCZ's superior in vitro affinity and in vivo agonistic potency (~100-fold) compared to CNO and C21 and demonstrates that DCZ retains the high affinity and potency of clozapine while improving selectivity for DREADDs. Overall, these studies illustrate the utility of PET for monitoring DREADD expression at local and anatomical projection sites as well as comparing DREADD occupancy by different chemogenetic actuators.

Pharmacologically selective actuator modules, or PSAMs, are another group of chemogenetic receptors with promising translational potential. As described in section 1.1.2, they were developed by combining mutated versions of the α7 nAChR ligand binding domain with different ion pore domains. Like DREADDs, clinical use of PSAMs will require a way to track the expression of the transgenic receptors in vivo innocuously and longitudinally. An FDA approved PET ligand has recently been developed for visualizing α7 nAChRs in humans, namely the radiolabeled α7 nAChR antagonist [^{18}F]ASEM (Horti et al., 2014). Just like [^{18}F]JHU37107 and [^{11}C]DCZ for DREADDs, [^{18}F]ASEM can be used to localize the expression of PSAMs in rodents (Fig. 3F-I) and potentially in NHPs and humans. For example, Magnus et al. (2019) demonstrated the use of PET with [^{18}F]ASEM to visualize PSAM^{4}-GlyR expression unilaterally in the mouse striatum. Expression areas identified by [^{18}F]ASEM PET in mice were consistent with expression areas of PSAM4-GlyR-IRES-EGFP in left dorsal striatum confirmed through [^{3}H] ASEM autoradiography and ex vivo fluorescence microscopy in striatal brain slices (Fig. 3H-I). Competitive binding PET experiments with [^{18}F]ASEM were also used to characterize brain penetrance and PSAM^{4} receptor occupancy of newly developed ultrapotent PSEMs (uPSEMs) in vivo. [^{18}F]ASEM binding was blocked by pretreatment with some of these novel uPSEMs including uPSEM^{792} and uPSEM^{817} at doses ranging from 0.3-1 mg/kg (Fig. 3H). In contrast to [^{18}F]JHU37107 and [^{11}C] DCZ for DREADDs, the fact that [^{18}F]ASEM has already been FDA approved for use as a PET radiotracer in humans makes it readily suitable for translational and clinical applications.

1.2.5 Other PET-reporters for mapping transgene expression

The use of selective PET-reporters is a relatively noninvasive and repeatable approach for visualizing DREADD and PSAM expression in rodents and NHPs. However, not all transgenic proteins (including opsins) have a readily available binding domain accessible to PET radiotracers. Consequently, there is a need to develop other types of PET-reporter systems to adapt this imaging approach for transgenic tools such as optogenetics. A variety of PET compatible transgene reporter systems have been developed over the past two decades with motivations for potential gene therapy applications. These systems typically utilize a reporter gene to express an enzyme, transporter protein or receptor that can selectively entrap or bind a specific PET radiotracer (Yaghoubi et al., 2012). The reporter genes are intended to be co-packaged with therapeutic transgenes and therefore provide a proxy confirmation of therapeutic transgene expression. One of the earliest enzyme-based transgene reporter systems was developed using herpes simplex virus thymidine kinase (HSV1-tk) in combination with radiolabeled substrates such as [^{124}I]2′-fluoro-2′-deoxy-1-β-D-arabinofuranosyl-5-iodouracil (FIAU), which accumulates in cells expressing the transgene and can then be visualized with PET (Blasberg and Tjuvajev, 1999; Tjuvajev et al., 2002). The norepinephrine transporter has also been utilized as a reporter gene in combination with [^{131}I]metaiodobenzylguanidine (Anton et al., 2004), and one of the first receptor-based transgene reporter systems was developed using a mutated dopamine D2 receptor in combination with [^{18}F]fluoroethylsisperone (FESP) (Liang et al., 2001). More recently, a PET reporter system using the PKM2 gene with the radiotracer [^{18}F]DASA-23 was demonstrated in mice transfected using AAV9 (Haywood et al., 2019). Additionally, *E. coli* dihydrofolate reductase (ecDHFR) was utilized by Shimojo et al. (2020) for mapping transgenic protein expression in rodents and marmosets with radiolabeled analogs of the ecDHFR antagonist trimethoprim (i.e., [^{18}F]FE-TMP). Importantly, they showed the ecDHFR-TMP system can be used in combination with transgenic neuromodulation tools such as DREADDs. Approaches like these can provide a proxy confirmation of the co-packaged transgene expression and can be adapted for identifying cells expressing a wide variety of transgenic constructs and neuromodulatory proteins.

Optogenetic technologies could greatly benefit from PET-compatible transgene reporters, because unlike chemogenetic receptors (which inherently possess a selective binding site), there is currently no available method to directly monitor opsin expression in a noninvasive and longitudinal manner. This limitation hinders translational development of optogenetics in NHPs and potential applications in humans because expression of opsins can only be confirmed through highly invasive or post-mortem procedures. Without verifying opsin expression, these tools cannot be confidently used to manipulate discrete neuronal populations, especially when targeting projection areas outside of the AAV injection site. Consequently, this presents an obstacle for clinical applications of optogenetics where medical decisions and patient outcomes would undoubtedly benefit from innocuous longitudinal tracking of opsin expression and function in targeted areas.

1.3 Summary and significance

1.3.1 Improving the translational capacity of transgenic tools

Modern advancements in transgenic neuromodulation technologies have revolutionized neuroscience research and clinical ambitions for gene therapies. However, to improve the translational capacity of these tools (i.e., chemogenetics and optogenetics), noninvasive methods for in vivo longitudinal monitoring are needed. The use of PET-compatible reporters is a promising strategy adaptable for this purpose, as selective radiotracers have been demonstrated to effectively localize chemogenetic receptors and other transgenic proteins in preclinical studies. Universal PET-reporter systems are necessary to expand translational applications of optogenetics and other transgenic technologies where exogenous proteins are introduced (e.g., CAR-T cells). Although PET imaging places some radioactive burden on subjects (albeit clinically safe), ongoing technological advancements in PET instrumentation are expected to increase the spatial resolution and sensitivity of this technique and therefore reduce subject radiation exposure by permitting lower doses of radiotracer (Hutton et al., 2018). Furthermore, the combination of PET with other modalities like MRI will enhance their utility for interrogating structural and functional neurobiology (Musafargani et al., 2018; Sander et al., 2020).

In addition to PET monitoring methods, the ability to safely deliver AAVs with high efficacy and precision is necessary for translational applications, and this will require innovations in genetic targeting technologies. Even with noninvasive methods for tracking transgenic tools in vivo, the challenge of transgene delivery remains, which in current practice requires intracranial injection of viral vectors into target brain regions. To overcome this challenge, efforts are underway to develop vectors that can be delivered systemically through intravenous injection and will pass through the blood-brain barrier to express in target regions of the brain. AAV capsid variants such as AAV-PHPs have been demonstrated to facilitate noninvasive, efficient, and trackable targeted gene delivery in rodent models (Challis et al., 2019; Seo et al., 2020). However, the efficacy of this technology has been shown to be strain-dependent in rodents and largely ineffective in NHPs, underscoring the need for further development in this area (Huang et al., 2019; Matsuzaki et al., 2018).

Another hurdle specific to practical applications of optogenetics is the challenge of delivering light to target areas. The development of new opsins with heightened sensitivity, especially at longer wavelengths (e. g., ChRmine), may provide some improvement because these wavelengths can penetrate deeper into tissue from an exogenous source (Chen et al., 2020; Duebel et al., 2015). Additionally, technologies are being developed to enable wireless and skull permeant light delivery into target brain areas (Kim et al., 2021; Wu et al., 2019). Although still an invasive technology, these advances may broaden the potential for translational optogenetic applications (Wang et al., 2020).

1.3.2 Conclusions and future directions

This introductory chapter provides an overview of the current state of research using transgenic tools in combination with PET imaging for in vivo mapping and manipulation of neuronal populations and circuits. Recent advances in these technologies (e.g., genetic engineering, transgene delivery systems and wireless light devices) may improve applications of chemogenetics and optogenetics for neuromodulation in NHPs and humans. However, the field greatly needs a versatile approach to localize and track the expression of transgenes in a noninvasive and longitudinal manner. We propose PET as an ideal translational imaging modality capable of meeting the need for tracking transgenic construct expression in vivo (i.e., chemogenetic receptors and transgenic opsins).

The following chapters describe a body of dissertation work aimed at advancing the utility of optogenetic and chemogenetic technologies by adapting translational PET applications for imaging their expression and function in vivo. We developed the first PET-compatible opsin and demonstrate its use for investigating structural and functional brain connectivity in rodents and NHPs. We also developed a dual chemogenetics approach by using a combination of DREADDs and PSAMs for bidirectional neuromodulation, and we show the utility of PET for localizing the expression of multiple transgenes in individual subjects. Together these projects will benefit the progress of transgenic technologies in NHP research and lay the groundwork to enable clinical monitoring of transgenes for a variety of gene therapy applications.

1.4 Tables and Figures for Chapter 1

Table 1. PET applications for brain imaging and example radiotracers

Applications	Description	Radiotracer examples
Brain activity	Measure cerebral blood flow or glucose metabolism as a proxy for brain activity	[^{15}O] water (cerebral blood flow), [^{18}F]FDG (glucose metabolism)
Neurotransmitter receptors and transporters	Evaluate neurotransmitter levels and receptor availability using radioligands selective for endogenous receptors and transporters	Dopamine: [^{11}C]raclopride and [^{18}F]fallypride Serotonin (5-HT): [^{11}C]Cimbi-36
Neuroinflammation and Neurodegeneration	Assess neuroinflammation and neurodegeneration using selective radioligands to probe relevant biomarkers	Translocator protein (TSPO) tracers: [^{18}F]GE-180 Neurofibrillary tau protein: [^{18}F]MK-6240
Neuro-oncology	Diagnose and monitor cancer in peripheral and central nervous system using relevant biomarkers	[^{18}F]FET for tumors, [^{18}F]FDG for diagnostic monitoring of tumors
Drug target engagement	Evaluate binding of radiolabeled drugs or blockade/displacement of receptor selective radioligands	Radiolabeled [^{11}C]psilocin or displacement of [^{11}C]Cimbi-36 at 5-HT2$_A$ receptors
Tracking transgene expression	Track transgene delivery and expression by co-packaging with PET-compatible reporter genes	Enzyme based: HSV1-tk reporter with [^{124}I]FIAU. Receptor based: Dopamine D2 receptor reporter with [^{18}F]FESP

Brain activity: [^{15}O] water for cerebral blood flow (Zhang et al., 2014) and [^{18}F]fluorodeoxyglucose (FDG) for neurometabolic glucose use (Villien et al., 2014). **Neurotransmitter receptors:** Dopamine D2/D3 antagonists [^{11}C]raclopride (Volkow et al., 1994) and [^{18}F]fallypride (Slifstein et al., 2010). Serotonin 5-HT2A agonist [^{11}C]Cimbi-36 (Ettrup et al., 2014). **Neuroinflammation:** Translocator protein (TSPO) tracer [^{18}F]GE-180 (Vomacka et al., 2017). **Neurodegeneration:** Neurofibrillary tau protein tracer [^{18}F]MK-6240 (Hostetler et al., 2016). **Neuro-oncology:** [^{18}F]fluoroethyltyrosine (FET) and [^{18}F]FDG for assessing brain tumors (Pauleit et al., 2009). **Drug target engagement:** Radiolabeled [^{11}C]psilocin (Amatamey et al., 1998). Psilocybin displacement of [^{11}C]Cimbi-36 at 5-HT2A receptors (Madsen et al., 2019). **Tracking transgene expression:** Enzyme-based HSV1-tk reporter [^{124}I]2′-fluoro-2′-deoxy-1-β-D-arabinofuranosyl-5-iodouracil (FIAU) (Tjuvajev et al., 2002). Receptor based dopamine D2 reporter [^{18}F]fluoroethylspiperone (FESP) (Liang et al., 2001).

Figure 1. Neuromodulation with chemogenetic and optogenetic tools.

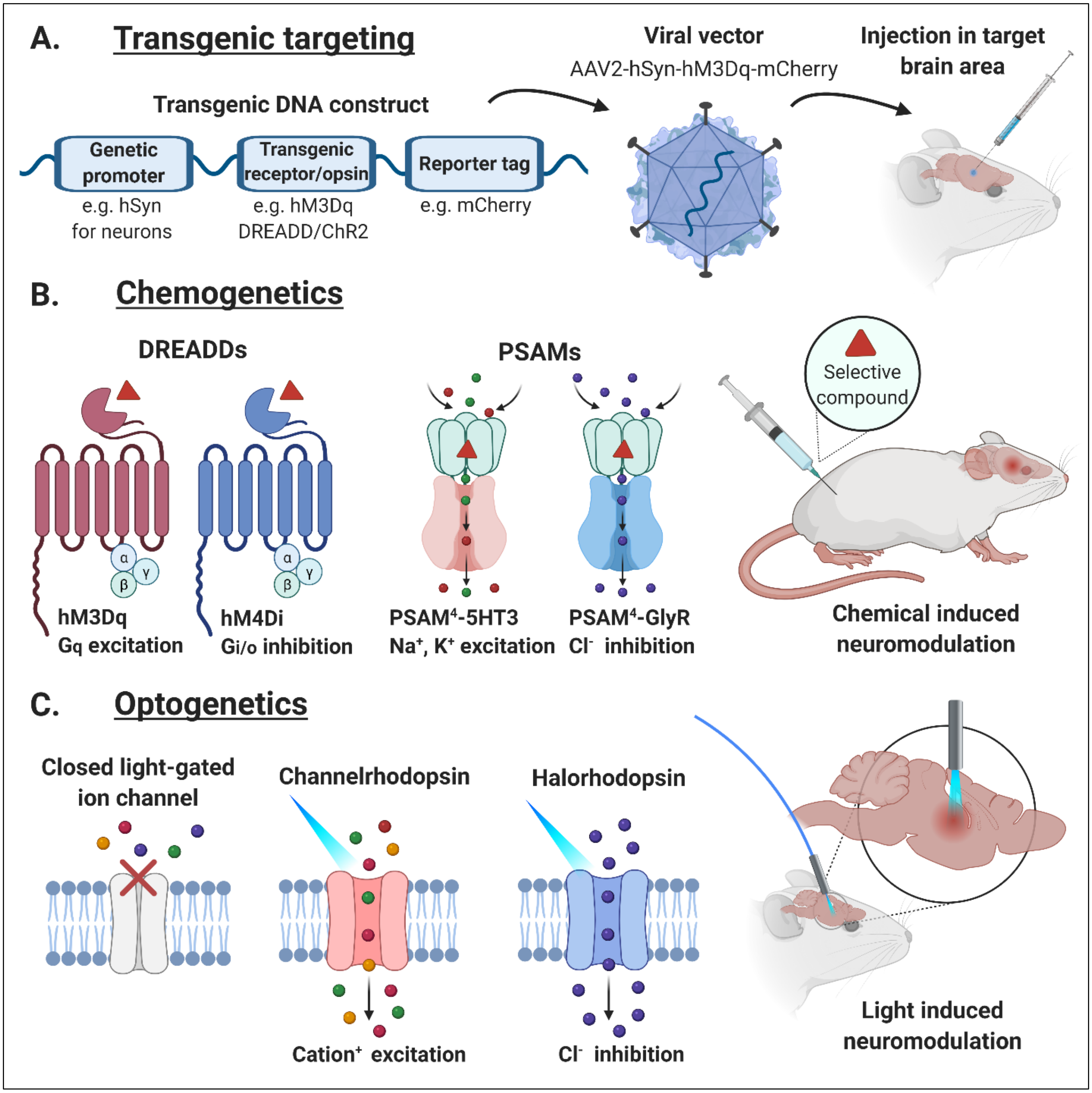

(**A**) Transgenic ssDNA combining a genetic promoter sequence (e.g., human synapsin 1 (hSyn) for neuronal expression) with transgenes for a neuromodulatory receptor/opsin (e.g., hM3Dq DREADD or Channelrhodopsin-2 (ChR2)) and reporter protein (e.g., mCherry fluorescent protein) is packaged into a viral vector (e.g., AAV serotype 2) and injected into a target brain area. (**B**) Chemogenetic tools utilize genetically engineered receptors (e.g., DREADDs and PSAMs) that can alter brain activity following administration of a selective compound. (**C**) Optogenetic tools rely on light-gated ion channels (e.g., channelrhodopsins and halorhodopsins) to modulate neuronal activity with light stimulation.

Figure 2. FDG-PET for measuring brain activity.

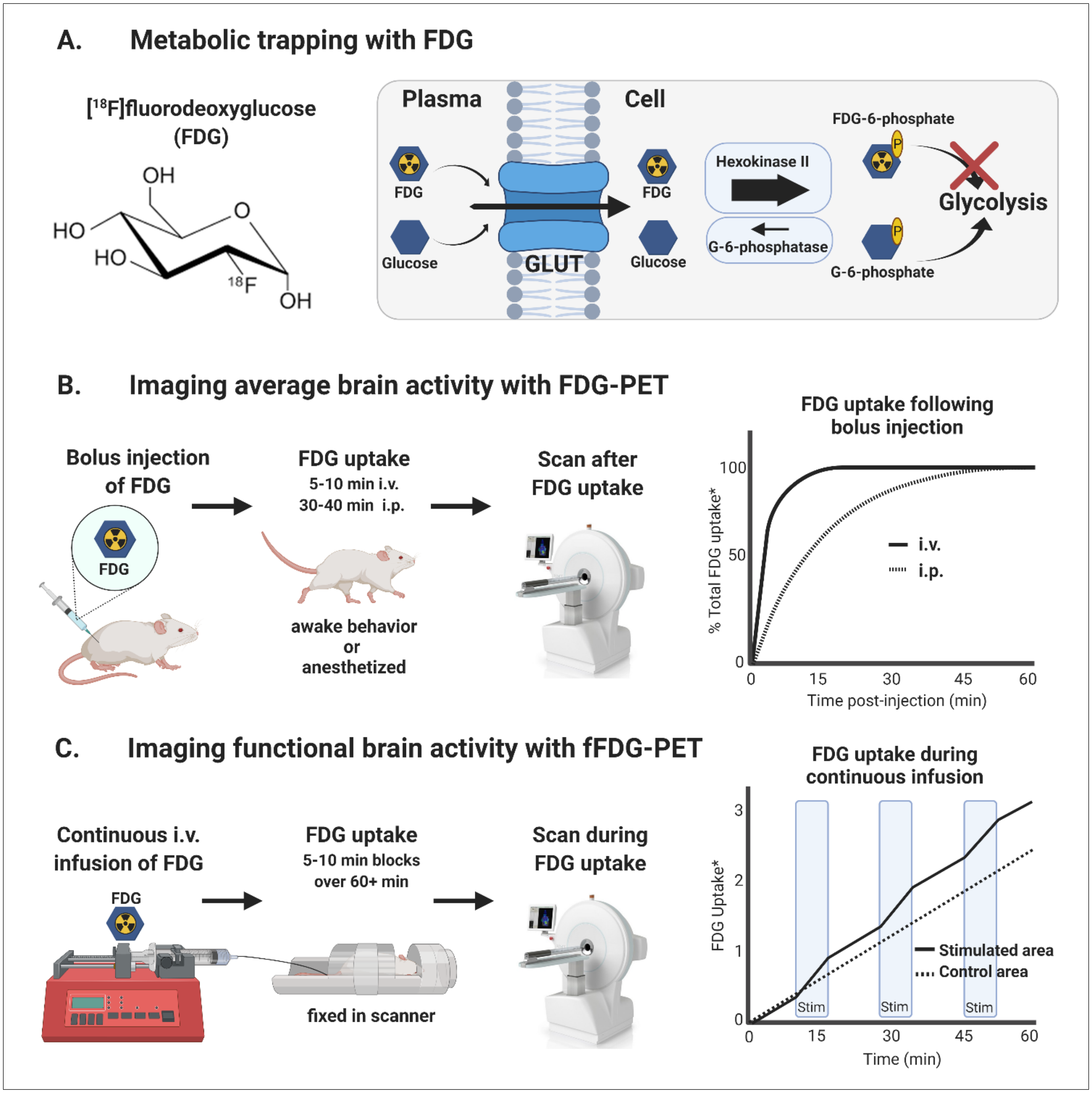

(**A**) Radiofluorinated glucose analog [^{18}F]fluorodeoxyglucose (FDG) is taken up by cells through glucose transporters (GLUT) and trapped in active brain regions. (**B**) Bolus injection of FDG can be used to image average brain activity after it occurs in anesthetized or awake and behaving animals (uptake period 5–10 min intravenous or 30–40 min intraperitoneal) (Aarons et al., 2012). (**C**) Continuous infusion of FDG can be used to measure brain activity over longer durations with improved temporal resolution in functional FDG-PET (fFDG-PET) (Villien et al., 2014). *Model data of FDG uptake for illustrative purposes.

Fig. 3. PET-reporters for in vivo mapping of chemogenetic receptor expression.

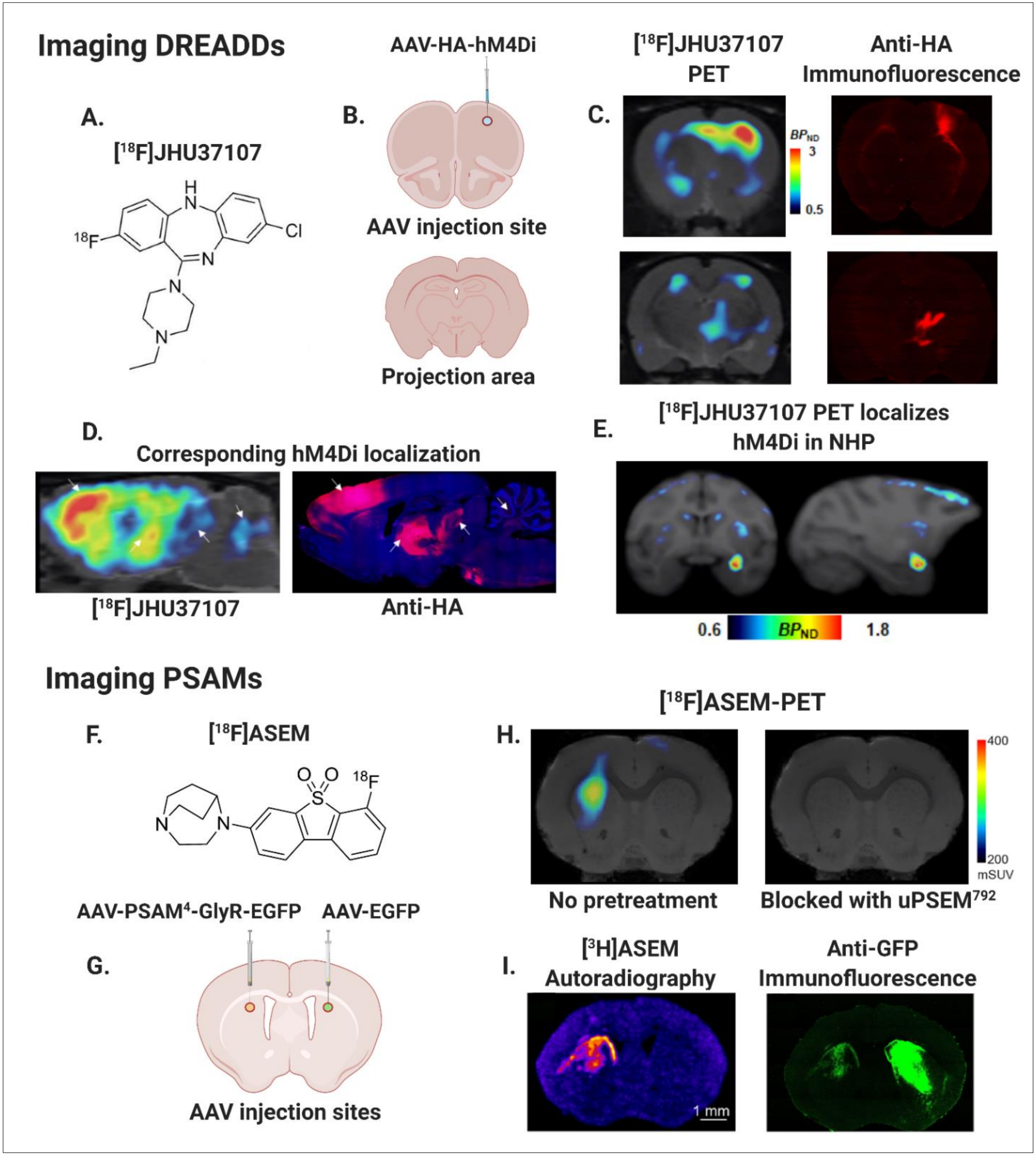

(**A–E**) Mapping DREADDs in rats and NHPs (modified from Bonaventura et al., 2019): (**A**) Chemical structure of DREADD radioligand [^{18}F]JHU37107. (**B**) AAV-HA-hM4Di injection site in rat right motor cortex (M1) and non-injected projection area. (**C**) Left: [^{18}F]JHU37107 PET reveals hM4Di expression at M1 injection site and putative projection sites, Right: Histological confirmation of hM4Di expression with hemagglutinin (HA) antibody immunofluorescence. (**D**) Anatomical localization of hM4Di from [^{18}F]JHU37107 PET in rats coincides with histological expression patterns of the HA-tagged DREADDs, arrows show corresponding anatomical sites of right M1 and motor cortical projection areas. (**E**) Localization of hM4Di in rhesus nonhuman primate (NHP) right amygdala with [^{18}F]JHU37107. (**F–I**) Mapping PSAMs in mice (modified from Magnus et al., 2019): (**F**) Chemical structure of FDA approved radiotracer [^{18}F]ASEM capable of imaging PSAMs. (**G**) Schematic of AAV injection sites in mouse left dorsal striatum (AAV-PSAM4-GlyR-EGFP) and right dorsal striatum (AAV-EGFP control). (**H**) Left: [^{18}F]ASEM PET showing left striatal PSAM4-GlyR expression, Right: [^{18}F]ASEM blocked following uPSEM792 pretreatment (1 mg/kg). (**I)** Left: Autoradiography of [3H]ASEM binding in left dorsal striatum, Right: Immunofluorescence with anti-green fluorescent protein (anti- GFP) antibody showing PSAM4-GlyR-EGFP expression in left striatum and EGFP control in right striatum. Lack of PET and autoradiography binding in right striatum demonstrates specificity of ASEM for PSAM^{4}-GlyR.

1.5 References:

Aarons A.R., Talan A., Schiffer W.K. (2012). Experimental protocols for behavioral imaging: seeing animal models of drug abuse in a new light. In: Carter C., Dalley J. (eds) Brain Imaging in Behavioral Neuroscience. *Current Topics in Behavioral Neurosciences*, vol 11. Springer, Berlin, Heidelberg. https://doi.org/10.1007/7854_2012_206

Alcacer, C., Andreoli, L., Sebastianutto, I., et al., 2017. Chemogenetic stimulation of striatal projection neurons modulates responses to Parkinson's disease therapy. *J. Clin. Invest.* 127 (2), 720–734. https://doi.org/10.1172/JCI90132

Alexander, G.M., Schwartzman, R.J., Bell, R.D., 1981. Quantitative measurement of local cerebral metabolic rate for glucose utilizing tritiated 2-deoxyglucose. *Brain Res.* 223 (1), 59–67. https://doi.org/10.1016/0006-8993(81)90806-4

Amatamey, S., Vollenweider, F.X., Patt, J., et al., 1998. 11C-radiolabeling of hallucinogenic psilocin, a potential radioligand for studying the role of serotonin receptors in psychotic symptom formation. *J. Labelled Cpd. Radiopharm.* 41 (7), 585–594. https://doi.org/10.1002/(SICI)1099-1344(199807)41:7<585::AIDJLCR115>3.0.CO;2-U

Anderson, S.A.R., Michaelides, M., Zarnegar, P., et al., 2013. Impaired periamygdaloidcortex prodynorphin is characteristic of opiate addiction and depression. *J. Clin. Invest.* 123 (12), 5334–5341. https://doi.org/10.1172/JCI70395

Anton, M., Wagner, B., Haubner, R., et al., 2004. Use of the norepinephrine transporter as a reporter gene for non-invasive imaging of genetically modified cells. *J Genet Med.* 6 (1), 119–126. https://doi.org/10.1002/jgm.472

Armbruster, B.N., Li, X., Pausch, M.H., et al., 2007. Evolving the lock to fit the key to create a family of G protein-coupled receptors potently activated by an inert ligand. *PNAS* 104 (12), 5163–5168. https://doi.org/10.1073/pnas.0700293104

Assaf, F., Schiller, Y., 2019. A chemogenetic approach for treating experimental Parkinson's disease. *Mov. Disord*. 34, 469–479. https://doi.org/10.1002/mds.27554

Bedbrook, C.N., Deverman, B.E., Gradinaru, V., 2018. Viral strategies for targeting the central and peripheral nervous systems. *Annu. Rev. Neurosci*. 41, 323–348. https://doi.org/10.1146/annurev-neuro-080317-062048

Bentourkia, M., Zaidi, H., 2007. Tracer kinetic modeling in PET. *PET Clinics* 2 (2), 267–277. https://doi.org/10.1016/j.cpet.2007.08.003

Blasberg, R.G. and Tjuvajev, J.G. (1999). Herpes simplex virus thymidine kinase as a marker/reporter gene for PET imaging of gene therapy. *Q J Nucl Med*. 43(2):163–9. PMID: 10429512. https://pubmed.ncbi.nlm.nih.gov/10429512/

Bliss-Moreau, E., Costa, V.D., Baxter, M.G., 2020. A pragmatic reevaluation of the efficacy of nonhuman primate optogenetics. *bioRxiv*. https://doi.org/10.1101/2020.12.10.420331

Bonaventura, J., Eldridge, M.A.G., Hu, F., et al., 2019. High-potency ligands for DREADD imaging and activation in rodents and monkeys. *Nat. Commun*. 10, 4627. https://doi.org/10.1038/s41467-019-12236-z

Boyden, E.S., Zhang, F., Bamberg, E., et al., 2005. Millisecond-timescale, genetically targeted optical control of neural activity. *Nat. Neurosci*. 8 (9), 1263–1268. https://doi.org/10.1038/nn1525

Büning, H., Srivastava, A., 2019. Capsid modifications for targeting and improving the efficacy of AAV vectors. Molecular Therapy: *Methods & Clinical Development* 12, 248–265. https://doi.org/10.1016/j.omtm.2019.01.008

Burnett, C.J., Krashes, M.J., 2016. Resolving behavioral output via Chemogenetic designer receptors exclusively activated by designer drugs. *J. Neurosci*. 36 (36), 9268–9282. https://doi.org/10.1523/JNEUROSCI.1333-16.2016

Busskamp, V., Picaud, S., Sahel, J., et al., 2012. Optogenetic therapy for retinitis pigmentosa. *Gene Ther*. 19, 169–175. https://doi.org/10.1038/gt.2011.155

Challis, R.C., Ravindra Kumar, S., Chan, K.Y., et al., 2019. Systemic AAV vectors for widespread and targeted gene delivery in rodents. *Nat. Protoc.* 14, 379–414. https://doi.org/10.1038/s41596-018-0097-3

Chan, K.Y., Jang, M.J., Yoo, B.B., et al., 2017. Engineered AAVs for efficient noninvasive gene delivery to the central and peripheral nervous systems. *Nat. Neurosci*. 20, 1172–1179. https://doi.org/10.1038/nn.4593

Chen, R., Gore, F., Nguyen, Q.A., et al., 2020. Deep brain optogenetics without intracranial surgery. *Nat. Biotechnol*. https://doi.org/10.1038/s41587-020-0679-9

Chen, X., Choo, H., Huang, X., et al., 2015. The first structure-activity relationship studies for designer receptors exclusively activated by designer drugs. *ACS Chem. Neurosci*. 6, 476–484. https://doi.org/10.1021/cn500325v

Cho, J., Ryu, S., Lee, S., et al., 2020. Optimizing clozapine for chemogenetic neuromodulation of somatosensory cortex. *Sci. Rep*. 10, 6001. https://doi.org/10.1038/s41598-020-62923-x

Conklin, B.R., Hsiao, E.C., Claeysen, S., et al., 2008. Engineering GPCR signaling pathways with RASSLs. *Nat. Methods* 5 (8), 673–678. https://doi.org/10.1038/nmeth.1232

Curado, T.F., Pho, H., Freire, C., et al., 2020. DREADD approach to treatment of sleep disordered breathing. *Am J Respir Crit Care Med* (online ahead of print). https://doi.org/10.1164/rccm.202002-0321OC

Deisseroth, K., 2011. Optogenetics. *Nat. Methods* 8 (1), 26–29. https://doi.org/10.1038/nmeth.f.324

Dimidschstein, J., Chen, Q., Tremblay, R., et al., 2016. A viral strategy for targeting and manipulating interneurons across vertebrate species. *Nat. Neurosci*. 19, 1743–1749. https://doi.org/10.1038/nn.4430

Duebel, J., Marazova, K., Sahel, J.A., 2015. Optogenetics. *Curr. Opin. Ophthalmol*. 26 (3), 226–232. https://doi.org/10.1097/ICU.0000000000000140

Durieux, P.F., Schiffmann, S.N., de Kerchove d'Exaerde, A., 2011. Targeting neuronal populations of the striatum. *Front. Neuroanat*. 5 (40) https://doi.org/10.3389/fnana.2011.00040

Ettrup, A., da Cunha-Bang, S., McMahon, B., et al., 2014. Serotonin 2A receptor agonist binding in the human brain with [^{11}C]Cimbi-36. Journal of cerebral blood flow and metabolism. *J. Cereb. Blood Flow Metab*. 34 (7), 1188–1196. https://doi.org/10.1038/jcbfm.2014.68

Frecha, C., Szecsi, J., Cosset, F., Verhoeyen, E., 2008. Strategies for targeting lentiviral vectors. *Current Gene Therapy* 8 (6), 449–460. https://doi.org/10.2174/156652308786848003

Galldiks, N., Lohmann, P., Albert, N.L., et al. (2019). Current status of PET imaging in neuro-oncology. Neuro-Oncology Advances, Volume 1, Issue 1, vdz010, https://doi.org/10.1093/noajnl/vdz010

Galvan, A., Raper, J., Hu, X., et al., 2019. Ultrastructural localization of DREADDs in monkeys. Eur. J. Neurosci. 50 (5), 2801–2813. https://doi.org/10.1111/ejn.14429

Gantz, S.C., Oritz, M.M., Belilos, A.J., Moussawi, K. (2020). Inhibitory ultrapotent chemogenetics activate dopamine D1 receptor-expressing medium spiny neurons. *bioRxiv* 2020.07.01.181925; https://doi.org/10.1101/2020.07.01.181925

Gaub, B.M., Berry, M.H., Holt, A.E., et al., 2015. Optogenetic vision restoration using rhodopsin for enhanced sensitivity. *Mol. Ther.* 23 (10), 1562–1571. https://doi.org/10.1038/mt.2015.121

Gomez, J.L., Bonaventura, J., Lesniak, W., et al., 2017. Chemogenetics revealed: DREADD occupancy and activation via converted clozapine. *Science* 357 (6350), 503–507. https://doi.org/10.1126/science.aan2475

Grund, T., Tang, Y., Benusiglio, D., et al., 2019. Chemogenetic activation of oxytocin neurons: temporal dynamics, hormonal release, and behavioral consequences. *Psychoneuroendocrinology* 106, 77–84. https://doi.org/10.1016/j.psyneuen.2019.03.019

Haywood, T., Beinat, C., Gowrishankar, G., et al., 2019. Positron emission tomography reporter gene strategy for use in the central nervous system. *PNAS* 116 (23), 11402–11407. https://doi.org/10.1073/pnas.1901645116

He, X., Jin, C., Ma, M., et al., 2019. PET imaging on neurofunctional changes after optogenetic stimulation in a rat model of panic disorder. *Front. Med.* 13, 602–609. https://doi.org/10.1007/s11684-019-0704-x

Horti, A.G., Gao, Y., Kuwabara, H., et al., 2014. ^{18}FASEM, a radiolabeled antagonist for imaging the α7-nicotinic acetylcholine receptor with PET. *J. Nuclear Med*. 55 (4), 672–677. https://doi.org/10.2967/jnumed.113.132068

Hostetler, E.D., Walji, A.M., Zeng, Z., et al., 2016. Preclinical characterization of ^{18}F-MK-6240, a promising pet tracer for in vivo quantification of human neurofibrillary tangles. *J. Nucl. Med*. 57 (10), 1599–1606. https://doi.org/10.2967/jnumed.115.171678

Hu, F., Morris, P.J., Bonaventura, J., et al., 2020. ^{18}F-labeled radiotracers for in vivo imaging of DREADD with positron emission tomography, *European Journal of Medicinal Chemistry* 113047. ISSN 0223-5234. https://doi.org/10.1016/j.ejmech.2020.113047

Huang Q, Chan KY, Tobey IG, et al. (2019). Delivering genes across the blood-brain barrier: LY6A, a novel cellular receptor for AAV-PHP.B capsids. *PLoS One*, 14(11): e0225206. https://doi.org/10.1371/journal.pone.0225206

Huang, S., 2000. Anatomy of SUV. *Nucl. Med. Biol.* 27 (7), 643–646. https://doi.org/10.1016/S0969-8051(00)00155-4

Hutton, B.F., Erlandsson, K., Thielemans, K., 2018. Advances in clinical molecular imaging instrumentation. *Clin Transl Imaging* 6, 31–45. https://doi.org/10.1007/s40336-018-0264-0

Iyer, S.M., Vesuna, S., Ramakrishnan, C., et al., 2016. Optogenetic and chemogenetic strategies for sustained inhibition of pain. *Sci. Rep*. 6, 30570. https://doi.org/10.1038/srep30570

Ji, B., Kaneok, H., Minamimoto, T., et al., 2016. Multimodal imaging for DREADD expressing neurons in living brain and their application to implantation of iPSCderived neural progenitors. *J. Neurosci*. 7, 13605. https://doi.org/10.1523/JNEUROSCI.1279-16.2016

K¨atzel, D., Nicholson, E., Schorge, S., et al., 2014. Chemical-genetic attenuation of focal neocortical seizures. *Nat. Commun.* 5, 3847. https://doi.org/10.1038/ncomms4847

Kaur, K., Kaushal, S., Copra, S.C., 2009. Varenicline for smoking cessation: a review of the literature. *Curr. Ther. Res.* 70 (1), 35–54. https://doi.org/10.1016/j.curtheres.2009.02.004

Kim, C.Y., Ku, M.J., Qazi, R., et al., 2021. Soft subdermal implant capable of wireless battery charging and programmable controls for applications in optogenetics. *Nat. Commun*. 12, 535. https://doi.org/10.1038/s41467-020-20803-y

Klawonn, A.M., Fritz, M., Nilsson, A., et al., 2018. Motivational valence is determined by striatal melanocortin 4 receptors. *J. Clin. Invest.* 128 (7), 3160–3170. https://doi.org/10.1172/JCI97854

Kügler, S., Kilic, E., B¨ahr, M., 2003. Human synapsin 1 gene promoter confers highly neuron-specific long-term transgene expression from an adenoviral vector in theadult rat brain depending on the transduced area. *Gene Ther.* 10, 337–347. https://doi.org/10.1038/sj.gt.3301905

Lee, H., Giguere, P.M., Roth, B.L., 2014. DREADDs: novel tools for drug discovery and development. *Drug Discov. Today* 19 (4), 469–473. https://doi.org/10.1016/j.drudis.2013.10.018

Liang, Q., Satyamurthy, N., Barrio, J.R., et al., 2001. Noninvasive, quantitative imaging in living animals of a mutant dopamine D2 receptor reporter gene in which ligand binding is uncoupled from signal transduction. *Gene Ther.* 8, 1490–1498. https://doi.org/10.1038/sj.gt.3301542

Lin, J.Y., 2011. A user's guide to channelrhodopsin variants: features, limitations and future developments. *Exp. Physiol.* 96 (1), 19–25. https://doi.org/10.1113/expphysiol.2009.051961.

Luo, L., Callaway, E.M., Svoboda, K., 2008. Genetic dissection of neural circuits. *Neuron* 57 (5), 634–660. https://doi.org/10.1016/j.neuron.2008.01.002

MacLaren, D.A., Browne, R.W., Shaw, J.K., et al., 2016. Clozapine N-oxide administration produces behavioral effects in Long–Evans rats: Implications for designing DREADD experiments. *eNeuro* 3 (5). https://doi.org/10.1523/ENEURO.0219-16.2016

Madsen, M.K., Fisher, P.M., Burmester, D., et al., 2019. Psychedelic effects of psilocybin correlate with serotonin 2A receptor occupancy and plasma psilocin levels. *Neuropsychopharmacol.* 44, 1328–1334. https://doi.org/10.1038/s41386-019-0324-9

Magnus, C.J., Lee, P.H., Atasoy, D., 2011. Chemical and genetic engineering of selective ion channel interactions. *Science* 333 (6047), 1292–1296. https://doi.org/10.1126/science.1206606

Magnus, C.J., Lee, P.H., Bonaventura, J., et al. (2019). Ultrapotent chemogenetics for research and potential clinical applications. Science 364 (6436): eaav5282. https://www.science.org/doi/10.1126/science.aav5282

Marchant, N., Whitaker, L., Bossert, J., et al., 2016. Behavioral and physiological effects of a novel kappa-opioid receptor-based DREADD in rats. *Neuropsychopharmacol* 41,402–409. https://doi.org/10.1038/npp.2015.149

Matsuzaki, Y., Konno, A., Mochizuki, R., et al., 2018. (2018). Intravenous administration of the adeno-associated virus-PHP.B capsid fails to upregulate transduction efficiency in the marmoset brain. *Neurosci. Lett.* 665, 182–188. https://doi.org/10.1016/j.neulet.2017.11.049

Mattis, J., Tye, K.M., Ferenczi, E.A., et al., 2012. Principles for applying optogenetic tools derived from direct comparative analysis of microbial opsins. *Nat. Methods* 9 (2),159–172. https://doi.org/10.1038/nmeth.1808

Mazzone, C.M., Pati, D., Michaelides, M., et al., 2018. Acute engagement of Gq-mediated signaling in the bed nucleus of the stria terminalis induces anxiety-like behavior. *Mol. Psychiatry* 23 (1), 143–153. https://doi.org/10.1038/mp.2016.218

Michaelides, M, Hurd, Y.L., 2015. DREAMM: A biobehavioral imaging methodology for dynamic in vivo whole-brain mapping of cell type-specific functional networks. *Neuropsychopharmacology* 40, 239–240. https://doi.org/10.1038/npp.2014.233

Michaelides, M., Anderson, A., Ananth, M., et al., 2013. Whole-brain circuit dissection in free-moving animals reveals cell-specific mesocorticolimbic networks. *J. Clin. Invest*. 123 (12), 5342–5350. https://doi.org/10.1172/JCI72117

Nagai, Y., Kikuchi, E., Lerchner, W., et al., 2016. PET imaging-guided chemogenetic silencing reveals a critical role of primate rostromedial caudate in reward evaluation. *Nat. Commun*. 7, 13605. https://doi.org/10.1038/ncomms13605

Nagai, Y., Miyakawa, N., Takuwa, H., et al., 2020. Deschloroclozapine, a potent and selective chemogenetic actuator enables rapid neuronal and behavioral modulations in mice and monkeys. *Nat. Neurosci*. 23, 1157–1167. https://doi.org/10.1038/s41593-020-0661-3

Oguchi, M., Okajima, M., Tanaka, S., et al., 2015. Double virus vector infection to the prefrontal network of the macaque brain. *PLoS One* 10 (7), e0132825. https://doi.org/10.1371/journal.pone.0132825

O’Shea, D.J., Kalanithi, P., Ferenczi, E.A., et al., 2018. Development of an optogenetic toolkit for neural circuit dissection in squirrel monkeys. *Sci. Rep*. 8, 6775. https://doi.org/10.1038/s41598-018-24362-7

Pauleit, D., Stoffels, G., Bachofner, A., et al., 2009. Comparison of ^{18}F-FET and ^{18}F-FDG PET in brain tumors. *Nucl. Med. Biol.* 36 (7), 779–787. https://doi.org/10.1016/j.nucmedbio.2009.05.005

Pei, Y., Rogan, S.C., Yan, F., Roth, B.L., 2008. Engineered GPCRs as tools to modulate signal transduction. *Physiology* 23, 313–321. https://doi.org/10.1152/physiol.00025.2008

Raper, J., Morrison, R.D., Daniels, J.S., et al., 2017. Metabolism and distribution of clozapine-N-oxide: implications for nonhuman primate chemogenetics. *ACS Chem. Neurosci*. 8 (7), 1570–1576. https://doi.org/10.1021/acschemneuro.7b00079

Reivich, M., Kuhl, D., Wolf, A., Greenberg, J., Phelps, M., Ido, T., et al., 1979. The [^{18}F] fluorodeoxyglucose method for the measurement of local cerebral glucose utilization in man. *Circ. Res*. 44, 127–137. https://doi.org/10.1161/01.RES.44.1.127

Musafargani, S., Ghosh, K.K., Mishra, S., et al., 2018. PET/MRI: a frontier in era of complementary hybrid imaging. Eur. *J. Hybrid Imaging* 2 (12). https://doi.org/10.1186/s41824018-0030-6

Rollema, H., Shrikhande, A., Ward, K.M., et al., 2010. Pre-clinical properties of the alpha4beta2 nicotinic acetylcholine receptor partial agonists varenicline, cytisine and dianicline translate to clinical efficacy for nicotine dependence. *Br. J. Pharmacol.* 160 (2), 334–345. https://doi.org/10.1111/j.1476-5381.2010.00682.x

Rothermel, M., Brunert, D., Zabawa, C., et al., 2013. Transgene expression in target defined neuron populations mediated by retrograde infection with adeno-associated viral vectors. *J. Neurosci.* 33 (38), 15195–15206. https://doi.org/10.1523/JNEUROSCI.1618-13.2013

Saha, G.B., 2005. Basics of PET. Physics, Chemistry and Regulations. *Springer Science and Business Media, Imaging*. https://doi.org/10.1007/b138655

Saloman, J.L., Scheff, N.N., Snyder, L.M., et al., 2016. Gi-DREADD expression in peripheral nerves produces ligand-dependent analgesia, as well as ligand independent functional changes in sensory neurons. *J. Neurosci*. 36 (42), 10769–10781. https://doi.org/10.1523/JNEUROSCI.348015.2016

Sander, C.Y., Hansen, H.D., Wey, H., 2020. Advances in simultaneous PET/MR for imaging neuroreceptor function. *J. Cereb. Blood Flow Metab.* 40 (6), 1148–1166. https://doi.org/10.1177/0271678X20910038

Saunders, A., Johnson, C.A., Sabatini, B.L., 2012. Novel recombinant adeno-associated viruses for Cre activated and inactivated transgene expression in neurons. *Frontiers in Neural Circuits* 6 (47), 1–10. https://doi.org/10.3389/fncir.2012.00047

Seo, J.W., Ingham, E.S., Mahakian, L., et al., 2020. Positron emission tomography imaging of novel AAV capsids maps rapid brain accumulation. *Nat. Commun*. 11 (2102) https://doi.org/10.1038/s41467-020-15818-4

Shevtosa, Z., Malik, J.M.I., Michel, U., et al., 2005. Promoters and serotypes: targeting of adeno-associated virus vectors for gene transfer in the rat central nervous system in vitro and in vivo. *Exp. Physiol*. 90, 53–59. https://doi.org/10.1113/expphysiol.2004.028159

Shimojo, M., Ono, M., Takuwa, H., et al., 2020. Genetically targeted reporter imaging of deep neuronal network in the mammalian brain. *BioRxiv* 04 (08), 032870. https://doi.org/10.1101/2020.04.08.032870

Slifstein, M., Kegeles, L.S., Xu, X., et al., 2010. Striatal and extrastriatal dopamine release measured with PET and [^{18}F] fallypride. *Synapse* 64, 350–362. https://doi.org/10.1002/syn.20734

Smith, K.S., Bucci, D.J., Luikart, B.W., Mahler, S.V., 2016. DREADDS: use and application in behavioral neuroscience. *Behav. Neurosci.* 130 (2), 137–155. https://doi.org/10.1037/bne0000135

Sokoloff, L., Reivich, M., Kennedy, C., Rosiers, M.H.D., Patlak, C.S., Pettigrew, K.D., Sakurada, O., Shinohara, M., 1977. The [^{14}C]deoxyglucose method for the measurement of local cerebral glucose utilization: theory, procedure, and normal values in the conscious and anesthetized albino rat1. *J. Neurochem.* 28, 897–916. https://doi.org/10.1111/j.1471-4159.1977.tb10649.x

Stachniak, T.J., Ghosh, A., Sternson, S.M., 2014. Chemogenetic synaptic silencing of neural circuits localizes a hypothalamus-midbrain pathway for feeding behavior. *Neuron* 82, 797–808. https://doi.org/10.1016/j.neuron.2014.04.008

Sternson, S.M., Roth, B.L., 2014. Chemogenetic tools to interrogate brain functions. *Annu. Rev. Neurosci.* 37, 387–407. https://doi.org/10.1146/annurev-neuro-071013-014048

Tague, E.P., Dotson, H.L., Tunney, S.N., et al., 2018. Chemogenetic control of gene expression and cell signaling with antiviral drugs. *Nat. Methods* 15, 519–522. https://doi.org/10.1038/s41592-018-0042-y

Taymans, J., Vandenberghe, L.H., Van Den Haute, C., et al., 2007. Comparative analysis of adeno-associated viral vector serotypes 1, 2, 5, 7, and 8 in mouse brain. *Hum. Gene Ther*. 18 (3), 195–206. https://doi.org/10.1089/hum.2006.178

Thanos, P.K., Robison, L., Nestler, E.J., Kim, R., Michaelides, M., Lobo, M.K., Volkow, N. D., 2013. Mapping brain metabolic connectivity in awake rats with μPET and optogenetic stimulation. *J. Neurosci.* 33 (15), 6343–6349. https://doi.org/10.1523/JNEUROSCI.499712.2013

Thompson, K.J., Khajehali, E., Bradley, S.J., et al., 2018. DREADD Agonist 21 is an effective agonist for muscarinic-based DREADDs in vitro and in vivo. *ACS Pharmacol. Transl. Sci*. 1 (1), 61–72.

Tjuvajev, J.G., Doubrovin, M., Akhurst, T., et al., 2002. Comparison of radiolabeled nucleoside probes (FIAU, FHBG, and FHPG) for PET imaging of HSV1-tk gene expression. *J. Nucl. Med.* 43 (8), 1072–1083. https://jnm.snmjournals.org/content/43/8/1072.full

Tremblay, S., Acker, L., Afraz, A., et al., 2020. An open resource for non-human primate optogenetics. *Neuron* 108, 1075–1090. https://doi.org/10.1016/j.neuron.2020.09.027

Tye, K.M., Deisseroth, K., 2012. Optogenetic investigation of neural circuits underlying brain disease in animal models. *Nat. Rev. Neurosci*. 13, 251–266. https://doi.org/10.1038/nrn3171

Upright, N.A., Baxter, M.G., 2020. Effect of chemogenetic actuator drugs on prefrontal cortex-dependent working memory in nonhuman primates. *Neuropsychopharmacology* 45, 1793–1798. https://doi.org/10.1038/npp.2015.293

Urban, D.J., Zhu, H., Marcinkiewcz, C.A., et al., 2015. Elucidation of the behavioral program and neuronal network encoded by dorsal raphe serotonergic neurons. *Neuropsychopharmacology* 41 (5), 1404–1415. https://doi.org/10.1038/npp.2015.293

Vardy, E., Robinson, J.E., Li, C., et al., 2015. A new DREADD facilitates the multiplexed chemogenetic interrogation of behavior. *Neuron* 86, 936–946. https://doi.org/10.1016/j.neuron.2015.03.065

Villien, M., Wey, H., Mandeville, J.B., et al., 2014. Dynamic functional imaging of brain glucose utilization using FDG-PET. *NeuroImage* 100, 192–199. https://doi.org/10.1016/j.neuroimage.2014.06.025

Volkow, N.D., Wang, G.-J., Fowler, J.S., et al., 1994. Imaging endogenous dopamine competition with [^{11}C]raclopride in the human brain. *Synapse* 16, 255–262. https://doi.org/10.1002/syn.890160402

Vomacka, L., Albert, N.L., Lindner, S., et al., 2017. TSPO imaging using the novel PET ligand [^{18}F]GE-180: quantification approaches in patients with multiple sclerosis. *EJNMMI Res.* 7, 89. https://doi.org/10.1186/s13550-017-0340-x

Walker, M.C., Kullman, D.M., 2020. Optogenetic and chemogenetic therapies for epilepsy. *Neuropsychopharmacology* 168, 107751. https://doi.org/10.1016/j.neuropharm.2019.107751

Wang, Y., Xie, K., Yue, H., et al., 2020. Flexible and fully implantable upconversion device for wireless optogenetic stimulation of the spinal cord in behaving animals. *Nanoscale* 12, 2406–2414. https://doi.org/10.1039/C9NR07583F

Watakabe, A., Ohtsuka, M., Kinoshita, M., et al., 2015. Comparative analyses of adeno-associated viral vector serotypes 1, 2, 5, 8 and 9 in marmoset, mouse and macaque cerebral cortex. *Neurosci. Res*. 93, 144–157. https://doi.org/10.1016/j.neures.2014.09.002

Weir, G., et al., 2017. Using an engineered glutamate-gated chloride channel to silence sensory neurons and treat neuropathic pain at the source. *Brain* 140, 2570–2585. https://doi.org/10.1093/brain/awx201

Wess, J., Nakajima, K., Jain, S., 2013. Novel designer receptors to probe GPCR signaling and physiology. *Trends Pharamacol Sci*. 34 (7), 385–392. https://doi.org/10.1016/j.tips.2013.04.006

Weston, M., Kaserer, T., Wu, A., et al. (2019). Olanzapine: a potent agonist at the hM4D (Gi) DREADD amenable to clinical translation of chemogenetics. *Sci. Adv.* 5(4), eaaw1567. https://doi.org/10.1126/sciadv.aaw1567

Williams, J.C., Denison, T. (2013). From optogenetic technologies to neuromodulation therapies. *Science Translational Medicine* 5(177): 177ps6. https://doi.org/10.1126/scitranslmed.3003100

Wu, X., Zhu, X., Chong, P., et al., 2019. Sono-optogenetics facilitated by a circulation delivered rechargeable light source for minimally invasive optogenetics. *Proc. Natl. Acad. Sci*. 116 (52), 26332–26342. https://doi.org/10.1073/pnas.1914387116

Yaghoubi, S.S., Campbell, D.O., Radu, C.G., et al., 2012. Positron emission tomography reporter genes and reporter probes: gene and cell therapy applications. *Theranostics* 2 (4), 374–391. https://doi.org/10.7150/thno.3677

Yizhar, O., Fenno, L.E., Davidson, T.J., et al., 2011. Optogenetics in neural systems. *Neuron* 71 (1), 9–34. https://doi.org/10.1016/j.neuron.2011.06.004

Zhang, F., Wang, L., Boyden, S., Deisseroth, K., 2006. Channelrhodopsin-2 and optical control of excitable cells. *Nat. Methods* 3, 785–792. https://doi.org/10.1038/nmeth936

Zhang, F., Wang, L., Brauner, M., et al., 2007. Multimodal fast optical interrogation of neural circuitry. *Nature* 446, 633–639. https://doi.org/10.1038/nature05744

Zhang, K., Herzog, H., Mauler, J., et al., 2014. Comparison of cerebral blood flow acquired by simultaneous [^{15}O]water positron emission tomography and arterial spin labeling magnetic resonance imaging. *J. Cereb. Blood Flow Metab.* 34, 1373–1380. https://doi.org/10.1038/jcbfm.2014.92

Zimmer, L, Luxen, A, 2012. PET radiotracers for molecular imaging in the brain: Past, present and future. *Neuroimage* 61 (2), 363–370. https://doi.org/10.1016/j.neuroimage.2011.12.037

Zimmermann, D., Zhou, A., Kiesel, M., et al., 2008. Effects on capacitance by overexpression of membrane proteins. Biochem. Biophys. Res. Commun. 369 (4), 1022–1026. https://doi.org/10.1016/j.bbrc.2008.02.153

CHAPTER 2: DEVELOPING A NOVEL PET COMPATIBLE OPSIN FOR TRANSLATIONAL OPTOGENETICS

This chapter has been adapted from a manuscript currently in revision at *Science Translational Medicine*:

Jordi Bonaventura[1,2*], Matthew A. Boehm[2,3*], Hank P. Jedema[4], Oscar Solis[2], Marco Pignatelli[5], Xiaowei Song[4], Hanbing Lu[6], Christopher T. Richie[7], Shiliang Zhang[8], Juan L. Gomez[2], Sherry Lam[2], Marisela Morales[9], Omar A. Gharbawie[10], Martin G. Pomper[11,12], Elliot A. Stein[13], Charles W. Bradberry[4], Michael Michaelides[2,12†]. Noninvasive opsin localization predicts structural and functional brain connectivity. (2022)

*Co-first authors contributed equally

[1]Departament de Patologia i Terapèutica Experimental, Institut de Neurociències, Universitat de Barcelona, L'Hospitalet de Llobregat, Catalonia
[2]Biobehavioral Imaging and Molecular Neuropsychopharmacology Unit, Neuroimaging Research Branch, National Institute on Drug Abuse Intramural Research Program, Baltimore, MD 21224, USA
[3]Department of Neuroscience, Brown University, Providence, RI 02906, USA
[4]Preclinical Pharmacology Section, National Institute on Drug Abuse Intramural Research Program; Baltimore, MD 21224, USA
[5]Department of Psychiatry and Taylor Family Institute for Innovative Psychiatric Research, Washington University School of Medicine, St Louis, MO, 63110, USA.
[6]Magnetiic Resonance Imaging and Spectroscopy Section Neuroimaging Research Branch, National Institute on Drug Abuse Intramural Research Program, Baltimore, MD 21224, USA
[7]Genetic Engineering and Viral Vector Core, National Institute on Drug Abuse Intramural Research Program; Baltimore, MD 21224, USA
[8]Confocal and Electron Microscopy Core, National Institute on Drug Abuse Intramural Research Program; Baltimore, MD 21224, USA
[9]Neuronal Networks Section, National Institute on Drug Abuse Intramural Research Program, Baltimore, MD 21224, USA
[10]Systems Neuroscience Center, Departments of Neurobiology & Bioengineering, University of Pittsburgh, Pittsburgh, PA 15261, USA
[11]Russell H. Morgan Department of Radiology and Radiological Science, Johns Hopkins University School of Medicine, Baltimore, MD 21205, USA
[12]Department of Psychiatry & Behavioral Sciences, Johns Hopkins University School of Medicine, Baltimore, MD 21205, USA
[13]Cognitive and Affective Neuroscience of Addiction Section, National Institute on Drug Abuse Intramural Research Program, Baltimore, MD 21224, USA

2.1 Abstract

Optogenetics is a widely used technology with potential for translational research and clinical therapeutics. A critical component of such applications is the ability to track the location of the transduced opsin in an in vivo manner. However, optogenetic technologies developed to date do not afford this function. To address this problem, we engineered ChRERα (pronounced ‘carrera'), an opsin that can be visualized in the brain in a noninvasive, longitudinal, and quantitative manner using PET imaging. ChRERα consists of the prototypical excitatory opsin Channelrhodopsin-2 (ChR2) and the ligand binding domain (LBD) of the human estrogen receptor alpha (ERα). ChRERα exhibits conserved ChR2 functionality and high affinity for [^{18}F]-16α-fluoroestradiol (FES), an FDA-approved PET radiopharmaceutical. Using PET and [^{18}F]FES, we demonstrate that AAV-mediated ChRERα expression in the brain can be visualized at the local site of AAV injection and at long-range terminal projection sites in rats and monkeys. We also show that ChRERα can be combined with multimodal in vivo imaging to predict and define the anatomical basis of regional metabolic activity and functional connectivity in the brain. In sum, ChRERα is the first opsin that can be used for in vivo circuit mapping to derive mechanistic brain structure-function relationships, expanding the utility of optogenetics and facilitating translational and clinical applications.

2.2 Introduction

Optogenetics is a widely used technology that enables cell type-specific manipulations of neuronal activity with millisecond precision (Boyden et al., 2005; Zhang et al., 2006, 2007). In addition to utility for preclinical neuroscience, optogenetics has strong clinical potential (Chow and Boyden, 2013; Iyer et al., 2016; Simunovic et al., 2019; Walker and Kullman, 2020) as evidenced recently by the partial recovery of visual function in a blind patient using optogenetic-based retinal therapy (Sahel et al., 2021).

The vast majority of preclinical optogenetic experiments to date have used rodents, and such efforts have contributed valuable insights to the fields of behavioral neuroscience, neurology, and psychiatry (Deubner et al., 2019). Nevertheless, findings from such studies would be further elevated if done in nonhuman primates (NHPs) who share strong neuroanatomical similarities to humans and can perform complex human-like behaviors and tasks (Kaas 2013; Wise 2008). Accordingly, research using NHPs is key for understanding complex systems and behaviors like sensory processing, motor control, decision-making, social interaction, and affective regulation. Furthermore, NHP research is essential for understanding relationships between nervous system abnormalities and maladaptive behaviors, and for the development of brain-targeted human therapies (Garbarini 2010; Kalin et al., 2003). Notwithstanding, NHP research has stronger ethical and economic constraints than rodent research. Such factors hinder feasibility of applications like optogenetics in NHPs because of the need for postmortem validation of transgene expression. In particular, transduction vectors cannot be easily optimized in NHPs, and long lags occur between in vivo NHP experimentation and postmortem validation of transgene expression.

Although progress in NHP optogenetics has been made in recent years (Tremblay et al., 2020), advances have been limited, and a variety of practical obstacles preclude widespread adoption of such applications (Bliss-Moreau et al. 2020; Deng et al., 2017; Galvan et al., 2017; Inoue et al., 2021). One critical factor limiting NHP optogenetic applications is the inability to monitor the anatomical distribution of opsin expression in a quantitative, noninvasive, and longitudinal manner. Except for NHP studies performing optogenetics in superficial brain regions (e.g., via a cranial window), current NHP optogenetics is mostly limited to targeting optical fibers to opsins expressed at the virus injection site. The main reason for this is that one cannot effectively predict opsin expression at distal terminal projection sites in deep brain regions, which is necessary for achieving pathway-specific optogenetic neuromodulation. In this way, pathway-specific optogenetic applications in NHPs are hindered by the need to rely on indirect anatomical knowledge (i.e., brain atlases) and do not account for inter-subject anatomical variability. Finally, the inability to monitor opsin expression is a barrier to potential clinical applications where treatment plans and patient outcomes would benefit from noninvasive, longitudinal tracking of the transduced construct in the brain.

The molecular imaging capabilities of positron emission tomography (PET) can address the challenge of in vivo opsin localization. The use of selective PET radiotracers has enabled noninvasive localization and quantification of several of exogenous proteins introduced by viral transduction in rodents, NHPs, and humans (Bonaventura et al., 2019; Magnus et al., 2019; Nagai et al., 2020, Yaghoubi et al., 2009, 2012). Furthermore, PET affords the highest detection sensitivity of any molecular imaging modality, and recent breakthroughs in PET detector technology have considerably improved spatial/temporal resolutions and radiation dose requirements (Mikhaylova et al., 2017; Du et al., 2018; Hutton et al., 2018). As such, PET is ideal for visualizing the location and quantifying the expression of exogenous transgenic proteins in living subjects (Boehm et al., 2021; Yaghoubi et al., 2012) and could therefore facilitate the growing interest to develop translational applications of optogenetics and chemogenetics for disorders including epilepsy, neuropathic pain, insomnia and motor dysfunction following ischemic stroke (Conti et al., 2020; Korczeniewska et al., 2022; Venner et al., 2019; Walker and Kullmann, 2020).

Many opsins have been created to date (Duebel et al., 2015; Nguyen et al., 2020), but developing dedicated high affinity and selective PET radioligands for any given opsin is impractical. A key reason for this is that other than the binding site for the covalently linked retinal, opsins lack targets for known small molecule ligands. An alternate approach is to develop a PET-based reporter system that could visualize the distribution of any opsin (or other proteins of interest), making it adaptable to a variety of gene therapy strategies by fusing a small protein tag to the protein of interest. Such a "universal" PET reporter system would need to satisfy four major requirements: (i) the radioligand used to detect it would need to exhibit high binding affinity and high in vivo selectivity for the specific fusion tag, (ii) the radioligand-tag reporter system would need to be scalable to different classes of opsins/proteins, (iii) the tag would need to be small enough to fit into a viral vector backbone and preferably of human origin (i.e., non-immunogenic), and (iv) it should not interfere with the exogenous protein's function or with endogenous physiology.

The human estrogen receptor alpha (ERα) is a multi-domain nuclear receptor. ERα is mainly found in reproductive tissues as well as in the kidney, liver, breast tissue and bone, but its expression levels in the brain relative to these other organs is low (Jia et al., 2015). The ligand binding domain (LBD) of ERα is in the C-terminal part of the protein and its binding properties are retained when detached from the DNA-binding domain (Kumar et al., 2011). An FDA-approved PET radioligand, [18F]16α-fluoroestradiol ([18F]FES), has been used to visualize ERα in animals and humans and shows low brain accumulation (Paquette et al., 2012; Katzenellenbogen 2021). We posited that the favorable anatomical distribution profile of ERα (i.e., low brain expression), and the high affinity of the ERα-LBD for [18F]FES would constitute a translational PET reporter system that will satisfy the above requirements to allow visualization of opsins in the brain.

2.3 Results

2.3.1 In vitro characterization of ChRERα binding and function

The cDNA for ERα-LBD (Addgene plasmid #105415) was appended to the C-terminus of the open reading frame of hChR2(H134R) (Addgene #26973) using a V5 epitope as a linker. The fusion product, hChR2(134R)-V5-ERα-LBD or "ChRERα", was inserted downstream of a CMV-IE promoter in pcDNA3.1 vector (Figure 1A). This plasmid was transfected along with other vectors containing V5-ERα-LBD or hChR2(H134R)-EYFP into HEK-293 cells.

To examine cellular distribution, we lysed cells and separated the lysates into cytosolic and membrane fractions. We used an anti-V5 antibody (Invitrogen PA1-993 polyclonal) and western blot to detect antigen expression. As expected, no immunoreactivity was detected for hChR2(H134R)-EYFP, whereas V5-ERα-LBD (a soluble protein) was strongly detected in the cytosolic and membrane fraction (Figure 1B). ChRERα was only detected in the membrane fraction with an apparent MW (~70 kDa) compatible with the fusion construct (Figure 1B).

Next, we tested whether ChRERα retained its binding affinity to 17β-estradiol (E2) and to FES using saturation and competition radioligand binding assays with [^{3}H]E2 in HEK-293 cells transfected with ERα-LBD or ChRERα. The membrane fractions of cells transfected with

ChRERα bound [^{3}H]E2 with similar affinity (KD = 0.39 ± 0.03) as those transfected with ERα-LBD (KD = 0.35 ± 0.03) (Figure 1C). Additionally, [^{3}H]E2 competition binding assays with FES showed that cells transfected with ChRERα bound FES (Ki = 0.4 ± 0.1 nM) with similar affinity as those transfected with the ERα-LBD (Ki = 0.3 ± 0.1 nM) (Figure 1D), indicating that fusion to hChR2(134R) did not affect the binding properties of ERα-LBD.

To assess its ion channel function, we transfected ChRERα or hChR2(134R)-EYFP into HEK293 cells and performed whole-cell patch clamp recordings in response to blue light (473 nm) stimulation. Steady state photocurrent amplitudes (ChRERα -65.9pA ±19.32; ChR2 -91.4 ± 17.02, Figure 1E) and voltage-current curves (Figure 1F) in cells transfected with ChRERα did not significantly differ from those observed in ChR2-transfected cells, demonstrating that ChRERα retains opsin function.

2.3.2 ChRERα trafficking and subcellular localization in the rat brain

ChRERα was packaged into an adeno-associated viral vector (AAV) (serotype 2/5) with the human synapsin 1 (hSyn1) promoter to facilitate neuronal transduction (AAV-ChRERα: AAV2/5-hSyn1-ChR2(H134R)-V5-ERαLBD; 1.32 x 1014 gc/ml; Boston Children's Hospital Viral Vector Core). AAV-ChRERα was injected into the right prelimbic/dorsal anterior cingulate cortex (PrL/ACd) area (AP 3.0, ML: 0.6, DV: -3.5 from bregma) in rats (Figure 2A). About five weeks later, rats were perfused with 4% PFA and ChRERα localization was assessed using immunohistochemistry (IHC) with an anti-ChR2 antibody (ARP #03-651180). ChRERα was expressed in cell bodies and axonal processes at the site of AAV injection (Figures 2B-D) and at downstream projection sites (i.e., right mediodorsal thalamus (MDT), zona incerta (ZI), and striatum) (Figures 2H-2K and Figures S1C-S1D). To visualize the subcellular location of ChRERα, immuno-electron microscopy (immuno-EM) was performed using the same anti-ChR2 primary antibody in a subset of rat brain slices. We observed plasma membrane ChRERα expression at the soma, dendrites, and synaptic axon terminals in the right PrL/ACd AAV injection area (Figures 2E-2G, Appendix Fig. A1A) and at the level of the MDT (Figures 2L-2N and Figure S1B) and ZI (Appendix Figs. A1E-F), confirming the subcellular membrane localization, anterograde trafficking, and retrograde AAV transduction of ChRERα.

2.3.3 ChRERα activation alters brain activity and behavior in rodents

To further examine the functional properties of ChRERα, we performed ex vivo slice electrophysiology in a cohort of mice injected with AAV-ChRERα in the PrL/ACd (AP: 2.0, ML: 0.3, DV: -2.0 from bregma). Coronal brain slices were collected 2-4 weeks following AAV-ChRERα injection, and whole cell patch-clamp recordings were acquired from pyramidal cells near the AAV injection site during blue light stimulation (Figures 3A-3D). Patching was performed blind given the absence of a fluorescent reporter, and ~20% of recorded cells showed consistently robust light-evoked depolarizations characteristic of opsin function.

Next, we used optogenetics combined with PET and [^{18}F]fluorodeoxyglucose (FDG) (Thanos et al., 2013; Boehm et al., 2021) to evaluate in vivo functional effects of ChRERα stimulation in rats. We injected AAV-ChRERα in the right PrL/ACd of rats (AP: 3.0, ML: 0.6, DV: -3.5 from bregma, Figure 3E) and then implanted an optic fiber 0.5 mm above this site about three weeks later. A separate group of rats without AAV-ChRERα were also implanted with optic fibers in right PrL/ACd to serve as controls for the light stimulation experiment. On the day of the experiment, rats were anesthetized with ~2% isoflurane and a bolus injection of FDG (~0.5 mCi, i.p.) was administered followed by light stimulation (473nm, 3ms-pulse trains at 50Hz – 300ms on, 700ms off) for 30-min. Rats were then scanned using a Mediso nanoScan® PET/CT scanner (20 min PET acquisition + CT) and FDG uptake was quantified as standard uptake values (SUV, g/ml) to account for injected radioactivity and animal body weight (Figure 3F). A voxel-wise analysis (i.e., two-sample t-test, SPM12) comparing the non-ChRERα control group (i.e., optic fiber implant in rats without AAV, $n = 4$) and AAV-ChRERα group (i.e., optic fiber implant in rats with AAV-ChRERα, $n = 5$) showed significant differences in FDG uptake ($t > 1.89$; $p < 0.05$, cluster threshold = 50 voxels/0.4mm^3) in multiple brain regions including the PrL/ACd stimulation site and brain regions with known anatomical connections with PrL/ACd (i.e., thalamus, striatum, nucleus accumbens (NAc), insular cortex (IC), hippocampus, infralimbic cortex (IL) and contralateral PrL/ACd (Jay et al., 1989, Shibata et al., 2005, Vertes, 2003) (Figure 3 and Appendix Fig. 2). Specifically, light stimulation in AAV-ChRERα rats induced significantly greater metabolic activity ($t > 3.0$; $p < 0.01$) in the right PrL/ACd as well as in the ipsilateral MDT (Figures 3G-3I), both areas where ChRERα expression was observed with IHC after AAV injection in right PrL/ACd (Figure 2). Light stimulation in AAV-ChRERα rats also induced greater metabolic activity (i.e., FDG uptake) bilaterally in the inferior colliculi, contralaterally in PrL/ACd, NAc and IC, and ipsilaterally in the lateral thalamus and brainstem (Figures 3G-3I and Appendix Fig. A2; $t > 3.0$, $p < 0.01$). Because the rate of FDG uptake is greatest in highly active brain regions (i.e., at synaptic terminal sites of neurons firing action potentials) (Sokoloff, 1984), these areas likely reflect the increased firing of stimulated PrL/ACd neurons at local synapses and at synapses in anatomically connected brain regions receiving excitatory projections from PrL/ACd (i.e., MDT, NAc and IC). In contrast, light-stimulation in ChRERα rats elicited lower FDG uptake compared to controls bilaterally in striatum and cerebellum, ipsilaterally in infralimbic cortex, motor cortex, septum, and contralaterally in ventral pallidum, lateral thalamus, hippocampus, and entorhinal cortex (Appendix Fig. A2). These brain regions are also known to have anatomical connections with PrL/ACd (Jay et al., 1989, Shibata et al., 2005, Vertes, 2003), but the lower FDG uptake compared to controls suggests they may receive predominately inhibitory projections from PrL/ACd given the net effect of PrL/ACd stimulation results in decreased activity in these brain areas. Post-mortem IHC confirmed ChRERα expression and optic fiber placement in the right PrL/ACd (Figure 3J).

Finally, to test whether ChRERα activation could modulate behavior, we chose to target the VTA-NAc pathway because this circuit has a clearer behavioral output than PrL/ACd stimulation. Specifically, VTA dopaminergic fibers are known to project to NAc, and activation of these VTA terminals in NAc has been shown to induce locomotion (Boekhoudt et al., 2016). Therefore, we injected AAV-ChRERα into the ventral tegmental area (VTA) of rats (AP: -5.5, ML: 0.8, DV: -8.2 from bregma), and four weeks later an optical fiber was implanted into the NAc (AP: 1.3, ML: 1.0, DV: -6.5) (Figure 3K). A separate group of rats without AAV-ChRERα were also implanted with optic fibers to serve as controls. On the day of the experiment, rats were tethered to an optic fiber in an open-field chamber (Figure 3K) and locomotor activity was recorded during periods with and without light stimulation (see method for protocol details). Light stimulation significantly increased locomotor activity in the AAV-ChRERα group as compared to the control group (Figures 3L-3M). The statistical analysis of distance traveled, which included two factors (AAV group and light stimulation) matched by subject, showed significant effects of light stimulation ($F(1,24) = 12.6$, $p = 0.001$) and an interaction effect between AAV transduction and light stimulation ($F(1,24) = 6.74$, $p = 0.01$) (Figure 3M). Postmortem IHC confirmed expression of ChRERα in the VTA (Figures 3N-3O).

2.3.4 FES-PET localizes ChRERα in the brain of individual rats

Next, we tested whether ChRERα expression could be visualized noninvasively with [^{18}F]FES in the rat brain. We first obtained [^{18}F]FES-PET scans in naïve male and female rats to establish baseline levels of [^{18}F]FES binding in the brain. Anesthetized rats were given a bolus injection of [^{18}F]FES (i.v. ~0.5mCi) and scanned for 90 minutes. Just as performed in the FDG-PET analysis, [^{18}F]FES-PET acquisition data was first converted to standard uptake values (SUV g/ml) to correct for animal body weight and injected radiotracer dose. However, because [^{18}F]FES exhibits reversable binding (instead of metabolic trapping as in FDG uptake), the image data was then quantified as SUV ratios (SUVR) and binding potentials (BP_{ND}) using the cerebellum as a nonspecific reference region in attempt to better represent specific binding (see methods for details). The cerebellum was chosen as the nonspecific reference region to due to its large size and low endogenous ERα levels (Khayum et al., 2014). As expected, the greatest level of [^{18}F]FES binding was detected in the pituitary (Figure 4A), which has high endogenous ERα expression (Khayum et al., 2014). Low specific binding was observed in the rest of the brain including the PrL/ACd (Figure 4A). After characterizing baseline [^{18}F]FES brain uptake in AAV-naïve rats (controls, n=5), we injected a separate group of rats (ChRERα, n=6) with AAV-ChRERα into the right PrL/ACd and scanned them with [^{18}F]FES 3-5 weeks after AAV injection (Figure 4B). A voxel-wise analysis (two-sample t-test, SPM12) revealed that compared to controls, rats injected with AAV-ChRERα showed significantly higher binding of [^{18}F]FES at the right PrL/ACd AAV site and in downstream projection areas (i.e., ipsilateral MDT) ($t = 1.89$, $p < 0.05$) (Figures 4C-4F and Appendix Fig. A3). These findings are consistent with the expected expression of ChRERα at the PrL/ACd AAV site and at anatomically connected regions such as MDT and striatum (Vertes, 2003) (see Figure 2 and Appendix Fig. A1). Importantly, [^{18}F]FES-PET localized ChRERα expression in individual rats with similar efficacy in females (n = 3) and males (n =3) (Appendix Figs. A3I-J). Furthermore, the pattern of

[^{18}F]FES binding in the brain coincided with ChRERα expression as confirmed via postmortem IHC (Figure 4G).

Additionally, [^{18}F]FES-PET was performed in a separate cohort of rats that were injected with half the volume (therefore half the total viral load/genome copies) of AAV-ChRERα (0.5 μl instead of 1 μl) in left primary motor cortex (M1) (AP: 2.0, ML: 3.0, DV: -2.1 from bregma, n = 5) (Figure 4H). As expected, post-AAV (3+ weeks) [^{18}F]FES-PET scans were capable of localizing ChRERα in left M1 of individual subjects (Figure 4I-4K). [^{18}F]FES binding to ChRERα showed regional specificity, as the right PrL/ACd group did not show substantial binding of [^{18}F]FES in M1 (Figure 4E), and the left M1 ChRERα group did not show higher [^{18}F]FES in the PrL/ACd compared to controls (Figure 4J). Interestingly, the average BP_{ND} near the AAV injection site in the left M1 group (0.52, n = 5) was approximately half that observed near the AAV injection site in the right PrL/ACd group (1.2, n = 6). This is consistent with their respective amounts of injected AAV which suggests [^{18}F]FES BP_{ND} is a quantitative measure that is relatively proportional to the density of ChRERα expression. IHC (with anti-ChR2) in the left M1 group confirmed ChRERα expression at the AAV injection site. Together these observations confirm the capacity for [^{18}F]FES-PET to visualize the anatomical location of ChRERα and approximate the relative density of expression in the brains of individual subjects.

2.3.5 [^{18}F]FES-PET localizes ChRERα in NHPs and predicts structural and functional brain connectivity

We next tested whether AAV-mediated ChRERα expression could be localized using [^{18}F]FES-PET in the squirrel monkey brain. Two male squirrel monkeys underwent structural magnetic resonance imaging (MRI) and pre-AAV [^{18}F]FES PET (Figure 5A) to map out an AAV stereotaxic injection location and determine baseline [^{18}F]FES distribution. As observed in rats, the highest [^{18}F]FES binding in monkeys was detected in the pituitary (Figure 5B). Additional

[^{18}F]FES signal, but of much lower extent, was observed in the brain along white matter tracts (Figure 5B). For AAV injections, monkeys were placed in a stereotactic apparatus and injected with AAV-ChRERα in the forelimb region of left M1 (three 1.0 μl injections at 100 nl/min, spaced 0.5mm dorsal to ventral, AAV titer 1.32 x 1014 gc/ml). The left M1 injection site was first approximated using individual structural MRIs and then specific sites for injection within the forelimb representation were determined with intracortical microstimulation.

In monkey 1, [^{18}F]FES binding (BP_{ND}) in left M1 increased from 0.12 at pre-AAV to 0.47 at five weeks following AAV injection (~4-fold increase, Figures 5C-5D and 5F). Additionally, we observed a ~10-fold increase of [^{18}F]FES (BP_{ND} from 0.1 to 1.1) in a region of the ipsilateral posterior parietal cortex (PPC) (Figures 5D and 5F), an area known to have anatomical connections with M1 (Gharbawie et al., 2011). In monkey 2, a ~3.5-fold increase in [^{18}F]FES was observed in left M1 seven weeks after AAV injection ($BP_{\mathrm{ND)}}$ from 0.15 pre-AAV to 0.53 post-AAV) (Figures 5E and 5F). However, we did not see the same large increase in the ipsilateral PPC of monkey 2 (BP_{ND} from 0.1 at pre-AAV vs. 0.15 at seven weeks post-AAV). This finding emphasizes the variability in expression that can occur when using AAVs because overall expression patterns depend on multiple factors including the spatial extent of viral load spread and the level of local/distal trafficking of expressed transgenic proteins. [^{18}F]FES scans were also quantified as SUV (g/ml) and SUV ratio ($\mathrm{SUVR_{CB}}$; cerebellum reference) which showed distribution patterns consistent with BP_{ND} (Appendix Fig. A4), suggesting that both methods are suitable for localizing ChRERα expression in individual animals.

To longitudinally track ChRERα expression, we performed additional [^{18}F]FES-PET scans for each monkey at different timepoints (i.e., 25-80 weeks post-AAV). The localized increases of [^{18}F]FES in left M1 observed in the initial post-AAV scans steadily declined over time in both monkeys, but they were still observable 40 weeks post-AAV in monkey 1 and in scans 25 and 80 weeks post-AAV in monkey 2 (Figures 5G-5H, Figure 6A and Appendix Figs. A4F-G).

To verify that areas with increased [^{18}F]FES binding reflect ChRERα expression and trafficking, IHC and immuno-EM with anti-ChR2 primary antibody (ARP #03-651180) were used for post-mortem assessment of ChRERα expression in monkey 2 following the last scan 80 weeks post-AAV. IHC revealed that ChRERα expression was highest in left M1 and was also present in the ipsilateral PPC (Figures 6B-6E, 6K). Importantly, both of these regions coincided with [^{18}F]FES hotspots observed in the 80-week post-AAV scan (Figure 6A). In addition, some IHC labelling and [^{18}F]FES binding was observed in right M1 (Appendix Figs. A5A-D, Figure 6A). Immunogold-EM was performed to visualize subcellular localization of ChRERα in these brain areas (i.e., left M1, left PPC and right M1). Immunogold labelling of ChRERα showed it was located in the endoplasmic reticulum (ER) and at the plasma membrane of soma, dendrites, myelinated axons, and synaptic axon terminals in left M1 (Figure 6F-6J), left PPC (Figure 6L-6N) and right M1 (Appendix Fig. A5E-G). These findings confirmed ChRERα's anterograde axon terminal trafficking, retrograde AAV-ChRERα transduction and expression, and plasma membrane localization in monkeys.

Finally, to explore the functional relevance of the M1-PPC circuit identified by [^{18}F]FES-PET (Figure 7A), we analyzed resting state fMRI (rsfMRI) data acquired from an independent cohort of 9 non-AAV-injected squirrel monkeys using the left M1 injection site as a seed in a whole brain functional connectivity analysis. We identified regions in the ipsilateral PPC and contralateral M1 that showed significant connectivity with the left M1 seed (Figure 7B-D). Importantly, this functional circuit overlapped with regions identified using [^{18}F]FES-PET in monkey 1 (Figure 7A and 7D), which showed the greatest [^{18}F]FES signal in the PPC, as well as with the smaller [^{18}F]FES PPC signal observed in monkey 2 (Figure 6A) and is consistent with known anatomical and functional connectivity of M1 in New World monkeys (Gharbawie et al., 2011; Stepniewska et al., 1993; 2020, Card and Gharbawie, 2022). Collectively, these findings highlight the utility of [^{18}F]FES-PET and ChRERα for in vivo mapping of anatomical projections and informing the structural basis of functional connectivity maps.

2.4 Discussion

Here we describe the development of ChRERα, a novel opsin whose expression in the brain can be localized noninvasively and longitudinally in both the rat and monkey using the FDA-approved PET radiopharmaceutical [^{18}F]FES. ChRERα retained the ligand binding properties of the ERα-LBD and the light-sensitive functional properties of ChR2. When transduced into the brain, ChRERα displayed plasma membrane localization in cell bodies, dendrites, and axon terminals in rats and monkeys, indicating appropriate subcellular trafficking of the opsin for enabling light induced neuronal activation. Since ChRERα lacks the DNA binding domain of ERα and is tethered to the membrane by the transmembrane domains of the opsin (i.e., it cannot enter the cell nucleus) we expected this construct to be inert under non-stimulated conditions. Indeed, we did not observe any effects when ChRERα was expressed in vitro or in vivo in the absence of light stimulation, whereas blue light effectively activated it to produce changes in physiology, metabolic brain activity and behavior. Importantly, we demonstrated the novel utility of this opsin by showing [^{18}F]FES-PET effectively localized ChRERα in individual rats and squirrel monkeys at both the local AAV injection site and in brain regions with known connectivity to the injection site. We did not observe significant differences in the efficacy of [^{18}F]FES to detect ChRERα in male versus female rats, suggesting that if sex differences existed in basal uptake of [^{18}F]FES, these did not affect detection of virally driven expression of ChRERα.

Existing NHP optogenetic applications have inherent limitations as they do not permit non-invasive longitudinal monitoring of opsin expression. Here, we used repeated within-subject scans in monkeys to profile ChRERα expression over a 1.5-year period after AAV injection. This is particularly important because it means that a histological snapshot of opsin expression at the end of the study would have missed the expression pattern of ChRERα during the preceding time period when experiments would have been performed. This highlights the utility of the present reporter system for translational optogenetic studies where knowledge regarding the spatial and temporal profiles of opsin expression would have major implications for successful translational and potential clinical implementation.

Translational and clinical optogenetic applications necessitate development of combined optogenetic and noninvasive brain imaging, especially in NHPs. Noninvasive multimodal functional imaging in NHPs can provide valuable insights into the neurobiological mechanisms underlying translationally relevant biomarkers and behaviors. Specifically, the ability to localize and quantify opsin expression at discrete anatomical sites in a longitudinal manner is critical for ascribing neural circuit involvement to normal behavior and disease states across the lifespan. Coupled with optogenetic manipulation, this approach can help inform findings and establish causality for associations observed from human functional brain connectivity (Gerits et al., 2012, Galvan et al., 2017) that is altered as a function of disease (Li et al., 2020) and can serve as a diagnostic or potential indicator of prognostic recovery (Boon et al., 2020). When combined with multimodal imaging (i.e., [^{18}F]FES-PET with [^{18}F]FDG-PET or MRI), our ChRERα data informed personalized brain structure-function relationships in individual rats and monkeys. This noninvasive circuit mapping allowed us to predict brain regional metabolic activity in rats and functional connectivity in monkeys. This multimodal validation serves as an example of how ChRERα can potentially be used to explore and characterize relationships between brain functional connectivity and its anatomical substrates.

The use of the ERα-LBD reporter system is not expected to be limited to ChR2 and may provide a modular solution to image other opsins, and potentially other effector proteins. In this way, the [^{18}F]FES/ERα-LBD may comprise a universal reporter system for noninvasive brain localization of transgenic constructs in rodents, NHPs and potentially in clinical applications. Notably, this does not only solve the problem of tracking proteins without a known and targetable LBD, but it could also facilitate standardization/optimization in gene therapy, which would facilitate comparisons between different gene therapy approaches in a personalized manner and across species.

A potential limitation of this technique in the brain is the intense accumulation of [^{18}F]FES within the pituitary. Due to partial volume effects in PET, this may limit the use of this reporter system in animals with small brains, especially if the targeted region is close to the pituitary. However, as we show here, this is not a meaningful limitation in rats or squirrel monkeys and would have even less bearing in larger brains with relatively small pituitary (e.g., macaque, human). Another potential limitation is that [^{18}F]FES accumulated, albeit it to a low extent, in white matter. Therefore, it may show higher non-specific accumulation in brains with high white matter content. This latter limitation can potentially be addressed, if necessary, by designing less lipophilic steroid analogs and by optimizing viral vector transduction to drive the optimal level of ChRERα expression for its detection. Additionally, the ERα-LBD may be mutated to further enhance [^{18}F]FES affinity. Finally, [^{18}F]FES radio metabolite analyses and arterial blood-derived input functions, which we did not perform here due to the small size of the animals used, but which are routinely performed in larger NHPs such as rhesus macaques or in humans, can likely aid to further improve ChRERα detection.

In sum, with the modular technology described in this study, we provide a novel tool to monitor the expression of transgenic proteins that lack a known LBD, and to analyze their neuroanatomical distribution in a noninvasive, quantitative, and longitudinal manner. We expect that this new system will help to transcend the current translational barriers facing optogenetics and other gene therapy-related technologies to facilitate clinical applications.

2.5 Methods

Plasmid cDNA and AAV production:

We generated a plasmid encoding a chimeric protein consisting of channelrhodopsin ChR2(H134R) and ERα-LBD tethered by a linker containing a V5 epitope (ChR2–V5–ERα-LBD or "ChRERα"), and a plasmid encoding the V5-tagged ERα-LBD without the ChR2 domain ("V5–ERα-LBD"). Polymerase chain reaction (PCR) was used to amplify ChR2 and ERα-LBD (Q5 Hotstart polymerase, New England Biolabs) with linkered primers. Amplicons were cloned into pcDNA3.1 using ligation-independent cloning (LIC, In-Fusion cloning mix, Takara, Inc.). The open reading frame for ERα-LBD was amplified with a V5-linker from pCK025 (a gift from Johannes Stuttmann (Addgene plasmid # 105415; http://n2t.net/addgene:105415; RRID: Addgene_105415)). The open reading frame for hChR2(H134R) was amplified from pAAV-hSyn-hChR2(H134R)-EYFP (a gift from Karl Deisseroth (Addgene plasmid # 26973; http://n2t.net/addgene:26973; RRID: Addgene_26973)). These constructs were transfected in vitro in HEK-293 cells for radioligand binding assays and patch-clamp recordings during light stimulation. The coding region for ChRERα was also cloned into a AAV packaging vector driven by the promoter for human synapsin 1 (Syn1) to facilitate expression in neurons. This plasmid was packaged into AAV serotype 5 viral particles (AAV2/5-Syn1-ChRERα; 1.32 x 10^{14} gc/ml, Boston Children's Hospital Viral Vector Core).

Cell culture and transfection

Human embryonic kidney (HEK-293) cells were grown in Dulbecco's modified Eagle's medium (DMEM; Gibco Thermo-Fisher Scientific, Waltham, MA, USA) with 5% bovine growth serum (BGS; HyClone, Logan, UT) and antibiotic/antimycotic supplements (Gibco) in an incubator at 37°C and 5% CO_2. HEK-293 cells were seeded on 150 mm dishes and transfected with plasmids expressing ChRERα or the control constructs V5-ERα-LBD or ChR2(H134R)-EYFP using calcium phosphate precipitation (NIDA-IRP GEVVC Project 19042; Harvey et al., 2008). Cell harvesting for Western blot and radioligand binding assays was performed approximately 48 hours after transfection.

Western Blot

Transfected HEK-293 cells were harvested and frozen at -80°C until undergoing cytosolic and membrane fraction preparation for Western Blot analysis. Frozen cell pellets were thawed and homogenized using a polytron in 10ml ice-cold buffer (50 mM Tris-HCl, pH 7.4 with protease inhibitor cocktail (Sigma)). The mixture was then centrifuged for 50-min at 4°C (20,000 rcf) and the supernatant collected as the cytosolic fraction. The remaining pellet was resuspended with a polytron in 10ml ice-cold Tris-HCl buffer and centrifuged again for 50-min at 4°C (20,000 rcf). The supernatant was then discarded, and the remaining pellet (membrane fraction) was stored at -80 °C until further use as the membrane fraction. Protein concentration was determined using the BCA assay kit (Pierce).

On the first day of the Western blot, the frozen membrane fraction was thawed and resuspended in ice-cold buffer (50 mM Tris-HCl, pH 7.4 with protease inhibitor cocktail) to achieve a concentration of ~2 mg of protein/ml. Aliquots containing 20µg of protein of the cytosolic and resuspended membrane fractions were mixed with 2x Laemmli sample buffer (1:1 volume) and β-mercaptoethanol was added as a reducing agent. Samples were then incubated at 95 °C for 5-min. Following incubation, samples were vortexed and placed on ice. An electrophoresis tank was filled with ice-cold running buffer (Bolt^{TM}, Thermofisher Scientific) and a precast gel (NuPage^{TM} Bis-Tris with a 4-12% polyacrylamide gradient, ThermoFisher Scientific). A molecular weight protein ladder (LICOR Biosciences Chameleon Duo pre-stained protein ladder) was loaded into a well of the gel along with the prepared cytosolic and membrane samples (~20µg) following quick centrifuge at 4°C. Electrophoresis was run for 15 min at 50 V, and then the voltage was increased to ~125V for about 1 hour. Following the run, the gel was removed, rinsed in ddH$_2$O, then placed in a transfer stack and run in an iBlot2 western blotting system (Thermo Scientific). The transferred stack membrane was rinsed in ddH$_2$O and then incubated in LI-COR Biosciences blocking buffer (LICOR Biosciences) for 1 hour at RT. The blocking buffer was then removed and replaced with primary antibody (V5 Rabbit Polyclonal; Invitrogen PA1-993) diluted in LICOR blocking buffer (1:1500) and incubated overnight at 4°C. On the second day, the membrane was rinsed with washing buffer (PBS 1x + 0.1% Tween-30; 3 x 5 min) and then incubated in secondary antibody (IRDye 800CW, Donkey anti-Rabbit, LICOR 926-32213) for 2 hours at RT. Following secondary antibody incubation, the membrane was washed with washing buffer (3 x 5 min, RT), rinsed in ddH$_2$O, air dried on filter paper and then imaged using a LICOR Odyssey CLx scanner (LICOR Biosciences).

Radioligand binding assays

Transfected HEK-293 cells were harvested 48 hrs after transfection. Cells were suspended in Tris-HCl 50 mM pH 7.4 supplemented with protease inhibitor cocktail (1:100, Sigma-Aldrich, St Louis, MO, USA). HEK-293 cells were disrupted with a Polytron homogenizer (Kinematica, Basel, Switzerland). Homogenates were centrifuged at 48,000 g (50 min, 4 °C) and washed twice in the same conditions to isolate the membrane fraction. Protein was quantified by the bicinchoninic acid method (aka Pierce). For saturation experiments, membrane suspensions (50 µg of protein/ml) were incubated during 2hr at RT in 50 mM Tris-HCl (pH 7.4) containing 10 mM MgCl2 and increasing concentrations of [^{3}H]E2 (0.1 to 5 nM, 88 Ci/mmol, Perkin-Elmer). Non-specific binding was determined in the same conditions with the presence of cold E2 (10 µM). For competition experiments, membrane suspensions (50 µg of protein/ml) were incubated for 2hr at RT in 50 mM Tris-HCl (pH 7.4) containing 10 mM MgCl2, [^{3}H]E2 (1 nM, 88 Ci/mmol, Perkin-Elmer), and increasing concentrations of cold E2 and FES (0.1 nM to 1 mM. Non-specific binding was determined in the presence of 10 µM of cold E2. In all cases, free and membrane-bound radioligand were separated by rapid filtration of 500-µl aliquots in a 96-well plate harvester (Brandel, Gaithersburg, MD, USA) and then washed with 2 ml of ice-cold Tris-HCl buffer. Microscint-20 scintillation liquid (65 µl/well, PerkinElmer) was added to the filter plates. Plates were incubated overnight at RT and radioactivity counts were determined in a MicroBeta2 plate counter (PerkinElmer, Boston, MA, USA) with an efficiency of 41%. Saturation curves and one-site competition curves were fitted using Prism 9 (GraphPad Software, La Jolla, CA, USA). Ki values were calculated using the Cheng-Prusoff equation (Cheng and Prusoff, 1973).

Electrophysiology in cell culture

HEK-293 cells transfected with either ChRERα or ChR2(H134R)-EYFP were exposed to blue light stimulation (473 nm, 1-sec pulses) during single cell patch-clamp recordings. Light stimulation was applied while holding cells at incremental voltages (-120 to 80mV) during patch-clamp recordings in extracellular solution (140mM NaCl, 5mM KCl, 2mM $CaCl_2$, 1mM $MgCl_2$, 10mM HEPES and 10mM glucose, pH 7.4). Steady state photocurrent amplitudes were measured for ChRERα or ChR2(H134R)-EYFP and plotted against holding voltage.

Experimental animal subjects

All animal experiments followed procedures approved by the NIDA-IRP animal care and use committee and complied with NIH guidelines and ethical regulations for animal research and husbandry. Wild-type Sprague-Dawley rats (Charles River, 250-500g weight, 12 male and 8 female) were used. Two male squirrel monkeys (*Saimiri sciureus*; ~17-20 years, 850g and 950g) were also used. One monkey was euthanized, and its brain was processed for IHC and immunocytochemistry. The other monkey died of natural causes (potential heart-failure).

Adeno-associated virus (AAV) injections

Rat surgeries: Animals were anesthetized with isoflurane and/or a mix of ketamine/xylazine and positioned in a stereotaxic apparatus (Kopf). A custom made AAV with 2/5 serotype carrying the ChRERα construct (ERα ligand channelrhodopsin-2 (hChR2-H134R) fused to ERα ligand binding domain through a V5 linker under the human synapsin 1 (hSyn) promoter ($AAV_{2/5}$-Syn1-ChRERα) was intracranially injected. Stereotaxic coordinates were determined from the Rat Atlas (Paxinos, George and Watson 6th edition) to target one of the following regions: PrL/ACd (AP = 3.0, ML = 0.6, DV = -3.5), VTA (AP: -5.5, ML: 0.8, DV: -8.2), or left M1 (AP = 2.0, ML = 3.0, DV = -2.0 and -2.1). Rats received 0.5 µl of AAV (1.32×10^{14} gc/ml) at a flow rate of 100 nl/min using a Hamilton Neuros 33G syringe driven with a Neurostar robotic injection system. Following surgery, the incision site was sutured, and analgesics were administered.

Monkey surgeries: Two adult male squirrel monkeys received intracranial injections of the AAV2/5-hSyn-ChRERα (1.32×10^{14} gc/ml) in the left M1 forelimb region. Animals were sedated with ketamine (10 mg/kg, IM) and then received atropine (0.02-0.05 mg/kg, IM) or glycopyrrolate (0.005-0.01 mg/kg, IM). Vital signs were continuously monitored (body temperature, heart and respiration rate, oxygen and CO2 levels). Isoflurane was delivered (1.0-2.0% in O_2) by mask until intubation and positioning in a stereotaxic apparatus. Injection sites were first estimated from individual structural MRIs and stereotaxic coordinates relative to center of fixed ear bars (i.e., AP = 14.2, ML = 10.6, DV = 26.0). Sites were then precisely defined with intracortical microstimulation (ICMS). A tungsten microelectrode was lowered to the approximate depth of layer 5 (1800 mm below surface). Trains of microstimulation pulses were delivered at each site (18 pulses, 0.2 ms pulse width, 300 Hz). Current amplitude was increased until a movement was evoked (up to 80 µA). The motor response was classified according to the location of muscle twitches (e.g., shoulder, elbow, etc). During motor mapping, anesthesia was maintained with ketamine infusion (~5-6 mg/kg/hr; iv) and isoflurane (0.25-0.5% in nitrous oxygen mixed 50:50). Injections proceeded once the target sites were finalized. Three injections separated by 0.5 mm (1.33 µl/injection) were made in each hemisphere at depths of 1.5, 2.0 and 2.5 mm below the cortical surface. A 5.0 µl Hamilton Neuros syringe was used (flow rate 0.33 µl/min, 5 min between injections). Following injections, the site was covered with artificial dura and sutured closed. Animals received post-operative care and their health was closely monitored, allowing a minimum of five weeks before any further experimentation.

Immunohistochemistry (IHC)

***Rats*: ** Rats were anesthetized with pentobarbital and transcardially perfused with PBS followed by 4% paraformaldehyde (PFA). The brains were stored in 4% PFA overnight at 4 °C, and then placed in phosphate buffered saline (PBS) with 30% sucrose for 3-4 days at 4 °C. Brains were frozen and sectioned on a cryostat (30-40 µm; Leica, Germany) and slices were collected in PBS. On the first day of IHC, brain slices were washed in PBS with 0.1% Triton X-100 (washing buffer) for 30-min (3x 10-minute washes at RT). Slices were then blocked with 3% bovine serum albumin in washing buffer (blocking buffer, 1 hour at RT) and incubated with anti-ChR2 primary antibody (1:500 in blocking buffer, mouse monoclonal ARP #03651180) at 4 °C overnight. Slices were soaked in washing buffer (3 x 10min at RT) and then incubated in a secondary antibody mix in PBS: anti-mouse AlexaFluor 488 (1:500) and DAPI (1:1000) for 2 hours at RT (protected from light). After secondary antibody incubation, slices were washed once more and then mounted onto glass slides using aqueous mounting medium (90% glycerol + 30mM Tris-HCl, pH 8.0) with a glass coverslip. Images were taken using a Leica DFC7000T microscope and processed with LasX software.

***Squirrel monkeys**:* One monkey was anesthetized and transcardially perfused with PBS followed by a fixative solution containing 4% PFA + 0.15% Glutaraldehyde + 0.15% picric acid. The brain was removed and separated into blocks. These blocks were stored at 4 °C in 4% PFA for three days (fresh PFA solution was changed daily) and then rinsed in PBS before transferring to a solution with 10% sucrose. The blocks were subsequently transferred to PBS with 20% sucrose and then 30% sucrose over the following two days and stored at 4 °C until sectioning. Blocks were sectioned using a cryostat (30-40 µm) and stored in a cryoprotectant solution at -80 °C or in PBS with 0.1% sodium azide at 4 °C. On the first day of IHC treatment, slices were transferred to fresh PBS and then rinsed with washing buffer (PBS with 0.1% Triton X-100) at RT (3 x 10-min). Slices were then incubated in blocking buffer (3% BSA in PBS) for 1 hour at RT, rinsed with PBS (3x 10-min wash), and soaked in a background suppressor solution (Biotium-TrueBlack IF Background Suppressor) for 10-min at RT. Slices were then transferred to a primary antibody solution (mouse anti-ChR2 1:300 in TrueBlack IF Blocking Buffer) and incubated overnight at 4 °C. On the second day of IHC, treated slices were rinsed with PBS (3x 10-min) and transferred to a secondary antibody solution (anti-mouse AlexaFluor594 or Cy3 1:500 and DAPI 1:1500 in TrueBlack IF Background Suppressor) for 2 hours at RT (protected from light). Following secondary antibody incubation, slices were rinsed with PBS (3x 10-min) and mounted onto a glass slide. The slice was then covered with Biotium-TrueBlack lipofuscin quencher (1:40 in PBS, 175ul) for 10-min at RT. The slide was then rinsed briefly in PBS (3x 10-sec) and covered with an aqueous mounting media (90% glycerol + 30mM Tris-HCl, pH 8.0) and a glass coverslip (product info). Images were taken using a Leica DFC7000T microscope and processed with LasX software.

Confocal fluorescence microscopy

Free floating coronal sections (40 µm) from rats with viral injection of pAAV$_{2/5}$-Syn1-ChRERα into the right PrL/ACd or left M1 and free-floating horizontal sections (80 µm) from monkey with viral injection of pAAV2/5-hSyn-ChRERα into the left M1 were incubated for 1 h in PB supplemented with 4% BSA and 0.3% Triton X-100. Sections were then incubated with primary antibody mouse anti-Channelrhodopsin2 (ChR2; 1:250, American Research Products, Inc., 03-651180) overnight at 4°C. After rinsing 3 × 10 min in PB, sections were incubated in the fluorescence secondary antibody Alexa Fluor® 594 AffiniPure Donkey Anti-Mouse IgG (H+L) (1:100, Jackson ImmunoResearch Laboratories, Inc., 715-585-151) for 2 h at room temperature. After rinsing, sections were mounted with mounting medium with DAPI on slides. Fluorescent images were collected with a Zeiss LSM880 with Cy7.5 Confocal System (Zeiss). Images were taken sequentially with different lasers with 20× objective. This experiment was successfully repeated three times.

Electron microscopy

Vibratome tissue sections (40 µm) from rats with viral injection of pAAV2/5-hSyn-ChRERα into the right PrL/ACd or left M1 and vibratome tissue sections (80 µm) from monkey with viral injection of pAAV2/5-hSyn-ChRERα into the left M1 were rinsed and incubated with 1% sodium borohydride to inactivate free aldehyde groups, rinsed, and then incubated with blocking solution 1% normal goat serum (NGS), 4% BSA in phosphate buffer (PB) supplemented with 0.02%

saponin. Sections were then incubated with primary antibody mouse anti-Channelrhodopsin2 (ChR2; 1:250, American Research Products, Inc., 03-651180) diluted in blocking solution for 24 h at 4°C. Sections were rinsed and incubated in the secondary antibody Nanogold-Fab' goat anti-mouse IgG (H+L) (1:100, Nanoprobes, 2002) overnight at 4°C. Sections were rinsed in PB, and then in double-distilled water, followed by silver enhancement of the gold particles with the Nanoprobe Silver Kit (2012, Nanoprobes) for 7 min at room temperature. Sections were rinsed with PB and fixed with 0.5% osmium tetroxide in PB for 25 min, washed in PB, followed by double distilled water, and then contrasted in freshly prepared 1% uranyl acetate for 35 min. Sections were dehydrated through a series of graded alcohols and with propylene oxide. Afterwards, they were flat embedded in Durcupan ACM epoxy resin (14040, Electron Microscopy Sciences). Resin-embedded sections were polymerized at 60°C for 2 days. Sections of 60 nm were cut from the outer surface of the tissue with an ultramicrotome UC7 (Leica Microsystems) using a diamond knife (Diatome). The sections were collected on formvar-coated single slot grids and counterstained with Reynold's lead citrate. Sections were examined and photographed using a Tecnai G2 12 transmission electron microscope (Thermo Fisher Scientific) equipped with the OneView digital micrograph camera (Gatan). Serial ultrathin sections were analyzed. Synaptic contacts were classified according to their morphology and immunolabel and photographed at a magnification of 6,800-13,000×. The morphological criteria used for identification and classification of cellular components or type of synapse observed in these thin sections were as previously described (Zhang et al, 2015). In the serial sections, a terminal, dendrite, or cell body containing greater than 5 immunogold particles was considered as immunopositive terminal, dendrite, or cell body. Pictures were adjusted to match contrast and brightness by using Adobe Photoshop (Adobe Systems Incorporated, Seattle, WA). This experiment was successfully repeated three times. Electron microscopy and confocal analysis quantification were blinded and performed as described previously (Zhang et al., 2015)

Slice electrophysiology

Slice electrophysiology experiments were carried out as previously described (Pignatelli et al., 2017; Pignatelli et al., 2020). Briefly, mice were injected with $AAV_{2/5}$-Syn1-ChRERα in PrL/ACd and three weeks later were anaesthetized with euthasol (Butler-Schein) before decapitation. Brains were rapidly removed and placed in ice-cold NMDG-based cutting solution (Ting et al., 2018) containing (in mM): 92 NMDG, 20 HEPES, 25 glucose, 30 NaHCO3, 2.5 KCl, 1.2 $NaPO_4$, 5 sodium ascorbate, 3 sodium pyruvate, 2 thiourea saturated with 95% O_2/5% CO_2 with an osmolarity of 303-306 mOsm. Coronal sections (300 µm) containing the vmPFC were obtained by using a Leica VT1200 Vibratome. Then, slices were then transferred to modified holding aCSF saturated with 95% O_2/5% CO_2 containing (in mM): 92 NaCl, 20 HEPES, 25 glucose, 30 $NaHCO_3$, 2.5 KCl, 1.2 $NaPO_4$, 5 sodium ascorbate, 3 sodium pyruvate, 2 thiourea (303-306 mOsm) at room temperature. Slices were allowed to incubate at room temperature in this solution for at least 1 hr before being transferred to the recording chamber.

The recording chamber was kept at 32 ˚C degrees and perfused with a pump at a flow rate of 1.5-2.0 ml per minute with aCSF containing (in mM): 126 NaCl, 2.5 KCl, 1.4 NaH2PO_4, 1.2 $MgCl_2$, 2.4 $CaCl_2$, 25 NaHCO3, and 11 glucose (303-305 mOsm) for recordings. Whole-cell recordings were made utilizing glass microelectrodes (2-3 MΩ) containing (in mM): 135 K-gluconate, 10 HEPES, 4 KCl, 4 Mg-ATP, and 0.3 Na-GTP. Cells were identified using IR-DIC optics on an inverted Olympus BX5iWI microscope. Optogenetically-evoked responses were elicited using a 473 nm laser (1 ms pulse) directed at the brain slice (Thor Labs). Neurons were voltage clamped at -70mV utilizing a Multiclamp 700B amplifier (Molecular Devices). Data were filtered at 2 kHz and digitized at 20 kHz using a 1440A Digidata Digitizer (Molecular Devices). Series-resistance (10-20 MΩ) was monitored using a -5 mV voltage step. Cells with >20% change in series resistance were discarded from further analysis.

FDG-PET with light stimulation

A group of rats (n = 5) were injected with $AAV_{2/5}$-Syn1-ChRERα in PrL/ACd (AP = 3.0, ML = 0.6, DV = -3.3) were later implanted with an optic fiber (ThorLabs) targeting just above the AAV injection site (AP = 3.0, ML = 0.6, DV = -3.1). For fiber implantation, a hole was made in the skull above the AAV site and an optic fiber cannula (2.5mm ferrule, 200µm core, ThorLabs) was stereotaxically lowered until the optic fiber was just above the injection site (AP = 3.0, ML = 0.6, DV = -3.1). The optic fiber cannula was secured with dental cement and supporting screws in the skull. A group of control rats (AAV naïve, n = 4) were also implanted with an optic fiber at these coordinates. These rats were anesthetized with isoflurane (~2%) in prone position and hooked up to an optic fiber patch cable connected to a controllable LED light source (473nm; Plexon Inc.). Anesthetized rats received an i.p. injection of [^{18}F]-FDG (~0.5mCi in 0.5 ml saline) and then underwent a 30-min light stimulation protocol (473nm, 3ms-pulse trains at 50Hz – 300ms on, 700ms off for 30-min) controlled by Radiant software (Plexon Inc). Following the [^{18}F]-FDG uptake stimulation period, rats were scanned in a Mediso nanoScan®/CT scanner for ~25 min (20 min PET plus ~5 min CT). Scan data was reconstructed using Nucline software with CT-based attenuation correction. The 20 min PET acquisitions were processed as static reconstructions for each animal and then analyzed using PMOD. Each animal's scan was registered to a template rat MRI brain (Schiffer) in PMOD. A pixelwise comparison was performed using Matlab (Mathworks) SPM12 (University College London) to assess potential differences in uptake of [^{18}F]-FDG between ChRERα vs. controls.

Locomotor behavior in rats

A group of rats (n = 5) were injected with AAV$_{2/5}$-Syn1-ChRERα unilaterally in the VTA (AP: -5.5, ML: 0.8, DV: -8.2), and were later implanted with an optic fiber (ThorLabs) as described previously, but this time targeting ipsilateral projections in the NAc (AP: 1.3, ML: -1.0, DV: -6.5). A group of rats with no-AAV were also implanted with optic fibers to serve as controls. During locomotor behavior experiments, awake rats were hooked up to an optic fiber patch cable connected to a controllable LED light source (473nm; Plexon Inc.) in an open-field chamber. Locomotor behavior was acquired with video recording using CinePlex software (Plexon Inc.), and total distance travelled was calculated during blocks with and without light stimulation (473nm, 3ms-pulse trains at 50Hz – 300ms on, 700ms off for 5-min). The statistical analysis of distance traveled included two factors (AAV group and light stimulation) matched by subject, to assess effects of light stimulation and the interaction effect between AAV-ChRERα transduction and light stimulation.

[^{18}F]FES-PET acquisition:

All PET/CT scans were acquired using a Mediso nanoScan® PET/CT scanner and data reconstruction was performed with Nucline nanoScan software (3.04.101.0000). *Rat scans:* Male and female Sprague Dawley rats (n = 10 male and 6 female) were anesthetized and maintained on isoflurane (1.5-2.5%) during the whole procedure. Tail vein catheters were inserted for intravenous radiotracer delivery. [^{18}F]FES was injected (0.5-1mCi in ~0.5ml followed by 0.5ml ml of saline) immediately at the start of scan, and scan duration lasted 90-120 minutes. Baseline scans were performed in a group of rats with no AAV to serve as controls (n = 5). Post-AAV scans were acquired at least three weeks following injection in the group of rats receiving AAV-ChRERα in right PrL/ACd (n = 6) or left M1 (n = 5). *Squirrel monkey scans*: Monkeys were anesthetized first with ketamine (i.m.) and then intubated and maintained on isoflurane (1.5-2.5%) oxygen mixture.

An i.v. line with injection port was established in the hindlimb and monkeys were placed supine in the PET scanner. A CT scan was performed prior to radioligand injection and PET acquisition. [^{18}F]FES (1.5-2 mCi) was diluted in sterile saline (~0.5ml) and injected into the port followed by saline (~1 ml). Animals were scanned for 90 minutes while physiological parameters (i.e., heart rate, body temp, respiration rate and oxygen saturation) were continuously monitored throughout the procedure. Monkeys were given fluids and carefully monitored during recovery after the scan.

[^{18}F]FES-PET analysis:

Rats*:* Each PET/CT scan was co-registered to a template rat MRI brain (Schiffer) in PMOD. [^{18}F]FES-PET acquisition data was first converted to standard uptake values (SUV g/ml) to correct for animal body weight and injected radiotracer dose. However, because [^{18}F]FES exhibits reversable binding (instead of metabolic trapping as in FDG uptake), the image data was then quantified as SUV ratios (SUVR) and binding potentials (BP_{ND}) using a nonspecific reference region in attempt to better represent specific binding. We chose to use a cerebellar gray matter atlas VOI as the nonspecific reference region due to the low endogenous binding observed at baseline and its relatively large. Time activity curves of SUV and SUVR were plotted and a period of 20-60min post injection was chosen (highest signal to noise) to calculate average VOI SUVRs. In addition, binding potential (BP_{ND}) was calculated using the pixel-based Logan reference tissue method (Logan et al., 1996) in PMOD with the grey matter CB was as the reference region and model parameters k2’=0.153 (determined with simplified reference tissue model (SRTM) preprocessing) and t = 20-60 min. VOIs were determined using a 2 mm sphere centered at the site of interest with a 50% isocontour filter applied.

Squirrel monkeys: Each PET/CT scan was co-registered to their individual structural MRIs. SUV, SUVR and BP_{ND} was calculated in the same way as performed in rats. Individual VOIs were determined using a 3 mm sphere centered at site of interest with a 50% isocontour filter. For defining the AAV injection site VOI, the 3 mm sphere was centered at the middle of the stereotaxic coordinate injection sites and a 50% isocontour filter was applied.

fMRI functional connectivity acquisition and analysis:

MRI data were acquired with a Bruker Biospin 9.4 T scanner on a Paravison 6.0.1 platform equipped with an active-shielded gradient coil and a quadrature transmitter/receiver RF coil (Bruker Medizintechnik, Karlsruhe, Germany). Functional images were acquired using a gradient-recalled echo-planar imaging (EPI) sequence (TR=1.5s, TE=15 ms, with an isotropic resolution of

1mm). Geometric distortions in EPI images were corrected using a reverse k-space trajectory EPI sequence developed in-house. Thirty-five functional scans (N=9 squirrel monkeys) were acquired under IV dexmedetomidine (10-16 µg/kg/hr) and 0.5% inhaled isoflurane (Brynildsen et al., 2016). Each functional connectivity acquisition lasted for 7.5 min. After manual skull-stripping, the preprocessing was done by a set of home-made scripts based on 3 data analysis packages: AFNI (version: 20200809), FSL (5.0.9), and FreeSurfer (version: stable 5, 20130513). In detail, images were processed by discarding the first 4 temporal samples, slice-timing correction, head motion correction, physiological noise correction (CompCor, Behzadi et al., 2007), band-pass filtering (0.01-0.1 Hz), nonlinear alignment to the VALiDATe29 template (Schilling et al., 2017), and smoothing to 2 mm using AFNI's 3dBlurToFWHM. Anatomical normalization was performed using linear robust alignment by FreeSurfer's mri_robust_register (Reuter et al. 2010), followed by FSL's non-linear alignment (FNIRT). Group level functional connectivity was based on voxel-wise inference and a statistical threshold determined using permutation testing (PALM; Winkler et al 2014) with threshold free cluster enhancement (TFCE; Smith & Nichols 2009) and multiple comparison correction maintaining FWE < 0.05.

2.6 Figures for Chapter 2

Figure 1. Development and *in vitro* characterization of ChRERα binding and function.

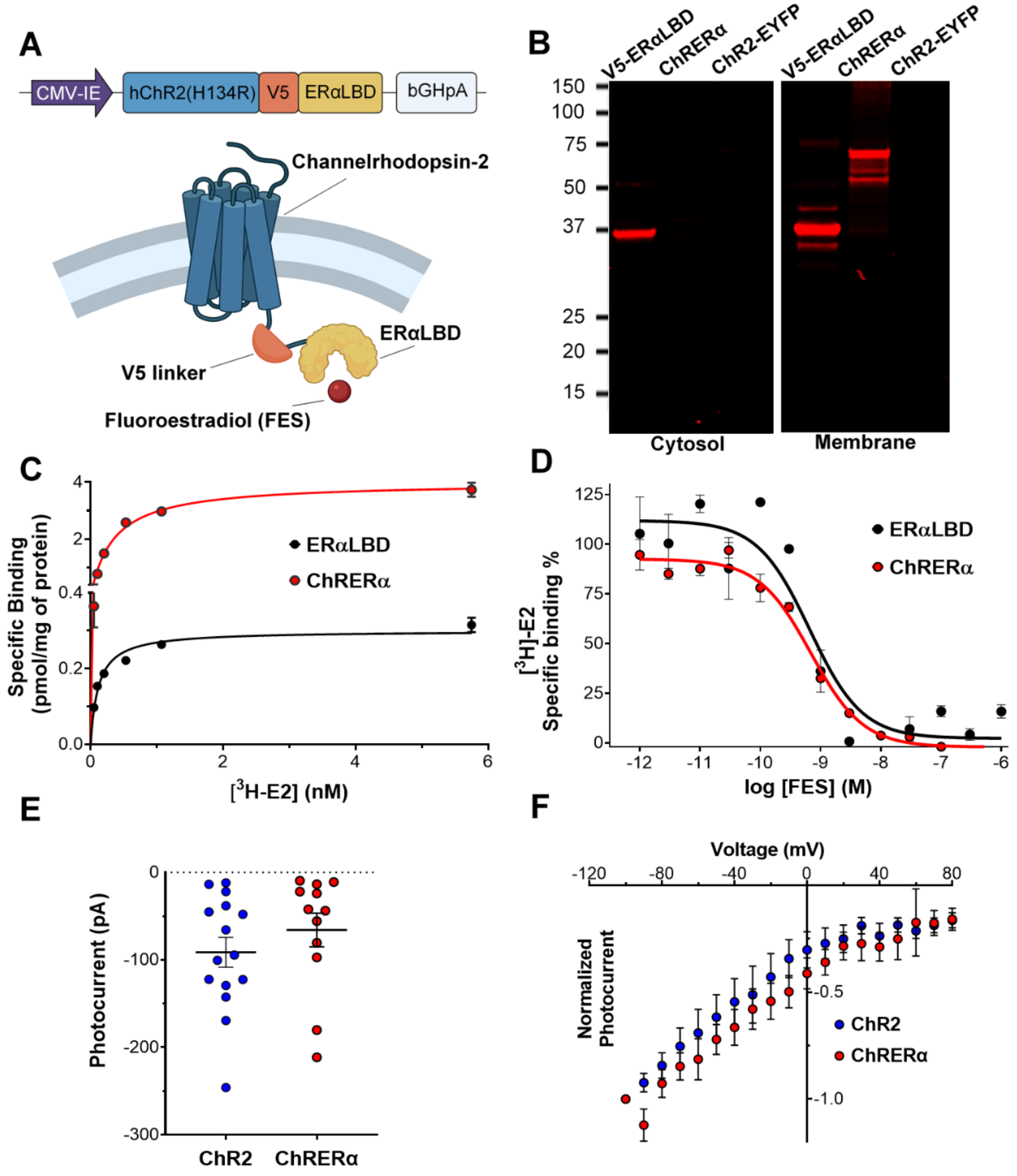

(**A**) Plasmid (top) and schematic representation (bottom) of ChRERα. (**B**) Western blot showing subcellular localization of the V5 epitope in cytosolic or membrane fractions of HEK-293 cells transfected with V5-ERαLBD, ChRERα or ChR2-EYFP. (**C**) [^{3}H]E2 binding saturation curves in membrane homogenates from HEK-293 cells transfected with ERαLBD (black) or ChRERα (red). (**D**) [^{3}H]E2 competition binding curves with FES in membrane homogenates from HEK-293 cells transfected with ERαLBD or ChRERα. Values for fitted parameters are described in the text. (**E**) Photocurrent amplitudes and (**F**) light-induced voltage-current curves of HEK-293 cells transfected with ChR2 (blue) or ChRERα (red). All data shown as mean ±SEM. Abbreviations: ChR2 (channelrhodopsin-2), ERαLBD (estrogen receptor alpha ligand binding domain), EYFP (enhanced yellow fluorescent protein), [^{3}H-E2] (tritiated estradiol).

Figure 2. ChRERα trafficking and subcellular localization in the rat brain.

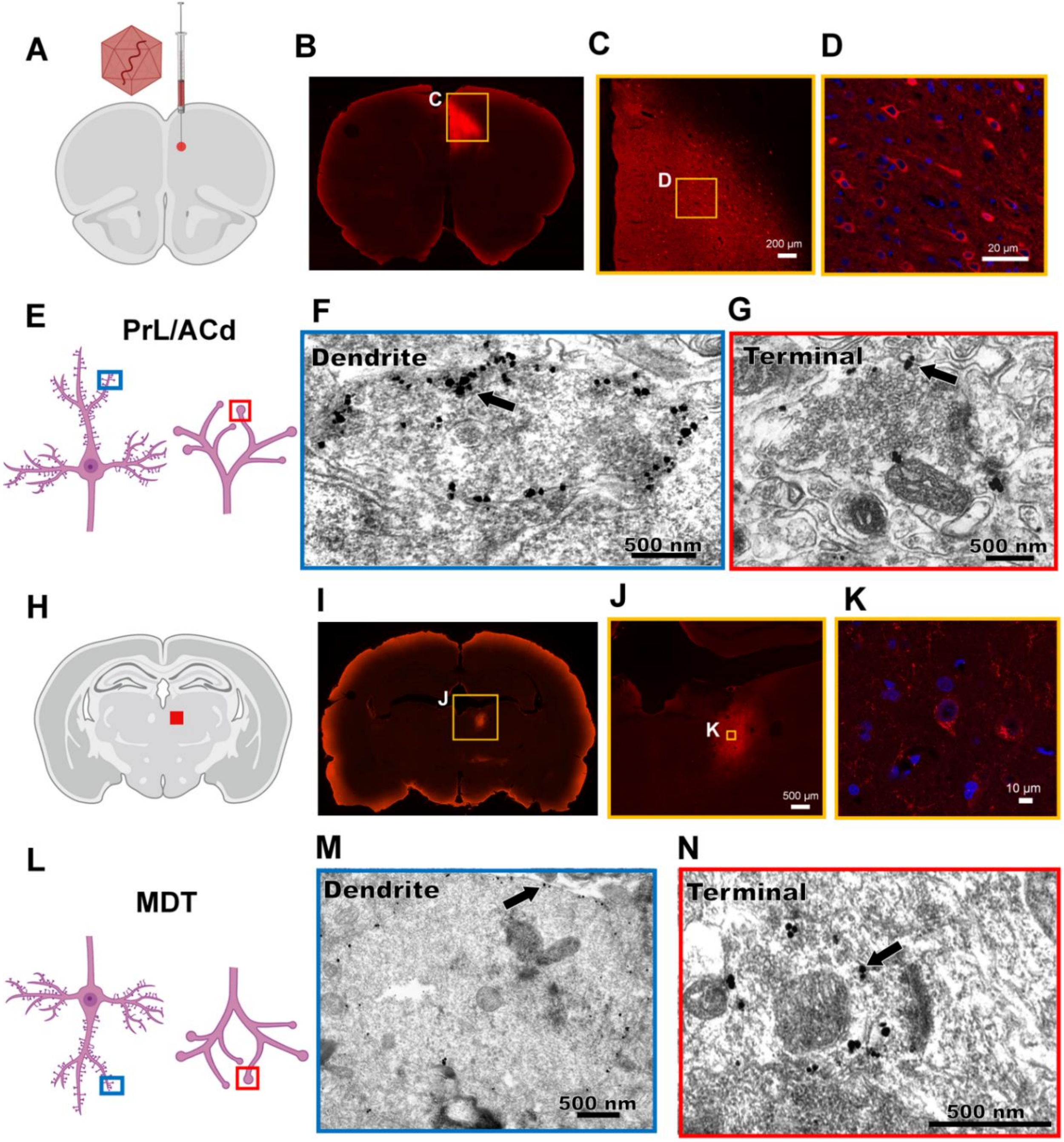

(**A**) AAV-ChRERα injection site in the right PrL/ACd (AP = 3.0, ML = 0.6, DV = -3.5). (**B-D**) IHC reveals ChRERα expression in cells in the right PrL/ACd (red = anti-ChR2, blue = DAPI). (**E**) Schematic of dendrite (left, blue box) and axon terminal (right, red box) localization of immuno-EM images. (**F-G**) Immunogold labelling of ChRERα expression in (**F**) right PrL/ACd dendrite and (**G**) axon terminal. (**H**) Schematic of right MDT projection site (red square). (**I-K**) IHC labeling of ChRERα in cells in the right MDT (red = anti-ChR2, blue = DAPI). (**L**) Schematic of dendrite localization (left, blue box) after retrograde transduction and anterograde axon terminal (right, red box) trafficking in the MDT. (**M-N**), Immunogold labelling of ChRERα expression in (**M**) MDT dendrite and (**N**) axon terminal. Abbreviations: PrL/ACd: Prelimbic/dorsal anterior cingulate, MDT: Mediodorsal thalamus.

Figure 3. ChRERα activation alters brain activity and behavior in rodents.

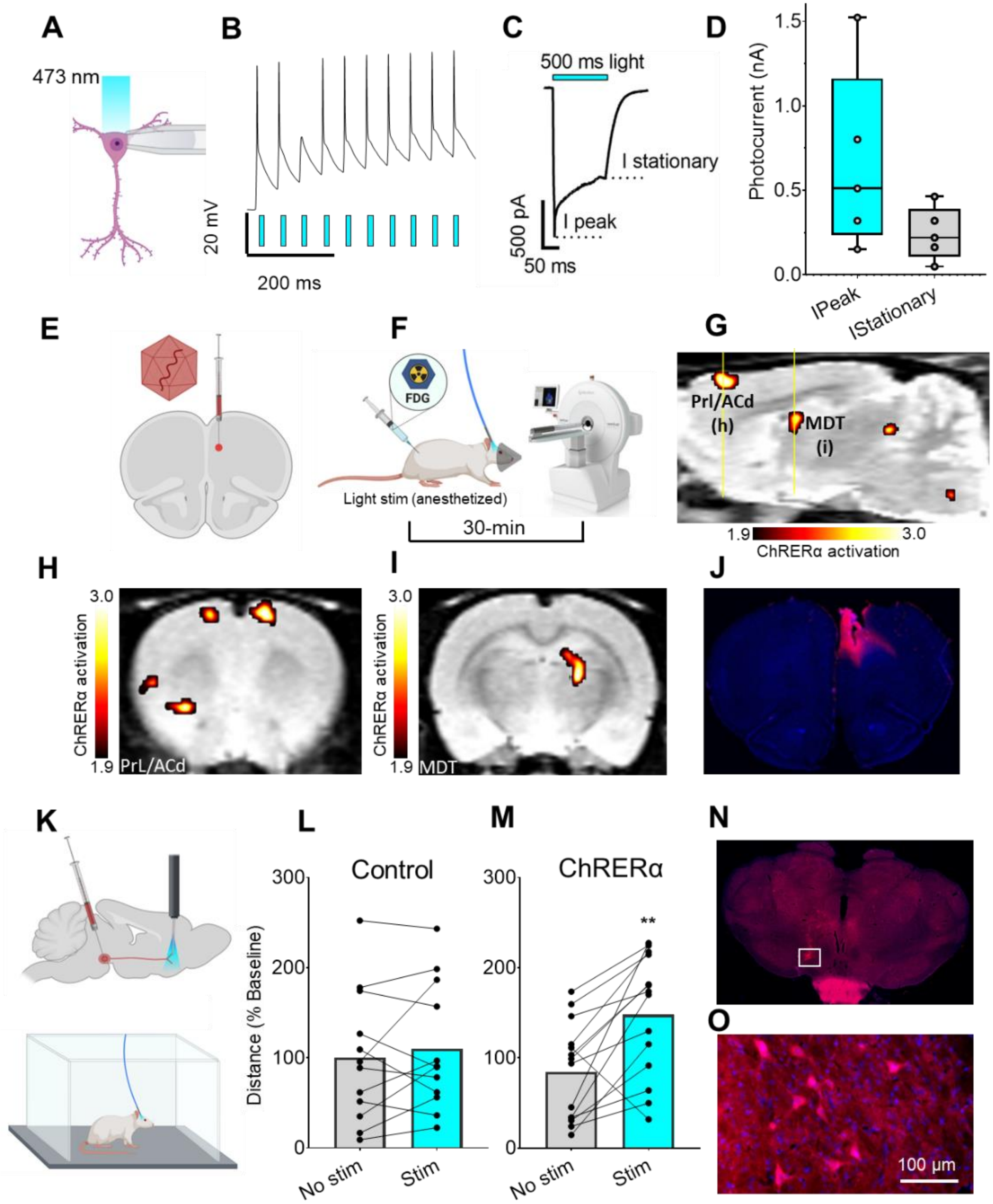

(**A-D**) Slice electrophysiology in mice. (**A**) Neuronal patch-clamp recordings during stimulation with 473nm light. (**B**) Firing pattern of photocurrent responses triggered by a train of light pulses. (**C**) Representative IPeak and IStationary of photocurrent response to 500ms light pulse. (**D**) Average IPeak and IStationary photocurrent values (nA). (**E-I**) FDG-PET in rats. (**E**) Schematic of AAV-ChRERα injection and optic fiber target in right PrL/ACd (ChRERα n = 5, Control n = 4). (**F**) FDG-PET experimental design – bolus i.p. FDG injection at start of 30-min light stimulation protocol (anesthetized) followed by PET/CT scan. (**G**) Sagittal view (right hemisphere) with regions of greater FDG uptake ($p < 0.05$, $t = 1.89$) in ChRERα vs. Control rats, (yellow lines indicate level of coronal images shown in **H** and **I**). (**H-I**) Coronal view with regions of significantly greater FDG uptake (ChRERα > Control) in (**H**) bilateral PrL/ACd, left insula and striatum, and (**I**) right MDT. (**J**) IHC confirms expression of ChRERα and optic fiber placement in the right PrL/ACd (red = anti-ChR2, blue = DAPI). (**K-N**) Locomotor behavior in rats. (**K**) Schematic of unilateral AAV-ChRERα injection in VTA and optic fiber placement in NAc (top), and open field optogenetic stimulation in awake rats (bottom). (**L-M**) Light stimulation significantly increased (**$p = 0.01$) distance traveled in (**M**) ChRERα rats but not in (**L**) control rats. (**N-O**) IHC confirms ChRERα expression in rat VTA (red = anti-ChR2, blue = DAPI), white box indicates area of high mag (**O**) in VTA. Abbreviations: PrL/ACd: Prelimbic/dorsal anterior cingulate, MDT: Mediodorsal thalamus.

Figure 4. Noninvasive localization of ChRERα in the brain of individual rats.

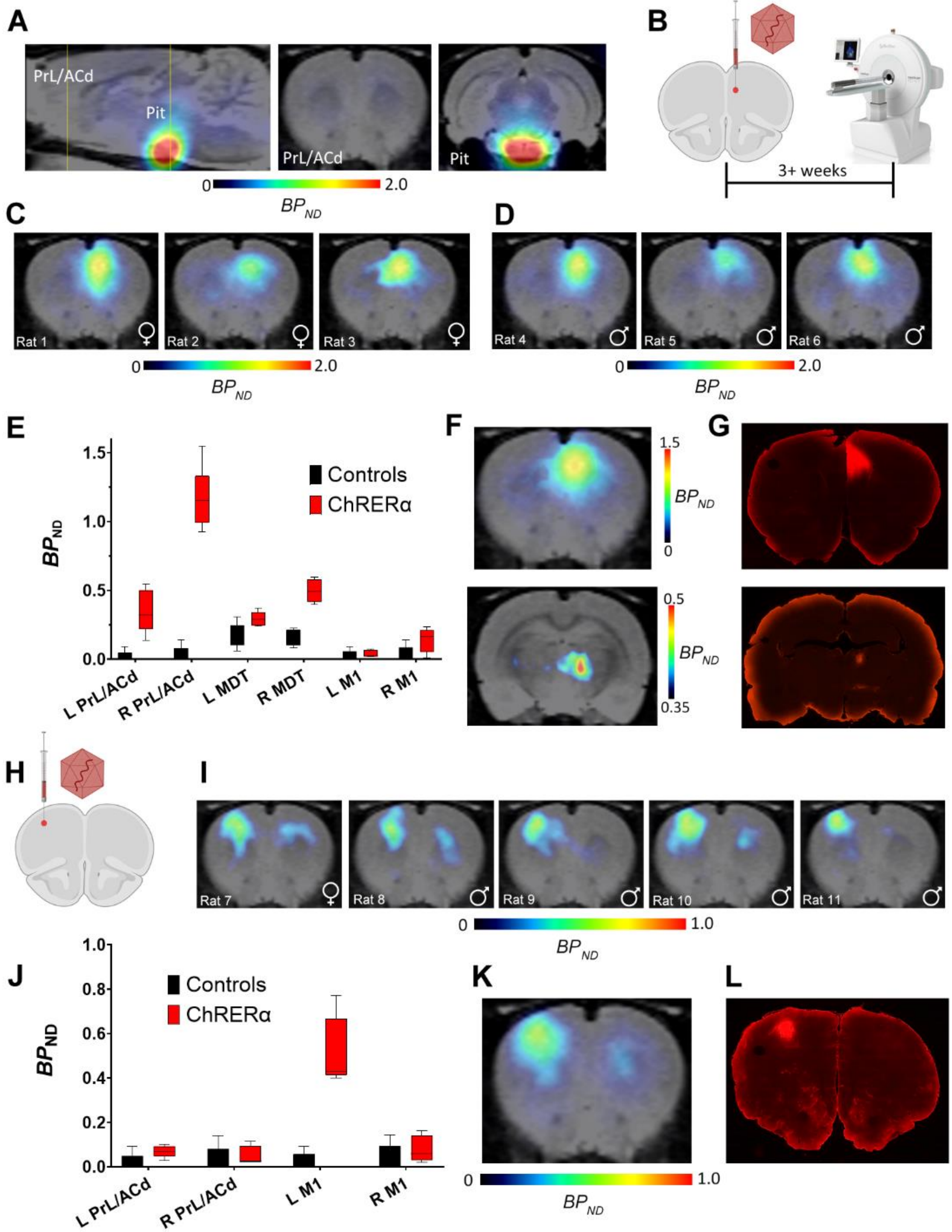

(**A**) Baseline [^{18}F]FES-PET in control rats (no AAV) shows high endogenous binding in the pituitary but low binding in the rest of the brain (yellow lines illustrate location of coronal cross sections). (**B**) Schematic of right PrL/ACd injection site for AAV-ChRERα in rats 3+ weeks prior to [^{18}F]FES-PET scan. (**C-D**) [^{18}F]FES binding localizes ChRERα near the AAV injection site in right PrL/ACd of (**C**) female (n = 3) and (**D**) male (n = 3) rats 3-5 weeks after receiving AAV-ChRERα. (**E**) Group BP_{ND} plot reveals higher binding in the right PrL/ACd and MDT in ChRERα (n = 6) vs. control (n = 5) rats. (**F**) Group average BP_{ND} of [^{18}F]FES in the right PrL/ACd (top) and MDT (bottom) in ChRERα rats (n = 6). (**G**) IHC confirms ChRERα expression in the right PrL/ACd and MDT (red = anti-ChR2). (**H**) Schematic of left M1 injection site for AAV-ChRERα in rats (n = 5). (**I**) Individual post-AAV [^{18}F]FES-PET scans of rats injected with AAV-ChRERα in left M1 (n = 5). (**J**) Group BP_{ND} plot of ChRERα (left M1 AAV, n = 5) vs. control (n = 5) rats shows higher binding in left M1 but not in PrL/ACd. (**K**) Group average BP_{ND} of [^{18}F]FES in left M1 of ChRERα rats (n = 5). (**L**) IHC confirms ChRERα expression (red = anti-ChR2) corresponding with the left M1 area localized with [^{18}F]FES-PET. Abbreviations: L: Left, M1: Motor cortex, MDT: Mediodorsal thalamus, PrL/ACd: Prelimbic/dorsal anterior cingulate, R: Right.

Figure 5. Localizing ChRERα in squirrel monkeys with [^{18}F]FES.

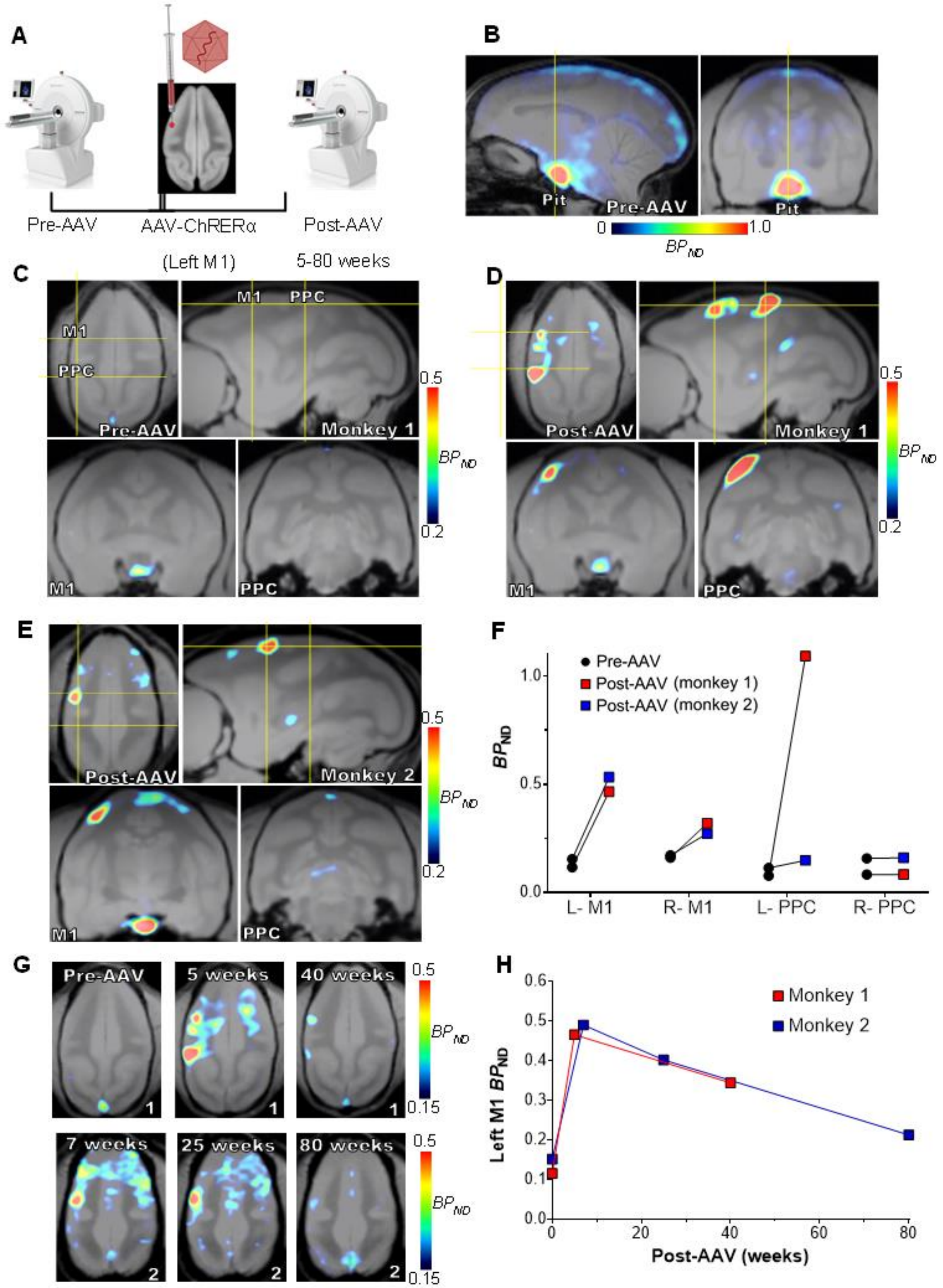

(**A**) Schematic of PET experimental design and left M1 injection site for AAV-ChRERα. (**B**) Pre-AAV baseline [^{18}F]FES-PET in a squirrel monkey (monkey 1) shows high endogenous binding in the pituitary but low levels in the rest of the brain. (**C**) Pre-AAV baseline [^{18}F]FES-PET in monkey 1 at the level of motor cortex (M1) and posterior parietal cortex (PPC). (**D**) Post-AAV [^{18}F]FES in monkey 1 localizes ChRERα near the left M1 AAV injection site and in the ipsilateral PPC five weeks after receiving AAV. (**E**) [^{18}F]FES localizes ChRERα near the left M1 AAV injection site in a second monkey (monkey 2) seven weeks post-AAV. (**F**) Pre-AAV and post-AAV BP_{ND} in left and right M1 and PPC for each monkey. (**G**) Longitudinal comparisons of [^{18}F]FES-PET in monkey 1 (top, pre-AAV, 5 weeks and 40 weeks post-AAV) and monkey 2 (bottom, 7, 25, and 80 weeks post-AAV). (**H**) Longitudinal comparisons of average BP_{ND} in left M1 in monkey 1 (red) and monkey 2 (blue). Abbreviations: L-M1 (left motor cortex), R-M1 (right motor cortex), L-PPC (left posterior parietal cortex), R-PPC (right posterior parietal cortex).

Figure 6. Subcellular ChRERα localization in left M1 and PPC in squirrel monkey.

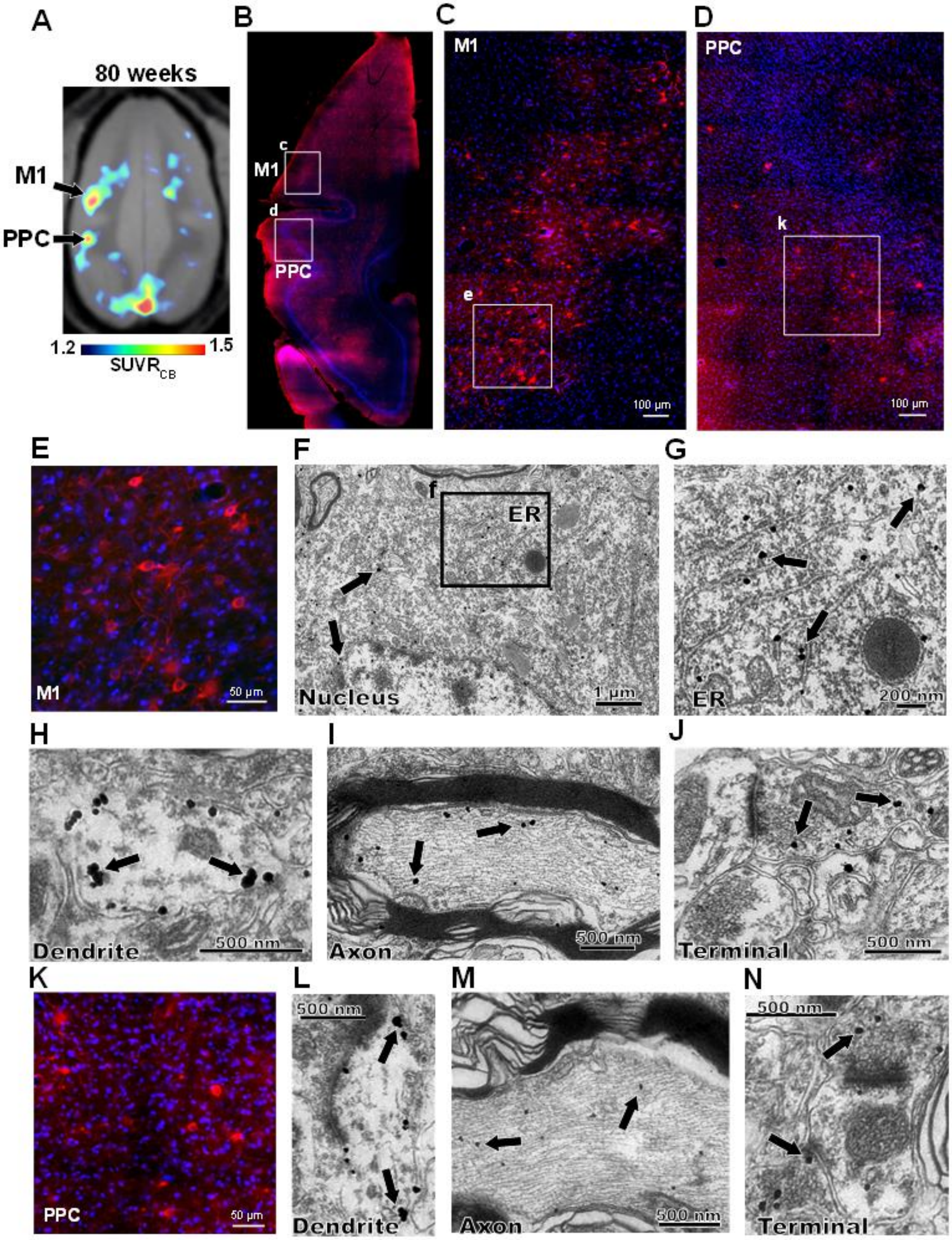

(**A**) $[^{18}F]$FES-PET 80 weeks after AAV-ChRERα injection in monkey 2 localized ChRERα expression in left M1 and PPC (SUVR$_{CB}$ scaled to optimize $[^{18}F]$FES signal. Black arrows indicate left M1 and PPC corresponding to IHC (**B-E, K)** and immuno-EM (**F-J, L-N**) images. (**B**) IHC in a left hemisphere horizontal brain slice confirms ChRERα expression in left M1 and PPC (red = anti-ChR2, blue = DAPI), white rectangles highlight regions in left M1 (high magnification shown in **C** and **E**) and PPC (high magnification shown in **D** and **K**). (**F-J**) Immuno-EM in left M1 reveals subcellular localization of ChRERα expression in (**F**) cell body (black rectangle highlights location of **G**), (**G**) ER, (**H**) dendrite, (**I**) myelinated axon and (**J**) axon terminal. (**L-N**) Immuno-EM in left PPC showing ChRERα located in (**L**) dendrite, (**M**) myelinated axon and (**N**) axon terminal. Abbreviations: ER (endoplasmic reticulum), M1 (motor cortex), PPC (posterior parietal cortex).

Figure 7. [^{18}F]FES-PET and ChRERα predict functional brain connectivity in monkeys.

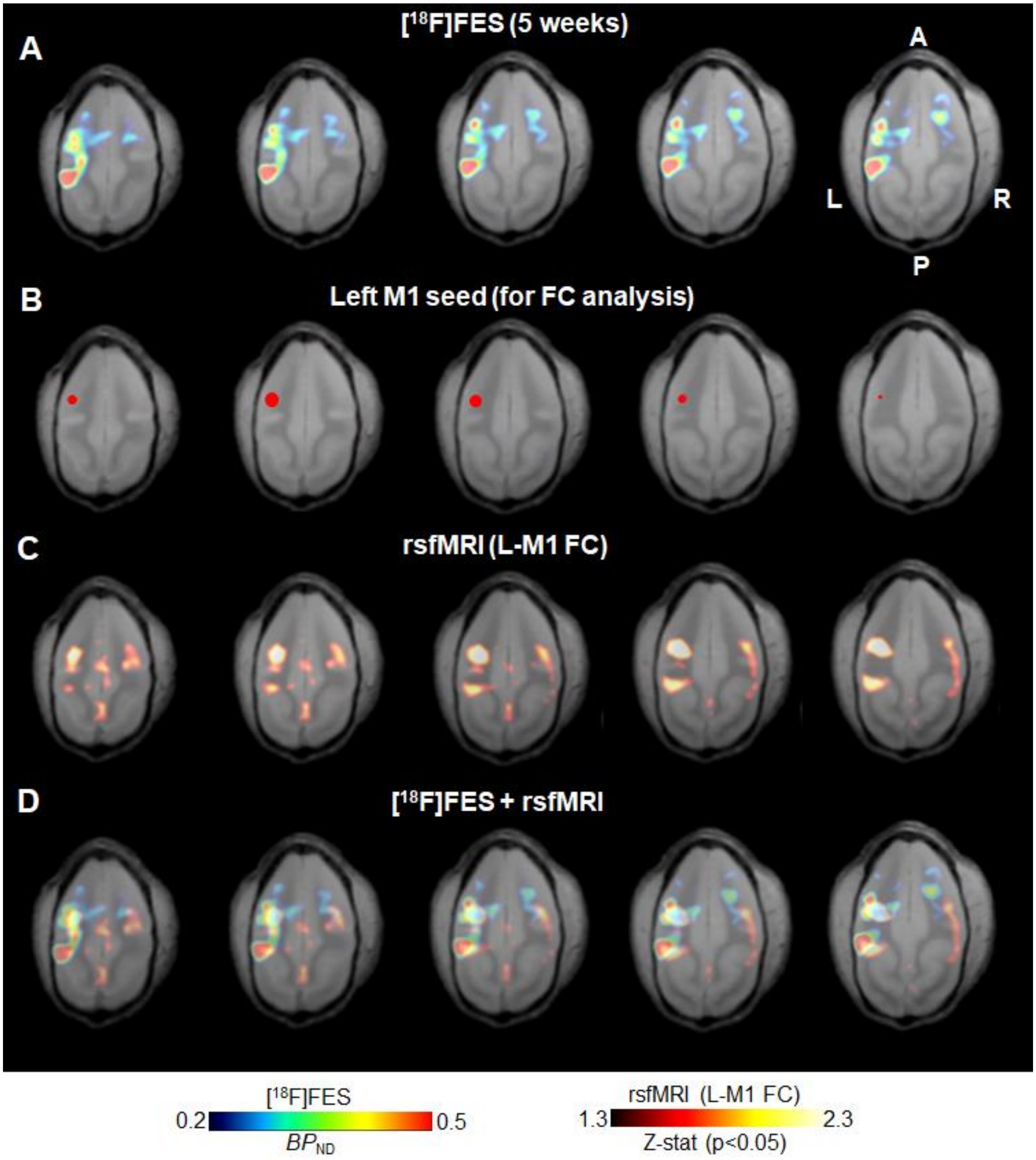

(**A**) Horizontal sections (left – most dorsal, right – most ventral) of [^{18}F]FES-PET from monkey 1 at 5 weeks post-AAV. (**B**) Left M1 seed (red 2mm sphere centered at AAV injection site) for functional connectivity analysis of resting state functional MRI (rsfMRI). (**C**) rsfMRI functional connectivity patterns of the left M1 seed in an independent group of squirrel monkeys (n = 9, 35 total scans) co-registered to monkey 1 structural MRI. (**D**) Overlapping patterns of [^{18}F]FES binding (ChRERα expression) and rsfMRI suggest structural and functional connectivity between left M1 and ipsilateral PPC, and in the contralateral hemisphere.

2.7 Acknowledgements

This work was supported by the National Institute on Drug Abuse Intramural Research Program (ZIADA000069 and ZIADA000622) and the National Institute of Biomedical Imaging and Bioengineering P41 (EB024495) to MGP. We thank Rong Ye and Kevin Yu of the Confocal and Electron Microscopy Core, NIDA IRP, for confocal and immuno-electron microscopic images used in this study.

Author Contributions

J.B. and M.A.B. designed, performed, and analyzed experiments/data. H.P.J. designed and performed squirrel monkey surgeries, experiments, and supervised cell electrophysiology studies. O.S. designed and performed histology experiments. M.P. designed, performed, and analyzed slice electrophysiology experiments and supervised cell electrophysiology studies. X.S. analyzed the squirrel monkey fMRI data. H.L. performed squirrel monkey MRI scans. C.T.R. designed and generated the ChRERα plasmid and provided resources. S.Z. performed IHC and immuno-EM experiments. J.L.G. performed PET experiments. S.L. performed radioligand binding and rodent experiments. M. Morales designed and provided resources for IHC and immuno-EM experiments. O.A.G. designed and performed squirrel monkey surgeries. M.G.P. provided resources for PET experiments. E.A.S. provided resources and supervision for the studies. C.W.B. designed squirrel monkey surgeries/experiments and provided resources and supervision for the studies. M.M. designed experiments and provided resources and supervision for the studies. J.B., M.A.B, and M.M wrote the manuscript with input from all coauthors. All co-authors contributed to reviewing the final version of the manuscript.

Declaration of Interest

MM has received research funding from AstraZeneca, Redpin Therapeutics, and Attune Neurosciences. All other co-authors report no conflicts of interest.

2.8 References:

Behzadi, Y., Restom, K., Liau, J., Lie, T.T. (2007). A component based noise correction method (CompCor) for BOLD and perfusion based fMRI. *NeuroImage* 37(1): 90-101 https://doi.org/10.1016/j.neuroimage.2007.04.042

Bliss-Moreau, E., Costa, V.D., Baxter, M.G. (2020). A pragmatic reevaluation of the efficacy of nonhuman primate optogenetics. bioRxiv 2020.12.10.420331. https://doi.org/10.1101/2020.12.10.420331

Boehm, M.A., Bonaventura, J., Gomez, J.L., Solís, O., Stein, E.A., Bradberry, C.W., Michaelides, M. Translational PET applications for brain circuit mapping with transgenic neuromodulation tools. *Pharmacol Biochem Behav*. 204: 173147. (2021). https://doi.org/10.1016/j.pbb.2021.173147

Boekhoudt, L., Omrani, A., Luijendijk, M.C.M., Wolterink-Donselaar, I.G., Wijbrans, E.C., van der Plasse, G., Adan, R.A.H. Chemogenetic activation of dopamine neurons in the ventral tegmental area, but not substantia nigra, induces hyperactivity in rats. *Eur Neuropsychopharmacol* 26(11): 1784-1793, (2016). https://doi.org/10.1016/j.euroneuro.2016.09.003

Bonaventura, J., Eldridge, M.A.G., Hu, F., et al. (2019). High-potency ligands for DREADD imaging and activation in rodents and monkeys. *Nature Communications* 10: 4627. https://doi.org/10.1038/s41467-019-12236-z

Boon, L.I., Hillebrand, A., Potters, W.V., et al. (2020). Motor effects of deep brain stimulation correlate with increased functional connectivity in Parkinson's disease: An MEG study. *Neuroimage: Clinical* 26: 102225 https://doi.org/10.1016/j.nicl.2020.102225

Boyden, E.S., Zhang, F., Bamberg, E., et al. (2005). Millisecond-timescale, genetically targeted optical control of neural activity. *Nature Neuroscience* 8(9): 1263-1268. https://doi.org/10.1038/nn1525

Brynildsen, J.K., Hsu, L.M., Ross, T.J., Stein, E.A., Yang, Y., Lu, H., 2016. Physiological characterization of a robust survival rodent fMRI method. *Magn Reson Imaging*. https://doi.org/10.1016/j.mri.2016.08.010

Card, N.S., and Gharbawie, O.A. (2022). Cortical connectivity is embedded in resting state at columnar resolution. *Progress in Neurobiology*, 213: 102263 https://doi.org/10.1016/j.pneurobio.2022.102263

Challis, R.C., Ravindra Kumar, S., Chan, K.Y., et al. (2019). Systemic AAV vectors for widespread and targeted gene delivery in rodents. *Nat. Protoc*. 14, 379–414. https://doi.org/10.1038/s41596-018-0097-3

Chen, R., Gore, F., Nguyen, Q.A., et al., (2020). Deep brain optogenetics without intracranial surgery. *Nat. Biotechnol*. https://doi.org/10.1038/s41587-020-0679-9

Cheng, Y., Prusoff, W. (1973). Relationship between the inhibition constant (KI) and the concentration of inhibitor which causes 50 per cent inhibition (I50) of an enzymatic reaction. *Biochemical Pharmacology* 22(23): 3099-3108. https://doi.org/10.1016/0006-2952(73)90196-2

Chow, B. Y. and Boyden, E. S. (2013). Optogenetics and translational medicine. *Sci. Transl. Med*. 5, 177ps5. https://doi.org/10.1126/scitranslmed.3003101

Conti, E., Scaglione, A., de Vito, G., et al. (2022). Combining optogenetic stimulation and motor training improves functional recovery and perilesional cortical activity. *Neurorehabilitation and Neural Repair*, 36(2): 107-118. https://doi.org/10.1177/15459683211056656

Deng, C., Yuan, H., Dai, J. (2017). Behavioral manipulation by optogenetics in nonhuman primate. *Neuroscientist* (5): 526-539. https://doi.org/10.1177/1073858417728459

Deubner, J., Coulon, B., and Diester, I. (2019). Optogenetic approaches to study the mammalian brain. *Current Opinion in Structural Biology*, 57: 157-163. https://doi.org/10.1016/j.sbi.2019.04.003

Du, J., Bai, X., Gola, A., et al. (2018). Performance of a high-resolution depth-encoding PET detector module using linearly-graded SiPM arrays. *Phys. Med. Biol.* 63, 035035. https://doi.org/10.1088/1361-6560/aaa707

Duebel, J., Marazova, K., Sahel, J.A., 2015. Optogenetics. *Curr. Opin. Ophthalmol*. 26 (3), 226–232. https://doi.org/10.1097/ICU.0000000000000140

Galvan, A., Stauffer, W.R., Acker, L., et al. (2017). Nonhuman primate optogenetics: recent advances and future directions. *J Neurosci.* 37(45): 10894-10903. https://doi.org/10.1523/JNEUROSCI.1839-17.2017

Garbarini, N. (2010). Primates as models for research. *Dis. Model. Mech.* 3: 15-19. https://doi.org/10.1242/dmm.004861

Gaub, B.M., Berry, M.H., Holt, A.E., et al. (2015). Optogenetic vision restoration using rhodopsin for enhanced sensitivity. *Molecular Therapy* 23(10): 1562-1571 https://doi.org/10.1038/mt.2015.121

Gerits, A., Farivar, R., Rosen, B.R., Wald, L.L., Borden, E.S., Vanduffel, W. (2012). Optogenetically induced behavioral and functional network changes in primates. *Current* Biology 22(18): 1722-1726. https://doi.org/10.1016/j.cub.2012.07.023

Gharbawie, O.A., Stepniewska, I., Kaas, J.K., (2011). Cortical connections of functional zones in posterior parietal cortex and frontal cortex motor regions in new world monkeys. *Cerebral Cortex*, 21: 1981-2002. https://doi.org/10.1093/cercor/bhq260

Howard, D.B., Powers, W., Wang, Y., Harvey, B.K. (2008). Tropism and toxicity of adeno-associated viaral vector verotypes 1, 2, 5, 6, 7, 8, and 9 in rat neurons and glia in vitro. *Virology* 372(1): 24-34. https://doi.org/10.1016/j.virol.2007.10.007

Hutton, B.F., Erlandsson, K. and Thielemans, K. (2018). Advances in clinical molecular imaging instrumentation. *Clin Transl Imaging* 6, 31–45. https://doi.org/10.1007/s40336-018-0264-0

Inoue, K., Matsumoto, M., Takada. (2021). Nonhuman primate optogenetics: current status and future prospects. *Adv Exp Med Biol.* 1293: 345-358. https://doi.org/10.1007/978-981-15-8763-4_22

Izpisúa-Belmonte, J.C., Callaway, E.M., Caddick, S.J., et al. (2015). Brains, genes and primates. *Neuron* 86(3): 617-631. https://doi.org/10.1016/j.neuron.2015.03.021

Iyer, S.M., Vesuna, S., Ramakrishnan, C., et al. (2016). Optogenetic and chemogenetic strategies for sustained inhibition of pain. *Scientific Reports* 6:30570. https://doi.org/10.1038/srep30570

Jay, T. M., Glowinski, J., & Thierry, A. M. (1989). Selectivity of the hippocampal projection to the prelimbic area of the prefrontal cortex in the rat. *Brain research*, 505(2), 337–340. https://doi.org/10.1016/0006-8993(89)91464-9

Jia, M., Dahlman-Wright, K., and Gustafsson, J. (2015). Estrogen receptor alpha and beta in health and disease. *Best Practice & Research Clinical Endocrinology & Metabolism*, 29(4): 557-568. https://doi.org/10.1016/j.beem.2015.04.008

Kaas, Jon H. (2013). The evolution of brains from early mammals to humans. *Wiley Interdiscip. Rev. Cogn. Sci.* 33-45. https://doi.org/10.1002/wcs.1206

Kalin, N, et al. (2003). Nonhuman primate models to study anxiety, emotion regulation and psychopathology. *Ann. N Y Acad. Sci.* 1008:189-200. https://doi.org/10.1196/annals.1301.021

Katzenellenbogen, J.A. (2021). The quest for improving the management of breast cancer by functional imaging: The discovery and development of 16α-[18F]fluoroestradiol (FES), a PET radiotracer for the estrogen receptor, a historical review. *Nuclear Medicine and Biology* 92: 24-37 https://doi.org/10.1016/j.nucmedbio.2020.02.007

Khayum, M.A., de Vries, E.F.J., Glaudemans, A., Dierckx, R., Doorduin, J. (2014). In vivo imaging of brain estrogen receptors in rats: A 16α-18F-Fluoro-17β-Estradiol PET Study. *Journal of Nuclear Medicine* 55(3): 481-487. https://doi.org/10.2967/jnumed.113.128751

Kimple, M. E., Brill, A. L. & Pasker, R. L. (2013). Overview of affinity tags for protein purification. *Curr Protoc Protein Sci.* 73, Unit 9.9. https://doi.org/10.1002/0471140864.ps0909s73

Korczeniewska, O. A., James, M. H., Eliav, T., Katzmann Rider, G., Mehr, J. B., Affendi, H., Aston-Jones, G., & Benoliel, R. (2022). Chemogenetic inhibition of trigeminal ganglion neurons attenuates behavioural and neural pain responses in a model of trigeminal neuropathic pain. *European journal of pain*, 26(3), 634–647. https://doi.org/10.1002/ejp.1887

Kumar, R., Zakharov, M.N., Khan, S.H., et al. (2011). The dynamic structure of the estrogen receptor. *J Amino Acids*, Article ID 812540. https://doi.org/10.4061/2011/812540

Li, W., Lao-Kim, N.P., Roussakis, A., et al. (2020). Longitudinal functional connectivity changes related to dopaminergic decline in Parkinson's disease. *Neuroimage: Clinical* 28: 102409 https://doi.org/10.1016/j.nicl.2020.102409

Logan J, Fowler JS, Volkow ND, Wang GJ, Ding YS, Alexoff DL. (1996). Distribution volume ratios without blood sampling from graphical analysis of PET data. *J Cereb Blood Flow Metab*, 16(5):834-840.

Magnus, C.J., Lee, P.H., Atasoy, D. (2011). Chemical and genetic engineering of selective ion channel interactions. Science Vol. 333, Issue 6047, pp. 1292-1296 https://doi.org/10.1126/science.1206606

Mikhaylova, E., Tabacchini, V., Borghi, G., et al. (2017). Optimization of an ultralow-dose high-resolution pediatric PET scanner design based on monolithic scintillators with dual-sided digital SiPM readout: a simulation study. *Phys. Med. Biol.* 62, 8402. https://doi.org/10.1088/1361-6560/aa8eb2

Nagai, Y., Miyakawa, N., Takuwa, H. et al. (2020). Deschloroclozapine, a potent and selective chemogenetic actuator enables rapid neuronal and behavioral modulations in mice and monkeys. *Nat Neurosci* 23, 1157–1167. https://doi.org/10.1038/s41593-020-0661-3

Nguyen, N.T., Ma, G., Zhou, Y., and Jing, J. (2020). Optogenetic approaches to control Ca^{2+} modulated physiological processes. *Current Opinion in Physiology* 17: 187-196 https://doi.org/10.1016/j.cophys.2020.08.004

Paquette, M., Ouellet, R., Archambault, M., et al. (2012). [18F]-fluoroestradiol quantitative PET imaging to differentiate ER+ and ER α- knockdown breast tumors in mice. *Nucl Med Biol.* 39(1): 57-64 https://doi.org/10.1016/j.nucmedbio.2011.06.004

Penuelas I., Mazzolini G., Boan JF., et al. (2005). Positron emission tomography imaging of adeno-viral-mediated transgene expression in liver cancer patients. Gastroenterology; 128: 1787-1795.

Pignatelli M, Umanah GKE, Ribeiro SP, Chen R, Karuppagounder SS, Yau HJ, Eacker S, Dawson VL, Dawson TM, Bonci A. (2017). Synaptic Plasticity onto Dopamine Neurons Shapes Fear Learning. *Neuron*. 93(2):425-440. https://doi.org/10.1016/j.neuron.2016.12.030. PMID: 28103482.

Pignatelli M, Tejeda HA, Barker DJ, Bontempi L, Wu J, Lopez A, Palma Ribeiro S, Lucantonio F, Parise EM, Torres-Berrio A, Alvarez-Bagnarol Y, Marino RAM, Cai ZL, Xue M, Morales M, Tamminga CA, Nestler EJ, Bonci A. (2020). Cooperative synaptic and intrinsic plasticity in a disynaptic limbic circuit drive stress-induced anhedonia and passive coping in mice. *Mol Psychiatry*. https://doi.org/10.1038/s41380-020-0686-8

Reuter, M., Rosas, D.H., Fischol, B. (2010). Highly accurate inverse consistent registration: A robust approach. *NeuroImage* 53(4): 1181-1196. https://doi.org/10.1016/j.neuroimage.2010.07.020

Sahel JA, Boulanger-Scemama E, Pagot C, Arleo A, Galluppi F, Martel JN, Esposti SD, Delaux A, de Saint Aubert JB, de Montleau C, Gutman E, Audo I, Duebel J, Picaud S, Dalkara D, Blouin L, Taiel M, Roska B. (2021). Partial recovery of visual function in a blind patient after optogenetic therapy. *Nat Med*. 2021 Jul;27(7):1223-1229. Epub 2021 May 24. PMID: 34031601. https://doi.org/10.1038/s41591-021-01351-4.

Schilling, K.G., Gao, Y., Stepniewska, I., Wu, T., Wang, F., Landman, B.A., Gore, J.C., Chen, L.M., Anderson, A.W. (2017). The VALiDATe29 MRI Based Multi-Channel Atlas of the Squirrel Monkey Brain. Neuroinform 15, 321–331 https://doi.org/10.1007/s12021-017-9334-0

Seo, J.W., Ingham, E.S., Mahakian, L., et al., (2020). Positron emission tomography imaging of novel AAV capsids maps rapid brain accumulation. Nat. Commun. 11 (2102) https://doi.org/10.1038/s41467-020-15818-4

Shibata, H., & Naito, J. (2005). Organization of anterior cingulate and frontal cortical projections to the anterior and laterodorsal thalamic nuclei in the rat. *Brain research*, 1059(1), 93–103. https://doi.org/10.1016/j.brainres.2005.08.025

Simunovic, M.P., Shen, W., et al. (2019). Optogenetic approaches to vision restoration. *Experimental Eye Research* 178, 15-26. https://doi.org/10.1016/j.exer.2018.09.003

Smith, S.M., Nichols, T.E. (2009). Threshold-free cluster enhancement: Addressing problems of smoothing, threshold dependence and localisation in cluster inference. *NeuroImage* 44(1): 83-98. https://doi.org/10.1016/j.neuroimage.2008.03.061

Sokoloff L. (1984). Modeling metabolic processes in the brain in vivo. *Annals of neurology*, 15 Suppl, S1–S11. https://doi.org/10.1002/ana.410150703

Stepniewska I., Preuss T.M., Kaas J.H. (1993). Architectonics, somatotopic organization, and ipsilateral cortical connections of the primary motor area (M1) of owl monkeys. J Comp Neurol 330:238–271. https://doi.org/10.1002/cne.903300207

Stepniewska, I., Friedman, R.M., Miller, D.J., Kaas, J.H. (2020). Interactions within and between parallel parietal-frontal networks involved in complex motor behaviors in prosimian galagos and a squirrel monkey. *Journal of Neurophysiology*, 123(1): 34-56. https://doi.org/10.1152/jn.00491.2013

Strick, P.L. and Kim, C.C. (1978). Input to primate motor cortex from posterior parietal cortex (area 5). I. Demonstration by retrograde transport. *Brain Research*, 157, 325-330. https://doi.org/10.1016/0006-8993(78)90035-5

Thanos, P.K., Robison, L., Nestler, E.J., Kim, R., Michaelides, M., Lobo, M., and Volkow, N.D. Mapping brain metabolic connectivity in awake rats with µPET and optogenetic stimulation. *J. Neurosci.* 33(15): 6343-6349. (2013) https://doi.org/10.1523/JNEUROSCI.4997-12.2013

Ting JT, Lee BR, Chong P, Soler-Llavina G, Cobbs C, Koch C, Zeng H, Lein E. (2018), Preparation of Acute Brain Slices Using an Optimized N-Methyl-D-glucamine Protective Recovery Method. J Vis Exp. (132):53825. https://doi.org/10.3791/53825

Tremblay, S., Acker, L., Afraz, A., et al. (2020). An open resource for non-human primate optogenetics. Neuron 108: 1075-1090. https://doi.org/10.1016/j.neuron.2020.09.027

Venner, A., Todd, W. D., Fraigne, J., Bowrey, H., Eban-Rothschild, A., Kaur, S., & Anaclet, C. (2019). Newly identified sleep-wake and circadian circuits as potential therapeutic targets. *Sleep*, 42(5), zsz023. https://doi.org/10.1093/sleep/zsz023

Vertes R. P. (2004). Differential projections of the infralimbic and prelimbic cortex in the rat. *Synapse*, 51(1), 32–58. https://doi.org/10.1002/syn.10279

Walker, M.C. and Kullmann, D.M. (2020). Optogenetic and chemogenetic therapies for epilepsy. *Neuropharmacology*, 168, 107751. https://doi.org/10.1016/j.neuropharm.2019.107751

Winkler, A.M., Ridgway, G.R., Webster, M.A., Smith, S.M., Nchols, T.E. (2014). Permutation inference for the general linear model. *NeuroImage* 92, 381-397. https://doi.org/10.1016/j.neuroimage.2014.01.060

Wise, S.P. (2008). Forward frontal fields: phylogeny and fundamental function. *Trends Neurosci.* 31, 599-608. https://doi.org/10.1016/j.tins.2008.08.008

Yaghoubi, S. S., Jensen, M. C., Satyamurthy, N., Budhiraja, S., Paik, D., Czernin, J., & Gambhir, S. S. (2009). Noninvasive detection of therapeutic cytolytic T cells with 18F-FHBG PET in a patient with glioma. Nature clinical practice. Oncology, 6(1), 53–58. https://doi.org/10.1038/ncponc1278

Yaghoubi, S.S., Campbell, D.O., Radu, C.G., Czernin, J. (2012). Positron Emission Tomography Reporter Genes and Reporter Probes: Gene and Cell Therapy Applications. *Theranostics* 2(4), 374-391. https://doi.org/10.7150/thno.3677

Yang, Y., Wu, M., Vázquez-Guardado, A., et al. (2021). Wireless multilateral devices for optogenetic studies of individual and social behaviors. Nat Neurosci 24, 1035–1045. https://doi.org/10.1038/s41593-021-00849-x

Zhang, F., Wang, L., Boyden, S., Deisseroth, K. (2006). Channelrhodopsin-2 and optical control of excitable cells. *Nature Methods* 3: 785-792. https://doi.org/10.1038/nmeth936

Zhang, F., Wang, L., Brauner, M., et al. (2007). Multimodal fast optical interrogation of neural circuitry. *Nature* 446: 633-639. https://doi.org/10.1038/nature05744

Zhang S, Qi J, Li X, Wang HL, Britt JP, Hoffman AF, Bonci A, Lupica CR, and Morales M (2015) Dopaminergic and glutamatergic microdomains in a subset of rodent mesoaccumbens axons. Nature Neuroscience, 18: 386-392.

Chapter 3: Developing a Dual Chemogenetics Approach for Bidirectional Neuromodulation in Rodents and NHPs

This chapter has been adapted from a combination of work presented/to be presented at the following conferences:

Boehm M, Levinstein M, Stein EA, and Michaelides M. A dual chemogenetic strategy for cell-type specific bidirectional neuromodulation. Poster presentation*, Society for Neuroscience Annual Meeting*, San Diego, CA, Nov 16, 2022

Boehm M, Jedema H, Bonaventura J, Gharbawie O, Gomez J, Stein EA, Bradberry CW, and Michaelides M. Validation of PET-compatible chemogenetic tools in squirrel monkeys. Oral presentation, *International Symposium of Functional Neuroreceptor Mapping (NRM)* virtual meeting, Dec 14, 2021

Boehm, MA, Jedema, H, Bonaventura, J, Gharbawie, O, Gomez, J, Stein, EA, Bradberry, CW, and Michaelides, M. (2021). Validation of PET-compatible chemogenetic tools in squirrel monkeys. *Journal of Cerebral Blood Flow and Metabolism*, 41(1, suppl): p. 44. https://doi.org/10.1177/0271678X211061050

Boehm M, Bonaventura J, Gomez J, Jedema H, Lu H, Stein EA, Bradberry CW, and Michaelides M. Advancing translational chemogenetic tools using positron emission tomography*.* Poster presentation*, Society for Neuroscience Annual Meeting*, Chicago, IL, Oct 20, 2019

3.1 Abstract

Chemogenetic technologies utilize transgenic receptors in conjunction with specific ligands to enable manipulation of target cell types. These tools provide a valuable method for selective neuromodulation and have potential for translational and clinical applications. DREADDs and PSAMs are two types of chemogenetic receptor systems used to modulate brain activity. Recent studies have demonstrated the use of PET imaging to assess functional effects of novel chemogenetic ligands and localize DREADD and PSAM expression in vivo. However, these emerging techniques have never been used in combination and merit further development. We demonstrate a dual chemogenetics approach by inducing co-expression of the DREADD – hM3Dq, and PSAM – PSAM^4-GlyR, using a combination of AAVs (AAV-Syn1-hM3Dq and AAV-Syn1-PSAM^4-GlyR) injected into the cortex of rats (Sprague Dawley) and squirrel monkeys (*Saimiri sciureus*). To assess the effects of chemogenetic stimulation on brain activity, we performed FDG-PET following injection of saline or 0.1 mg/kg of the hM3Dq agonist – JHU37160 (J60), or PSAM^4-GlyR agonist – uPSEM^{817}. A voxel-wise analysis in rats showed administration of J60 and uPSEM^{817} (i.p.) both resulted in higher FDG uptake locally at the AAV injection site compared to within-subject saline scans ($n = 5$, $p < 0.05$). However, hM3Dq and PSAM^4-GlyR actuation (with J60 and uPSEM^{817}, respectfully) produced different effects on brain activity in regions outside of the AAV injection site (e.g., somatosensory cortex, striatum, insular cortex, hippocampus, amygdala, thalamus, hypothalamus, and cerebellum), and different effects on locomotor behavior (i.e., distance traveled, rotations, average velocity). In addition, PET with [^{18}F]J07 and [^{18}F]ASEM was used to visualize hM3Dq and PSAM^4-GlyR in rat M1, respectively, and post-mortem immunohistochemistry confirmed brain expression of hM3Dq and PSAM^4-GlyR with ~50% of cells showing co-expression of both receptors. In squirrel monkey experiments, animals underwent PET scans with [^{18}F]J07, [^{18}F]ASEM, and FDG (with saline/J60/uPSEM^{817} pretreatment) before and after receiving co-injection of hM3Dq/PSAM^4-GlyR AAVs in left cortex (i.e., premotor or dlPFC). Pre-AAV scans with [^{18}F]J07 ($n = 3$) and [^{18}F]ASEM ($n = 4$) displayed endogenous binding in cortex (BP_{ND} 0.3-0.5), but post-AAV scans ($n = 2$) showed relatively greater binding near the left cortical AAV site (BP_{ND} 0.7-0.9), in comparison to this location in a control AAV site in the opposite hemisphere (BP_{ND} 0.5-0.6). In pre-AAV scans with FDG, no differences in uptake were observed following J60 or uPSEM^{817} (0.1mg/kg, i.v.) compared to saline ($n = 4$, $p < 0.05$). However, post-AAV scans revealed chemogenetic-specific effects on FDG uptake near each animal's AAV site (i.e., corresponding with area of enhanced [^{18}F]J07 and [^{18}F]ASEM binding) as well as other brain regions. Together, these experiments demonstrate for the first time that hM3Dq and PSAM^4-GlyR can be co-expressed to elicit distinct effects on brain activity and behavior in rats and NHPs. Additionally, these findings support the feasibility of imaging multiple transgenic constructs (i.e., chemogenetic receptors) within the same subjects using translational PET imaging techniques.

3.2 Introduction

Chemogenetic neuromodulation technologies are valuable tools for neuroscience research (Burnett and Krashes, 2016; Smith et al., 2016; Sternson and Roth, 2014; Vardy et al., 2015) and offer translational potential for developing clinical applications for disorders including epilepsy, neuropathic pain, Parkinson's disease, insomnia and sleep apnea (Assaf and Schiller, 2019; Curado et al., 2020; Iyer et al., 2016; Kätzel et al., 2014; Walker and Kullman, 2020; Weir et al., 2017). Chemogenetics is based on the premise that a neuronal system can be manipulated by inducing expression of a transgenic receptor that binds selectively to an otherwise inert exogenous agonist. The most widely used chemogenetic neuromodulation tools utilize modified GPCRs (i.e., metabotropic chemogenetic receptors) or LGICs (i.e., ionotropic chemogenetic receptors) to promote or inhibit neuronal activity upon administration of a highly selective and potent chemogenetic agonist (Armbruster et al., 2007; Conklin et al., 2008; Song et al., 2022; Wess et al., 2013). Although chemogenetics lack the temporal control of optogenetics, the ease of administering a drug versus targeted light stimulation offers translational advantages and affords brain circuit modulations in freely behaving subjects without the need for an external device/light source.

DREADDs are a family of metabotropic chemogenetic receptors that utilize mutant versions of specific GPCRs (i.e., modified muscarinic acetylcholine receptors, opioid receptors and adrenergic receptors) activated by selective potent agonists instead of endogenous ligands (Armbruster et al., 2007; Conklin et al., 2008; Pei et al., 2008; Vardy et al., 2015). These tools can be leveraged to excite or inhibit neuronal activity depending on the type of chemogenetic receptor-coupling used. For instance, activation of the DREADD receptor 'hM3Dq' stimulates the Gq protein signaling pathway, promoting intracellular calcium release and thereby increasing neuronal activity. Therefore, hM3Dq is sometimes referred to as an "excitatory" DREADD due to its propensity to increase neuronal activity (i.e., neuronal firing of action potentials). In contrast, the hM4Di receptor stimulates inhibitory Gi/o protein signaling which decreases neuronal firing through hyperpolarization of post-synaptic membranes by activation of G-protein inwardly rectifying potassium (GIRK) channels and suppression of presynaptic neurotransmitter release (Lee et al., 2014; Zhu and Roth). Consequently, hM4Di is sometimes referred to as an "inhibitory" DREADD due to its ability to decrease neuronal activity.

Alternatively, PSAMs are ionotropic chemogenetic receptors that utilize nAChRs coupled with the ion pore domains of various LGICs to directly modulate membrane ion conductance (Magnus et al., 2011). The latest generation of PSAMs (PSAM^4) were recently developed through screening mutations in the α7 nAChR-LBD in search of enhanced channel interaction with the smoking cessation drug varenicline (Magnus et al., 2019). By combining these modified nAChR-LBDs with ion pore domains, chimeric LGICs were created to modulate neuronal activity in response to varenicline at concentrations much lower than clinical doses targeting endogenous nicotinic receptors (Kaur et al., 2009; Rollema et al., 2010). Similar to DREADDs, different types of PSAMs can be used to increase or decrease neuronal activity. PSAM^4-5HT3 utilizes the serotonin receptor 3 (5-HT3R) cation channel and its activation can increase neuronal activity, whereas PSAM^4-GlyR uses the inhibitory glycine receptor (GlyR) chloride channel, and its activation can decrease neuronal activity (Magnus et al., 2019). Due to these different properties, PSAM^4-5HT3 is mainly viewed as excitatory and used to activate neurons, whereas PSAM^4-GlyR is intended to be an inhibitory "neuronal silencer" (Magnus et al., 2019). However, overall effects on in vivo brain activity are nuanced and interpretations should be made carefully when using these tools to explore brain activity/behavior relationships. For example, agonism of PSAM^4-GlyR in mouse striatum has been found to increase neuronal activity as opposed to inhibiting/silencing activity (Gantz et al., 2021). Therefore, further investigation is required to characterize the effects of PSAM^{4}-GlyR agonism on brain activity in vivo.

Recent efforts in the field have focused on refining DREADD and PSAM applications by enhancing the selectivity and potency of chemogenetic receptor agonists (e.g., JHU37160 (J60) and deschloroclozapine (DCZ) for DREADDs; uPSEM^{817} for PSAMs) and utilizing PET imaging methods for assessing chemogenetic receptor expression (i.e., [^{18}F]JHU37107 ([^{18}F]J07) and [^{11}C]DCZ for DREADDs; [^{18}F]ASEM for PSAMs) and function (FDG-PET) in vivo (see Chapter 1) (Boehm et al., 2021; Bonaventura et al., 2019, Magnus et al., 2019, Nagai et al., 2020). However, these emerging techniques have never been used in combination and merit further characterization to refine their usage and facilitate translational applications of chemogenetics.

DREADDs are metabotropic chemogenetic receptors (i.e., agonism initiates GPCR signaling cascades), whereas PSAMs are ionotropic chemogenetic receptors (i.e., agonism opens LGIC to directly modulate membrane ion conductance) meaning that DREADDs and PSAMs induce their effects on brain activity through very different cellular mechanisms (Song et al., 2022). Thus, a direct comparison of their effects on brain activity (i.e., DREADD vs. PSAM in same brain region within the same subjects) could provide insight into potential advantages or disadvantages of using metabotropic (i.e., DREADDs) vs ionotropic (i.e., PSAMs) chemogenetic receptors. Additionally, the combined use of an “excitatory” DREADD (i.e., hM3Dq) and “inhibitory” PSAM (i.e., PSAM^{4}-GlyR) could potentially enable bidirectional neuromodulation which could have utility when interrogating brain circuit-behavior relationships (i.e., testing if activation vs. inhibition of a specific brain area produces opposing behavioral effects).

Therefore, we sought to develop a dual chemogenetics approach for bidirectional neuromodulation using a co-injection of two AAVs (i.e., $AAV_{2/5}$-Syn1-HA-hM3Dq and $AAV_{2/5}$-Syn1-$PSAM^4$-GlyR-3XFLAG) to co-express an “excitatory” DREADD (i.e., hM3Dq) and an “inhibitory” PSAM (i.e., $PSAM^4$-GlyR) in the brains of rats and squirrel monkeys. To assess the efficacy of this approach, we performed FDG-PET to measure brain activity following administration of saline (for use as within-subject control) or 0.1 mg/kg of J60 (hM3Dq agonist) or $uPSEM^{817}$ ($PSAM^4$-GlyR agonist). Rat FDG-PET experiments were performed in awake and freely moving subjects (i.e., during the 40-min [^{18}F]FDG uptake period following i.p. saline/J60/$uPSEM^{817}$ and [^{18}F]FDG administration) to allow assessment of locomotor behaviors prior to being anesthetized for scanning (after the 40-min [^{18}F]FDG uptake period). Monkey FDG-PET experiments were performed in anesthetized subjects that were administered i.v. saline/J60/$uPSEM^{817}$ and [^{18}F]FDG. In addition to FDG-PET, we performed PET scans with the DREADD-selective radiotracer [^{18}F]J07 and the α7-nAChR radiotracer [^{18}F]ASEM to visualize brain expression of hM3Dq and $PSAM^4$-GlyR, respectively. Post-mortem immunohistochemistry (using anti-HA for hM3Dq and anti-FLAG for $PSAM^4$-GlyR) was also performed to confirm brain expression of hM3Dq and $PSAM^4$-GlyR.

In rat experiments, we chose to co-inject the AAVs (to co-express hM3Dq and $PSAM^4$-GlyR) in the primary motor cortex (M1) because this brain region has a wide range of neuroanatomical connections (i.e., afferent and efferent projections) with other cortical areas (e.g., somatosensory cortex, contralateral motor cortex, cingulate cortex) as well as subcortical brain areas (e.g., dorsal striatum, motor thalamus, cerebellum) (Alloway et al., 2009; Hosp et al., 2013, Jeong et al., 2016; McGeorge et al., 1989; Oka et al., 1978; Thach, 1987), and this allowed us to test our ability to image receptor expression (i.e., hM3Dq and $PSAM^4$-GlyR) in multiple brain areas outside the AAV injection site. Additionally, chemogenetic stimulation of M1 is of translational interest because it has been shown to promote recovery of motor function following ischemic stroke (Hu et al., 2019). Notably, we chose to co-inject the two AAVs unilaterally in M1 with the aim of eliciting lateralized effects on brain activity (i.e., hemisphere specific effects in FDG uptake) and/or locomotor behaviors (i.e., rotations/direction bias).

In squirrel monkey experiments, we co-injected the AAVs (to co-express hM3Dq and PSAM^4-GlyR) unilaterally in different cortical areas of two subjects (i.e., left premotor AAV co-injection in one monkey; left dlPFC AAV co-injection in a second monkey) in an exploratory approach to test whether these dual chemogenetic/PET imaging methods (i.e., combining DREADDs/PSAMs with [^{18}F]FDG (brain activity), [^{18}F]J07 (hM3Dq expression), and [^{18}F]ASEM (PSAM^4-GlyR expression) PET imaging) would reveal distinct structural/functional connectivity patterns between the individual subjects (i.e., premotor afferent/efferent projections vs. dlPFC afferent/efferent projections). Importantly, monkeys also received a “control” AAV injection (i.e., AAV-ChRmERα) in the respective site of the opposite hemisphere (i.e., right premotor or right dlPFC). This allowed us to assess whether potential increases in post-AAV PET-reporter binding (i.e., [^{18}F]J07 and [^{18}F]ASEM) could occur as a biproduct of post-surgery tissue damage/inflammation (as opposed to actual hM3Dq/PSAM^4-GlyR expression).

Together these experiments provide for the first time a direct in vivo comparison of hM3Dq (metabotropic chemogenetic receptor) and PSAM^4-GlyR (ionotropic chemogenetic receptor) through AAV-mediated co-expression in the same brain area. Combining this “dual chemogenetic” approach with FDG-PET enabled us to characterize effects of these receptors on brain activity, and the PET-reporters [^{18}F]J07 and [^{18}F]ASEM permitted visualization of hM3Dq and PSAM^4-GlyR brain expression, respectively. Our findings demonstrate the feasibility of combining these methods for interrogating brain circuits and also shed light on the limitations of current chemogenetic technologies.

3.3 Results

3.3.1 AAV-mediated co-expression of hM3Dq and PSAM^4-GlyR in rat brain

To test the feasibility of using AAV-mediated transduction to co-express hM3Dq and PSAM^4-GlyR in vivo, a co-injection of AAV$_{2/5}$-Syn1-HA-hM3Dq (AAV-hM3Dq) and AAV$_{2/5}$-Syn1-PSAM^4-GlyR-3XFLAG (AAV-PSAM^4-GlyR) was delivered into the primary motor (M1) cortex (left or right M1: AP: 2.0, ML: 3.0/-3.0, DV: -2.0, -2.1) of rats (Sprague Dawley, n = 10: 5 female and 5 male) (see Figure 1A.). Six weeks later, one of these rats was perfused (1xPBS/4% PFA) and the brain was processed to confirm AAV transduction efficacy via immunofluorescence microscopy. To detect hM3Dq expression in rat brain slices, a primary antibody for the HA epitope tag (mouse anti-HA.11, BioLegend #901501) was used in combination with anti-mouse secondary antibody (anti-mouse AlexaFluor 488, Invitrogen). In addition, PSAM^4-GlyR was detected using a primary antibody for the FLAG tag (rabbit anti-DYKDDDDK, Invitrogen #PA1984B) in combination with anti-rabbit secondary antibody (anti-rabbit AlexaFluor 647, Invitrogen) and DAPI nuclear counterstain in the same brain slices. Figure 1B. shows a left hemisphere brain slice with immuno-labeling of PSAM^4-GlyR (red, left), hM3Dq (green, center) and a combined overlay image with DAPI counterstain (blue, right). In Figure 1C., a 20x view of the left M1 AAV site shows a comparison of channel overlays revealing different overall expression patterns of PSAM^4-GlyR and hM3Dq, although some cells displayed co-expression of both receptors (yellow, white arrows in bottom right panel highlight co-expression). Approximately 70% of DAPI positive cells at the left M1 site expressed one or both receptors, and of the cells expressing PSAM^4-GlyR and/or hM3Dq, ~40% showed expression of both receptors (Figure 1D.)

3.3.2 Measuring effects of hM3Dq and PSAM4-GlyR agonism on brain activity with FDG-PET in rats

Once we verified successful AAV transduction and co-expression of hM3Dq and PSAM^4-GlyR, we next sought to explore chemogenetic effects on brain activity by performing FDG-PET in a group of rats expressing hM3Dq/PSAM^4-GlyR in left (n = 5) or right (n = 3) M1 (Figure 2). Animals were pretreated with saline or 0.1 mg/kg (i.p.) of the chemogenetic agonists J60 (for hM3Dq) or uPSEM^{817} (for PSAM^4-GlyR) 10-min prior to receiving a bolus injection of FDG (~0.5 mCi i.p.). Animals were then placed in an open-field chamber for 40-min to allow for awake uptake of the FDG in active brain regions before being anesthetized (~2% isoflurane) and scanned (20-min PET acquisition + CT on Mediso nanoScan®) (see Figure 2A). FDG-PET data was then processed (static reconstruction, Nucline nanoScan software 3.04.101.000) and quantified as standard uptake values (SUV, g/ml) and SUV ratios (i.e., $SUVR_{WB}$ = SUV normalized to whole-brain average, see methods section 3.10.4). A group comparison (one-way ANOVA within-subject, n = 6) of average whole brain FDG uptake (SUV g/ml) across treatments (Figure 2B) showed significantly greater average whole brain uptake in scans with J60 (avg SUV = 3.6 g/ml ± 0.3 SD) compared to saline (avg SUV = 3.0 g/ml ± 0.3 SD, p = 0.036). However, no significant differences in whole brain FDG uptake were observed in comparison to scans with uPSEM^{817} (avg SUV = 2.9 g/ml ± 0.7 SD) (Figure 2B). To investigate regional differences in brain activity between treatments, a voxel-wise analysis (see methods section 3.10.4) was performed in the group of rats with hM3Dq/PSAM^4-GlyR in left M1 (n = 5, one-way ANOVA within-subject, $p < 0.05$). Administration of J60 and uPSEM^{817} both resulted in relatively higher FDG uptake locally at the left M1 AAV injection site compared to within-subject saline scans (~10-15% greater SUVR_{WB} vs. saline, $p < 0.05$, see Figure 2C, G), but the treatments produced different effects in brain regions outside of the AAV injection site (see Figs 2C-G). Activation of hM3Dq with J60 elicited higher uptake contralaterally in the right striatum, entorhinal cortex (EC) and insular cortex (IC), ipsilaterally in the left hippocampus and cerebellum, and bilaterally in areas of the somatosensory cortex (S1) (Figure 2C, G). Lower FDG uptake was seen in a few areas including the pons and medulla (Figure 2E, G). In contrast, activation of PSAM^4-GlyR with uPSEM^{817} resulted in lower uptake in many regions (e.g., cingulate cortex, striatum, hippocampus, amygdala, thalamus) but did not produce higher uptake in brain regions outside of the AAV injection area and ipsilateral somatosensory cortex (Figure 2D, F, G) ($n = 5$, $p < 0.05$).

3.3.3 Chemogenetic induced locomotor effects in rats

During the awake FDG uptake period following i.p. injection in rats (~40 min), locomotor behavior was recorded in an open field chamber to assess potential behavioral effects of hM3Dq and PSAM^4-GlyR actuation. Chemogenetic-specific effects were observed in locomotor measures such as total distance travelled, total number of rotations and average velocity (one-way ANOVA within-subject, $n = 7$, $p < 0.05$) (see Figure 3). Specifically, in trials with uPSEM^{817} treatment (i.e., PSAM^4-GlyR agonist), rats moved an average total distance of 32.3 m (± 4.2 SEM) compared to 24.3 m (± 2.7 SEM) during saline trials (Tukey’s post-hoc $p = 0.038$) (Figure 3A, C). In trials with J60, rats moved an average total distance of 27.2 m (± 2.4 SEM), but this was not significantly different from saline ($p = 0.17$) (Figure 3A, B). However, an increase in average velocity was observed (2.3cm/s in J60 trials vs 1.9 cm/s in saline trials) (Figure 3D-E). In addition to total distance travelled, rats showed a greater number of rotations in trials with uPSEM^{817} (24 rotations ± 3.6 SEM) compared to saline (15 roations ± 2.8 SEM), but this rotational behavior was not observed in trials with J60 (14 rotations ± 2 SEM) (Figure 3H-I).

3.3.4 Imaging hM3Dq with [^{18}F]J07 and PSAM^{4}-GlyR with [^{18}F]ASEM in rats

After observing distinct functional effects of hM3Dq and PSAM^{4}-GlyR on brain activity and locomotion in rats, we next sought to test if we could image co-expression of hM3Dq and PSAM^{4}-GlyR using PET with [^{18}F]J07 and [^{18}F]ASEM, respectfully A pair of rats (i.e., one "control" with AAV-ChRERα and one "hM3Dq/PSAM^{4}-GlyR" with hM3Dq/PSAM^{4}-GlyR AAVs in right M1) underwent PET scans with [^{18}F]J07 (~0.5mCi i.v., anesthetized) ~12 months following intracranial AAV injection (Figure 4A-D). The rat that received the hM3Dq/PSAM^{4}-GlyR AAVs showed a localized area of enhanced [^{18}F]J07 binding ($BP_{\mathrm{ND}} = 1.3$) in right M1 compared to the same region in the control animal ($BP_{\mathrm{ND}} = 0.8$) (Figure 4A-D). A voxel-wise analysis could not be performed in the same manner as FDG-PET given only one hM3Dq/PSAM^{4}-GlyR rat and one control rat were scanned. However, the regional difference in BP_{ND} observed between the hM3Dq/PSAM^{4}-GlyR and control rat in right M1 (i.e., AAV site) was not observed in a contralateral VOI mirror in left M1 ($BP_{\mathrm{ND}} = 0.8$ in both rats), indicating the higher [^{18}F]J07 binding was localized to the AAV injection site and therefore likely represents putative hM3Dq expression in right M1. The same hM3Dq/PSAM^{4}-GlyR rat was also scanned with [^{18}F]ASEM in attempt to detect PSAM^{4}-GlyR expression in the brain (Figure 4E). Localized binding of [^{18}F]ASEM was detected in the same right M1 region as observed in the [^{18}F]J07 scan (Figure 4C-F). Post-mortem immunofluorescent labeling using anti-HA (for hM3Dq) and anti-FLAG (for PSAM^{4}-GlyR) in rat brain slices confirmed brain expression of hM3Dq and PSAM^{4}-GlyR locally at the M1 AAV site (Figure 4G-L). Approximately 70% of

DAPI+ cells in the local M1 AAV site expressed either one or both chemogenetic receptors (Figure 4K, n = 6). Of the cells expressing hM3Dq and/or PSAM^4-GlyR, 50-60% showed expression of both receptors, whereas 15-25% had only one or the other (Figure 4L, n = 6).

3.3.5 Dual imaging of hM3Dq and PSAM^4-GlyR with [^{18}F]J07 and [^{18}F]ASEM in squirrel monkeys

We next sought to implement the same dual chemogenetics approach (i.e., combined use of hM3Dq and PSAM^4-GlyR AAVs) in NHPs. Therefore, we conducted a series of PET experiments in squirrel monkeys using [^{18}F]J07 and [^{18}F]ASEM as chemogenetic PET-reporters and also FDG-PET to measure brain activity following pretreatment with J60 (hM3Dq agonist) or uPSEM^{817} (PSAM^4-GlyR agonist). We first scanned monkeys prior to the introduction of chemogenetic AAVs to characterize endogenous binding of [^{18}F]J07 (n = 3) and [^{18}F]ASEM (n = 4) as well as potential off-target effects of J60/uPSEM^{817} (0.1 mg/kg, i.v.) on brain activity (i.e., FDG uptake) (n = 4) (See Appendix C Fig. C3-C4 and Appendix D Fig. D1).

Pre-AAV brain uptake of [^{18}F]J07 peaked 10-20 min following i.v. injection (avg SUV = 3.5 g/ml ± 0.3 SEM) and decreased to 30-40% of peak levels at 90 min (n = 3), whereas [^{18}F]ASEM brain uptake peaked 20-30 min following injection (avg SUV = 2.8 g/ml ± 0.2 SEM) and remained at 60-70% of peak levels at 90 min (n = 4) (Appendix Figs. C4 and D1A). Average regional SUV ratios ($SUVR_{WB}$ = SUV normalized to within-subject whole brain average) showed highest binding in cortical areas for both [^{18}F]J07 and [^{18}F]ASEM ($SUVR_{WB}$ = 1.1 ± 0.01 SEM) and relatively low in cerebellum ($SUVR_{WB}$ = 0.7 ± 0.02 SEM) at 60-90min after radiotracer injection (Appendix Fig. D1B). Therefore, cerebellum was used as a non-specific reference region to quantify BP_{ND} as described previously with FES-PET in Chapter 2. Average whole brain BP_{ND} in pre-AAV monkeys was 0.33 ± 0.03 SEM in [^{18}F]J07 scans and 0.25 ± 0.02

SEM in [^{18}F]ASEM scans, and endogenous binding was highest in cortex for both radiotracers (BP_{ND} = 0.47 ± 0.05 SEM with [^{18}F]J07 and 0.37 ± 0.03 SEM with [^{18}F]ASEM) (Appendix Fig. D1D-E).

In squirrel monkey experiments, we co-injected the AAVs (to co-express hM3Dq and PSAM^{4}-GlyR) unilaterally in different cortical areas of two subjects (i.e., left premotor AAV co-injection in one monkey; left dlPFC AAV co-injection in a second monkey) in an exploratory approach to test whether these dual chemogenetic/PET imaging methods (i.e., combining DREADDs/PSAMs with [^{18}F]FDG (brain activity), [^{18}F]J07 (hM3Dq expression), and [^{18}F]ASEM (PSAM^{4}-GlyR expression) PET imaging) would reveal distinct structural/functional connectivity patterns between the individual subjects (i.e., premotor afferent/efferent projections vs. dlPFC afferent/efferent projections). Importantly, monkeys also received a "control" AAV injection (i.e., AAV-ChRmERα) in the respective site of the opposite hemisphere (i.e., right premotor or right dlPFC). This allowed us to assess whether potential increases in post-AAV PET-reporter binding (i.e., [^{18}F]J07 and [^{18}F]ASEM) could occur as a biproduct of post-surgery tissue damage/inflammation (as opposed to actual hM3Dq/PSAM^{4}-GlyR expression).

To assess the efficacy of [^{18}F]J07 and [^{18}F]ASEM for visualizing hM3Dq and PSAM^{4}-GlyR expression (respectively), two monkeys were co-injected with AAV-hM3Dq and AAV-PSAM^{4}-GlyR unilaterally in cortex (co-mixture ~3x10^{13} gc/ml, 9µl total). We targeted the left premotor cortex in one monkey and the left dlPFC in a second monkey to test whether these dual chemogenetic/PET imaging methods could reveal distinct expression patterns between the individual subjects (i.e., localized binding of [^{18}F]J07 and [^{18}F]ASEM in premotor afferent/efferent projections in one monkey vs. dlPFC afferent/efferent projections in the second monkey). Monkeys also received a "control" AAV injection (i.e., AAV-ChRmERα, ~1x10^{14}

gc/ml, 9µl total) at the respective contralateral location in right cortex (i.e., right premotor or right dlPFC). This allowed us to assess whether potential increases in post-AAV PET-reporter binding (i.e., [^{18}F]J07 and [^{18}F]ASEM) could occur as a biproduct of post-surgery tissue damage/inflammation (as opposed to actual hM3Dq/PSAM^{4}-GlyR expression). Post-AAV scans (8-12 months following surgery, Figure 5) with [^{18}F]J07 (n = 2) and [^{18}F]ASEM (n = 2) showed relatively greater binding near the left cortical AAV site ([^{18}F]J07 avg $BP_{\mathrm{ND}} = 0.7$, [^{18}F]ASEM avg $BP_{\mathrm{ND}} = 0.4$) in comparison to the control AAV site in the opposite hemisphere ([^{18}F]J07 avg $BP_{\mathrm{ND}} = 0.6$, [^{18}F]ASEM avg $BP_{\mathrm{ND}} = 0.3$) (Figure 5A-B). A voxel-wise statistical analysis could not be performed given there were only two subjects (and monkeys were injected in different brain regions). Importantly however, the within-subject differences in binding between left and right AAV target sites was not observed in pre-AAV scans which suggests it is representative of hM3Dq and PSAM^{4}-GlyR expression.

Notably, average BP_{ND} at the AAV injection was relatively lower in [^{18}F]ASEM scans (avg $BP_{\mathrm{ND}} = 0.4$) compared to [^{18}F]J07 scans (avg $BP_{\mathrm{ND}} = 0.7$). Because BP_{ND} is a measure that reflects both receptor density and radiotracer affinity, this difference could be attributed to a lower radiotracer affinity of [^{18}F]ASEM for PSAM^{4}-GlyR compared to the affinity of [^{18}F]J07 for hM3Dq. This is supported by the fact that we observed similar hM3Dq/PSAM^{4}-GlyR expression levels in rats following co-injection of the same AAVs. Therefore, to normalize for potential differences in radiotracer affinity/endogenous binding, BP_{ND} ratios for the AAV-based VOIs were also calculated with respect to within-subject global brain average (Figure 5C-D). In [^{18}F]J07 scans, the average BP_{ND} ratio of the left AAV site was 1.9 (± 0.2 SEM) in pre-AAV controls (n = 3) compared to 3.8 (± 0.5 SEM) in monkeys that received hM3Dq/PSAM^{4}-GlyR AAVs (n = 2). In [^{18}F]ASEM scans, the average BP_{ND} ratio of the left AAV site was 1.7 (± 0.2

SEM) in pre-AAV controls (n = 4) compared to 3.3 (± 0.6 SEM) in monkeys that received hM3Dq/PSAM^4-GlyR AAVs (n = 2). Relative BP_{ND} ratio differences in pre- vs post-AAV scans were also observed to a lower degree in the contralateral AAV site ([^{18}F]J07 BP_{ND} = 2.0 pre-AAV vs 3.1 post-AAV; [^{18}F]ASEM BP_{ND} = 1.8 pre-AAV vs. 2.5 post-AAV). This could potentially represent expression in contralateral projection terminals. Post-mortem immunohistochemistry will be performed to confirm that expression in brain slices corresponds with brain areas showing localized binding in PET-reporter scans (i.e., [^{18}F]J07 and [^{18}F]ASEM).

3.3.6 Measuring effects of J60 and uPSEM^{817} on brain activity in squirrel monkeys with FDG-PET (pre- and post-AAVs)

In squirrel monkey FDG-PET experiments, animals were administered FDG (anesthetized, i.v.) following administration of saline or 0.1 mg/kg of J60 or uPSEM^{817} (i.v.) before or after co-injection with hM3Dq/PSAM^4-GlyR AAVs in left premotor cortex or left or dlPFC. We first sought to test whether administration of J60 or uPSEM^{817} at the 0.1mg/kg dose would produce measurable effects on brain activity (i.e., FDG uptake) in the absence of chemogenetic receptors (i.e., off-target effects at endogenous sites). In pre-AAV scans, no differences in FDG uptake were observed following pretreatment with J60 or uPSEM^{817} compared to saline (within-subject, n = 4, $p < 0.05$), suggesting a lack of off-target brain effects (i.e., activation of endogenous receptors) from J60 and uPSEM^{817} at the 0.1mg/kg dose (see Figure C3 in Appendix C.).

Given the findings from pre-AAV FDG scans verified 0.1 mg/kg as an acceptable dose (i.e., no off-target effects on brain activity), we next performed the same set of scans (i.e., FDG-PET with pretreatment of saline or 0.1mg/kg J60 or uPSEM^{817}) in the two monkeys that received hM3Dq/PSAM^4-GlyR AAVs in left premotor or dlPFC (subjects from Figure 4). Due to the slightly different AAV injection locations in the two monkeys, an exploratory group voxel-wise analysis could not be performed in the same manner as in rat experiments (where all animals received co-injection of hM3Dq/PSAM^4-GlyR AAVs in same M1 area). Alternatively, scans from each monkey were analyzed using VOIs based on their individual left cortical AAV injection sites (i.e., premotor or dlPFC) and fitted to local hM3Dq/PSAM^4-GlyR expression patterns identified with [^{18}F]J07 and [^{18}F]ASEM PET (see Figure 5 and Appendix Fig D2)**.** We observed relatively higher FDG uptake at the left cortical AAV site following treatment with J60 and uPSEM^{817} (avg SUV = 2.8 g/ml and 2.6 g/ml, respectfully) compared to within subject saline scans (avg SUV = 2.3 g/ml). When normalized to average uptake in the rest of the brain (i.e., SUVR$_{WB}$), treatment with J60 and uPSEM^{817} showed ~10% greater regional activity at the hM3Dq/PSAM^4-GlyR AAV site compared to within subject saline scans (Figure 5). However, distinct activation patterns were observed in brain regions outside of the AAV site following J60 and uPSEM^{817} compared to within-subject saline scans. These findings parallel what was observed in rat FDG experiments but interpretations about structural/functional connectivity patterns are greatly limited by the lack of subjects in monkey experiments.

3.4 Discussion

Chemogenetic neuromodulation systems (i.e., metabotropic DREADDs and ionotropic PSAMs) enable targeted manipulations of brain activity and afford useful applications in neuroscience (Burnett and Krashes, 2016; Song et al., 2022; Sternson and Roth, 2014) with translational potential for epilepsy, neuropathic pain, Parkinson’s disease, sleep disorders, and motor function recovery following ischemic stroke (Assaf and Schiller, 2019; Curado et al., 2020; Hu et al., 2019; Kätzel et al., 2014; Weir et al., 2017). In this group of experiments, we set out to develop a dual chemogenetics approach for bidirectional neuromodulation and characterize the effects of two types of chemogenetic technologies (i.e., hM3Dq and PSAM^4-GlyR) on brain activity in rats and squirrel monkeys. We also tested the ability of recently developed PET-reporters [^{18}F]J07 and [^{18}F]ASEM to localize brain expression of hM3Dq and PSAM^4-GlyR, respectively.

In rat experiments, co-injection of hM3Dq and PSAM^4-GlyR AAVs into motor cortex resulted in successful transduction and expression of both chemogenetic receptors, and co-expression was observed in 40-60% of cells in the brain area around the M1 injection site (Figure 1). Administration of J60 (hM3Dq agonist) and uPSEM^{817} (PSAM^4-GlyR 0.1mk/kg, i.p.) in rats (3-5 months after receiving hM3Dq/PSAM^4-GlyR AAVs in right or left M1) induced chemogenetic-specific effects on brain activity (i.e., FDG uptake, see Figure 2) and locomotor behaviors (i.e., total distance traveled, avg velocity and # of rotations, see Figure 3) in comparison to within-subject saline treatment. Specifically, actuation of hM3Dq with J60 in FDG-PET experiments resulted in greater average whole brain uptake (i.e., global brain activity) in comparison to within-subject saline scans (avg SUV = 3.5 g/ml with J60 vs. 3.0 g/ml with saline, $p < 0.05$, $n = 6$). This finding is consistent with the "excitatory" nature of hM3Dq, which activates the Gq-coupled signaling pathway to promote intracellular calcium release and neuronal firing (Alexander et al., 2009). However, no significant global effect was observed in scans with uPSEM^{817} (PSAM^4-GlyR agonist, avg SUV = 2.9 g/ml). This finding was somewhat surprising because PSAM^4-GlyR activation opens chloride channels and has been described previously as a "neuronal silencer" (Magnus et al., 2019). Therefore, lower global FDG uptake (compared to within-subject saline trials) might be expected in uPSEM^{817} trials as a reflection of decreased neuronal activity. However, other reports have found PSAM^4-GlyR agonism can increase activity in the striatum of mice (Gantz et al., 2021) which suggests the effects of PSAM^4-GlyR on brain activity are nuanced and cannot be viewed simply as "inhibitory". If some brain regions were activated while others inhibited by PSAM^4-GlyR stimulation, a global effect may not be observed on the whole brain scale.

Interestingly, treatment with J60 (hM3Dq agonist) and uPSEM^{817} (PSAM^4-GlyR agonist) both induced significantly greater regional uptake (i.e., local brain activity) than saline in the area of the M1 AAV site (~10-20% greater $SUVR_{WB}$, $p < 0.01$) and also in distal brain regions with known anatomical connections with M1 (i.e., S1 and contralateral M1, ~5-10% greater $SUVR_{WB}$ vs. saline, $p < 0.05$). These shared effects were unexpected given hM3Dq and PSAM^4-GlyR are considered predominately excitatory vs. inhibitory, respectively (Roth, 2016; Magnus et al., 2019). When considering their distinct cellular mechanisms (i.e., Gq signaling pathway vs. chloride ion conductance), greater regional uptake in M1 would be expected from hM3Dq agonism (which would promote neuronal action potentials through intracellular calcium release), but not for PSAM^4-GlyR which is intended to inhibit neuronal activity/action potentials through chloride ion conductance (which would lower regional FDG uptake). This finding suggests that PSAM^4-GlyR agonism in M1 increases local brain activity instead of acting as a neuronal silencer. Another possible interpretation may be that metabolic demand is increased locally in M1 due to overactive endogenous ion pumps trying to respond to the unnatural level of chloride influx from PSAM^4-GlyR agonism. This might result in increased FDG uptake (i.e., metabolic demand) without truly representing an increase in neuronal activity/action potentials. However, excitation of D1-expressing medium spiny neurons by PSAM^4-GlyR agonism with a similar compound (uPSEM^{792}) has been observed previously in the mouse striatum (Gantz et al., 2021), and thought to be the result of a shift in the chloride reversal potential (to more depolarized potentials after prolonged Cl^- accumulation during PSAM^4-GlyR agonism) and a loss of GABA-mediated inhibition. Therefore, the use of PSAM^4-GlyR as a “neuronal silencer” may not be as straightforward or predictable in vivo depending on the transduced brain region/cell types and level of receptor expression.

Nevertheless, J60 (hM3Dq agonist) and uPSEM^{817} (PSAM^{4}-GlyR agonist) elicited distinct FDG uptake patterns in brain regions outside of the M1 AAV site, with J60 showing more areas with significantly higher uptake compared to saline (e.g., ipsilateral hippocampus, ipsilateral hypothalamus, bilateral VTA, $p < 0.05$) and uPSEM^{817} showing more areas with significantly lower uptake compared to saline (e.g., bilateral cingulate cortex, ipsilateral striatum, contralateral hypothalamus, $p < 0.05$). These findings are more consistent with the expected excitatory effects from hM3Dq agonism with J60 and expected inhibitory effects of PSAM^{4}-GlyR agonism with uPSEM^{817}. In addition, many of the regions showing differences in FDG compared to saline have known anatomical projections to the M1 AAV site (i.e., striatum, somatosensory cortex, cingulate cortex, thalamus, VTA) (Alloway et al., 2009; Hosp et al., 2013, Jeong et al., 2016; McGeorge et al., 1989; Oka et al., 1978; Thach, 1987) and therefore likely represent the effects of chemogenetic agonism at M1 efferent/afferent projections expressing hM3Dq and PSAM^{4}-GlyR. However, given we induced expression using the pan-neuronal genetic promoter synpasin 1, it is difficult to fully interpret the mechanisms underlying the net effects on FDG uptake. This is because we do not know the extent of hM3Dq and PSAM^{4}-GlyR expression in different cell-types (e.g., glutamatergic pyramidal cells vs., GABAergic interneurons) and activation of these cells could produce opposing network effects. Therefore, future studies aimed at interrogating brain connectivity could benefit from using more specific genetic promoters (e.g., CamKII for expression in glutamatergic cells or mDlx for GABAergic cells).

In addition to the chemogenetic-specific effects in FDG uptake (i.e., brain activity), we also observed chemogenetic-specific effects on locomotor measures such as total distance travelled, total number of rotations and average velocity (one-way ANOVA within-subject, $n = 7$, $p < 0.05$) (see Figure 3). Specifically, rats moved a greater average total distance in trials with uPSEM^{817} (i.e., PSAM^{4}-GlyR agonist) and also showed a significantly greater number of rotations (i.e., traveling in a circle) compared to when treated with saline ($p < 0.05$). These effects were not observed in trials with J60 treatment, but rats did move with significantly greater average velocity compared to saline trials ($p < 0.05$). It remains unclear whether these behavioral effects are attributed to chemogenetic activation and/or disinhibition of neuronal activity given the differing effects in M1 and distal brain regions. Similarly, because FDG uptake occurred in awake rats, some of the differences in regional FDG uptake could be attributed to the locomotor effects observed. However, the fact that activation in left M1 was observed in both J60 (hM3Dq agonist) and uPSEM^{817} (PSAM^{4}-GlyR agonist) trials and that the greater distance travelled/rotations was observed only in uPSEM^{817} trials suggests the locomotor behavioral effects may be more attributed to the different changes in activity in regions downstream from M1 (e.g., disinhibition of motor thalamic areas). Future studies could better explore lateralized behavior by comparing groups of subjects injected in opposite hemispheres (i.e., testing whether rats with PSAM^{4}-GlyR in left M1 predominately rotate in the opposite direction than rats with PSAM^{4}-GlyR in right M1).

In monkey FDG-PET experiments, we first tested whether administration of 0.1 mg/kg J60 or uPSEM^{817} produced brain activity changes in animals without AAVs/chemogenetic receptor expression ($n = 4$). We found no effect of drug treatment on global or regional FDG uptake in comparison to within-subject saline scans, suggesting this dose is acceptable for use as chemogenetic agonists without off-target effects at endogenous brain sites (see Appendix C. Fig. C3). This is consistent with previous findings of using 0.1 mg/kg dose in rodents and NHPs

(Bonaventura et al., 2019; Magnus et al., 2019). In post-AAV scans (n = 2), we found no differences in global brain uptake (i.e., whole brain average) between treatments. A group voxel-wise analysis of FDG-PET could not be performed in monkeys as it was in rats because each monkey was injected in slightly different cortical areas (i.e., left premotor or left dlPFC). However, individual within-subject comparisons showed relative regional differences in FDG uptake across scans (i.e., within-subject saline vs. J60 vs. uPSEM^{817}). Similar to the FDG-PET findings in rats, treatment with J60 and uPSEM^{817} in monkeys co-expressing hM3Dq and PSAM^{4}-GlyR both produced relatively greater uptake near the AAV injection site than in saline scans, but they elicited different effects in distal regions such as contralateral cortical areas (Figure 6.). However, these findings should be interpreted cautiously given the lack of statistical analysis due to the limited number of subjects in post-AAV monkey experiments. It is also important to note that monkey FDG-PET experiments were performed in anesthetized animals (as opposed to awake subjects in rat experiments). Previous studies combining chemogenetic activation with FDG-PET have shown that distinct brain networks can be activated during conditions of awake vs. anesthetized chemogenetic activation (Michaelides et al., 2013), with anesthetized stimulation producing changes in FDG accumulation more proximal to the manipulated anatomical circuits, and awake stimulation producing FDG changes beyond the manipulated anatomical circuit (likely recruited as a function of the chemogenetic induced behavioral effects).

Nonetheless, together the rat and monkey FDG-PET results underscore the nuanced effects that chemogenetic stimulation can have on local and downstream brain regions in vivo. Surprisingly, PSAM^{4}-GlyR agonism produced relatively greater FDG uptake at the local AAV site (compared to within-subject saline scans) even though PSAM^{4}-GlyR was designed to be a “neuronal silencer”. Therefore, the combination of hM3Dq and PSAM^4-GlyR cannot be used as a clear-cut bidirectional neuromodulation system of purely “excitatory” or “inhibitory” capabilities because net effects on brain activity were not this straightforward (especially with PSAM^4-GlyR agonism). These findings along with functional discrepancies reported in the literature (Magnus et al., 2019; Gantz et al., 2021) suggest ionotropic chemogenetic receptors (at least those utilizing chloride channels) may have less predictable/consistent action across brain regions than metabotropic chemogenetic receptors (i.e., DREADDs). However, the optimal chemogenetic approach will largely depend on the goal of the application as well as the extent of chemogenetic receptor expression in specific cell-types.

In PET scans with [^{18}F]J07 and [^{18}F]ASEM, endogenous binding was observed throughout the brain in squirrel monkeys pre-AAV (Avg brain [^{18}F]J07 BP_{ND} = 0.33 (n = 3) and was highest in cortical areas ((n = 4) (see Appendix C, Figs. C3-4 and Appendix D, Fig. D1). However, in post-AAV scans both radiotracers enabled the visualization of receptor expression near the cortical AAV injection site (see Chapter 2, Figs. 4-5 and Appendix D, Fig. D2). Notably, average BP_{ND} at the cortical injection site post-AAV was relatively higher in [^{18}F]J07 scans compared to [^{18}F]ASEM scans in rats and monkeys. BP_{ND} is a measure that is reflective of both radiotracer affinity and receptor density, so this difference likely represents a lower affinity of [^{18}F]ASEM for PSAM^4-GlyR compared to the affinity of [^{18}F]J07 for hM3Dq (as opposed to a lower density of PSAM^4-GlyR vs. hM3Dq receptors). This is supported by our post-mortem IHC findings of relatively similar expression levels of hM3Dq/PSAM^4-GlyR near the AAV site. Overall, these findings support the use of these PET-reporters for localizing in vivo brain expression of chemogenetic receptors and shows for the first time they can be used in combination to visualize DREADDs and PSAMs in the same subject. However, endogenous binding of [^{18}F]J07 and

[^{18}F]ASEM in the brain limits the sensitivity of this approach, so these methods would benefit from more selective chemogenetic PET-reporters and/or adopting a more sensitive reporter system (i.e., such as the ERαLBD/[^{18}F]FES approach described in Chapter 2).

3.5 Methods

Animal subjects

All animal experiments followed procedures approved by the NIDA-IRP animal care and use committee and complied with NIH guidelines and ethical regulations for animal research and husbandry. Wild-type Sprague-Dawley rats (Charles River, 250-500g weight, n = 10, 5 female and 5 male) were used for rodent experiments. Four male squirrel monkeys (*Saimiri sciureus*; ~12-20 years, 0.8-1 kg) were also used. At the conclusion of the study, rats and monkeys were euthanized and the brains were removed and processed for use in IHC and future immuno-electron microscopy.

Co-injection of hM3Dq and PSAM^4-GlyR AAVs

Rat surgeries:

Intracortical AAV injections were perform as described in Ch. 2, but with a co-mixture of AAVs: AAV2/5-Syn1-PSAM-GlyR-3XFLAG (2.61 x 10^{13} gc/ml) and AAV2/5-Syn1-hM3Dq (3.5 x 10^{13} gc/ml) (Addgene, 250ul each virus for a total of 500ul). AAVs were mixed and co-injected unilaterally into either left or right motor cortex (target coordinates: AP = 1.8, ML = ±3.0, DV = 2, -2.1). Animals recovered for a minimum of four weeks following surgery before participating in experiments.

Monkey surgeries:

Intracortical AAV injections were performed in anesthetized animals (similar to methods described in Ch. 2 monkey surgeries), but without electrophysiological motor mapping to identify the injection site. Injections sites were predetermined using measurements and stereotaxic coordinates based on individual structural MRIs. AAVs were delivered as a co-mixture of the same two AAVs used in rats: AAV2/5-Syn1-PSAM-GlyR-3XFLAG (2.61 x 10^{13} gc/ml) and AAV2/5-Syn1-HA-hM3Dq (3.5 x 10^{13} gc/ml) administered in three injections of 3ul separated by 0.5mm DV. Virus mixture was corrected to deliver equivalent amounts of gc/ml for each AAV. An additional AAV (AAV-ChRmERα) was injected in the contralateral hemisphere to serve as a control and a pilot for ChRmERα FES-PET (see Appendix, AAV2/5-Syn-ChRmine-ERaLBD and AAV2/5-Syn-ChRmine-ERaLBD-KV2.1, 1.7 x 10^{13} gc/ml).

Immunohistochemistry

IHC were performed as described in Chapter 2 methods, but with using different antibodies to detect hM3Dq and $PSAM^4$-GlyR. A primary antibody for the anti-HA tag (mouse host, Biolegend #90501) in combination with secondary AlexaFlour 488 (anti-mouse, InVitrogen) was used to detect hM3Dq. To detect $PSAM^4$-GlyR, a primary antibody for the FLAG tag (anti-DYKDDDDK, rabbit host, InVitrogen) was used in combination with secondary AlexaFluor 647 (anti-rabbit, InVitrogen). After secondary antibody incubation, slices were washed once more and then mounted onto glass slides using aqueous mounting medium (90% glycerol + 30mM Tris-HCl, pH 8.0) with a glass coverslip. Images were taken using a Leica DFC7000T microscope and processed with LasX software.

FDG-PET experiments

All PET/CT scans were acquired using a Mediso nanoScan® PET/CT scanner and data reconstruction was performed with Nucline nanoScan software (3.04.101.0000). Data was quantified as SUV (g/ml) and SUV ratios (i.e., $SUVR_{WB}$ = SUV normalized to whole brain average). All PET image analyses were performed using PMOD (software version 3.711) and Matlab (Mathworks) Statistical Parametric Mapping 12 (SPM12, University College London). FDG was sourced from Cardinal Health.

Rat FDG-PET:

Rat PET/CT scans were co-registered to a template rat brain atlas (Px Rat, W. Schiffer) and PET scans were converted from kBq/cc to SUV (g/ml) to correct for injected radioactivity and animal body weight. To assess effects on global brain activity, a within-subject one-way ANOVA was used to compare average whole brain SUV during saline, J60 and $uPSEM^{817}$ trials (n = 6). One rat (female, AAV right M1) developed a large mammary tumor during the study and was therefore excluded from group FDG analysis. A second rat (male, left M1) was excluded from the within-subject one-way ANOVA comparison of whole brain SUV due to receiving relatively lower injected activity in one of the three scans (i.e., ~100 µCi less FDG injected in

uPSEM^{817} scan vs saline/J60 scans). However, this animal's data was included in analyses that applied within-scan whole brain/global normalization (i.e., $\mathrm{SUVR}_{\mathrm{WB}}$ and within-subject voxel-wise analysis) because these correct for effects of global variation between scan days (i.e., variation from differences in blood glucose levels/body temp/specific activity of FDG). A voxel-wise analysis was performed on rats with hM3Dq/PSAM^4-GlyR AAVs in left M1 (n = 5) using SPM12 in MATLAB. A within-subject one-way ANOVA was used with post-hoc treatment contrasts to identify areas with significantly more or less FDG uptake in scans with J60 or uPSEM^{817} compared to saline ($p < 0.05$, cluster minimum 50 voxels). Probabilistic threshold-free cluster enhancement was applied to correct for multiple comparisons (Spisák et al., 2019).

Monkey FDG-PET:

In monkey FDG-PET experiments, pretreatment with saline or 0.1mg/kg J60 or uPSEM817 was administered i.v. in anesthetized animals 15-min prior to i.v. injection of FDG (~1.5 mCi), therefore FDG uptake was in anesthetized animals vs. awake (as in rat). Animals were scanned 30-60 minutes and scans were co-registered to individual structural MRIs.

PET scans with $[^{18}\mathrm{F}]$J07 and $[^{18}\mathrm{F}]$ASEM

All PET/CT scans were acquired using a Mediso nanoScan® PET/CT scanner and data reconstruction was performed with Nucline nanoScan software (3.04.101.0000). $[^{18}\mathrm{F}]$J07 and $[^{18}\mathrm{F}]$ASEM were sourced from Johns Hopkins Medicine Radiology Department. Radiotracer injections were i.v. (~1.5 mCi) followed by saline flush (0.5-1 ml). Monkeys and Sprague Dawley rats (n = 2 males) were anesthetized and maintained on isoflurane (1.5-2.5%) during the whole procedure. In both rats and monkeys, tail vein catheters were inserted for intravenous radiotracer delivery (bolus i.v.). $[^{18}\mathrm{F}]$J07 or $[^{18}\mathrm{F}]$J07 (~0.5 mCi for rats, ~1.5mCi for monkeys) followed by 0.5ml flush of saline immediately at the start of scan, and scan duration lasted 90 minutes. Raw scans underwent dynamic reconstruction (CT attenuation correction, 3 x 20s; 4 x 30s; 2 x 60s, 3 x 300s, 7 x 600s). Rat PET/CT scans were co-registered to a template rat brain atlas (Px Rat, W. Schiffer), and monkey PET/CT scans were co-registered to individual structural MRIs. SUV and $\mathrm{SUVR}_{\mathrm{WB}}$ (SUV normalized to whole brain average) was calculated in the same way as previously described. BP_{ND} was calculated with the pixel-based Logan reference tissue method, using PMOD and the grey matter CB was again used as the reference region (Logan et al., 1996). BP_{ND} ratios were calculated to normalize for within-subject whole brain averages (whole brain VOI excluding left/right AAV VOIs).

3.6. Figures for Chapter 3

Figure 1. AAV-mediated co-expression of hM3Dq and PSAM^4-GlyR in left M1 of rat.

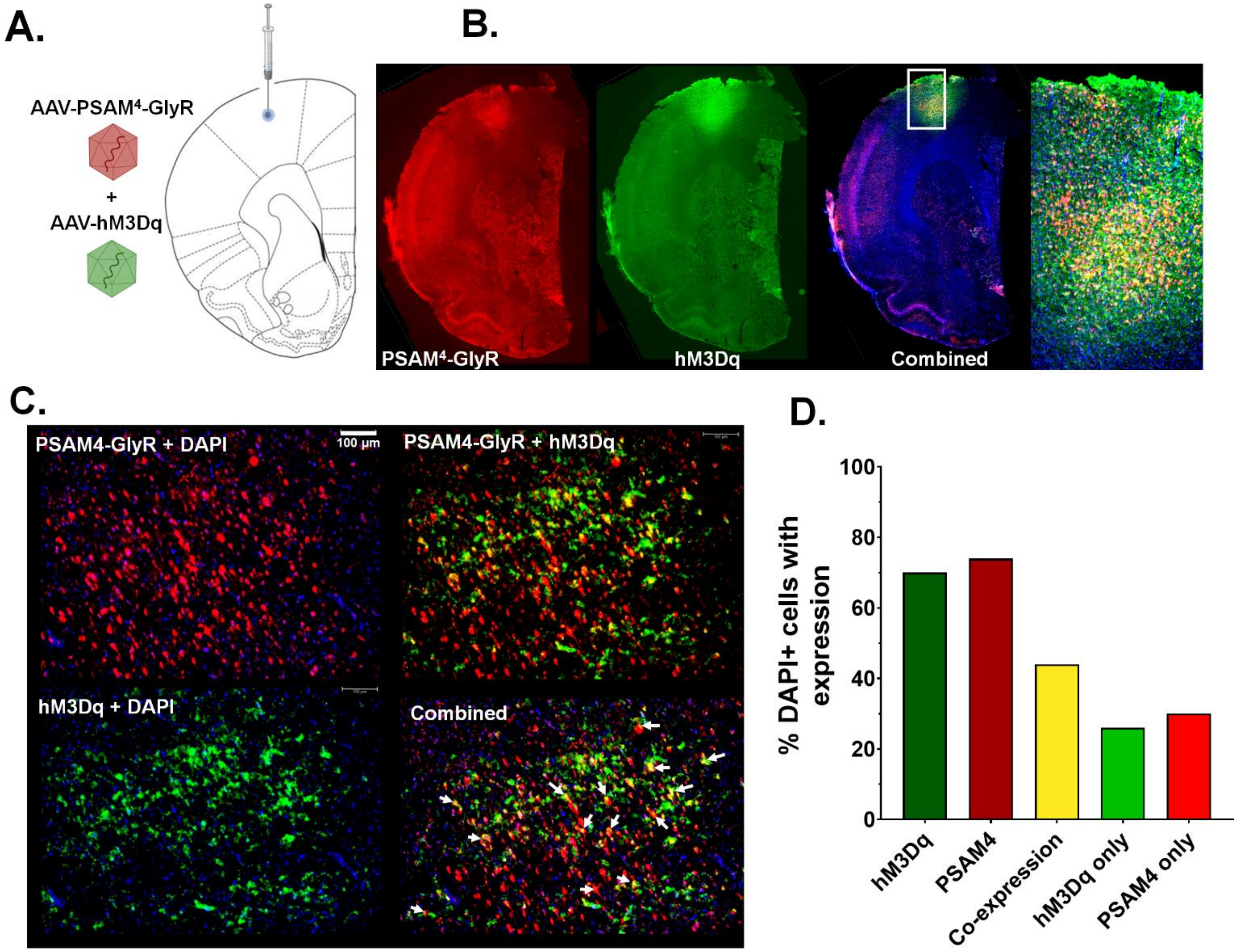

A. Co-injection of AAV$_{2/5}$-Syn1-HA-hM3Dq (AAV-hM3Dq) and AAV$_{2/5}$-Syn1-PSAM4-GlyR-3XFLAG (AAV-PSAM4-GlyR) in left M1 of rat (AP: 2.0, ML: 3.0, DV: -2.0) of rats (Sprague Dawley, n = 10: 5 female and 5 male) (see Figure 1A.). **B.** IHC confirms expression of PSAM^4-GlyR (left, red = anti-FLAG) and hM3Dq (middle, green = anti-HA) in left M1, with some cells expressing both receptors (right, blue = DAPI). White box on the 'Combined' slice indicates area of focus shown in the image on far right. **C.** 20x panel view of the left M1 AAV site shows a comparison of channel overlays revealing different expression patterns of PSAM^4-GlyR (red) and hM3Dq (green). Some cells displayed co-expression of both receptors (yellow, white arrows in bottom right panel indicate co-expression). **D.** Comparison of % DAPI cells showing expression of hM3Dq and/or PSAM^4-GlyR at the left M1 site.

Figure 2. Measuring effects of hM3Dq and PSAM4-GlyR on brain activity with FDG-PET

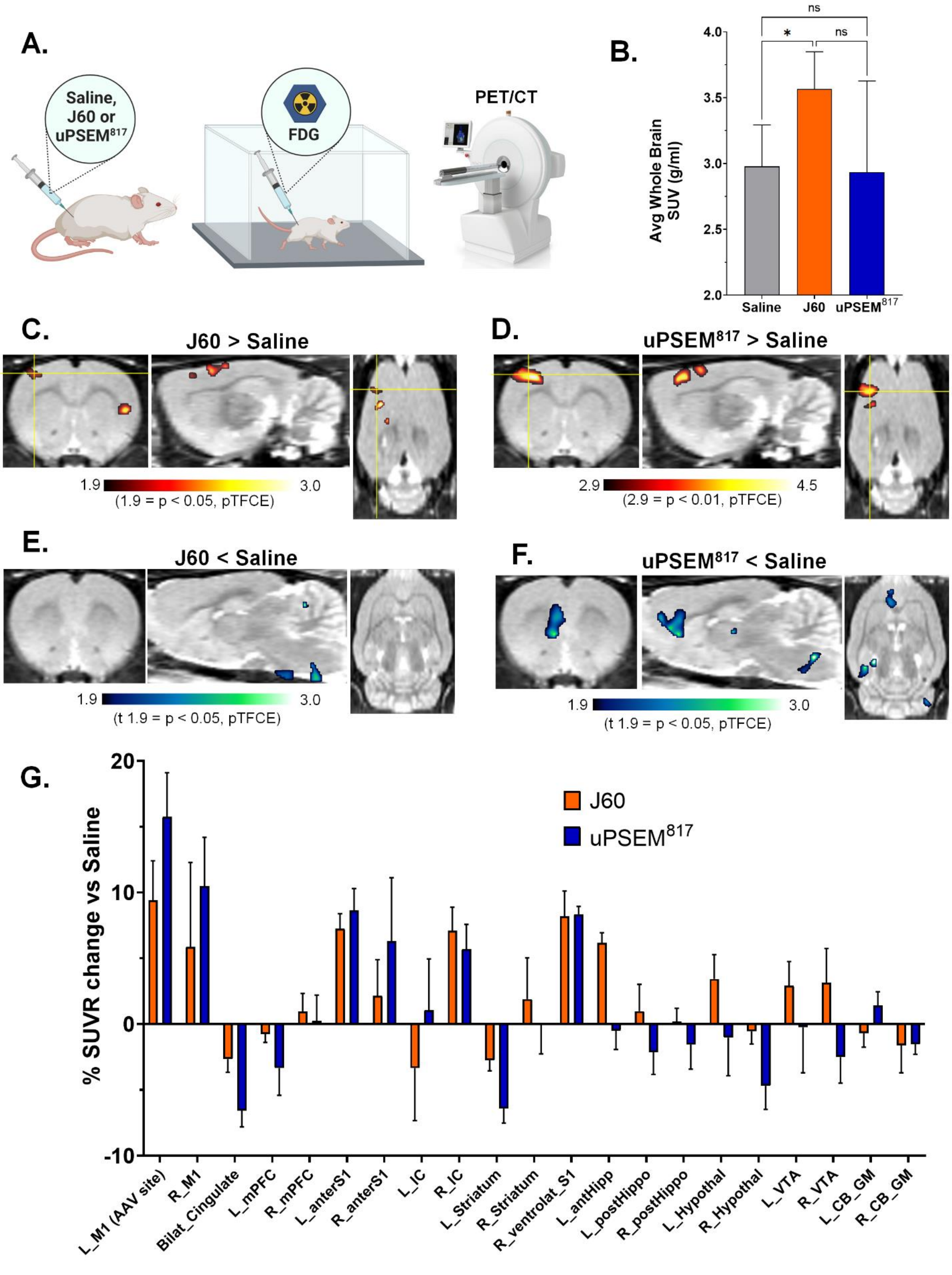

Figure 2. Measuring effects of hM3Dq and PSAM^4-GlyR on brain activity with FDG-PET. **A.** Schematic of experimental design: Rats pretreated with i.p. saline or 0.1 mg/kg J60 (hM3Dq agonist) or uPSEM817 (PSAM^4-GlyR agonist) 10-min before administration of FDG (~0.5mCi, bolus i.p.) for awake uptake in an open field chamber for 40-min. Rats were then anesthetized and PET/CT scans were performed to image FDG brain uptake. **B.** Average whole brain standard uptake value (SUV, g/ml) after treatment with saline, J60 or uPSEM817 (n = 7, 3 females and 4 males, left M1 AAV: n = 5, right M1 AAV: n = 2), * = $p < 0.05$. **C-D.** Brain areas showing significantly greater FDG uptake following treatment with J60 (**C**) or uPSEM^{817} (**D**) compared to within-subject saline scans (one-way ANOVA within-subject, n = 5, post-hoc $t > 1.86$ = $p < 0.05$, $t > 2.9$ = $p < 0.01$, pTFCE). Yellow crosshairs indicate XYZ plane and is centered in area of left M1 AAV injection site. **E-F.** Brain areas showing significantly lower FDG uptake following treatment with J60 (**E**) or uPSEM^{817} (**F**) compared to within-subject saline scans (one-way ANOVA, post-hoc $t > 1.86$: $p < 0.05$, pTFCE). **G.** VOI comparison of % SUVR$_{WB}$ change in FDG-PET scans with J60 or uPSEM^{817} vs. saline (VOIs derived from voxel-wise SPM12 analysis). Abbreviations: L_M1 (AAV site) = left motor cortex AAV site, R_M1 = right motor cortex (AAV site mirror VOI), Bilat_Cingulate = bilateral cingulate cortex, L_mPFC = left medial prefrontal cortex, R_mPFC = right medial prefrontal cortex, L_anterS1 = left anterior somatosensory cortex, R_anterS1 = right anterior somatosensory cortex, L_IC = left insular cortex, R_IC = right insular cortex, R_ventrolat_S1 = right ventrolateral somatosensory cortex, L_antHipp = left anterior hippocampus, L_postHippo = left posterior hippocampus, R_postHippo = right posterior hippocampus, L_Hypothal = left hypothalamus, R_Hypothal = right hypothalamus, L_VTA = left ventral tegmental area, R_VTA = right ventral tegmental area, L_CB_GM = left cerebellar grey matter, R_CB_GM = right cerebellar grey matter.

Figure 3. PSAM^4-GlyR and hM3Dq actuation produce distinct effects on locomotor behavior in rats

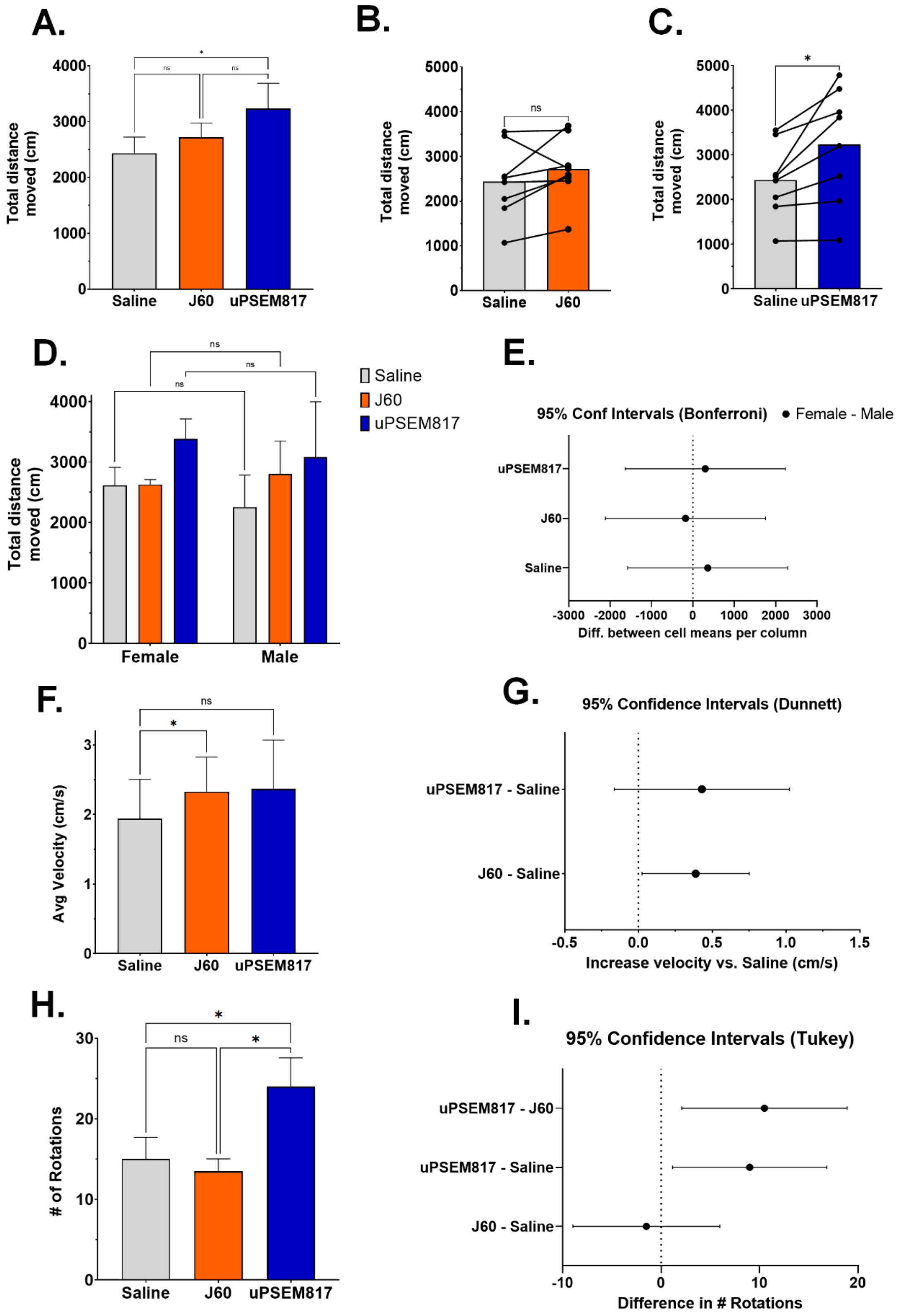

Figure 3. PSAM4-GlyR and hM3Dq actuation produce distinct effects on locomotor behavior in rats. A-C. Total distance moved following i.p. treatment with saline or 0.1mg/kg J60 (hM3Dq agonist) or uPSEM^{817} (PSAM^4-GlyR agonist) (one-way ANOVA within-subject, * = $p < 0.05$). **D.** Comparison of female vs. male distance travelled shows no significant effect of sex on total distance travelled and no significant interaction of sex with treatment effect (two-way ANOVA, n = 3 female and 4 male). **E.** Plot of 95% confidence intervals for female vs. male distance travelled by treatment (Bonferroni). **F.** Average velocity (cm/s) by treatment comparison (one-way ANOVA, within-subject, * = $p < 0.05$). **G.** Plot of 95% confidence intervals for average velocity by treatment (Dunnett). **H.** Comparison of # of rotations by treatment (one-way ANOVA within-subject, * = $p < 0.05$). **I.** Plot of 95% confidence intervals for total number of rotations by treatment (Tukey).

Figure 4. PET localization of hM3Dq and PSAM^4-GlyR in rat M1 with [^{18}F]J07 and [^{18}F]ASEM coincides with immunofluorescent labeling in post-mortem histology

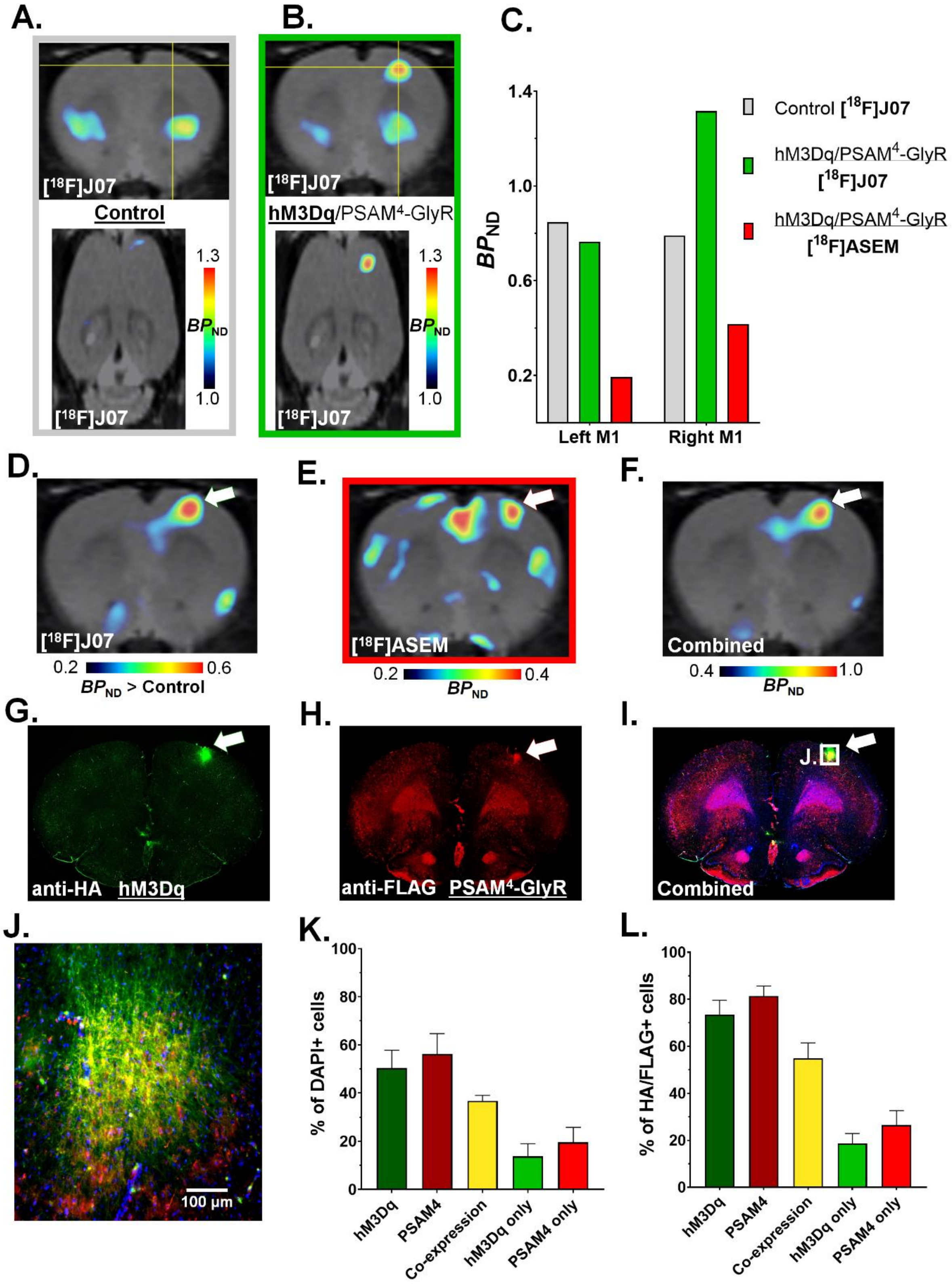

Figure 4. Imaging hM3Dq and PSAM^4-GlyR with [^{18}F]J07 and [^{18}F]ASEM in rats.

A. [^{18}F]J07 scan in control rat with no hM3Dq/PSAM^4-GlyR AAVs, yellow crosshairs indicate approximate injection site in AAV group. **B.** [^{18}F]J07 scan in rat 12 months after co-injection of hM3Dq/PSAM^4-GlyR AAVs in right M1, yellow crosshairs indicate approximate AAV injection site. **C.** Comparison of BP_{ND} in left and right M1 in control rat during [^{18}F]J07 scan (grey) and in a hM3Dq/PSAM^4-GlyR rat during [^{18}F]J07 scan (green) and [^{18}F]ASEM scan (red) (green and red bars indicate BP_{ND} from same hM3Dq/PSAM^4-GlyR rat). **D.** PET image showing areas with greater [^{18}F]J07 BP_{ND} in hM3Dq/PSAM^4-GlyR rat vs. control rat (image subtraction). White arrow indicates area of putative hM3Dq expression. **E.** PET image showing [^{18}F]ASEM BP_{ND} in same hM3Dq/PSAM^4-GlyR rat 10 months after co-injection of hM3Dq/PSAM^4-GlyR AAVs in right M1. White arrow indicates area of putative PSAM^4-GlyR expression. **F.** Combined PET image of [^{18}F]J07 and [^{18}F]ASEM BP_{ND} in hM3Dq/PSAM^4-GlyR rat (image sum). **G.** Immunofluorescent staining with anti-HA (green = hM3Dq), white arrow indicates area of hM3Dq expression in right M1 **H.** Immunofluorescent staining with anti-FLAG (red = PSAM^4-GlyR), white arrow indicates area of PSAM^4-GlyR expression in right M1. **I.** Combined immunofluorescent image with anti-HA (green = hM3Dq), anti-FLAG (red = PSAM^4-GlyR and DAPI (blue = nuclear counterstain), white arrow indicates area of hM3Dq and PSAM^4-GlyR co-expression in right M1 (white box indicates area of focus in **J.**). **J.** 20x image of combined immunofluorescent labeling of hM3Dq (green) and PSAM^4-GlyR (red) on cells (DAPI = blue) in right M1 (i.e., AAV injection site). **K.** Percentages of DAPI positive cells showing expression of hM3Dq and/or PSAM^4-GlyR near right M1 AAV site. **L.** Percentages of hM3Dq/PSAM^4-GlyR expression among cells positive for one or both.

Figure 5. Localizing hM3Dq and PSAM4-GlyR in squirrel monkeys with [^{18}F]J07 and [^{18}F]ASEM

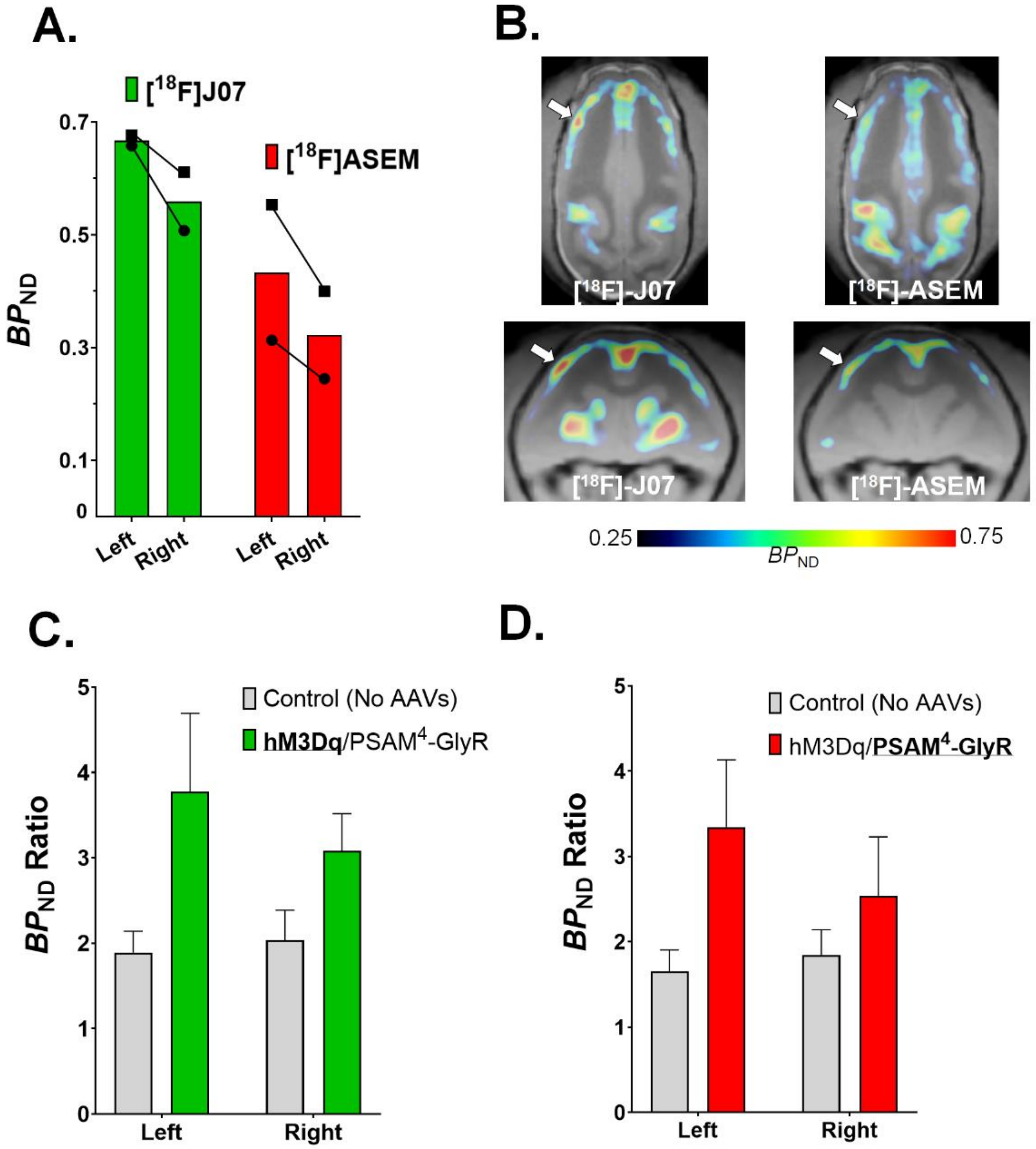

Figure 5. Localizing hM3Dq and PSAM4-GlyR in squirrel monkeys with [^{18}F]J07 and [^{18}F]ASEM. A. Average BP_{ND} of [^{18}F]J07 (green) and [^{18}F]ASEM (red) in "Left" (hM3Dq/PSAM^4-GlyR) and "Right" (ChRmERα) AAV sites 9-12 months following intracranial surgery (n = 2). Individual values are plotted for each monkey (squares = subject 1, circles = subject 2). **B.** PET image in horizontal plane showing BP_{ND} of [^{18}F]J07 (left) and [^{18}F]ASEM (right) in monkey post-AAV, white arrow indicates area of hM3Dq/PSAM^4-GlyR AAV injection. **C.** Average BP_{ND} Ratios (normalized to within-subject whole brain average) of [^{18}F]J07 in left and right AAV sites (or respective sites in non-AAV subjects) in monkeys pre-AAV (grey, n = 3) and post-AAV (green, n = 2). **D.** Average BP_{ND} Ratios of [^{18}F]ASEM in left and right AAV sites (or respective sites in non-AAV subjects) in monkeys pre-AAV (grey, n = 4) and post-AAV (green, n = 2).

Figure 6. **Measuring effects of hM3Dq and PSAM4-GlyR on brain activity with FDG-PET in squirrel monkeys (4-6 month post-AAV)**

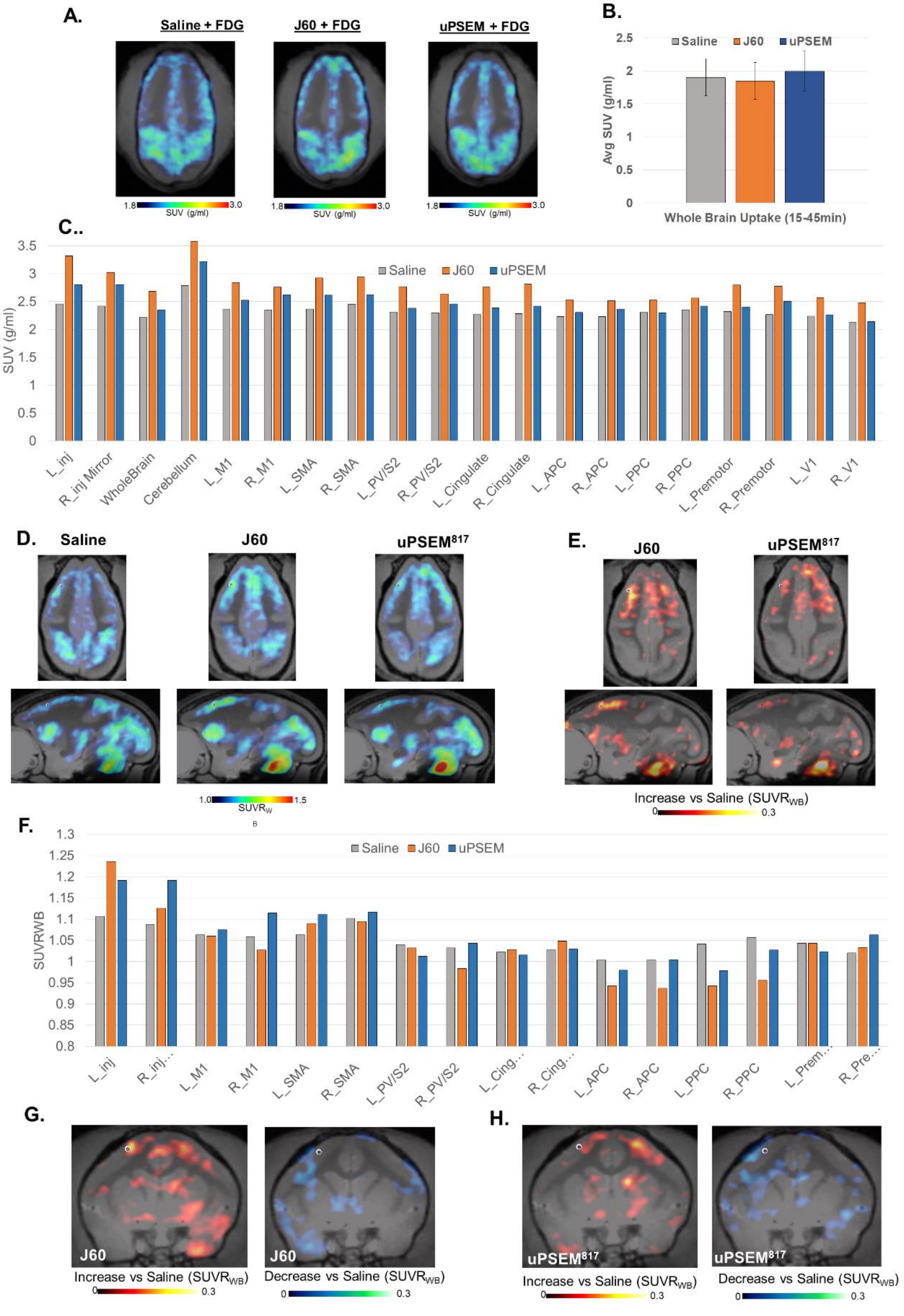

Figure 6. Measuring effects of hM3Dq and PSAM4-GlyR on brain activity with FDG-PET in squirrel monkeys (4-6 months post-AAV).

A. Horizontal plane PET image (overlayed on structural MRI) of avg FDG uptake in squirrel monkey (SUV g/ml) following pretreatment with saline, 0.1 mg/kg J60 or 0.1 mg/kg uPSEM^{817}. **B.** Average whole brain FDG uptake (SUV g/ml) comparison by treatment: saline vs. J60 vs. uPSEM^{817} (n = 2). **C.** Average FDG uptake (SUV g/ml) in regional VOIs of squirrel monkey following treatment with saline/J60/uPSEM^{817}. **D.** Horizontal plane PET image of average relative FDG brain uptake (SUV normalized to whole brain average = SUVR$_{WB}$), white dot indicates hM3Dq/PSAM^{4}-GlyR AAV injection site. **E.** Image showing areas with greater SUVR$_{WB}$ compared to within-subject saline scan (image subtraction) following treatment with J60 (left) or uPSEM^{817} (right). **F.** Average relative FDG uptake (SUVR$_{WB}$) in regional VOIs of squirrel monkey following treatment with saline/J60/uPSEM^{817}. **G-H.** Coronal image comparison of monkey brain areas with greater SUVR$_{WB}$ (left, red-yellow colors) or lower SUVR$_{WB}$ (right, blue-green colors) compared to within-subject saline scan following treatment with J60 (**G**) or uPSEM^{817} (**H**), white dot indicates co-injection site of hM3Dq/PSAM^{4}-GlyR AAVs.

3.7 Acknowledgements

This work was supported by the National Institute on Drug Abuse Intramural Research Program (ZIADA000069 and ZIADA000622). We thank NIDA-IRP vet staff (Dr. Ira Baum and Dr. Jazmyne Taylor and Phil White) for assistance in monkey experiments and Johns Hopkins Medicine Dept. of Radiology (Bob Dannals and Andrew Horti) for radiosynthesis of [^{18}F]ASEM and [^{18}F]J07.

Author Contributions

M.A.B. designed, performed, and analyzed all experiments/data. H.P.J. performed squirrel monkey surgeries and assisted in PET experiments. J.B. assisted in rodent and squirrel monkey PET experiments. M.L. assisted in rodent PET experiments. E.A.S. provided resources and supervision for the studies. C.W.B. designed squirrel monkey surgeries/experiments and provided resources and supervision for the studies. M.M. designed experiments and provided resources and supervision for the studies.

Declaration of Interest

MM has received research funding from AstraZeneca, Redpin Therapeutics, and Attune Neurosciences. All other co-authors report no conflicts of interest.

3.8 References

Alexander, G.M., Rogan, S.C., Abbas, A.I., Roth, BL, et al. 2009. Remote control of neuronal activity in transgenic mice expressing evolved G protein-coupled receptors. *Neuron* 63(1): 27-39 https://doi.org/10.1016/j.neuron.2009.06.014

Alloway, K. D., Smith, J. B., Beauchemin, K. J., & Olson, M. L. (2009). Bilateral projections from rat MI whisker cortex to the neostriatum, thalamus, and claustrum: forebrain circuits for modulating whisking behavior. *The Journal of Comparative Neurology*, 515(5), 548–564. https://doi.org/10.1002/cne.22073

Armbruster, B.N., Li, X., Pausch, M.H., et al., 2007. Evolving the lock to fit the key to create a family of G protein-coupled receptors potently activated by an inert ligand. *PNAS* 104 (12), 5163–5168. https://doi.org/10.1073/pnas.0700293104

Assaf, F., Schiller, Y., 2019. A chemogenetic approach for treating experimental Parkinson's disease. *Mov. Disord*. 34, 469–479. https://doi.org/10.1002/mds.27554

Boehm MA, Bonaventura J, Gomez J, Solis O, Stein EA, Bradberry CW, and Michaelides M. 2021. Translational PET imaging applications for brain circuit mapping and manipulation with transgenic tools. Pharmacology, Biochemistry and Behavior, 204: 173147. https://doi.org/10.1016/j.pbb.2021.173147

Bonaventura, J., Eldridge, M.A.G., Hu, F., et al., 2019. High-potency ligands for DREADD imaging and activation in rodents and monkeys. *Nat. Commun*. 10, 4627. https://doi.org/10.1038/s41467-019-12236-z

Burnett, C.J., Krashes, M.J., 2016. Resolving behavioral output via Chemogenetic designer receptors exclusively activated by designer drugs. *J. Neurosci*. 36 (36), 9268–9282. https://doi.org/10.1523/JNEUROSCI.1333-16.2016

Cicirata, F., Angaut, P., Cioni, M., Serapide, M. F., & Papale, A. (1986). Functional organization of thalamic projections to the motor cortex. An anatomical and electrophysiological study in the rat. *Neuroscience*, 19(1), 81–99. https://doi.org/10.1016/0306-4522(86)90007-2

Conklin, B.R., Hsiao, E.C., Claeysen, S., et al., 2008. Engineering GPCR signaling pathways with RASSLs. *Nat. Methods* 5 (8), 673–678. https://doi.org/10.1038/nmeth.1232

Curado, T.F., Pho, H., Freire, C., et al., 2020. DREADD approach to treatment of sleep disordered breathing. *Am J Respir Crit Care Med*. https://doi.org/10.1164/rccm.202002-0321OC

Fagundes-Pereyra, W. J., Teixeira, M. J., Reyns, N., Touzet, G., Dantas, S., Laureau, E., & Blond, S. (2010). Motor cortex electric stimulation for the treatment of neuropathic pain. *Arquivos de neuropsiquiatria*, 68(6), 923–929. https://doi.org/10.1590/s0004-282x2010000600018

Gantz, SC, Ortiz, MM, Belilos AJ and Moussawi, K. 2021. Excitation of medium spiny neurons by 'inhibitory' ultrapotent chemogenetics via shifts in chloride reversal potential. *eLife* 10:e64241. https://doi.org/10.7554/eLife.64241

Horti, A.G., Gao, Y., Kuwabara, H., et al., 2014. ^{18}FASEM, a radiolabeled antagonist for imaging the α7-nicotinic acetylcholine receptor with PET. *J. Nuclear Med*. 55 (4), 672–677. https://doi.org/10.2967/jnumed.113.132068

Hosp, J. A., & Luft, A. R. (2013). Dopaminergic meso-cortical projections to M1: role in motor learning and motor cortex plasticity. *Frontiers in neurology*, 4, 145. https://doi.org/10.3389/fneur.2013.00145

Hu, F., Morris, P.J., Bonaventura, J., et al., 2020. ^{18}F-labeled radiotracers for in vivo imaging of DREADD with positron emission tomography, *European Journal of Medicinal Chemistry* 113047. ISSN 0223-5234. https://doi.org/10.1016/j.ejmech.2020.113047

Jeong, M., Kim, Y., Kim, J., Ferrante, D. D., Mitra, P. P., Osten, P., & Kim, D. (2016). Comparative three-dimensional connectome map of motor cortical projections in the mouse brain. *Scientific Reports*, 6, 20072. https://doi.org/10.1038/srep20072

Kätzel, D., Nicholson, E., Schorge, S., et al., 2014. Chemical-genetic attenuation of focal neocortical seizures. *Nat. Commun.* 5, 3847. https://doi.org/10.1038/ncomms4847

Logan J, Fowler JS, Volkow ND, Wang GJ, Ding YS, Alexoff DL. (1996). Distribution volume ratios without blood sampling from graphical analysis of PET data. *J Cereb Blood Flow Metab*, 16(5):834-840.

Magnus, C.J., Lee, P.H., Atasoy, D., 2011. Chemical and genetic engineering of selective ion channel interactions. *Science* 333 (6047), 1292–1296. https://www.science.org/doi/10.1126/science.aav5282

Magnus, C.J., Lee, P.H., Bonaventura, J., et al. (2019). Ultrapotent chemogenetics for research and potential clinical applications. Science 364 (6436): eaav5282. https://doi.org/10.1126/science/aav5282

McGeorge, A. J., & Faull, R. L. (1989). The organization of the projection from the cerebral cortex to the striatum in the rat. *Neuroscience*, 29(3), 503–537. https://doi.org/10.1016/0306-4522(89)90128-0

Oka, H., & Jinnai, K. (1978). Common projection of the motor cortex to the caudate nucleus and the cerebellum. *Experimental brain research*, 31(1), 31–42. https://doi.org/10.1007/BF00235802

Pagano, R. L., Fonoff, E. T., Dale, C. S., Ballester, G., Teixeira, M. J., & Britto, L. (2012). Motor cortex stimulation inhibits thalamic sensory neurons and enhances activity of PAG neurons: possible pathways for antinociception. *Pain*, 153(12), 2359–2369. https://doi.org/10.1016/j.pain.2012.08.002

Pei, Y., Rogan, S.C., Yan, F., Roth, B.L., 2008. Engineered GPCRs as tools to modulate signal transduction. *Physiology* 23, 313–321. https://doi.org/10.1152/physiol.00025.2008

Roseboom PH, Mueller SAL, Oler JA, Fox AS, Riedel MK, Elam VR, Olsen ME, Gomez JL, Boehm MA, DiFilippo AH, Christian BT, Michaelides M, Kalin NH. (2021). Evidence in primates supporting the use of chemogenetics for the treatment of human refractory neuropsychiatric disorders. Molecular Therapy, 29(8): https://doi.org/10.1016/j.ymthe.2021.04.021

Roth, BL. 2016. DREADDs for neuroscientists. *Neuron* 89(4): 683-694 https://doi.org/10.1016/j.neuron.2016.01.040

Smith, K. S., Bucci, D. J., Luikart, B. W., & Mahler, S. V. (2016). DREADDS: Use and application in behavioral neuroscience. *Behavioral neuroscience*, 130(2), 137–155. https://doi.org/10.1037/bne0000135

Song, J., Patel, R. V., Sharif, M., Ashokan, A., & Michaelides, M. (2022). Chemogenetics as a neuromodulatory approach to treating neuropsychiatric diseases and disorders. *Molecular therapy: Journal of the American Society of Gene Therapy, 30(3), 990–1005.* https://doi.org/10.1016/j.ymthe.2021.11.019

Spisák T., Spisák Z., Zunhammer, M., Bingel, U., Smith, S., Nichols, T., Kinces, T. 2019. Probabilistic TFCE: a generalized combination of cluster size and voxel intensity to increase statistical power. *Neuroimage* 185: 12-26. https://doi.org/10.1016/j.neuroimage.2018.09.078

Sternson, S.M., Roth, B.L., 2014. Chemogenetic tools to interrogate brain functions. *Annu. Rev. Neurosci.* 37, 387–407. https://doi.org/10.1146/annurev-neuro-071013-014048

Thach W. T. (1987). Cerebellar inputs to motor cortex. *Ciba Foundation symposium*, 132, 201–220. https://doi.org/10.1002/9780470513545.ch13

Vardy, E., Robinson, J.E., Li, C., et al., 2015. A new DREADD facilitates the multiplexed chemogenetic interrogation of behavior. *Neuron* 86, 936–946. https://doi.org/10.1016/j.neuron.2015.03.065

Walker, M.C., Kullman, D.M., 2020. Optogenetic and chemogenetic therapies for epilepsy. *Neuropsychopharmacology* 168, 107751. https://doi.org/10.1016/j.neuropharm.2019.107751

Weir, G., et al., 2017. Using an engineered glutamate-gated chloride channel to silence sensory neurons and treat neuropathic pain at the source. *Brain* 140, 2570–2585. https://doi.org/10.1093/brain/awx201

Wess, J., Nakajima, K., Jain, S., 2013. Novel designer receptors to probe GPCR signaling and physiology. *Trends Pharamacol Sci*. 34 (7), 385–392. https://doi.org/10.1016/j.tips.2013.04.006

Zhu H and Roth BL (2014). Silencing synapses with DREADDs. *Neuron* 82(4): 723-725 https://doi.org/10.1016/j.neuron.2014.05.002

Chapter 4: Discussion and Future Directions

4.1 Summary of Optogenetic Experiments

4.1.1 ChRERα – the first PET-compatible opsin

Optogenetic technologies enable the manipulation of target neuronal populations and circuits with precise spatiotemporal control. This capability offers preclinical and therapeutic utility, but a major translational challenge is the need to monitor the location and function of opsins without invasive procedures. We propose a solution to this challenge using PET, a versatile translational molecular imaging technique that can be used to visualize transgenic constructs with compatible radiotracers (e.g., chemogenetic receptors).

To adapt this approach for optogenetics, we developed the first PET compatible opsin - ChRERα - by attaching the ERαLBD to the excitatory ChR2. As described in Chapter 2, in vitro validation experiments in HEK-293 cells show ChRERα retains the original ERα-LBD affinity for binding estradiol and fluoroestradiol (Ch. 2, Figure 1C-D) In addition, blue light stimulation (473 nm) of cells transfected with ChRERα elicited photocurrents indistinguishable from cells transfected with ChR2, thus ChRERα retains the functional properties of the original excitatory opsin in vitro (Ch. 2, Figure 1E-F).

To test whether ChRERα expression can be visualized with PET in vivo, we performed scans with the FDA approved radiotracer [^{18}F]-FES before and after intracranial injections of a ChRERα AAV (AAV$_{2/5}$-hSyn-ChR2-V5-ERαLBD) in cortical areas of rats and squirrel monkeys (Ch. 2, Figs 4 & 5; Appendix A, Figs S3 & S4). FES-PET scans in rats post-AAV (3-5 weeks following surgery) and monkeys (5-7 weeks following surgery) showed localized increases in FES-PET signal near the AAV injection site as well as in established cortical and subcortical projection areas. Interestingly, these localized increases were still observed in monkey FES-PET scans performed 1-1.5 years after the AAV injection. However, BP_{ND} near the AAV injection site decreased ~50% in a scan 1.5 years post-AAV compared to 7 weeks post-AAV in the same monkey suggesting a gradual loss of expression/cell turnover. This finding underscores the importance of quantitative longitudinal tracking of transgene expression as it’s likely to change over time. Immunofluorescence microscopy (with anti-ChR2 primary antibody) was used as post-mortem confirmation of ChRERα expression and coincided with brain areas showing localized increases in FES-PET signal post-AAV. In addition, immuno-EM revealed successful trafficking of ChRERα to the cell membrane with expression in multiple cellular compartments including dendrites, myelinated axons and terminals. This project demonstrates the application of the first transgenic opsin designed for compatibility with a PET radiotracer. Importantly, FES-PET was capable of localizing ChRERα in individual rodents and nonhuman primates, and repeated within subject scans revealed longitudinal changes in opsin expression. This approach holds utility for visualizing a variety of opsins (and other transgenic constructs) to advance the translational potential of optogenetics and related technologies. Therefore, we’ve begun to adapt the ERαLBD PET-reporter system for imaging other opsins with a focus on red-light sensitive opsins.

4.1.2 Adapting ERαLBD/FES PET-reporter system to image other opsins

We have begun efforts to adapt the ERαLBD/[^{18}F]FES PET-reporter technique to visualize the in vivo expression of other transgenic constructs (i.e., red-light sensitive opsins and chemogenetic receptors). We first focused on application in red-light sensitive opsins (i.e., ChRmine and JAWS) as these allow for deeper light penetration and may offer translational advantages for the development of skull-permeant light delivery systems (Chen et al., 2021). We attached the ERαLBD to ChRmine to make the PET-compatible red-light sensitive opsin “ChRmERα” (see Appendix B, Fig. B1A). We injected ChRmERα AAV (with Syn1 promoter) into the cortex of rats (n = 2) and squirrel monkeys (n = 2), and then performed [^{18}F]FES-PET to visualize in vivo ChRmERα expression near the AAV injection site (see Appendix Figure B1). We have also piloted this approach with the inhibitory red-light sensitive opsin JAWS (i.e., AAV-Syn1-JAWS-ERαLBD) and a PSAM^{4} chemogenetic receptor (i.e., AAV-Syn1-PSAM^{4}-GlyR-ERαLBD) in rats (see Appendix B, Fig. B2). These initial findings demonstrate the feasibility of adapting the ERαLBD/[^{18}F]FES PET-reporter technique to visualize a variety of transgenic constructs in vivo.

4.2 Summary of Chemogenetic Experiments

4.2.1 Developing a dual chemogenetics approach using DREADDs and PSAMs for bidirectional neuromodulation.

Chemogenetic technologies provide a valuable method for selective neuromodulation of targeted cell populations and have potential for translational and clinical applications. DREADDs and PSAMs are two types of chemogenetic systems (i.e., metabotropic and ionotropic, respectively) used to modulate brain activity, and recent studies have demonstrated the use of PET imaging to assess the efficacy of novel chemogenetic ligands and localize DREADD and PSAM expression. However, these emerging techniques have never been applied in combination and merit further development to enhance their translational capabilities. Therefore, we sought to develop a novel dual chemogenetics approach for bidirectional neuromodulation by inducing co-expression of the DREADD – hM3Dq, and PSAM – PSAM^{4}-GlyR, using a combination of AAVs (AAV$_{2/5}$-Syn1-HA-hM3Dq and AAV$_{2/5}$-Syn1-PSAM^{4}-GlyR-3XFLAG) injected into cortical areas of rats and squirrel monkeys.

As mentioned previously, the hM3Dq DREADD is considered to be “excitatory” given its action through Gq protein signaling pathways resulting in extracellular calcium release and an increase in neuronal firing. In contrast, PSAM^4-GlyR is a ligand gated chloride channel thought to have inhibitory effects on neuronal firing through hyperpolarization. However, the actual effects of these chemogenetic receptors on brain activity in vivo has shown to be more nuanced and can depend on levels of expression among different neuronal populations and interactions at circuit and network levels (Bonaventura et al., 2019; Gantz et al., 2021). To assess the effects of chemogenetic stimulation on brain activity, we performed FDG-PET following injection of saline or 0.1 mg/kg of the hM3Dq agonist – J60, or PSAM^4-GlyR agonist – uPSEM^{817} (Ch. 3, Figs 2 & 5; Appendix C, Figs C2 and C4). A voxel-wise analysis in rats showed administration of J60 and uPSEM^{817} (i.p.) both resulted in higher FDG uptake locally at the AAV injection site compared to within-subject saline scans ($n = 5$, $p < 0.05$, pTFCE). However, they produced different effects in brain regions outside of the AAV injection site. Activation of hM3Dq with J60 elicited higher uptake in some areas (e.g., striatum, hippocampus, S1) and lower in others (e.g., hypothalamus, colliculus), whereas activation of PSAM^4-GlyR with uPSEM^{817} resulted in lower uptake in multiple regions (e.g., S1, EC, IC, striatum, hippocampus, amygdala, thalamus) but did not produce higher uptake in any brain regions outside of the AAV injection area and ipsilateral S1 ($n = 5$, $p < 0.05$). Locomotor behavior during FDG uptake (awake, i.p.) showed chemogenetic-specific effects in total distance travelled, total number of rotations and average velocity (Ch 3., Figure 3).

A pair of rats (one with hM3Dq/PSAM^4-GlyR AAV in right M1 and one with control AAV) were also scanned with the DREADD radiotracer [^{18}F]J07 in attempt to localize hM3Dq expression (Ch. 3, Figure 4). The rat that received a hM3Dq/PSAM^4-GlyR showed a localized area of enhanced [^{18}F]J07 binding ($BP_{\mathrm{ND}} = 1.3$) in right M1 compared to the same region in the control animal ($BP_{\mathrm{ND}} = 0.8$). This difference was not observed in a contralateral VOI mirror in left M1 (BP_{ND} = 0.8 in both rats), indicating the higher [^{18}F]J07 binding was localized to the AAV injection site and therefore represents hM3Dq expression in right M1. Post-mortem immunohistochemistry confirmed brain expression of hM3Dq and PSAM^4-GlyR right M1, and 50-60% of cells that showed expression had co-expression of both receptors.

In squirrel monkey experiments, animals underwent FDG-PET (anesthetized, i.v.) following administration of saline or 0.1 mg/kg of J60 or uPSEM^{817} (i.v.) before and after co-injection of hM3Dq and PSAM^4-GlyR AAVs in left dlPFC or premotor cortex. In pre-AAV scans, no differences in FDG uptake were observed with J60 or uPSEM^{817} treatment compared to saline (within-subject, n = 4, $p < 0.05$), indicating these chemogenetics agonists do not produce off-target effects at the 0.1 mg/kg dose. Monkeys were also scanned with the radiotracers [^{18}F]J07 and [^{18}F]ASEM, which have been used to image DREADD and PSAM receptors, respectively. Pre-AAV brain uptake of [^{18}F]J07 peaked 10-20 min following injection (i.v.) and decreased to 30-40% of peak levels at 90 min (n = 3), whereas [^{18}F]ASEM brain uptake peaked 20-30 min following injection and remained at 60-70% of peak levels at 90 min (n = 4). Two monkeys were co-injected with AAV-hM3Dq and AAV-PSAM^4-GlyR in left cortex and a control AAV (non-chemogenetic) in right cortex. Post-AAV scans with [^{18}F]J07 and [^{18}F]ASEM showed greater binding near the left cortical AAV site in comparison to the control AAV site in the opposite hemisphere (see Chapter 2, Fig. 6 and Appendix D, Fig. D2). Post-mortem histology was used to verify expression of hM3Dq and PSAM^4-GlyR in rats and corresponded with brain regions showing high binding of both [^{18}F]J07 and [^{18}F]ASEM.

Together these experiments demonstrate hM3Dq and PSAM^4-GlyR can be co-expressed to elicit distinct effects on brain activity and behavior. However, PSAM^4-GlyR activation increased brain activity in the local targeted area as opposed to decreasing activity, and therefore this dual chemogenetic approach (combing hM3Dq and PSAM^4-GlyR) cannot be used for pure bidirectional modulation. In addition, [^{18}F]J07 and [^{18}F]ASEM were capable of localizing hM3Dq and PSAM^4-GlyR expression at the local AAV site, but the sensitivity of this approach is limited by endogenous binding of the radiotracers. Therefore, the development of radiotracers/PET-reporter systems with enhanced selectivity are needed to improve the capability of visualizing chemogenetic receptors in vivo.

4.3 Comparing [^{18}F]-FES, [^{18}F]J07, and [^{18}F]ASEM for imaging transgenic receptor/opsin expression

The findings from these optogenetic and chemogenetic PET-reporter experiments demonstrate the capability of [^{18}F]-FES, [^{18}F]J07, and [^{18}F]ASEM to localize the expression of ChRERα, hM3Dq and PSAM^4-GlyR in rats and squirrel monkeys. However, a direct comparison of these PET-reporters in monkeys without these constructs (i.e., pre-AAV) indicate the radiotracers exhibit different levels of endogenous binding in the brain (Appendix D, Figure D1.). Whole brain levels of [^{18}F]-FES peaked at 2-5 min following injection (i.v.) and dropped to less than 10% of peak levels by 60 min and the greatest binding was observed in the pituitary. In contrast, brain levels of [^{18}F]J07 peaked 10-20 min following injection and remained at 30-40% of peak levels at 90 min (n = 3), whereas [^{18}F]ASEM brain uptake peaked 20-30 min following injection and remained at 60-70% of peak levels at 90 min (n = 4). These findings show [^{18}F]-FES has much lower endogenous brain binding than [^{18}F]J07 or [^{18}F]ASEM (especially in cortical areas) and therefore provides S:N advantages for localizing transgene expression in the brain.

The two squirrel monkeys that received a co-injection of hM3Dq and PSAM^4-GlyR AAVs also received an injection of AAV-ChRmERα in the opposite brain hemisphere (see Appendix B). This allowed us to confirm the specificity of the three types of PET-reporters and directly compare their performance in localizing expression of their respective receptor/opsin targets (i.e., [^{18}F]J07 for hM3Dq, [^{18}F]ASEM for PSAM^{4}-GlyR, and [^{18}F]-FES for ChRmERα). Binding of [^{18}F]J07 at the left cortical AAV injection site was slightly greater than [^{18}F]ASEM in post-AAV scans. The two radiotracers showed different distributions of endogenous binding that added noise to the signal, but both demonstrated an ability to confirm hM3Dq/ PSAM^{4}-GlyR expression in comparison to control/within-subject pre-AAV scans. In comparison, FES-PET localization of ChRmERα in the opposite hemisphere showed a much cleaner signal that was specific to the cortical AAV injection site. This is consistent with the lower levels of endogenous brain binding observed in pre-AAV scans with [^{18}F]-FES compared to [^{18}F]J07 and [^{18}F]ASEM. Overall, these findings suggest using [^{18}F]-FES/ ERαLBD as a PET-reporter system may offer significant S:N advantages in the brain compared to the current reporters for localizing expression of chemogenetic receptors.

4.4 Applications and Significance

4.4.1 Characterizing structural/functional connectivity relationships

This body of work demonstrates the utility of combing chemogenetics and optogenetics with multi-modal imaging (i.e., FDG-PET, fMRI, and selective PET-reporters) for interrogating structural and functional brain connectivity patterns. Most studies investigating neuroanatomical brain connections with biological tracers rely on performing post-mortem histology measures, but PET-reporters capable of localizing transgene expression allow visualization of anatomical projections and structural brain connectivity in living subjects. When PET-reporters are combined with transgenic neuromodulation tools such as chemogenetics and optogenetics, it enables controlled manipulation of specific brain networks whose functional effects can then be visualized and interpreted through whole-brain imaging methods such as FDG-PET and fMRI.

When used in combination, these tools offer synergistic advantages that provide great utility for understanding the brain and developing translational applications. We show examples of this in rodents and NHPs by corresponding the expression patterns identified through PET-reporters (i.e., [^{18}F]-FES/ ERαLBD and [^{18}F]J07/hM3Dq) with functional brain measures such as FDG-PET and fMRI. For example, in rat ChRERα experiments we observed overlap of enhanced [^{18}F]-FES (expression) and FDG (brain activity) signal in brain regions downstream from the PrL/ACd stimulation site including ipsilateral striatum and mediodorsal thalamus. These findings are consistent with the known structural/functional connectivity between PrL/ACd and these brain regions (Vertes, 2003). Additionally, in rat dual chemogenetic FDG-PET experiments, we used VOI-based correlation matrices to explore functional relationships between brain areas in conditions of awake resting state (i.e., saline pretreatment) and during activation of hM3Dq or PSAM^{4}-GlyR with J60 or uPSEM^{817}, respectively (see Appendix C, Fig. C1).

In squirrel monkeys injected with AAV-ChRERα in the hand/forearm area left M1, we identified ChRERα expression in ipsilateral PPC with FES-PET, suggesting a structural circuit between this area and left M1. When followed up with rsfMRI analysis on an independent group of monkeys, a seed placed at the relative left M1 site showed substantial positive functional connectivity with ipsilateral PPC (Ch. 2, Figure 7.). This functional connectivity pattern largely overlapped with the FES-PET signal in ChRERα animals, therefore providing multi-model imaging evidence of structural and functional connectivity between these brain areas. This corroborates evidence of the PPC-M1 circuit has been consistently observed among primates (Kaas et al., 2020; Zarzecki et al., 1978) and is involved in organized complex movements (i.e., reaching/grasping)(Gharbawie et al., 2011). M1 is also known to have many neuroanatomical connections (i.e., afferent and efferent projections) with subcortical regions (e.g., striatum, thalamus, cerebellum) (Kelly, 2003; Tokuno and Tanji, 1993, Thach et al., 1987), and therefore ongoing work is being performed to assess the potential overlap between localized FES-PET signal and IHC-confirmed expression in brain areas such as motor-thalamic projection sites.

4.4.2 Advancing optogenetic/chemogenetic capabilities for NHP research

The need to confirm expression of transgenic receptors and opsins presents a bottleneck for optogenetic and chemogenetic studies in NHPs where animal longevity is highly valued making histological confirmation more difficult to obtain (Bliss-Moreau et al., 2022; Tremblay et al., 2020). To address this challenge, there has been an interest in the field to develop PET-reporters for imaging transgene expression, with recent success in imaging chemogenetic receptors (Bonaventura et al., 2019, Magnus et al., 2019; Nagai et al., 2020). We’ve expanded on this progress and improved the technology by making a PET-report system that is both more selective for use in the brain and is adaptable to imaging other transgenes, making it much more versatile and scalable. The ERαLBD/[^{18}F]FES PET-reporter approach can be adapted to image a variety of transgenic constructs which should facilitate the development of refined viral vectors and chemogenetic/optogenetic applications in NHPs. To demonstrate this point of versatility, we've already successfully imaged a red-light sensitive opsin paired with ERαLBD (i.e., ChRmERα) in the cortex of squirrel monkeys. We've also piloted imaging two red-light sensitive opsins (i.e., ChRmERα and JAWS-ERα) and a chemogenetic receptor (i.e., PSAM^4-ERα) in rats (see Appendix B).

4.4.3 Translational potential - imaging gene therapy technologies

Not only is there a need to image transgenes in preclinical research, but clinical applications of gene therapies could benefit from the translational PET imaging approaches we've demonstrated because they offer a mode for relatively noninvasive longitudinal monitoring of gene therapy location/function in the body and brain. Gene therapies are becoming increasingly capable for treating a variety of conditions with promising clinical trials underway for vision restoration, muscular spinal atrophy, and cancer treatment (Aiyegbusi et al., 2020; Naveen et al., 2021; Sahel et al., 2021). There is also growing interest in developing chemogenetic and optogenetic treatments for disorders including epilepsy, neuropathic pain, Parkinson's disease, sleep apnea/insomnia and motor disfunction related to ischemic stroke (Assaf et al., 2019; Conti et al., 2020; Curado et al., 2020; Korczeniewska et al., 2022; Venner et al., 2019; Walker and Kullmann, 2020). The adaption of our PET imaging techniques could facilitate the clinical implementation of these treatments by allowing clinicians to track the location, quantity and function of transgenic tools.

For example, an inhibitory DREADD (i.e., hM4Di) could be used in the treatment of focal epilepsy if it was transduced in targeted neurons of the pathogenically hyperactive brain region. Drug treatment with a low dose DREADD agonist such as J60 would theoretically reduce activity in the targeted brain cells to prevent seizure while unaffecting endogenous receptors, therefore limiting unwanted off-target effects on brain activity. Similarly, a chemogenetic treatment for neuropathic pain could be achieved by using an inhibitory DREADD targeted to the specific cells (i.e., trigeminal nerve cells) involved in a patient's condition. A drug treatment would then only affect cells expressing the chemogenetic receptor, so off-target drug effects would greatly be minimized if expression were successfully targeted to the specific cells involved in the sensory nerve signaling of the patient's pain. The PET-reporter [^{18}F]J07 could be used by clinicians to confirm the location of hM4Di expression and longitudinally track the location/density of receptors in the targeted brain area. FDG-PET and/or fMRI could also be used to quantify the specific chemogenetic effects on brain activity and adjust dosing.

Alternatively, the ERαLBD/[^{18}F]FES PET-reporter system we demonstrated could be used to facilitate therapeutic applications of optogenetics. For example, a closed-looped optogenetic system could be used to detect potential seizure onset in epilepsy patients and prevent seizures from occurring using an inhibitory opsin. A red-light sensitive inhibitory opsin (i.e., JAWS) may even be compatible with a skull permeant light-device, and a ERaLBD paired version (i.e., JAWS-ERα) could be used to confirm the right target location and allow tracking of the inhibitory opsin location/density over time. Similarly, excitatory ERaLBD paired opsins (i.e., ChRERα) could be clinically useful for various purposes such as facilitating motor function recovery following ischemic stroke (Conti et al., 2022) as these applications would benefit from the ability to accurately visualize opsin expression in the target region over time.

4.5 Limitations and Future Directions

4.5.1 Refining transgene delivery systems

Even with noninvasive localization, there's still the challenge of transgene delivery which is predominately performed through intracranial surgery in preclinical neuroscience. There is a great interest in refining genetic targeting and delivery methods, thus the PET imaging approaches we demonstrated could offer a useful mode for testing the effectiveness of novel AAV transgene delivery strategies. For example, efforts are underway to develop viral vectors that can pass through the blood-brain barrier to enable a less invasive (i.e., no intracranial surgery required) transgene delivery system (i.e., viral delivery to the brain via intravenous injection) AAV capsid variants such as AAV-PHPs have been demonstrated to facilitate noninvasive, efficient, and trackable targeted gene delivery in rodent models (Challis et al., 2019; Seo et al., 2020). However, the efficacy of this technology has been shown to be strain-dependent in rodents and largely ineffective in NHPs, underscoring the need for further development in this area (Huang et al., 2019; Matsuzaki et al., 2018). Our FES-PET imaging approach (i.e., adding ERαLBD to transgenic proteins such as with ChRERα) could facilitate the refinement of transgene delivery technologies by providing a reliable mode for testing the efficacy of novel methods for inducing transgene expression in living subjects. In addition, this imaging approach enables the ability to characterize the longevity of transgenic constructs in subjects over time (i.e., using repeated PET scans) to better understand and refine their application. The utility PET offers can provide a crucial function to advance these technologies into translational applications for investigating the nervous system and treating disease.

4.5.2 Strategies for improving sensitivity and specificity

The sensitivity and specificity of transgene detection/visualization is limited by the extent of endogenous binding that a PET-reporter exhibits in the targe tissue (e.g., density of neurotransmitter receptors). Within-subject baseline scans (i.e., pre-AAV surgery) can be used for comparison to help better decipher endogenous background noise from the specific signal of transgene expression (see Appendix D, Fig. D3). Additionally, a within-subject comparison of post-AAV scans with and without pretreatment with a highly selective nonradioactive ligand could improve interpretation of signal specificity (i.e., a “blocking” or competitive displacement scan). For example, pretreatment with selective chemogenetic compounds has been used to demonstrate the specificity of PET-reporters for DREADDs (i.e., J60 and [^{18}F]J07; Bonaventura et al., 2019) and PSAMs (i.e., uPSEM^{792} and [^{18}F]ASEM; Magnus et al., 2019). With respect to imaging ERαLBD constructs (e.g., ChRERα) with [^{18}F]FES, the specificity of S:N could potentially be improved by pretreatment with nonradioactive estradiol an hour or two before scanning in attempt to promote the internalization of endogenous ERs (thereby reducing background signal noise). However, the pharmacokinetics of this approach would need to be optimized to prevent cold estradiol from reducing specific signal (i.e., cold estradiol competition with [^{18}F]FES to bind the transgenic ERαLBD). In addition, potential changes in a subject’s endogenous ER levels over time (e.g., sexual development/aging, estrous cycles in females) could present challenges to longitudinally quantifying the amount of ERαLBD. Such considerations merit further investigation to expand the utility of FES-PET for imaging transgene expression.

4.6 Conclusions

This body of work demonstrates the development and application of a variety of translational PET imaging techniques leveraged in combination with transgenic neuromodulation tools (i.e., chemogenetics and optogenetics) to interrogate structural and functional brain connectivity in rodents and NHPs. Most importantly, it offers substantial contributions to advance the translational applications of chemogenetics and optogenetics by enabling in vivo localization of transgenic constructs (i.e., chemogenetic receptors and opsins) to confirm expression and visualize distribution throughout the brain. We've developed a universal PET-reporter system (i.e., ERαLBD/[^{18}F]FES) that can be applied to a variety of transgenic constructs, and this will greatly facilitate preclinical research in NHPs as well as open the door for developing clinical gene therapy applications.

4.7 References

Aiyegbusi, O.L., Macpherson, K., Elston, L. et al. 2020. Patient and public perspectives on cell and gene therapies: a systematic review. *Nat Commun* 11, 6265https://doi.org/10.1038/s41467-020-20096-1

Bliss-Moreau, E, Costa, D.V., Baxter, M.G. 2022. A pragmatic reevaluation of the efficacy of nonhuman primate optogenetics for psychiatry, *Oxford Open Neuroscience*, Volume 1, 2022, kvac006, https://doi.org/10.1093/oons/kvac006

Bonaventura, J., Eldridge, M.A.G., Hu, F., et al., 2019. High-potency ligands for DREADD imaging and activation in rodents and monkeys. *Nat. Commun*. 10, 4627. https://doi.org/10.1038/s41467-019-12236-z

Chen, R., Gore, F., Nguyen, Q.A., et al., (2020). Deep brain optogenetics without intracranial surgery. *Nat. Biotechnol*. https://doi.org/10.1038/s41587-020-0679-9

Gantz, SC, Ortiz, MM, Belilos AJ and Moussawi, K. 2021. Excitation of medium spiny neurons by 'inhibitory' ultrapotent chemogenetics via shifts in chloride reversal potential. *eLife* 10:e64241. https://doi.org/10.7554/eLife.64241

Gharbawie, O.A., Stepniewska, I., Kaas, J.K., (2011). Cortical connections of functional zones in posterior parietal cortex and frontal cortex motor regions in new world monkeys. *Cerebral Cortex*, 21: 1981-2002. https://doi.org/10.1093/cercor/bhq260

Huang Q, Chan KY, Tobey IG, et al. (2019). Delivering genes across the blood-brain barrier: LY6A, a novel cellular receptor for AAV-PHP.B capsids. *PLoS One*, 14(11): e0225206. https://doi.org/10.1371/journal.pone.0225206

Kaas, J.H., Qi, H.K., and Stepniewska, I. (2020) Evolution of Parietal-Frontal Networks in Primates. *Evolutionary Neuroscience*, ch 27: 657-667. https://doi.org/10.1016/B978-0-12-820584-6.00027-1

Kelly, R. M., & Strick, P. L. (2003). Cerebellar loops with motor cortex and prefrontal cortex of a nonhuman primate. *The Journal of Neuroscience* : the official journal of the Society for Neuroscience, 23(23), 8432–8444. https://doi.org/10.1523/JNEUROSCI.23-23-08432.2003

Magnus, C.J., Lee, P.H., Bonaventura, J., et al. (2019). Ultrapotent chemogenetics for research and potential clinical applications. Science 364 (6436): eaav5282. https://www.science.org/doi/10.1126/science.aav5282

Matsuzaki, Y., Konno, A., Mochizuki, R., et al., 2018. (2018). Intravenous administration of the adeno-associated virus-PHP.B capsid fails to upregulate transduction efficiency in the marmoset brain. *Neurosci. Lett.* 665, 182–188. https://doi.org/10.1016/j.neulet.2017.11.049

Nagai, Y., Miyakawa, N., Takuwa, H., et al., 2020. Deschloroclozapine, a potent and selective chemogenetic actuator enables rapid neuronal and behavioral modulations in mice and monkeys. *Nat. Neurosci*. 23, 1157–1167. https://doi.org/10.1038/s41593-020-0661-3

Naveed, A., Calderon, H. 2021. Onasemnogene Abeparvovec (AVXS-101) for the Treatment of Spinal Muscular Atrophy. *The Journal of Pediatric Pharmacology and Therapeutics,* 26 (5): 437–444. https://doi.org/10.5863/1551-6776-26.5.437

Sahel JA, Boulanger-Scemama E, Pagot C, Arleo A, Galluppi F, Martel JN, Esposti SD, Delaux A, de Saint Aubert JB, de Montleau C, Gutman E, Audo I, Duebel J, Picaud S, Dalkara D, Blouin L, Taiel M, Roska B. (2021). Partial recovery of visual function in a blind patient after optogenetic therapy. *Nat Med*. 2021 Jul;27(7):1223-1229. Epub 2021 May 24. PMID: 34031601. https://doi.org/10.1038/s41591-021-01351-4.

Tokuno, H., & Tanji, J. (1993). Input organization of distal and proximal forelimb areas in the monkey primary motor cortex: a retrograde double labeling study. *The Journal of Comparative Neurology*, 333(2), 199–209. https://doi.org/10.1002/cne.903330206

Tremblay, S., Acker, L., Afraz, A., et al. (2020). An open resource for non-human primate optogenetics. Neuron 108: 1075-1090. https://doi.org/10.1016/j.neuron.2020.09.027

Zarzecki, P., Strick, P. L., & Asanuma, H. (1978). Input to primate motor cortex from posterior parietal cortex (area 5). II. Identification by antidromic activation. *Brain research*, 157(2), 331–335. https://doi.org/10.1016/0006-8993(78)90036-7

Appendices

Appendix A. Supplementary Information for Chapter 2…………………………….....128

Appendix B. Applying the ERαLBD PET-reporter to image other opsins……..….133

Appendix C. Supplementary Information for Chapter 3……………………………..135

Appendix C. Supplementary Information for Chapter 4……………………………..141

Appendix A. Supplemental Figures for Chapter 2

Figure A1. Anti-ChR2 IHC and immuno-EM confirm ChRERα expression in the right PrL/ACd AAV site and in downstream projection areas in rats, related to Figure 2.

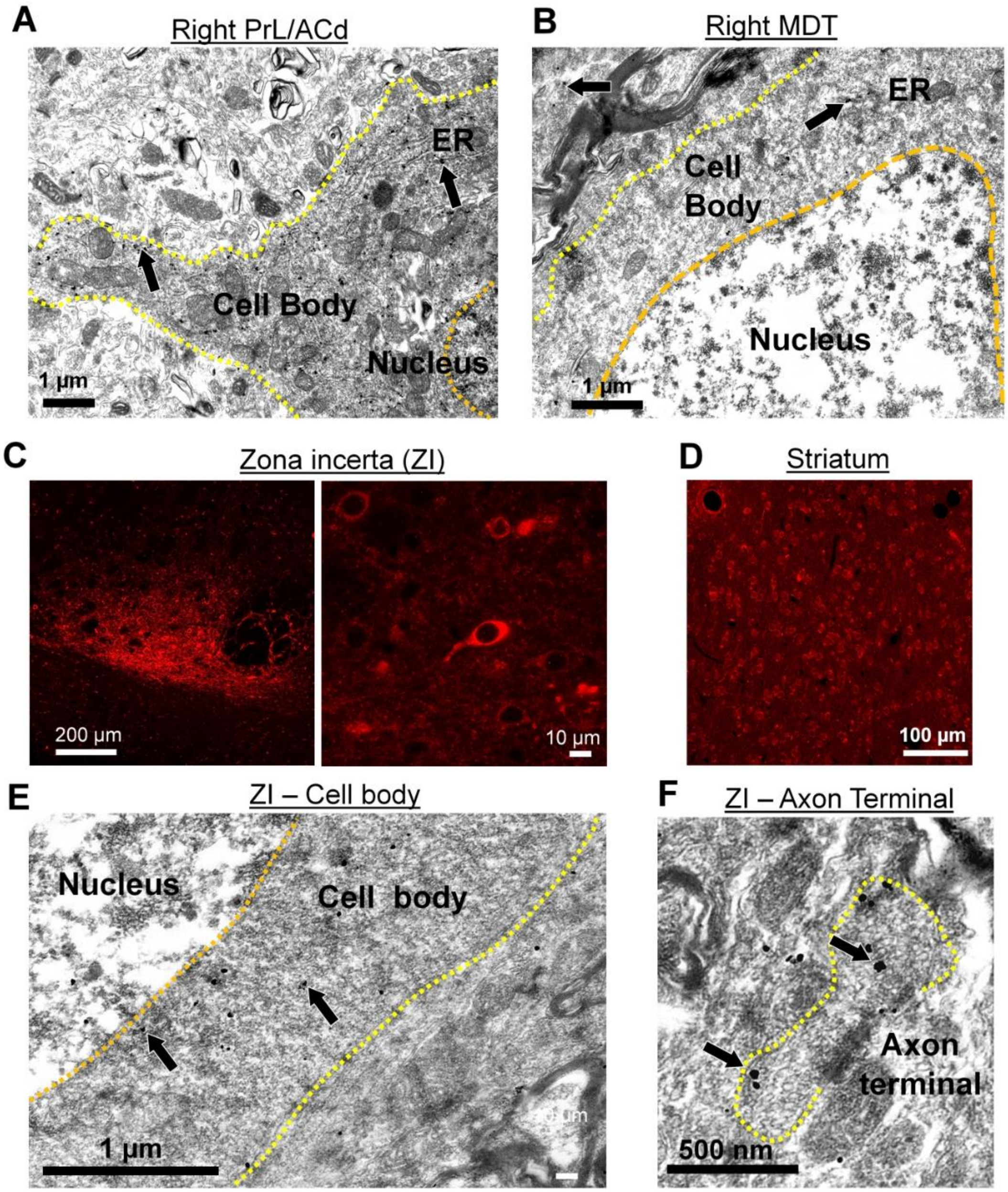

(**A**) Immuno-EM image showing anti-ChR2 immunogold labeling of ChRERα in right PrL/ACd cells along the membrane and in the ER. (**B**) Immuno-EM images in the MDT showing anti-ChR2 immunogold labeling of ChRERα in cells along the membrane and in the ER. (**C**) IHC images showing anti-ChR2 labelling of ChRERα expressing cells in the right zona incerta (ZI). (**D**) IHC images showing anti-ChR2 labelling of ChRERα expressing cells in the striatum. (**E**-**F**) Immuno-EM images showing anti-ChR2 immunogold labeling of ChRERα in the cell body (**E**) and an axon terminal (**F**) of the right ZI.

Figure A2. Effects of light stimulation on brain activity in ChRERα vs. Control Rats using FDG-PET, related to Figure 3.

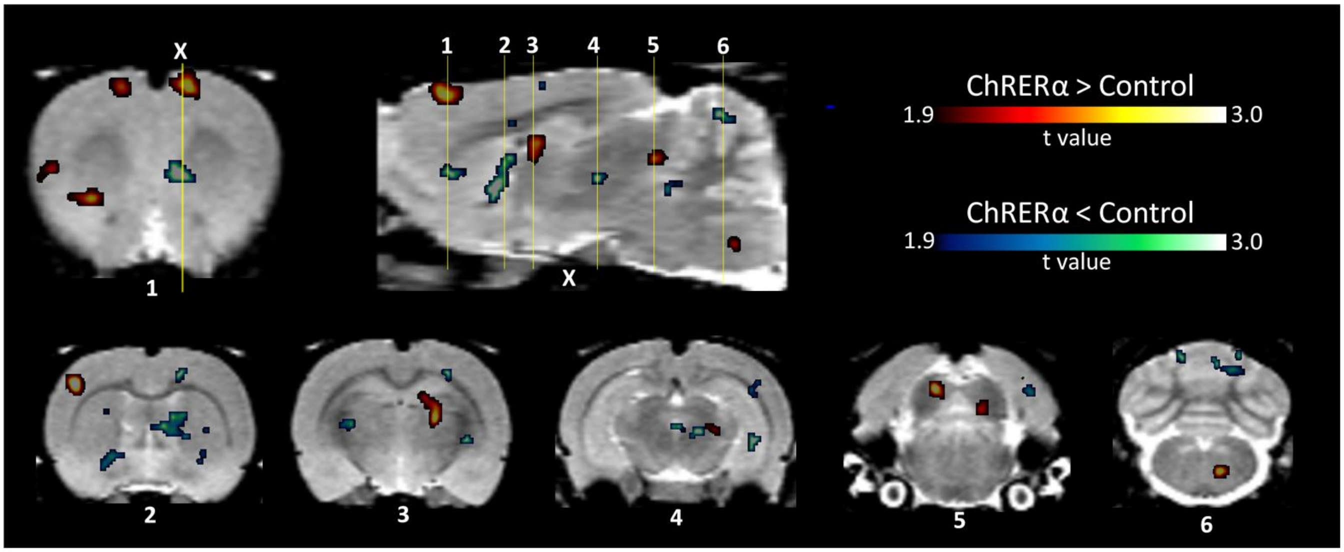

Figure A2. Effects of light stimulation on brain activity in ChRERα vs. Control Rats using FDG-PET, related to Figure 3. FDG-PET reveals brain areas showing light-induced activation and inhibition ($p < 0.01$, $t = 3.0$). Numbers 1-6 label the coronal sections indicated by yellow lines shown in the sagittal slice (X).

Figure A3. Visualizing ChRERα in rats with [18F]FES-PET (SUV and SUVR), related to Figure 4.

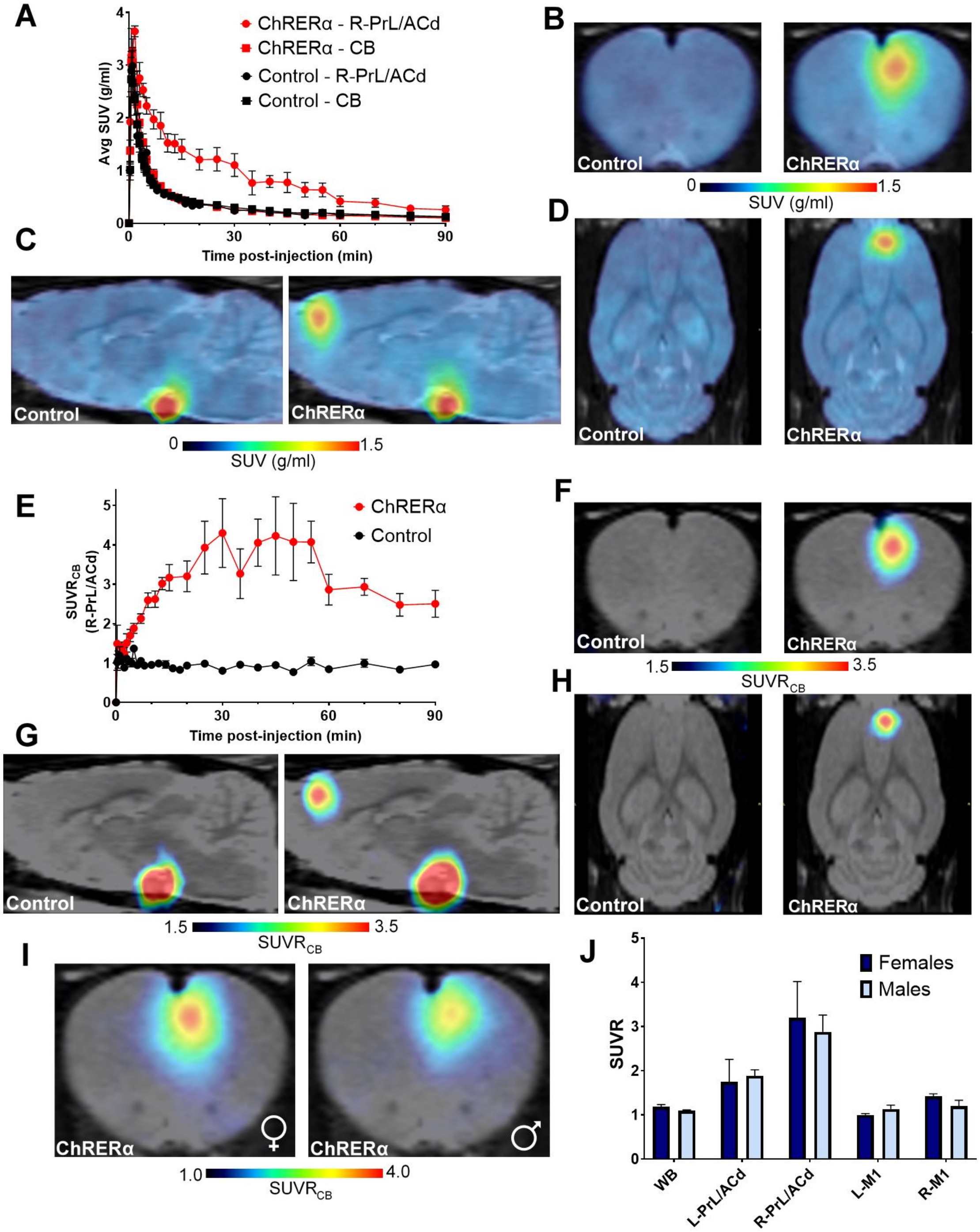

(**A**) Time activity curves of average SUV (g/ml) in right PrL/ACd and cerebellum (CB) in control rats (black, n = 5) and ChRERα rats 3-5 weeks post AAV (red, n = 6). (**B-D**) Average SUV (g/ml) 20-50min following injection with [^{18}F]FES. (**E**) Time activity curves of average SUVR$_{CB}$ (CB ref) in control rats (black, n = 5) ChRERα rats 3-5 weeks post AAV (red, n = 6). (**F-H**) Average SUVR$_{CB}$ (20-50min) in control (n=5) and ChRERα rats (n=6). (**I-J**) Comparison of SUVR$_{CB}$ in female (n=3) and male (n=3) ChRERα rats.

Figure A4. Visualizing ChRERα in squirrel monkeys with $[^{18}F]$FES-PET, related to Figure 5.

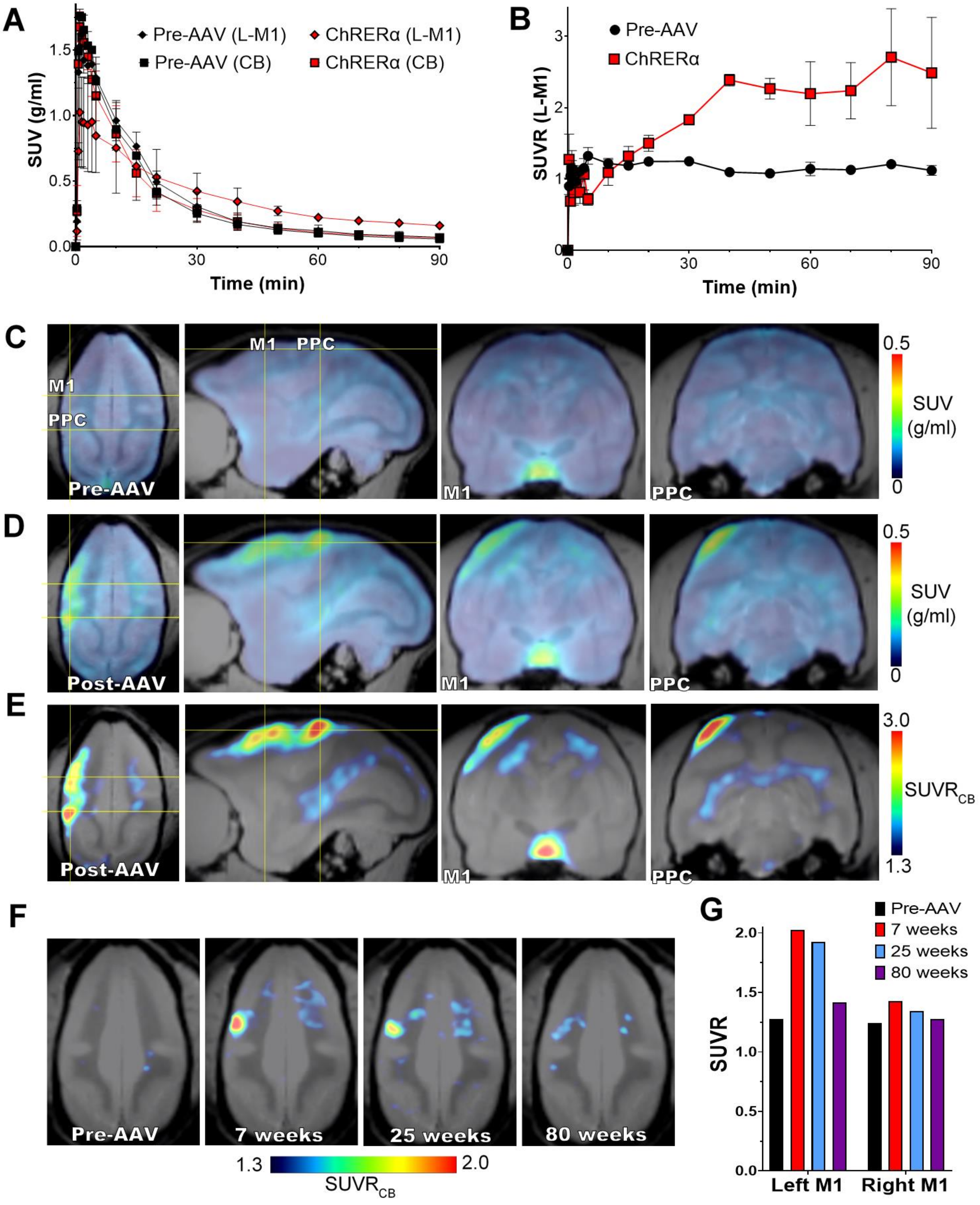

Figure A4. Visualizing ChRERα in squirrel monkeys with [^{18}F]FES-PET, related to Figure 5. (**A**) Pre-AAV (black) and 5-7 weeks post AAV-ChRERα (red) time activity curves of average SUV (g/ml) in left M1 (L-M1) and cerebellum (CB) (n = 2). (**B**) Pre-AAV (black) and 5-7 weeks post AAV-ChRERα (red) time activity curves of average SUVR (CB ref) in left M1 (L-M1) (n = 2). (**C**-**D**) Average SUV (g/ml) 30-60min following injection with [^{18}F]FES in a squirrel monkey pre-AAV (row **C**) and at 5 weeks post AAV-ChRERα (row **D**). (**E**) Average SUVR (CB ref) 30-60min following injection with [^{18}F]FES at 5 weeks post AAV-ChRERα. (**F**-**G**) Longitudinal comparisons of average SUVR (CB ref, 30-60min) in a second monkey.

Figure A5: Anti-ChR2 IHC and immuno-EM confirm ChRERα expression in contralateral M1 in squirrel monkey, related to Figure 6.

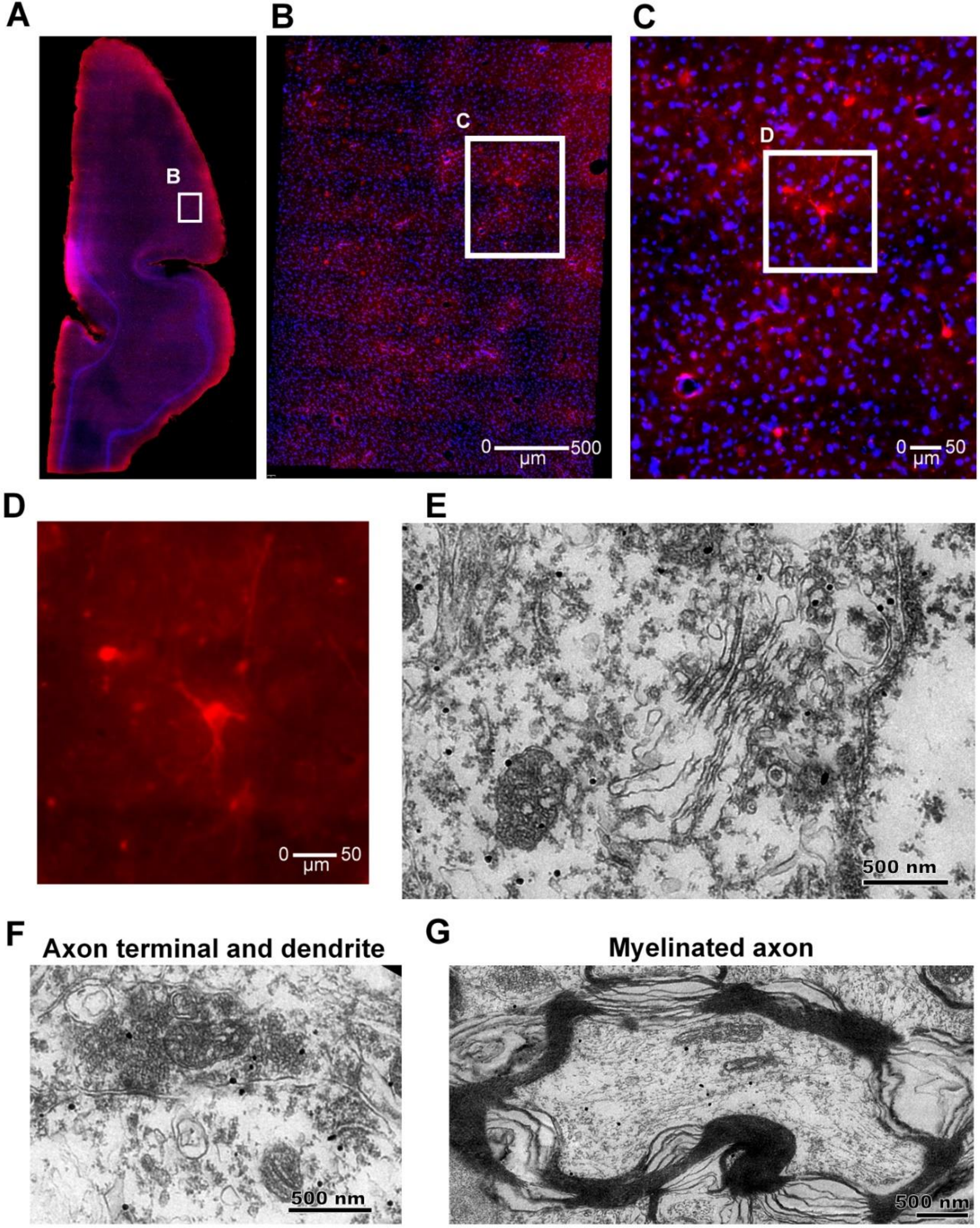

(**A**-**D**) IHC of a right hemisphere brain slice reveals ChRERα expression in right M1 (red = anti-ChR2, blue = DAPI), white rectangle in **A** = location of higher mag image shown in **B**, white rectangle in **B** = location of higher mag image shown in **C**, white rectangle in **C** = location of higher mag image shown in **D**. (**E**-**G**) Anti-ChR2 immuno-EM reveals subcellular localization of ChRERα expression in right M1 (**E**) cell body, axonal terminal and dendrite (**F**), and myelinated axon (**G**).

Appendix B. Adapting the ERαLBD/[^{18}F]FES PET-reporter system to image other transgenic constructs

Figure B1. Attaching ERαLBD to image red-light sensitive opsins (i.e., ChRmine)

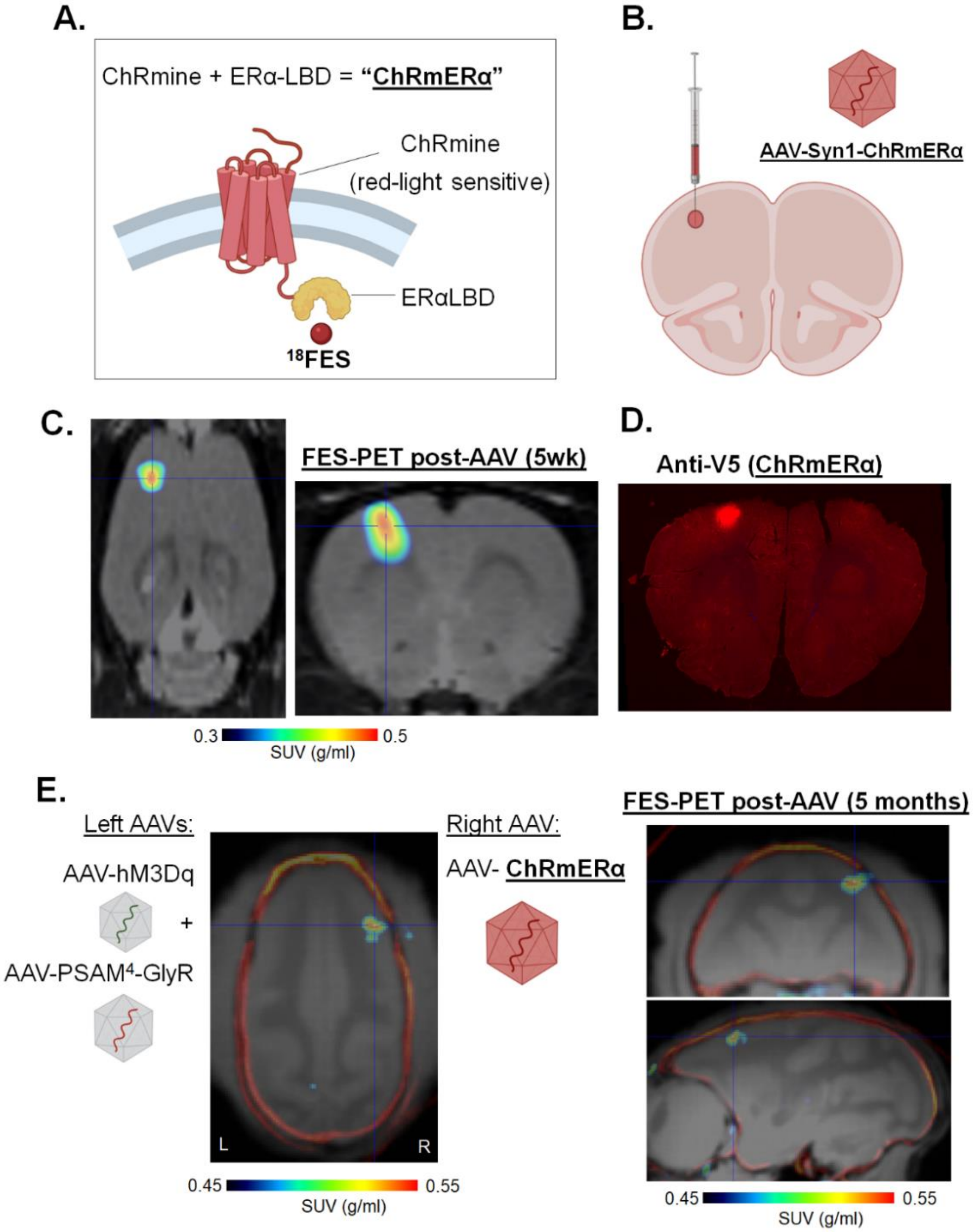

A. Schematic of "ChRmERα": combining ChRmine with ERαLBD to create a PET-compatible red-light sensitive opsin. **B.** Left motor cortex injection site for AAV-Syn1-V5-ChRmERα (AAV- ChRmERα) in rat. **C.** [^{18}F]FES-PET localizes ChRmERα in left M1 of rat ~5 weeks following intracranial injection of AAV-ChRmERα (avg SUV 10-50min). **D.** Immunofluorescent staining of rat brain tissue with anti-V5 (red) confirms ChRmERα expression in left M1. **E.** [^{18}F]FES-PET localizes ChRmERα in right cortex of squirrel monkey ~5 months following intracranial injection of dual chemogenetic AAVs (AAV-hM3Dq and AAV-PSAM^{4}-GlyR) in left cortex and AAV-ChRmERα in right cortex.

Figure B2. Imaging other transgenic constructs with ERαLBD and [^{18}F]FES-PET (i.e., PSAM-ERα and JAWS-ERα)

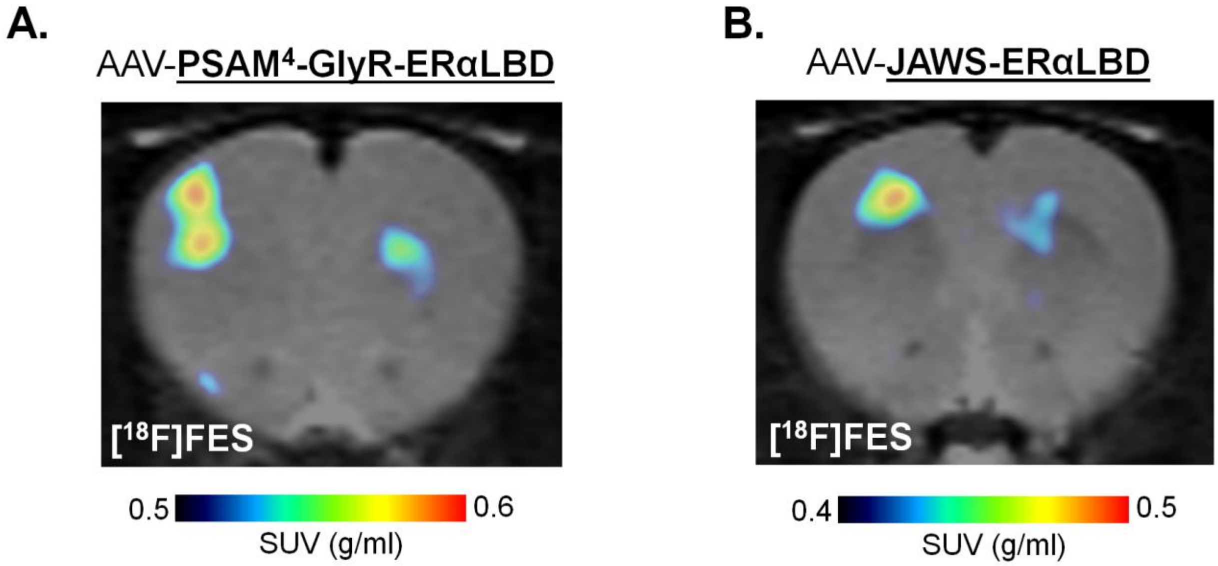

Figure B2. Imaging other transgenic constructs with ERαLBD and [^{18}F]FES-PET (i.e., PSAM-ERα and JAWS-ERα). A. [^{18}F]FES-PET in rat 6 months following intracranial injection of AAV-PSAM^4-GlyR-ERαLBD in left M1 (avg SUV g/ml 10-60min). **B.** [^{18}F]FES-PET in rat 6 months following intracranial injection of AAV-JAWS-ERαLBD in left M1 (avg SUV g/ml 10-60min).

Appendix C. Supplementary material for Chapter 3

Figure C1. Measuring brain activity with FDG-PET in rats: Group VOI correlation matrices showing effects of hM3Dq and PSAM^4-GlyR activation vs Saline

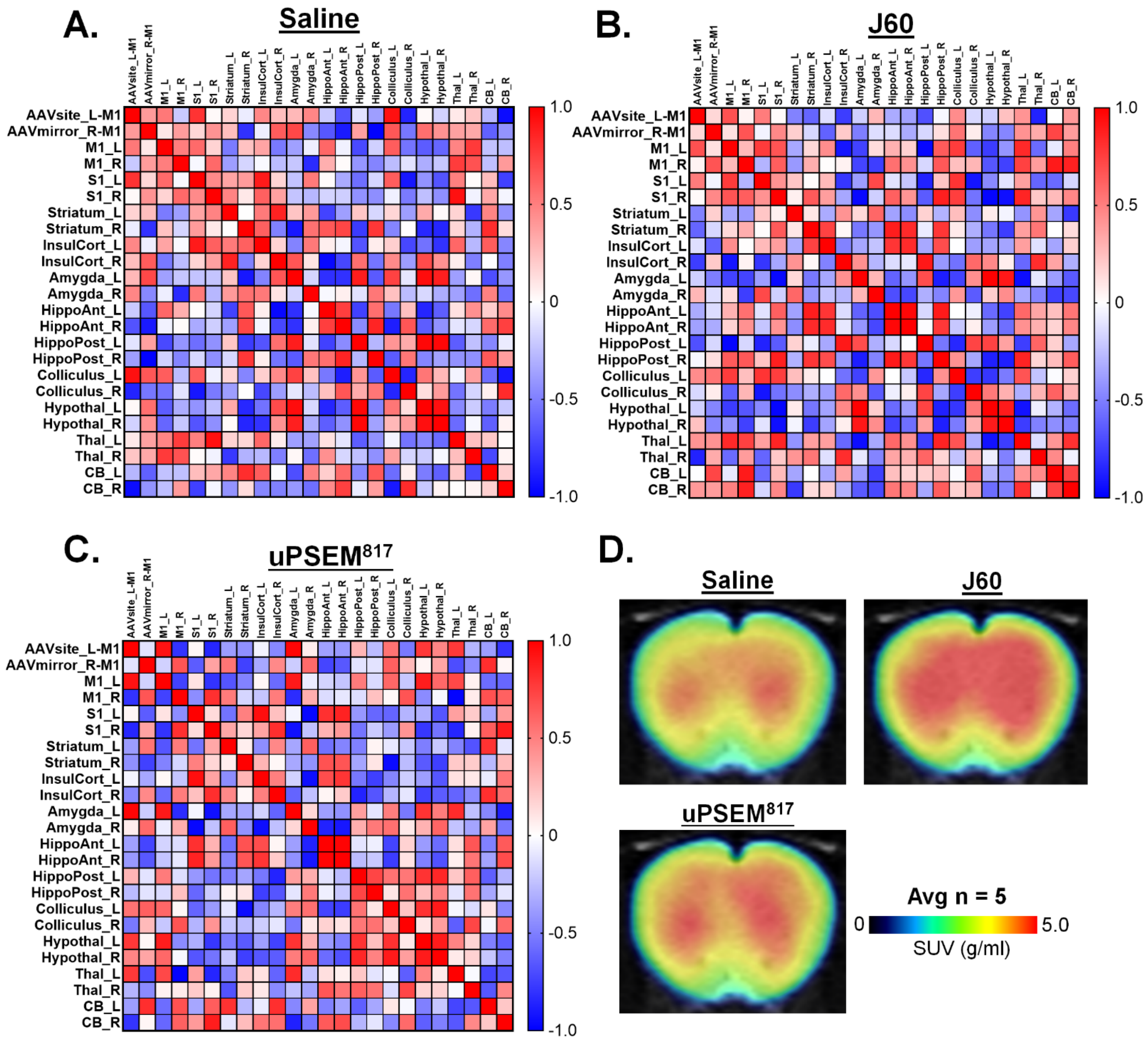

A-C. VOI correlation matrices from FDG-PET scans in hM3Dq/PSAM^4-GlyR rats (left M1 AAVs, n = 5) following treatment with saline (**A.**), 0.1 mg/kg J60 (**B.**) or 0.1 mg/kg uPSEM^{817} (**C.**). **D.** Coronal PET image of average FDG (SUV g/ml) in hM3Dq/PSAM^4-GlyR rats (left M1 AAVs, n = 5) following treatment with saline (top left), 0.1 mg/kg J60 (top right) or 0.1 mg/kg uPSEM^{817} (bottom left).

Figure C2. Localizing hM3Dq and PSAM^4-GlyR in rats with [^{18}F]J07 and [^{18}F]ASEM

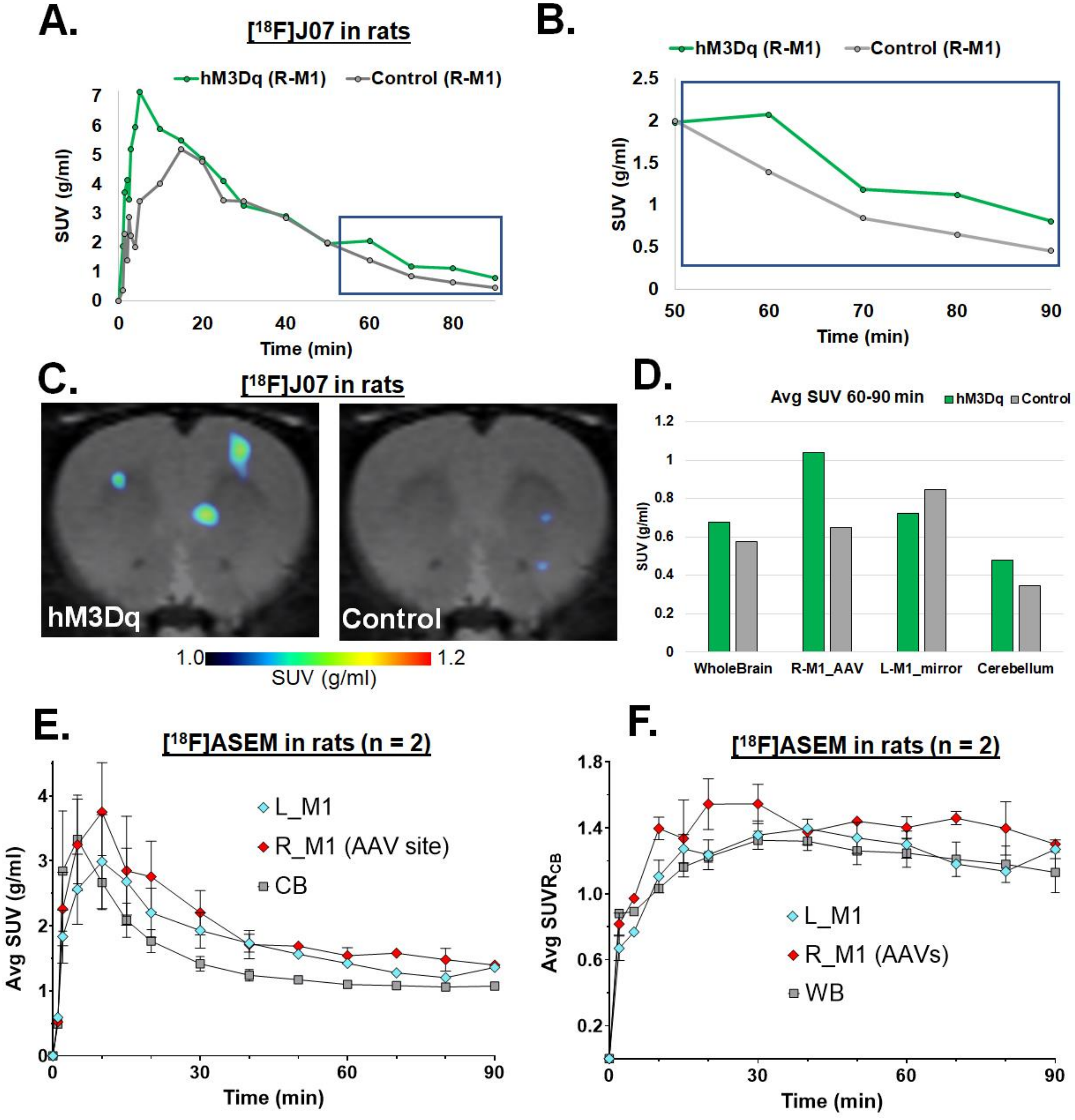

Figure C2. Localizing hM3Dq and PSAM4-GlyR in rats with [18F]J07 and [18F]ASEM.

A. Time activity curve of average SUV (g/ml) of [^{18}F]J07 in right M1 (AAV site) of a rat with hM3Dq/PSAM^4-GlyR AAVs (green) or control AAV (grey, AAV-ChRmERα), blue square indicates timeframe shown in **B** and averaged SUV period in **C** and **D**. **C.** Side by side comparison of [^{18}F]J07 (avg SUV 60-90min) in rat 10 months following intracranial M1 injection of hM3Dq/PSAM^4-GlyR AAVs (left) or control AAV (right). **D.** Avg SUV (g/ml) in whole brain, right M1 (AAV site), left M1 (AAV mirror) and cerebellum in hM3Dq/PSAM^4-GlyR rat (green) or control (grey). **E.** Time activity curve showing average SUV (g/ml) of [^{18}F]ASEM in right M1 (AAV site, red), left M1 (AAV mirror, light blue) and cerebellum (CB, grey) in two rats ~8 months following co-injection of hM3Dq/PSAM^4-GlyR AAVs in right M1 (n = 2). **F.** Time activity curve showing average SUV ratio ($SUVR_{CB}$ = SUV normalized to cerebellum average) of [^{18}F]ASEM in right M1 (AAV site, red), left M1 (AAV mirror, light blue) and whole brain (WB, grey) in two rats ~8 months following co-injection of hM3Dq/PSAM^4-GlyR AAVs in right M1 (n = 2).

Figure C3. Pre-AAV FDG-PET scans in squirrel monkeys

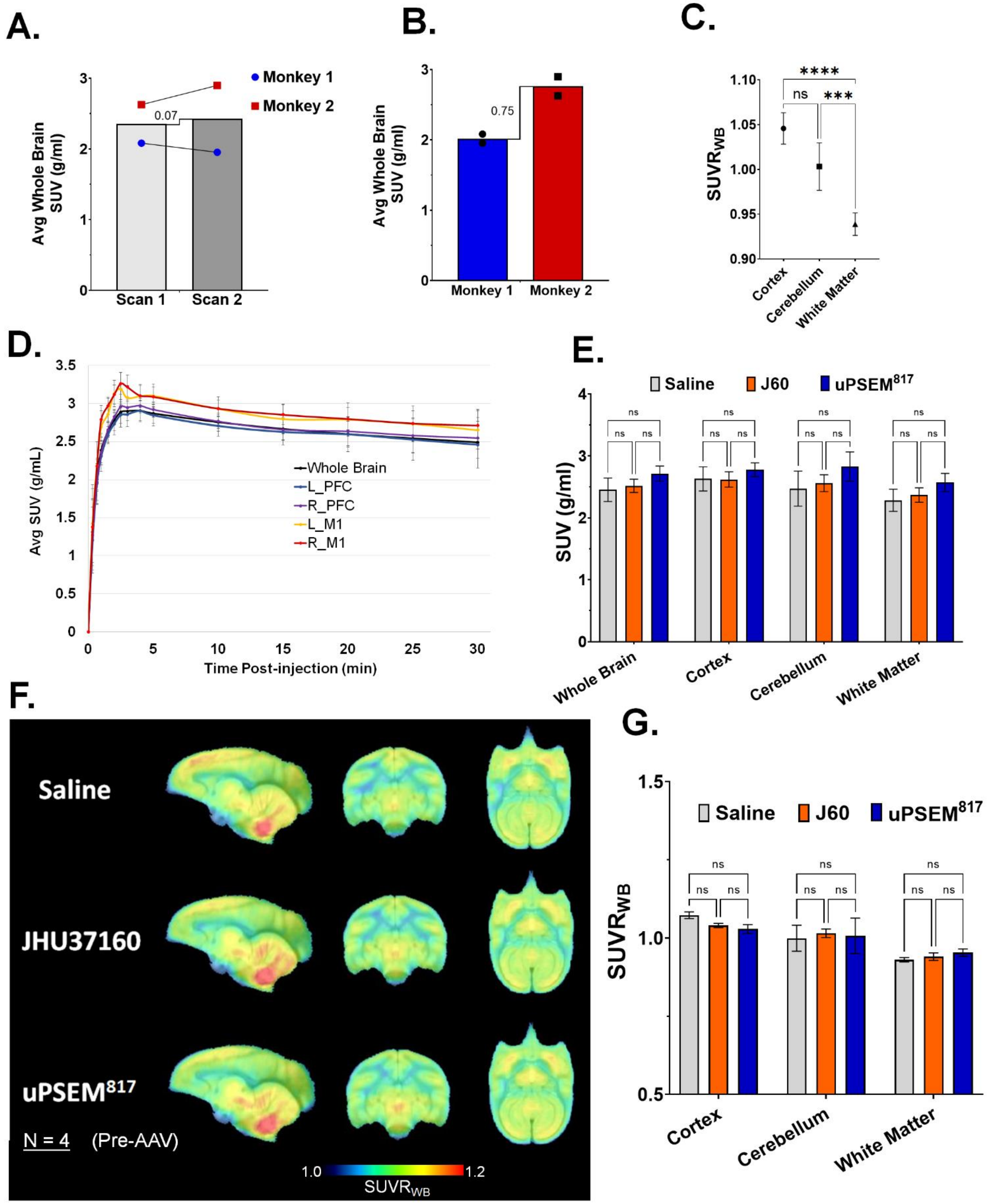

Figure C3. Pre-AAV FDG-PET scans in squirrel monkeys. A-B. Average whole brain uptake in baseline scan/re-scan (1-2 weeks apart) in two monkeys (blue circle = monkey 1, red square = monkey 2) prior to the introduction of AAVs. Average SUV (g/ml) is plotted by scan day (average within-subject difference between scan days = 0.07 g/ml) (**A**) and by subject (**B**) (average between-subject difference across scan days = 0.75 g/ml). **C.** Average SUV ratio (SUVR_{WB} = SUV normalized by whole brain average) in cortex, cerebellum and white matter from pre-AAV monkey FDG-PET scans (n = 4). **** = $p < 0.0001$, *** = $p < 0.001$. **D.** Time activity curves of dynamic FDG uptake in whole brain and cortical brain regions (prefrontal cortex (PFC) and motor cortex (M1)) following i.v. injection (~1.5 mCi) in baseline/saline treatment scans (n = 4). **E.** Group comparison by treatment (saline = grey, J60 = orange and uPSEM^{817} = blue) of average FDG uptake (SUV g/ml) in whole brain, cortex, cerebellum and white matter (n = 4, error bars = SEM). **F.** FDG-PET image comparisons of SUVR_{WB} (avg n = 4) in monkeys following treatment with saline (top), J60 0.1mg/kg (middle) or uPSEM^{817} (bottom). **G.** Comparisons of SUVR_{WB} (avg n = 4, error bars = SEM) in cortex, cerebellum and white matter following treatment with saline (grey), J60 0.1mg/kg (orange) or uPSEM^{817} (blue).

Figure C4. Pre-AAV [^{18}F]ASEM and [^{18}F]J07 PET scans in squirrel monkeys

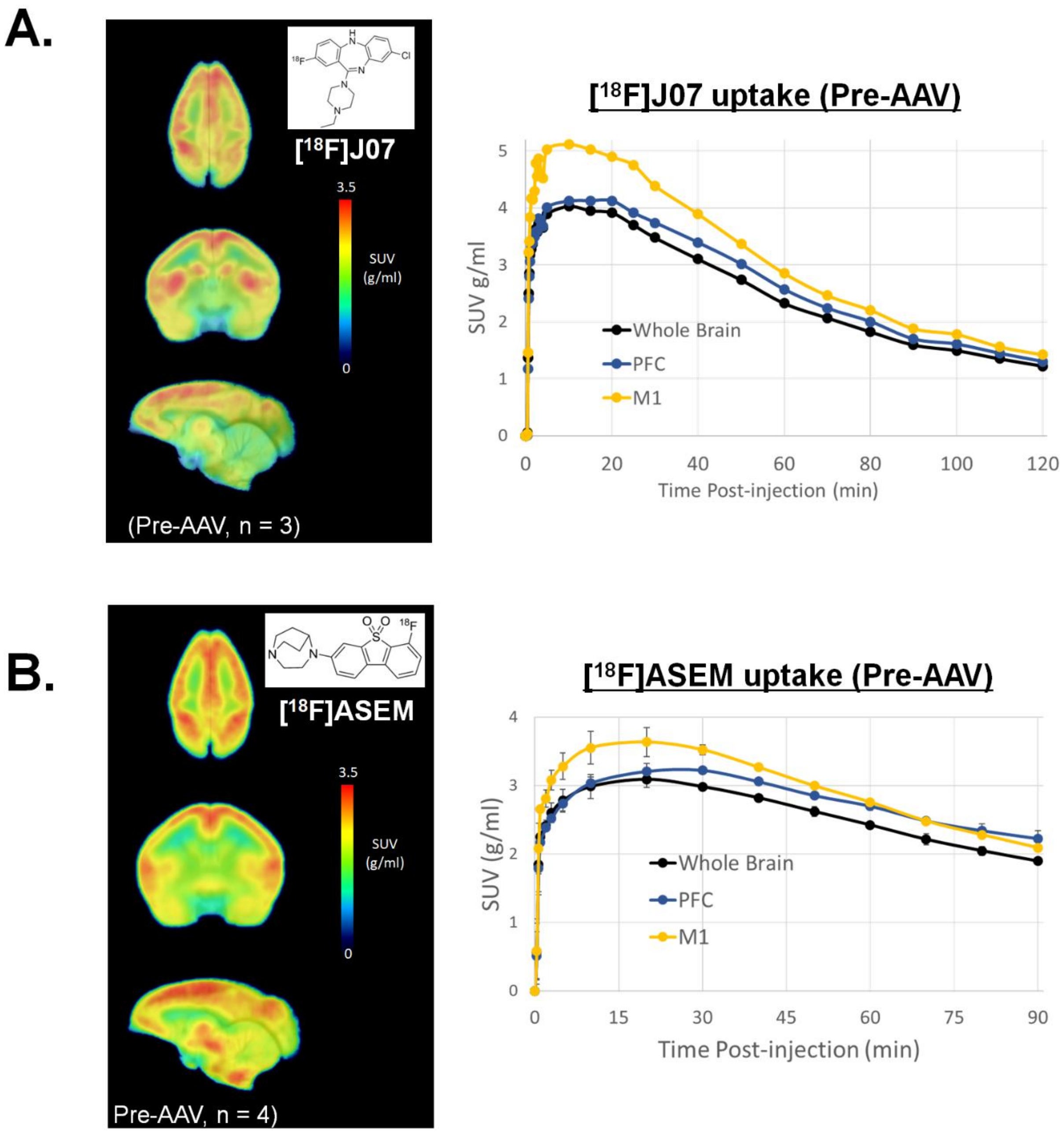

A. Left: PET image of average [^{18}F]J07 monkey scans pre-AAV (SUV g/ml, n = 3). Right: Time activity curve of average [^{18}F]J07 in whole brain, prefrontal cortex (PFC) and motor cortex (M1) in monkeys pre-AAV (SUV g/ml, n = 3). **B.** Left: PET image of average [^{18}F]ASEM monkey scans pre-AAV (SUV g/ml, n = 4). Right: Time activity curve of average [^{18}F]ASEM in whole brain, prefrontal cortex (PFC) and motor cortex (M1) in monkeys pre-AAV (SUV g/ml, n = 4).

Appendix D. Supplementary material for Chapter 4

Figure D1. Endogenous binding comparison of [^{18}F]ASEM, [^{18}F]J07 and [^{18}F]FES in pre-AAV squirrel monkeys

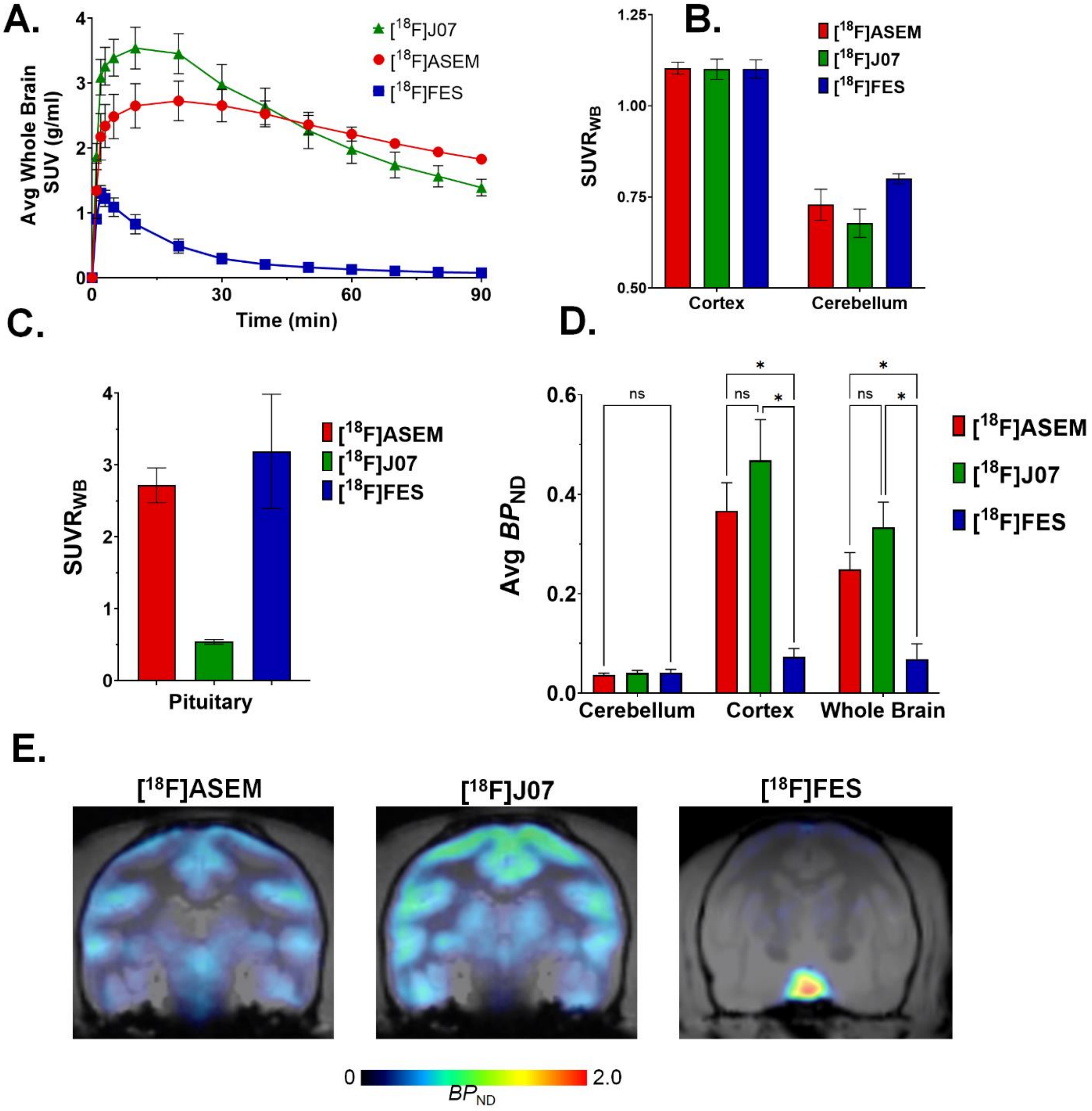

A. Time activity curves of average whole brain SUV following i.v. injection of radiotracers [^{18}F]ASEM (n = 4, red), [^{18}F]J07 (n = 3, green) and [^{18}F]FES (n = 2, blue) in monkeys without chemogenetic or optogenetic constructs. **B.** Average SUVR$_{WB}$ of cortex and cerebellum 60-90min post radiotracer injection. **C.** Average SUVR$_{WB}$ of pituitary 60-90min post radiotracer. **D.** Average *BP*$_{ND}$ comparison in cerebellum, cortex and whole brain follow [^{18}F]ASEM, [^{18}F]J07 or [^{18}F]FES (n = 2, blue). **E.** Representative PET images of [^{18}F]ASEM, [^{18}F]J07 and [^{18}F]FES endogenous binding in squirrel monkey.

Figure D2. A comparison of [^{18}F]J07, [^{18}F]ASEM and [^{18}F]FES for localizing transgene expression in squirrel monkeys

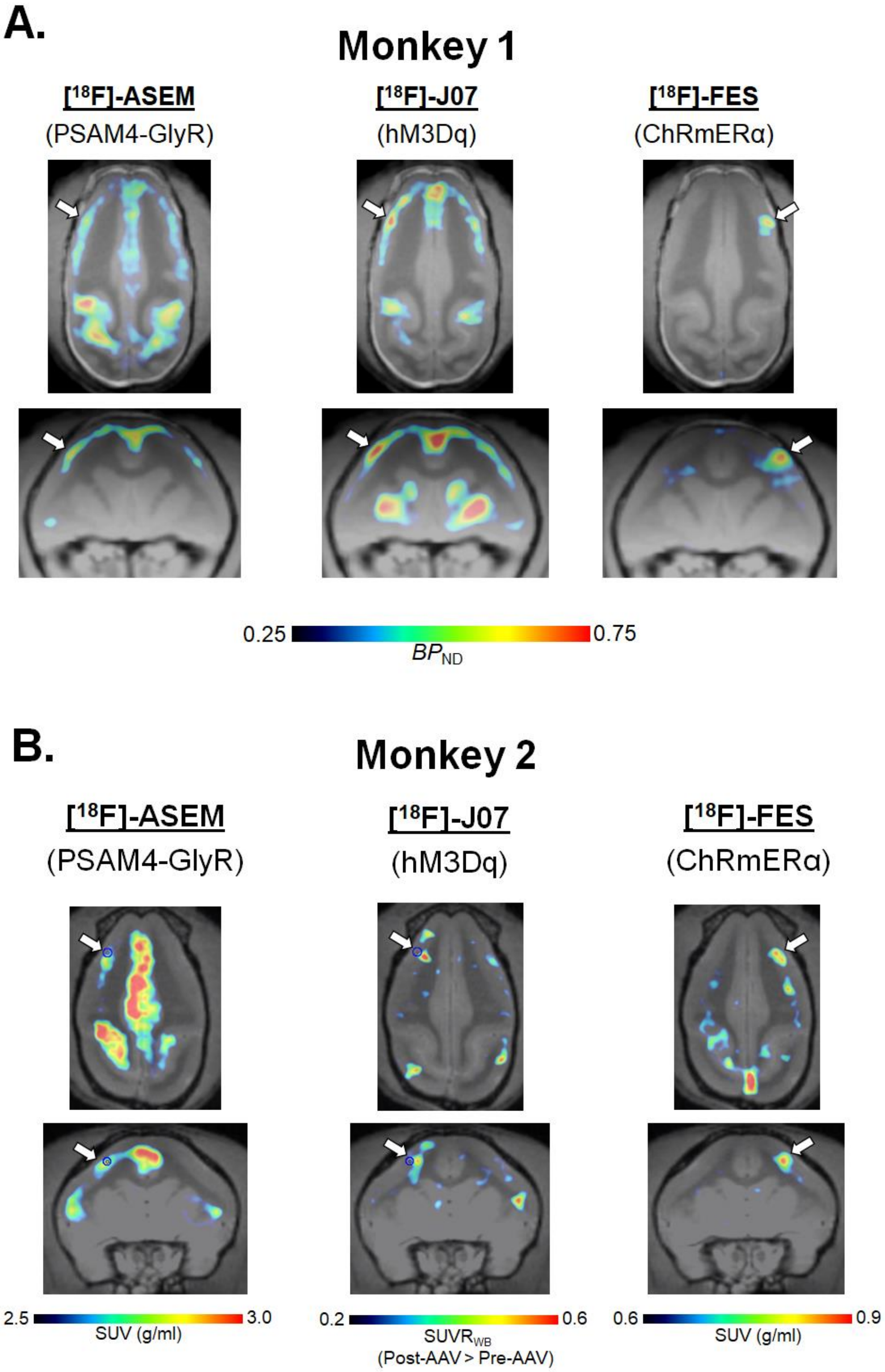

Figure D2. A comparison of [^{18}F]J07, [^{18}F]ASEM and [^{18}F]FES for localizing transgene expression in squirrel monkeys. A. Comparison of BP_{ND} in monkey 1 PET scans with [^{18}F]ASEM (left), [^{18}F]J07 (middle), and [^{18}F]FES (right) 6-10 months post-AAV surgery, white arrows indicate approximate area of AAV injections (hM3Dq/PSAM^4-GlyR AAVs in left hemisphere, ChRmERα AAV in right hemisphere. **B.** Comparison of monkey 2 PET scans with [^{18}F]ASEM (left, SUV g/ml), [^{18}F]J07 (middle, $\mathrm{SUVR}_{\mathrm{WB}}$ baseline subtraction), and [^{18}F]FES (right, SUV g/ml) 6-10 months post-AAV surgery, white arrows indicate approximate area of AAV injections (hM3Dq/PSAM^4-GlyR AAVs in left hemisphere, ChRmERα AAV in right hemisphere.

Figure D3. Baseline image subtraction method with FES-PET improves S:N for cleaner ChRERa visualization in squirrel monkey

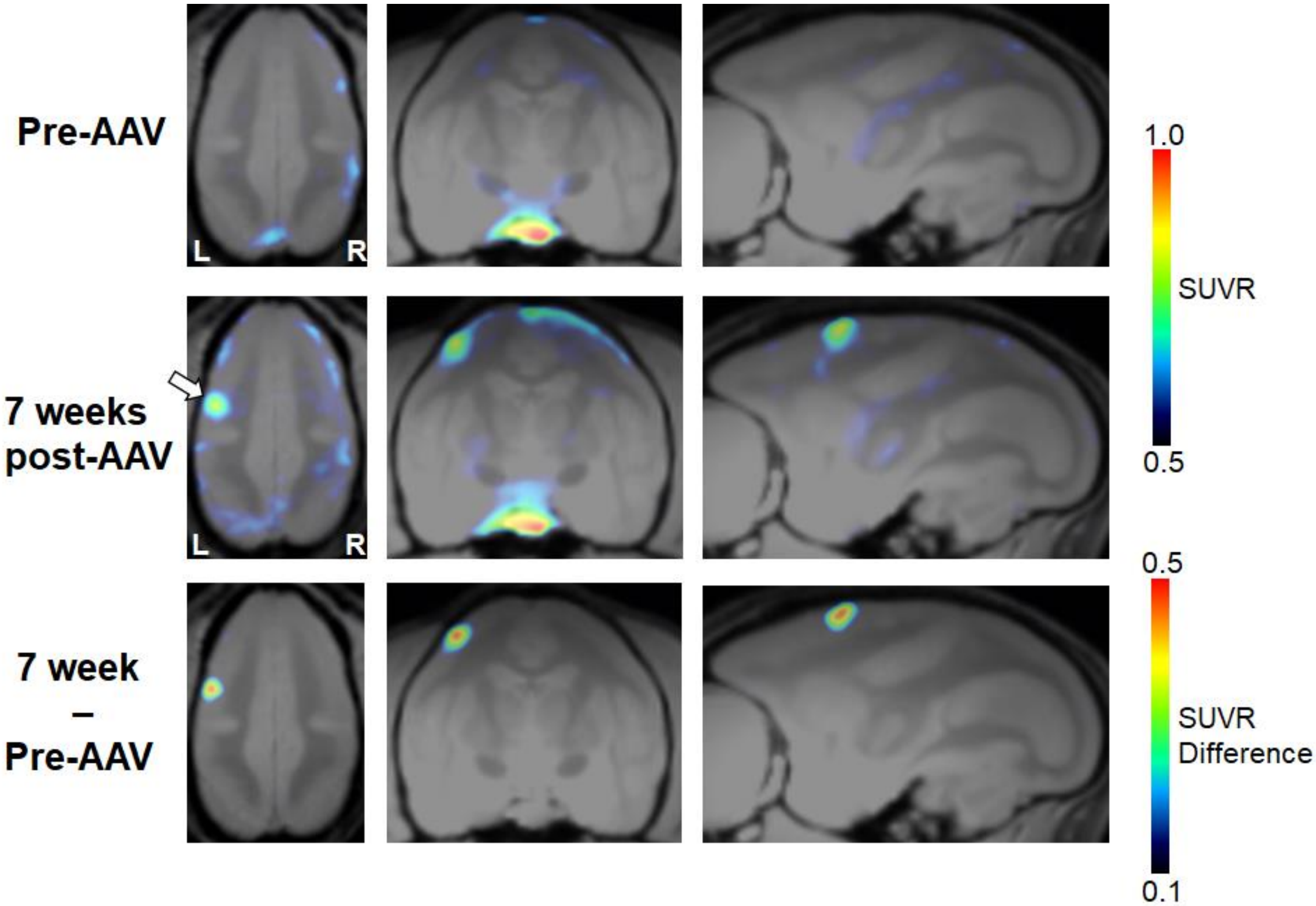

Top: FES-PET scan in squirrel monkey pre-AAV (i.e., baseline/endogenous binding), (SUVR = SUVR_{Pit}). **Middle:** FES-PET scan in same monkey 7 weeks post-AAV (AAV-ChRmERα in left M1), (SUVR = SUVR_{Pit}). **Bottom:** PET image subtraction ("7 weeks post-AAV" – "Pre-AAV) showing SUVR difference (i.e., greater FES-PET in post-AAV vs pre-AAV).